

**Photoinduced, Copper-catalyzed C–N and
C–C Bond Formation and Photocatalytic
Co-mediated Nitrite Reduction to N₂O:
Reactivity and Mechanism**

THESIS BY

Tanvi Siraj Ratani

In Partial Fulfillment of the Requirements for
the degree of
Doctor of Philosophy

The logo for the California Institute of Technology (Caltech), featuring the word "Caltech" in a bold, orange, sans-serif font.

CALIFORNIA INSTITUTE OF TECHNOLOGY
Pasadena, California

2018
(Defended: October 30, 2017)

© 2017

Tanvi Siraj Ratani

All Rights Reserved

Acknowledgments

Contrary to popular or romantic notions of the life of a scientist, modern science cannot be done in a social vacuum or in an ivory tower. It is as human an enterprise as anything one might find in the “real” world, if not more so. Scientific training and competence is impacted deeply by advisors, institutions, and colleagues; early inspiration in scientific curiosity, by teachers, role models, and peers. I have had the privilege of going on this formative journey that is graduate school thanks to the influence of many people who have pushed, criticized, encouraged, and improved me, and I would like to take some time now to acknowledge them.

First and foremost, I must thank Jonas Peters for taking a “green” young chemist into his group five years ago. I’m a little less “green” now, I hope, and I owe him for much of my scientific growth. Jonas has allowed me a healthy amount of creative independence to follow my curiosity, while also patiently (and persistently) teaching me to make statements that are rigorously correct. Watching Jonas these past five years, I’ve learned that being a scientific leader means more than being a fountain of knowledge, which he undoubtedly is; it also means resolving conflict, sticking to your guns, and asking the tough questions. I’m sure I will continue to emulate his style as I progress in my career.

I would also like to thank my thesis committee, Professors Greg Fu, Harry Gray, and Theo Agapie for their advice during my exams, on my research, and about my future. Greg has been a second advisor since my copper days. I admire his meticulous approach to chemistry, and I hold myself to a higher intellectual standard because of him. Harry

has always been my cheerleader, and dealt with me as though I were one of his own students. I appreciate his kindness as much as I do his intelligence.

In one way or another, Jay Winkler has had a hand in almost every major experiment I have done. He built the laser set-ups, wrote the programs to run them, wrote codes to analyze the data, and has never once said that a measurement is not possible to make. Whether it's kinetics, how to run an experiment, or panic at the thought of ruining millions of dollars of equipment, I've always been able to knock on Jay's office door when I needed to chat. In addition to Jay, Oliver Shafaat and Wes Sattler mentored me immensely when I was learning the ins and outs of "bespoke" laser configurations and Matlab. I'm thankful for Wes' random photochemistry quizzes which kept (and keep) me on my toes, and am excited to work with him at Dow.

I have had the good fortune of incredibly talented coworkers, far too many to name individually. I specifically thank those who I wrote manuscripts with for their efforts: Shoshana Bachman, for showing me the ropes of organic methodology the way Greg likes it; Joe Ahn, for his insights during the long and rewarding journey that was our C–N paper; and Ben Matson for his computational skills, initial work on nitrite reduction, and friendship.

When I first came to Caltech, the formidable Jon Rittle (forever JR) helped me with my first synthesis, and many more since. I took over Charlene Tsay's chemistry when I first got started in the group, and gained from her both valuable synthetic insight and a Downton buddy at dinner. John Anderson, Hill Harman, Dan Suess, Sam MacMillan, Tzu-Pin Lin, Charles McCrory, and Henry Fong have all discussed chemistry with me, and I appreciate the insightful conversations which shaped my early years. I

thank Chris Uyeda for opening up some beautiful cobalt chemistry which I discuss in Chapter 4.

Matt Chalkley has always been wise beyond his years, both scientifically and in his social graces. It's been a pleasure to sit next to you these last few years. Gaël Ung was another neighbor who ensured I kept my sanity through most of grad school, and showed me the value of kindness at a pressure-cooker Institute. Sid Creutz took me on many outdoor adventures, and is the only person in the world I trust to keep me alive as I hang onto a rope 150 feet up in the air. I enjoyed our trips to Yosemite and Joshua Tree, and learned how important it is to keep doing the things you love amid the crazy hours in graduate school.

I admire Dr. (!) Trixia Buscagan's ability to stand up for herself (and so many other women) in difficult situations. Shabnam Hematian is a thorough scientist, and I have been lucky to have such an expert NO chemist read my drafts and show me how to properly purify NO gas; she has been a role model to me in many ways, and an excellent friend. Julianne Just has offered a thoughtful perspective on many life decisions, and I am grateful for her friendship and cat advice. I thank Nina Gu, Kareem Hannoun, Marcus Drover, Gerri Roberts, Jian He, and Nik Thompson for discussions about life, journals, and science. Many thanks to Cooper Citek for knowing everything about everything and carrying Team Inspector Gadget to many second place trivia victories! To all the people I have overlapped with in the group, including Kumiko Yamamoto, Mark Nesbit, Trevor del Castillo, Javier Fajardo, Koichi Nagata, Miles Johnson, Joe Roddy, and Meaghan Deegan, I wish you the best of luck in what will undoubtedly be great careers.

I would like to thank many good friends outside of my home lab at Caltech who have made grad school not just tolerable, but so incredibly fun. Brian Sanders has been a trivia, football, and cat-appreciation buddy. It has been fun to discuss lasers and weird life phobias/situations with him. I thank Wes Kramer, Bryan Hunter, Jieun Shin, and Brendon McNicholas for their friendship and less-than-sober company at SCIPs. I admire the way Josh Buss pours all of himself into whatever he is doing, whether it is rewriting problem sets to look nice or his own chemistry. I look forward to reading your future work. Liz O'Brien has been an empathetic and driven friend with whom I could share my triumphs and failures equally, freely, and without judgment. I can't wait to hang out with you and your family at The Shore. I'm thankful to Aaron and Wes Sattler for inviting me to fun-/science-filled LA and pool shenanigans; I'm sure that our friendship will be a long one, especially now that we will be on the same coast. Thanks also to Paul Walton, Jenna Bush, Noah Duffy, and JingXin Liang (and, of course, Stella Bella) for entertaining conversations, too much wine (and cheddar-esque cheese only), and Ice House nights. To Ubah Ali and Ashley Hill, thank you for the phone calls and the visits – it's been so important to have perspective from the outside world.

I would be remiss without thanking the exceptional staff scientists at Caltech who have helped me acquire and think about my data on many occasions. Dave VanderVelde helped me from day one with low temperature NMR, and has since assisted with many NMR experiments. Nathan Dalleska was instrumental in acquiring the GC-MS data in Chapter 4. Mona Shahgholi is a wizard at acquiring mass spec data, and I have appreciated her input and goodwill over the years. Larry Henling has helped with the

crystal structures in this thesis (and those that were too horrible to publish). I thank him for his patience with my awful crystals, his sense of humor, and for his friendship.

My love for science, and chemistry in particular, started long before I had the opportunity to come to Caltech. My first chemistry teacher, Mr. Cook, at Heritage High School in Saginaw, MI was so patient with my constant barrage of questions too early in the morning (Why is glass clear? Why are metals shiny?). He encouraged me to answer my questions with experiments early on, and I knew then that I was going to do chemistry forever. Thanks also to Mr. and Mrs. Richardson for showing me the beauty in the humanities, which is truly a half of me. I must acknowledge Professors Raoul Kopelman and Nate Szymczak at Michigan for allowing me to bang around in lab until I figured out what was going on. Nate has been a mentor to me even at Caltech, checking in on me every once in a while and showing genuine care for my overall progress and well-being.

I now thank the people who have shown me the most love in my life. Dirk Schild has been a friend and partner to me these last few years, and showed me the beauty of his love and acceptance, even when I had difficulty accepting myself. Thank you. Finally, Mummy and Papa, I'm so thankful for all the opportunities you have provided me. You knew what I needed before I could even form the words, and you made me feel like I could achieve anything I set my mind to. I love you more than anything else. I promise I'll come home a lot more often now!

Abstract

Photocatalytic reactions with first-row transition metals are presented as a method for sustainable chemistry with great potential for new forms of reactivity and mechanistic pathways. Chapters 2 and 3 of this thesis discuss mechanism and reactivity of photoinduced, copper-catalyzed bond constructions. The Peters and Fu groups have reported that a variety of couplings of nitrogen, sulfur, oxygen, and carbon nucleophiles with organic halides can be achieved under mild conditions (-40 to 30 °C) through the use of light and a copper catalyst. Insight into the various mechanisms by which these reactions proceed may enhance our understanding of chemical reactivity and facilitate the development of new methods. We apply an array of tools (EPR, NMR, transient absorption, and UV-vis spectroscopy; ESI-MS; X-ray crystallography; DFT calculations; reactivity, stereochemical, and product studies) to investigate the photoinduced, copper-catalyzed coupling of carbazole with alkyl bromides. Our observations are consistent with pathways wherein both an excited state of the copper(I) carbazolide complex ($[\text{Cu}^{\text{I}}(\text{carb})_2]^-$) and an excited state of the nucleophile ($\text{Li}(\text{carb})$) can serve as photoreductants of the alkyl bromide. The catalytically dominant pathway proceeds from the excited state of $\text{Li}(\text{carb})$, generating a carbazyl radical and an alkyl radical. The cross-coupling of these radicals is catalyzed by copper via an out-of-cage mechanism in which $[\text{Cu}^{\text{I}}(\text{carb})_2]^-$ and $[\text{Cu}^{\text{II}}(\text{carb})_3]^-$ (carb = carbazolide), both of which have been identified under coupling conditions, are key intermediates, and $[\text{Cu}^{\text{II}}(\text{carb})_3]^-$ serves as the persistent radical that is responsible for predominant cross-coupling. This study underscores the versatility of copper(II) complexes in engaging with radical intermediates that are generated by disparate pathways, *en route* to targeted bond constructions.

In Chapter 3, we establish that photoinduced, copper-catalyzed alkylation can also be applied to C-C bond formation, specifically, that the cyanation of unactivated secondary alkyl chlorides can be achieved at room temperature to afford nitriles, an important class of target molecules. In the presence of an inexpensive copper catalyst (CuI ; no ligand coadditive) and a readily available light source (UVC compact fluorescent light bulb), a wide array of alkyl halides undergo cyanation in good yield. Our

initial mechanistic studies are consistent with the hypothesis that an excited state of $[\text{Cu}(\text{CN})_2]^-$ may play a role, via single electron transfer, in this process. This investigation provides a rare example of a transition metal-catalyzed cyanation of an alkyl halide, as well as the first illustrations of photoinduced, copper-catalyzed alkylation with either a carbon nucleophile or a secondary alkyl chloride.

Chapter 4 presents a mechanistic study of the photocatalytic reduction of nitrite to nitrous oxide with the use of an Ir photocatalyst ($[\text{Ir}(\text{ppy})_2(\text{phen})][\text{PF}_6]$) and a bimetallic CoMg co-catalyst with a diimine-dioxime ligand platform. Insights into the mechanism of this reaction may enhance our current understanding of N–N coupling processes relative to other pathways of reactivity for nitrosyl ligands, such as nitroxyl (HNO) dimerization. We propose a mechanism in which a coordinated and an uncoordinated $\bullet\text{NO}$ are coupled at a single Co center. One electron reduction of $[(\text{Cl})(\text{NO})\text{Co}(\text{Me}^{\text{e}}\text{doen})\text{Mg}(\text{Me}_3\text{TACN})(\text{H}_2\text{O})][\text{BPh}_4]$ ($\{\text{CoNO}\}^8$), a species we show to be catalytically relevant, forms a $\{\text{CoNO}\}^9$ species that is characterized by UV-Vis, EPR, and FT-IR spectroscopy and whose electronic structure is supported by density functional theory (DFT). We formulate the $\{\text{CoNO}\}^9$ as a 5-coordinate, $S = 3/2$ Co(II) antiferromagnetically coupled with an anionic $S = 1$ $^3\text{NO}^-$ ligand. Experimental data suggest a mechanism in which this $\{\text{CoNO}\}^9$ intermediate can release $\bullet\text{NO}$, thereby reducing the Co(II) center to Co(I). This free $\bullet\text{NO}$ can react with another $\{\text{CoNO}\}^9$ complex to generate a $\text{Co}(\text{NONO})$ intermediate which was observed by step-scan time-resolved IR spectroscopy and whose assignment was supported with DFT calculations. This $\text{Co}(\text{NONO})$ species, which can generate N_2O and H_2O , is formulated as a neutral hyponitrite intermediate with significant neutral radical character on both nitrosyl nitrogen atoms and a weak N–N bond.

Published Content and Contributions

This dissertation contains material adapted with permission from the following published manuscripts:

1. Ahn, J. M.;[†] **Ratani, T. S.**;[†] Hannoun, K. I.; Fu, G. C.; Peters, J. C. *J. Am. Chem. Soc.* **2017**, *139*, 12716–12723.

DOI: 10.1021/jacs.7b07052

TSR participated in experiments, data analysis, and manuscript preparation.

2. **Ratani, T.S.**;[†] Bachman, S.;[†] Fu, G. C.; Peters, J. C. *J. Am. Chem. Soc.* **2015**, *137*, 13902–13907.

DOI: 10.1021/jacs.5b08452

TSR participated in experiments, data analysis, and manuscript preparation.

[†]Equal Contributions

Table of Contents

Acknowledgements.....	iii
Abstract.....	viii
Published Content and Contributions	x
Table of Contents.....	xi
List of Figures.....	xv
List of Schemes.....	xx
List of Tables	xxi
Abbreviations.....	xxiii
Chapter 1 : Introduction	1
1.1 Motivations.....	2
1.2 Photoinduced, Copper-Catalyzed Cross-Coupling Reactions.....	5
1.3 Photoredox Catalysis for Nitrite Reduction	15
1.4 Time-Resolved Laser Spectroscopy.....	17
1.5 Chapter Summaries	20
1.6 References	22
Chapter 2 : Photoinduced, Copper-Catalyzed Alkylation of Amines: A Mechanistic Study of the Cross-Coupling of Carbazole with Alkyl Bromides.....	27
2.1 Introduction.....	28
2.2 Results and Discussion.....	31
2.2.1 Background.....	31
2.2.2 Stoichiometric coupling of $[\text{Cu}^{\text{I}}(\text{carb})_2]\text{Li}$ (1) with an alkyl bromide	31
2.2.3 Excitation of $[\text{Cu}^{\text{I}}(\text{carb})_2]\text{Li}$	32
2.2.4 Single electron transfer (SET) from $[\text{Cu}^{\text{I}}(\text{carb})_2]\text{Li}^*$ to an alkyl bromide.....	33
2.2.5 SET from $[\text{Li}(\text{carb})]^*$ to an alkyl bromide.....	34
2.2.6 Evidence for the presence of $[\text{Cu}^{\text{I}}(\text{carb})_2]\text{Li}$ under catalysis conditions.....	39
2.2.7 Evidence for the presence of $[\text{Cu}^{\text{II}}(\text{carb})_3]\text{Li}$ (2) under catalysis conditions ...	39
2.2.8 Evidence for out-of-cage C–N bond formation via a free-radical intermediate under catalysis conditions	46
2.2.9 Evaluation of a radical chain mechanism under catalysis conditions.....	48
2.3 Conclusions	49
2.4 References	51

Chapter 3 : Photoinduced, Copper-Catalyzed Carbon–Carbon Bond Formation with Alkyl Electrophiles: Cyanation of Unactivated Secondary Alkyl Chlorides at Room Temperature	56
3.1 Introduction.....	57
3.2 Results and Discussion.....	59
3.2.1 Optimization and Scope.....	59
3.2.2 Mechanistic Observations.....	64
3.3 Conclusion.....	70
3.4 References.....	71
Chapter 4 : Photocatalytic Nitrite Reduction on Heterobimetallic Cobalt-Magnesium Complexes: Mechanistic Insights into N–N Bond Formation	77
4.1 Introduction.....	78
4.2 Results and Discussion.....	82
4.2.1 Photocatalysis with [(Br)(μ -OAc)Co(^{Me} doen)Mg(Me ₃ TACN)][BPh ₄] (1).....	82
4.2.2 Identification of (NO ₂)Co(^{Me} doen)Mg(Me ₃ TACN) complex under photochemical conditions.....	83
4.2.3 Characterization and reactivity of a {CoNO} ⁹ complex.....	86
4.2.4 N–N Coupling Step.....	91
4.3 Conclusions.....	98
4.4 References.....	100
Appendix A : Supplementary Information for Chapter 2	108
A.1 General Information.....	109
A.2 Preparation of Substrates.....	114
A.3 Procedures for Photoinduced Cross-Couplings.....	117
A.3.1 General procedure for the coupling of alkyl bromides.....	117
A.3.2 Procedure for the photolytic reaction in the absence of copper.....	118
A.3.3 Procedure for standard photolytic reactions at varying reaction concentrations.....	119
A.3.4 Procedure for stoichiometric coupling of [Cu ^I (carb) ₂ Li* with 2-bromo-4-phenylbutane (Eq 4 in Chapter 2).....	119
A.3.5 Procedure for the time-course analysis of reactions with and without [Li(MeCN) _n][Cu(carbazolide) ₂].....	120
A.4 Preparation of Metal Carbazolides.....	123
A.4.1 Preparation of [Li(MeCN) _n][Cu(carbazolide) ₂].....	123
A.4.2 Preparation of Li(carbazolide) (13390-92-6).....	123
A.4.3 Preparation of [K(benzo-15-crown-5) ₂][Cu ^{II} (carbazolide) ₃].....	124

A.5 Procedures for Freeze-Quench EPR Studies	125
A.5.1 Stoichiometric reaction between [Li(MeCN)][Cu(carb) ₂] and 2-bromo-4-phenylbutane under irradiation	125
A.5.2 Detection of EPR active [Li(CH ₃ CN) _n][Cu ^{II} (carb) ₃] in a catalytic reaction mixture	125
A.5.3 Generation and detection of EPR active [Li(CH ₃ CN) _n][Cu ^{II} (carb) ₃] via metallation.....	126
A.5.4 Detection of EPR active [Li(CH ₃ CN) _n][Cu ^{II} (carb) ₃] via oxidation of [Li(MeCN)][Cu(carb) ₂].....	126
A.6 Procedures for UV-vis studies.....	128
A.6.1 Molar absorptivity of [Li(CH ₃ CN) _n][Cu ^{II} (carb) ₃] at 580 nm	128
A.6.2 Detection of [Li(CH ₃ CN) _n][Cu ^{II} (carb) ₃] during catalysis	129
A.6.3 Generation and detection of [Li(CH ₃ CN) _n][Cu ^{II} (carb) ₃] via oxidation of [Li(MeCN)][Cu(carb) ₂].....	130
A.6.4 Molar absorptivity of [Li(MeCN)][Cu(carbazolide) ₂] at 365 nm.....	131
A.6.5 Molar absorptivity of lithium carbazolide at 365 nm	132
A.7 Procedures for DOSY Analysis.....	134
A.8 Actinometric Studies	136
A.8.1 Determination of light intensity	136
A.8.2 Determination of quantum yield for stoichiometric model reaction.....	136
A.9 Stern-Volmer Quenching and Determining Quenching Efficiency	138
A.9.1 Quenching of [Li(MeCN)][Cu(carbazolide) ₂] with electrophile	138
A.9.2 Quenching of lithium carbazolide with electrophile.....	140
A.9.3 Self-quenching of [Li(MeCN)][Cu(carbazolide) ₂]	141
A.9.4 Self-quenching of lithium carbazolide	143
A.9.5 Quenching efficiency of lithium carbazolide.....	144
A.10 Reactivity of [Li(CH ₃ CN) _n][Cu ^{II} (carb) ₃].....	146
A.10.1 Decomposition of [Li(CH ₃ CN) _n][Cu ^{II} (carb) ₃]	146
A.10.2 Decomposition of [Li(CH ₃ CN) _n][Cu ^{II} (carb) ₃] in the presence of TEMPO-H	146
A.11 Computational Methods	148
A.12 Characterization data for new coupling products.....	151
A.13 ¹ H, ² H, and ¹³ C NMR spectra of new compounds.....	154
A.14 X-Ray Crystallography Data	172
A.15 References	181

Appendix B : Supplementary Information for Chapter 3	183
B.1 General Information	184
B.2 Preparation of Electrophiles	185
B.3 Photoinduced, Copper-Catalyzed Cyanation Reactions	188
B.4 Electrophile Competition Experiments	202
B.5 ¹ H NMR Spectra	203
Appendix C : Supplementary Information for Chapter 4	220
C.1 General Information	221
C.2 Procedure for Photocatalytic Nitrite Reduction.....	224
C.3 UV-Vis Absorbance and Fluorimetry Experiments	226
C.4 Stern-Volmer Quenching.....	227
C.5 EPR Spectroscopy of {CoNO} ⁹	229
C.6 Infrared Spectroscopy	231
C.7 GC-MS Data	234
C.8 Step-scan TRIR Data	236
C.9 Synthesis of [(NO)Co(^{Me} doen)Mg(Me ₃ TACN)][(BPh ₄) ₂] (5)	238
C.10 DFT Calculations.....	240
C.11 X-Ray Structure of 5	242
C.12 References	276

List of Figures

Chapter 1

Figure 1.1: Reactivity of Cu(I)-nucleophile complexes with (a) 1-bromonaphthalene and 4-chlorobenzonitrile and (b) <i>o</i> -(allyloxy)iodobenzene	9
Figure 1.2: Reactivity of P(<i>m</i> -tol) ₃ Cu(carb) with deuterated <i>o</i> -(allyloxy)iodobenzene ..	11
Figure 1.3: The scope of C–N bond forming reactivity accessed with photoinduced, Cu-catalyzed cross coupling reactions.....	12
Figure 1.4: Expanding the scope of photoinduced, Cu-catalyzed cross coupling reactions to thiol, alcohol, and cyanide nucleophiles	13

Chapter 2

Figure 2.1: Outline of a possible pathway for photoinduced, copper-catalyzed cross-couplings	29
Figure 2.2: Outline of a possible pathway for the photoinduced, copper-catalyzed cross-coupling of Li(carb) with an alkyl bromide.....	32
Figure 2.3: (a) Difference absorption spectra of [Cu ^I (carb) ₂ Li]* at selected time delays (b) Quenching of [Cu ^I (carb) ₂ Li]* by 2-bromo-4-phenylbutane	33
Figure 2.4: EPR spectra of [Cu ^I (carb) ₂ Li] in the presence of 2-bromo-4-phenylbutane or Magic Blue.....	34
Figure 2.5: Impact of a copper catalyst on C–N cross-coupling.	35
Figure 2.6: (a) Absorption and emission spectra of [Li(carb)]	36
Figure 2.7: Quenching of [Li(carb)]* by 2-bromo-4-phenylbutane	38
Figure 2.8: Outline of a new possible pathway for photoinduced, copper-catalyzed cross-coupling of Li(carb) with an alkyl bromide.	39
Figure 2.9: EPR evidence for [Cu ^{II} (carb) ₃ Li] (2), generated through three independent pathways.	40
Figure 2.10: UV–vis spectra of [Cu ^{II} (carb) ₃ Li] (2), generated through three independent pathways.....	42
Figure 2.11: (a) X-ray crystal structure of [Cu ^{II} (carb) ₃][K(THF) ₆] (b) DFT-computed spin-density plot of [Cu ^{II} (carb) ₃] [−]	43
Figure 2.12: Appearance of an absorption band for [Cu ^{II} (carb) ₃ Li] upon irradiation of a catalytic reaction mixture.....	45

Figure 2.13: Product distribution in the photoinduced, copper-catalyzed coupling of Li(carb) with 2-bromo-4-phenylbutane	46
---	----

Chapter 3

Figure 3.1: Outline of one of the possible pathways for photoinduced, copper-catalyzed cyanations of unactivated secondary alkyl chlorides	65
---	----

Figure 3.2: Absorption spectrum of $[\text{Cu}(\text{CN})_2]\text{TBA}$ in CH_3CN at room temperature.	69
--	----

Chapter 4

Figure 4.1: Initially proposed mechanism of electrocatalytic nitrite reduction	84
---	----

Figure 4.2: UV-Vis spectra of an irradiated catalytic mixture with and without Co.....	86
---	----

Figure 4.3: (a) FT-IR spectrum of putative $\{\text{CoNO}\}^9$ (b) EPR spectrum of putative $\{\text{CoNO}\}^9$	89
--	----

Figure 4.4: (a) Appearance of Co(I)- NO_2 species upon reduction of $\{\text{CoNO}\}^8$ in the presence of $[\text{N}(n\text{-Bu})_4][\text{NO}_2]$	90
---	----

Figure 4.5: TRIR data of photoreduced $\{\text{CoNO}\}^8$	93
--	----

Figure 4.6: Summary of DFT data obtained via optimization of three $\{\text{Co}(\text{NO})_2\}^{10}$ isomers	97
---	----

Appendix A

Figure A.1: Emission spectrum of 100-W Blak-Ray Long Wave Ultraviolet Lamp	111
--	-----

Figure A.2: Time-course analysis of the standard reaction mixture in the absence of Cu(I).....	120
---	-----

Figure A.3: Time-course analysis of the standard catalysis reaction mixture.	121
--	-----

Figure A.4: X-Band EPR spectra of $[\text{K}(\text{benzo-15-crown-5})_2][\text{Cu}^{\text{II}}(\text{carbazolide})_3]$ in butyronitrile glass.....	124
---	-----

Figure A.5: EPR spectra of $[\text{Cu}^{\text{I}}(\text{carb})_2]\text{Li}$ and 2-bromo-4-phenylbutane (photoirradiated) or Magic Blue	127
---	-----

Figure A.6: Absorbance at 580 nm as a function of concentration of Cu(II)	129
--	-----

Figure A.7: Appearance of Cu(II) absorption band at short irradiation times of reaction mixture.	130
--	-----

Figure A.8: Absorbance at 580 nm at short irradiation times of reaction mixture.	130
--	-----

Figure A.9: UV-vis spectra of $[\text{Li}(\text{MeCN})][\text{Cu}(\text{carbazolide})_2]$ at various concentrations in CH_3CN at room temperature in 1 mm cuvette.....	132
---	-----

Figure A.10: Absorbance at 365 nm as a function of [Li(MeCN)][Cu(carbazolide) ₂] concentration.....	132
Figure A.11: UV-vis spectra of lithium carbazolidine at various concentrations.....	133
Figure A.12: Absorbance at 365 nm as a function of lithium carbazolidine concentration; path length = 1 mm.	133
Figure A.13: The hydrodynamic volume of lithium carbazolidine as a function of increasing lithium carbazolidine concentration.	135
Figure A.14: Transient absorbance decays for [Li(MeCN)][Cu(carbazolide) ₂] with varying electrophile concentrations.	139
Figure A.15: Luminescence decay of the emissive excited state of [Li(MeCN)][Cu(carbazolide) ₂].	140
Figure A.16: Luminescence decays for lithium carbazolidine with varying electrophile concentrations.	141
Figure A.17: Transient absorbance decays for [Li(MeCN)][Cu(carbazolide) ₂] at varying concentrations.	142
Figure A.18: Transient absorbance decays for lithium carbazolidine at varying concentrations.	143
Figure A.19: EPR spectra of freshly made Li[Cu ^{II} (carb) ₃], reaction of Li[Cu ^{II} (carb) ₃] with TEMPO–H, and TEMPO.....	147
Figure A.20: ¹ H NMR spectra of a mixture of carbH and [Li(CH ₃ CN)][Cu ^I (carb) ₂] and of a mixture of [Li(CH ₃ CN) _n][Cu ^{II} (carb) ₃] and TEMPOH.	147
Figure A.21: Relaxed surface scan for the reaction between [Cu ^I (carb) ₂] [−] and carb radical.....	149
Figure A.22: Absorbance spectrum of [Cu ^{II} (carb) ₃] [−] calculated by TD-DFT.	149
Figure A.23: Difference density plot for the most intense calculated absorption band of [Cu ^{II} (carb) ₃] [−] at 623 nm.	150
Figure A.24: ¹ H NMR spectrum of (E)-6-bromohept-1-ene-1-d.....	154
Figure A.25: ¹³ C{ ¹ H} NMR spectrum of (E)-6-bromohept-1-ene-1-d.....	155
Figure A.26: ² H NMR spectrum of (E)-6-bromohept-1-ene-1-d.....	156
Figure A.27: ¹ H NMR spectrum of 9-(hept-6-en-2-yl)-9H-carbazole.....	157

Figure A.28: $^{13}\text{C}\{^1\text{H}\}$ NMR spectrum of 9-((2-methylcyclopentyl)methyl-d)-9H-carbazole.	158
Figure A.29: ^1H NMR spectrum of 9-((2-methylcyclopentyl)methyl)-9H-carbazole ...	159
Figure A.30: ^1H NMR spectrum of 9-((2-methylcyclopentyl)methyl-d)-9H-carbazole.	160
Figure A.31: $^{13}\text{C}\{^1\text{H}\}$ NMR spectrum of 9-((2-methylcyclopentyl)methyl-d)-9H-carbazole.	161
Figure A.32: $^{13}\text{C}\{^1\text{H}\}$ NMR spectrum of 9-((2-methylcyclopentyl)methyl-d)-9H-carbazole.	162
Figure A.33: ^2H NMR spectrum of 9-((2-methylcyclopentyl)methyl-d)-9H-carbazole	163
Figure A.34: ^1H NMR spectrum lithium carbazolidide.	164
Figure A.35: ^1H NMR spectrum $\text{Li}(\text{MeCN})[\text{Cu}(\text{carbazolidide})_2]$	165
Figure A.36: ^7Li NMR of lithium carbazolidide at various concentrations.....	166
Figure A.37: ^1H NMR of lithium carbazolidide at various concentrations	167
Figure A.38: ^2H NMR spectrum of a crude reaction mixture of the reaction between (E)-6-bromohept-1-ene-1-d and $\text{Li}(\text{carb})$	168
Figure A.39: ^1H - ^1H COSY trace of the major diastereomer.....	168
Figure A.40: ^1H - ^1H NOESY trace of the major (<i>cis</i>) diastereomer.....	169
Figure A.41: ^1H - ^1H COSY trace of the minor diastereomer	170
Figure A.42: ^1H - ^1H NOESY trace of the minor (<i>trans</i>) diastereomer.....	171

Appendix B

Figure B.1: Placement of UV Germicidal Compact Lamps around a ring clamp	188
Figure B.2: Placement of cardboard box and fan relative to the UV lamps	190

Appendix C

Figure C.1: Variation in turnover number and volume of of N_2O	225
Figure C.2: UV-vis absorption spectrum of Co catalyst and Ir photosensitizer.....	226
Figure C.3: Emission spectrum of Ir photosensitizer..	226
Figure C.4: Luminescence decays for PS with varying NEt_3 concentrations.	227
Figure C.5: Luminescence decays for PS with varying $[\text{Co}]$	228
Figure C.6: EPR spectra and simulation of putative $\{\text{CoNO}\}^9$	229
Figure C.7: EPR spectrum of putative $\{\text{Co}^{15}\text{NO}\}^9$	230

Figure C.8: Harrick demountable liquid flow cell (DLC-S25) with CaF ₂ windows and 500 μm path length Teflon spacers.	231
Figure C.9: Background/control solution IR (CD ₃ CN) of PS and NEt ₃	232
Figure C.10: Solution IR difference spectrum putative {Co ¹⁵ NO} ⁹	232
Figure C.11: ATR-IR (film) spectra of 5 and 5 - ¹⁵ NO..	233
Figure C.12: Headspace analysis of a reaction of {CoNO} ⁸ and CoCp ₂	234
Figure C.13: Appearance of ^{15,15} N ₂ O at m/z = 31 (and m/z = 46).....	235
Figure C.14: TRIR data collected after photoreduction of 4 - ¹⁵ NO	236
Figure C.15: A 3-dimensional rendering of TRIR results in Figure C.14.....	237
Figure C.16: A 3-dimensional rendering of TRIR results in Figure 4.5	237
Figure C.17: ¹ H NMR spectrum of 5	239
Figure C.18: Summary of broken symmetry solutions for {CoNO} ⁹	241

List of Schemes

Chapter 1

Scheme 1.1: Scope of Ullmann-type reactivity.....	5
Scheme 1.2: Two possible pathways for the catalytic Ullmann reaction.....	6
Scheme 1.3: Four possible mechanisms for aryl halide activation in Ullmann coupling reactions	7
Scheme 1.4: One possible pathway for photoinduced, copper-catalyzed cross-coupling reactions	14
Scheme 1.5: Reductive and oxidative quenching pathways in photoredox chemistry	16

Chapter 4

Scheme 4.1: Possible pathways for N–N reductive coupling of NO during molecular (homogeneous) and heterogeneous catalysis	80
Scheme 4.2: Possible mechanistic scenarios for {CoNO} ⁹ reactivity.	95
Scheme 4.3: Outline of a viable mechanistic cycle proposed for photocatalytic nitrite reduction to nitrous oxide.	98

List of Tables

Chapter 2

Table 2.1: Effect of reaction concentration on ratio of cyclized (H) to uncyclized (I) product.	48
---	----

Chapter 3

Table 3.1: Photoinduced, copper-catalyzed cyanation of an unactivated secondary alkyl chloride: Effect of reaction parameters ^a	60
Table 3.2: Photoinduced, copper-catalyzed cyanation of unactivated secondary alkyl chlorides: Scope	62
Table 3.3: Photoinduced, copper-catalyzed cyanation of unactivated secondary alkyl bromides: Scope.....	64
Table 3.4: Cyanation of cyclohexyl halides.....	66
Table 3.5: Attempted use of an Ir photoredox catalyst for cyanation of cyclohexyl chloride	68

Chapter 4

Table 4.1: Photocatalytic Nitrite Reduction with a Co co-catalyst.....	83
---	----

Appendix A

Table A.1: Variation of yields of H and I as a function of alkyl bromide concentration.	119
Table A.2: Yields of debromination, homocoupling, and C–N cross-coupled product over time in the absence of Cu.....	121
Table A.3: Yields of debromination, homocoupling, and C–N cross-coupled product over time under catalysis conditions.....	122
Table A.4: Measured molar absorptivity (580 nm) of $[\text{Li}(\text{CH}_3\text{CN})_n][\text{Cu}^{\text{II}}(\text{carb})_3]$ at various concentrations.	128
Table A.5: Measured hydrodynamic radii and volumes.....	134
Table A.6: Excited state lifetime of $[\text{Li}(\text{MeCN})][\text{Cu}(\text{carbazolide})_2]$ as a function of electrophile concentration.	139
Table A.7: Excited state lifetime of lithium carbazolidine as a function of electrophile concentration.....	141

Table A.8: Excited state lifetime of [Li(MeCN)][Cu(carbazolide) ₂] as a function of concentration.....	142
Table A.9: Excited state lifetime of Li(carb) as a function of concentration.....	144
Table A.10: Free Energies of computed molecules	150
Table A.11: Crystal data and structure refinement for [K(THF) ₆][Cu(carbazolide) ₃]...	172
Table A.12: Fractional atomic coordinates ($\times 10^4$) and equivalent isotropic displacement parameters ($\text{\AA}^2 \times 10^3$) for [K(THF) ₆][Cu(carbazolide) ₃].....	173
Table A.13: Anisotropic displacement parameters ($\text{\AA}^2 \times 10^3$) for [K(THF) ₆][Cu(carbazolide) ₃].....	174
Table A.14: Hydrogen atom coordinates ($\text{\AA} \times 10^4$) and isotropic displacement parameters ($\text{\AA}^2 \times 10^3$) for [K(THF) ₆][Cu(carbazolide) ₃].....	176
Table A.15: Bond angles for [K(THF) ₆][Cu(carbazolide) ₃].....	178

Appendix C

Table C.1: Effect of [1] on N ₂ O Yields.	225
Table C.2: Excited state lifetime of 2 as a function of [NEt ₃].....	228
Table C.3: Excited state lifetime of 2 as a function of [1].....	228
Table C.4: Crystal data and structure refinement for 5	242
Table C.5: Atomic coordinates ($\times 10^5$) and equivalent isotropic displacement parameters ($\text{\AA}^2 \times 10^4$).....	244
Table C.6: Bond lengths [\AA] and angles [$^\circ$] for 5	246
Table C.7: Anisotropic displacement parameters ($\text{\AA}^2 \times 10^4$) for 5	263
Table C.8: Hydrogen coordinates ($\text{\AA} \times 10^4$) and isotropic displacement parameters ($\text{\AA}^2 \times 10^3$) for 5	265
Table C.9: Torsion angles [$^\circ$] for 5	268
Table C.10: Hydrogen bonds for 5 [\AA and $^\circ$].	275

Abbreviations

Å	Ångström(s), 10^{-10} m
Ac	Acetyl
Anal.	Analysis
app	Apparent
aq.	Aqueous
Ar	Aryl group
A(X)	Hyperfine coupling constant due to nucleus X
Boc	<i>tert</i> -butoxycarbonyl
bp	Boiling point
br	Broad
Bu	Butyl
i-Bu	<i>iso</i> -butyl
<i>n</i> -Bu	Butyl or <i>norm</i> -butyl
<i>t</i> -Bu	<i>tert</i> -butyl
Bn	Benzyl
^{13}C	Carbon-13 isotope
°C	Degrees Celsius
calc'd.	Calculated
Carb	Carbazolide
CCDC	Cambridge Crystallographic Data Centre
cf.	Consult or compare to (Latin: confer)
CFL	Compact fluorescent light
cm^{-1}	Wavenumber(s)
conc.	Concentrated
Cy	Cyclohexyl group

d	Doublet
DBU	1,8-diazabicyclo[5.4.0]undec-7-ene
DME	1,2-dimethoxyethane
DMF	N,N-dimethylformamide
DMSO	Dimethylsulfoxide
dr	Diastereomeric ratio
ee	Enantiomeric excess
E	<i>Trans</i> (entgegen) olefin geometry
ϵ	Extinction coefficient in units of $M^{-1} \text{ cm}^{-1}$
E^0	Reduction or oxidation potential
e.g.	For example (Latin: <i>exempli gratia</i>)
EI	Electron impact
EPR	Electron paramagnetic resonance
ESI	Electrospray ionization
Et	Ethyl
<i>et al.</i>	And others (Latin: <i>et alii</i>)
eq	Equation
equiv	Equivalent(s)
EWG	Electron withdrawing group
FID	Flame Ionization Detection
G	Gauss
g	Gram(s)
GC	Gas chromatography
H	Hour(s)
^1H	Proton
^2H	Deuterium
<i>n</i> -Hex	Hexyl or <i>norm</i> hexyl group

hv	Light
HPLC	High performance liquid chromatography
HRMS	High resolution mass spectrometry
Hz	Hertz
<i>i.e.</i>	That is (Latin: <i>id est</i>)
IR	Infrared (spectroscopy)
irrad.	Irradiate(d)
<i>J</i>	Coupling constant
K	Kelvin or equilibrium constant
<i>k</i>	Rate constant
kcal	Kilocalorie(s)
kg	Kilogram(s)
L	Liter or neutral ligand
λ	Wavelength
λ_{\max}	Wavelength of local maximum intensity
LA	Lewis acid
m	Multiplet or meter(s)
M	Molar or molecular ion
μ	Micro or bridging
Me	Methyl
mg	Milligram(s)
MHz	Megahertz
min	Minute(s)
mL	Milliliter(s)
MLCT	Metal-to-ligand charge transfer
MO	Molecular orbital
mol	Mole(s)

Mp	Melting point
MS	Mass spectrometry
mV	Millivolt
m/z	Mass-to-charge ratio
N	Normal
nm	Nanometer(s)
NMR	Nuclear magnetic resonance
NOE	Nuclear Overhauser Effect
NOESY	Nuclear Overhauser Effect Spectroscopy
Nu/Nuc	Nucleophile
<i>o</i>	Ortho
π	Pi symmetry orbital or interaction
π^*	Pi symmetry antibonding orbital or interaction
<i>p</i>	Para
ps	Picosecond(s)
^{31}P	Phosphorus-31
<i>n</i> -pent	Pentyl or <i>norm</i> -pentyl
ns	Nanosecond(s)
Ph	Phenyl
pH	Hydrogen ion concentration in aqueous solution
phen	Phenanthroline
ppy	Phenylpyridine
Pr	Propyl
<i>i</i> -Pr	Isopropyl
<i>n</i> -Pr	Propyl or <i>norm</i> -propyl
PS	Photosensitizer
q	Quartet

R	Alkyl group
rf	Retention factor
rt	Room temperature
s	Singlet or seconds
σ	Sigma symmetry orbital or interaction
σ^*	Sigma symmetry antibonding interaction
S	Sinister
sat.	Saturated
SCE	Saturated calomel electrode
SET	Single electron transfer
S _N 2	Bimolecular nucleophilic substitution
SS	Step-scan
t	Triplet
TBACN	Tetra- <i>n</i> -butylammonium cyanide
TBAI	Tetra- <i>n</i> -butylammonium iodide
Temp	Temperature
TEMPO	2,2,6,6 -tetramethylpiperidine N-oxide
THF	Tetrahydrofuran
TLC	Thin layer chromatography
tol	Tolyl
TRIR	Time-resolved infrared
Ts	Para-toluenesulfonyl (tosyl)
UV	Ultraviolet
W	Watt
X	Anionic ligand or halide
Z	<i>Cis</i> (zusammen) olefin geometry
*	Excited State

Chapter 1 : Introduction

On the arid lands there will spring up industrial colonies without smoke and without smokestacks; forests of glass tubes will extend over the plains and glass buildings will rise everywhere; inside of these will take place the photochemical processes that hitherto have been the guarded secret of the plants, but that will have been mastered by human industry which will know how to make them bear even more abundant fruit than nature, for nature is not in a hurry and mankind is. And if in a distant future the supply of coal becomes completely exhausted, civilization will not be checked by that, for life and civilization will continue as long as the sun shines! If our black and nervous civilization, based on coal, shall be followed by a quieter civilization based on the utilization of solar energy, that will not be harmful to progress and to human happiness.

Ciamician, G. *Science* **1912**, *36*, 385–395.

1.1 Motivations

By 2050, rapid global population (and economic) growth is projected to lead to at least double the current rate of energy consumption.¹ While this rate of energy use could potentially be met by the current fossil fuel reserves, a variety of climate models predict catastrophic effects on global climate patterns from the resulting carbon emissions.² Thus, searching for alternative, carbon-neutral sources of energy is one of the most important goals of our time, and could significantly improve quality of life in the immediate future. An attractive, renewable option for energy is, of course, the sun. More solar energy is available in one hour than the planet uses in an entire year. To this end, the use of chromophores and photocatalysts for the conversion of solar energy to chemical energy has been used to mimic natural photosynthesis, leading to applications in water splitting,³ CO₂ reduction,⁴ and solar cells.⁵ Once it was recognized that such photoredox catalysis could occur under exceptionally mild conditions and access novel reaction mechanisms, this methodology grew rapidly for novel bond-constructions in organic synthesis and other types of reactivity.⁶

The work in this thesis is unified by the central theme of photocatalysis for sustainable bond-forming and bond-breaking processes. Further attempts at improving

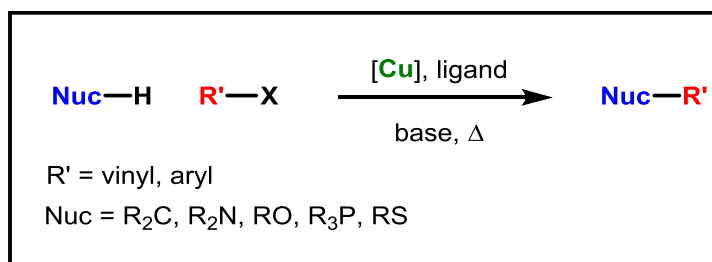
sustainability include the use of earth-abundant first-row transition metals (Cu and Co) for bond formation instead of more scarce and costly noble metals (e.g., Pd). However, it is important to note that in addition to their cost-effectiveness and potential for global implementation, first-row transition metals can also afford divergent or complementary reactivity compared to their second- and third-row counterparts.^{7,8} One of the greatest differences in the reactivity between 3d metals and their heavier congeners is that while the former undergo one-electron oxidation state changes, the latter typically go through two-electron oxidation state changes; one-electron chemistry can lead to radical intermediates which have been traditionally difficult to control. This one-electron chemistry can be either enhanced or prevented based on the judicious choice of ligands and reaction conditions.⁹

New, divergent reactivity can also be accessed under photolytic conditions compared with thermal reaction manifolds. Photocatalysts can function as both one electron oxidants and reductants, and can convert visible light into substantial amounts of chemical energy; these features can directly access reactive organic intermediates (e.g., radicals) which are not possible under non-photochemical conditions.^{6a} When used in conjunction with other transition metal catalysts, they have the ability to access two discrete catalytic platforms, one photochemical and the other non-photochemical/thermal. The excited photocatalyst can activate the reaction substrate, which can interact with the transition metal catalyst; or, it can activate the transition metal catalyst for further reaction with the reaction substrate.¹⁰ The propensity of group 3d transition metals to undergo one-electron chemistry makes them particularly suited as either photocatalysts¹¹

or as co-catalysts in a photocatalytic system.¹² This thesis will discuss the successful application of Cu and Ir/Co transition metal systems for photocatalysis.

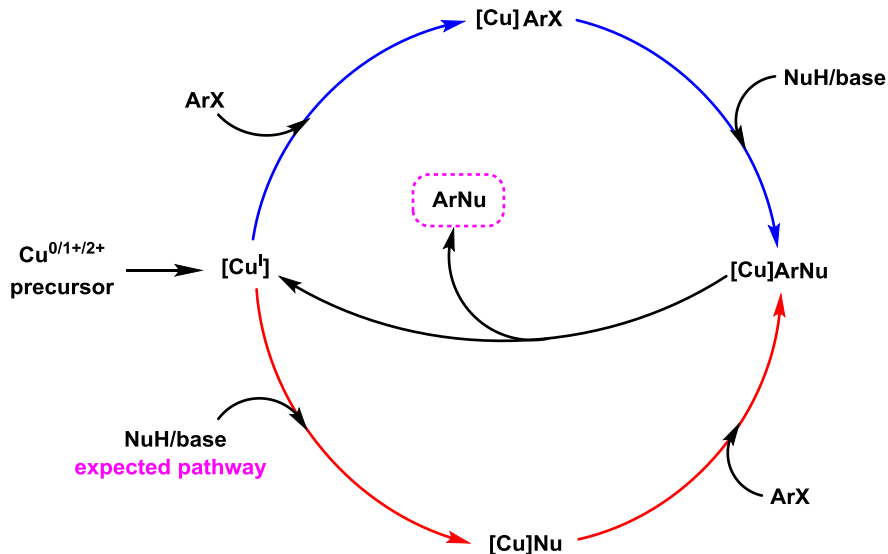
1.2 Photoinduced, Copper-Catalyzed Cross-Coupling Reactions

Scheme 1.1: Scope of Ullmann-type reactivity



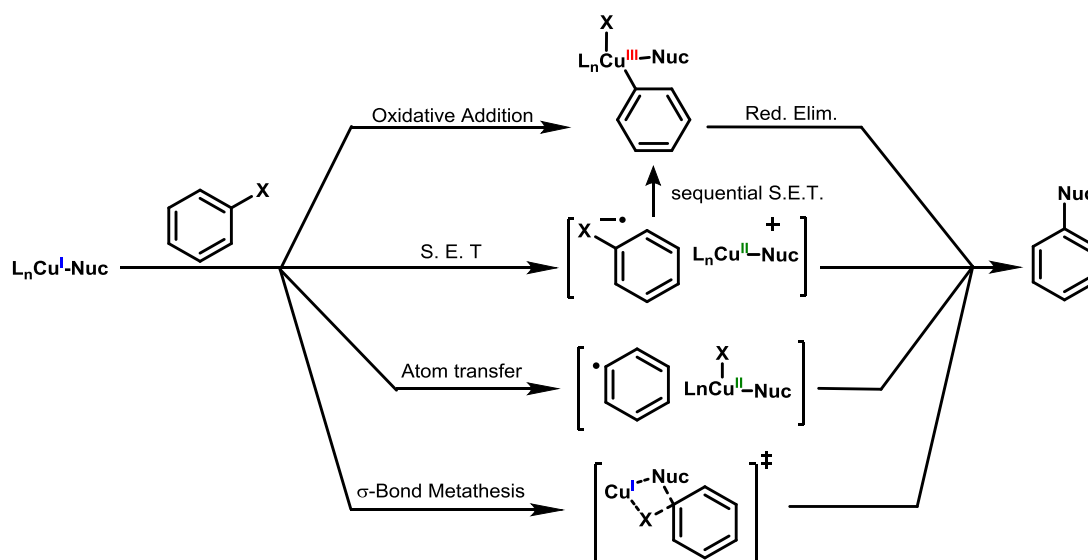
Cu-mediated C–C and carbon–heteroatom bond-forming reactivity, referred to as “Ullmann-type” chemistry (Scheme 1.1), has been known since the early 1900s, several decades before Ni and Pd catalyzed cross coupling was discovered. The formation of C–N (*N*-aryl amides and aryl amides),¹³ C–O (ethers),¹⁴ and C–C bonds¹⁵ was performed with stoichiometric, and later catalytic, amounts of copper. However, the ubiquity of this Cu-catalyzed transformation was limited by harsh reaction conditions (high-boiling polar solvents), which led to a low substrate scope; high, sometimes stoichiometric or excess, Cu loadings due to the low solubility of Cu salts; and long reaction times with suboptimal yields.¹⁶ Meanwhile, Pd catalysis became the industrial and academic workhorse for a variety of organic transformations, characterized by high reaction rates, high efficiency, and broad scope. However, since the mid-1990s, copper catalysis has seen a resurgence after new copper/ligand systems enabled the formation of C–N, C–C, and C–O bonds with catalytic Cu loadings and much milder conditions than before.¹⁷ The exact reason for the ligand-effect was not known, but presumed to be due to increased catalytic solubility or reduced metal aggregation. The development of Cu catalysis has since led to systems that rival Pd catalysis.¹⁶

Scheme 1.2: Two possible pathways for the catalytic Ullmann reaction.



Upon gaining more tractable reactivity for copper catalyzed Ullmann chemistry, the mechanism of the reaction under catalytic conditions was investigated. Many reports suggest that Cu(I)-catalyzed C–N and C–O bond forming reactions proceed *via* a Cu(I)-nucleophile complex (Scheme 1.2, bottom pathway preferred).¹⁸ The subsequent aryl halide activation step has generated some debate in the literature, and can proceed by a variety of pathways. Several mechanisms have been proposed for this step. The most widely-accepted pathway is the oxidative addition of the aryl halide to the Cu(I)-nucleophile complex to generate a Cu(III) intermediate. Another possible mechanism is outer-sphere single electron transfer (SET) from the Cu(I)-nucleophile complex to the aryl halide, resulting in a radical pair with a Cu(II) intermediate and a radical anion. A third pathway is halogen atom transfer or an inner-sphere electron transfer to generate a Cu(II)-halide complex. Finally, a σ -bond metathesis mechanism which proceeds through a 4-center transition state has also been proposed, though there is little experimental evidence to support this latter mechanism (Scheme 1.3).¹⁹

Scheme 1.3: Four possible mechanisms for aryl halide activation in Ullmann coupling reactions. Adapted from reference 19.



Until recently (2012), the vast majority of evidence pointed to the Cu(I)/Cu(III) pathway for aryl halide activation, involving oxidative addition of the aryl halide. Huffman and Stahl have shown that N-arylation is feasible with a well-defined macrocyclic arylcopper(III) complex in the presence of nitrogen nucleophiles, with one explanation being reductive elimination from an unobserved Cu(III)(aryl)(nucleophile) species.²⁰ Stahl and Ribas later demonstrated both oxidative addition of an aryl halide across a Cu(I) center to generate a Cu(III) and reductive elimination (under acidic conditions) of an aryl halide from Cu(III) to (re)generate a Cu(I).²¹

Similarly, work by Hartwig and coworkers ruled out the presence of free radicals and Cu(II) intermediates in thermal C–N, C–O, and C–S Ullmann coupling reactions, suggesting a Cu(I)/Cu(III) pathway (or inner sphere electron transfer).²² Cu(I)-nucleophile complexes were isolated with a variety of ligands, including phenanthroline (phen) and 1,2-diamines, and shown to be kinetically and chemically competent for the

catalytic coupling reaction.^{22,23} Competition experiments with Cu-nucleophile complexes between 1-bromonaphthalene (favored for a concerted oxidative addition reaction) and 4-chlorobenzonitrile (favored for outer-sphere SET due to its more positive reduction potential) consistently favored reaction with 1-bromonaphthalene (Figure 1.1a).²² This result suggests a mechanism for aryl halide activation that does not proceed by outer-sphere electron transfer. Reactivity of Cu(I) nucleophile complexes with a fast radical clock, *o*-(allyloxy)iodobenzene (rate of cyclization = $9.6 \times 10^9 \text{ s}^{-1}$ in DMSO), yielded only uncyclized products (Figure 1.1b), suggesting a lack of free aryl radicals during catalysis. The result does not rule out in-cage recombination of the aryl radical with a Cu-nucleophile species which occurs at a rate faster than the rate of cyclization, though the high rate ($> 10^{12} \text{ s}^{-1}$) required for this step makes it unlikely.²²

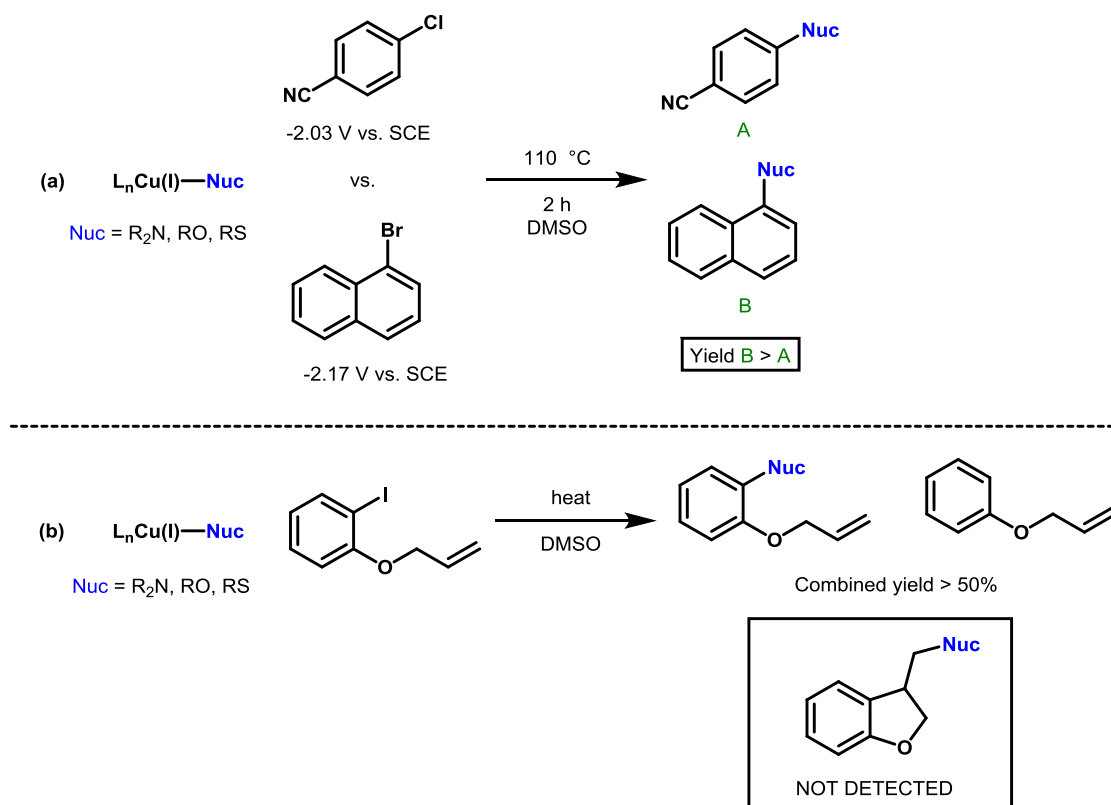


Figure 1.1: Reactivity of Cu(I)-nucleophile complexes with (a) 1-bromonaphthalene and 4-chlorobenzonitrile and (b) *o*-(allyloxy)iodobenzene

Computational investigations of ligand-directed C–O *versus* C–N Ullmann coupling with iodobenzene suggest that, in some cases, the oxidative addition/reductive elimination pathway for aryl halide activation is disfavored relative to Cu(II) radical pathways.¹⁹ However, Liu *et al.* conducted another computational study on product selectivity with a different nucleophile which instead favored an oxidative addition/reductive elimination pathway.²⁴ Thus, it is possible that the mechanism of aryl halide activation can vary based on the halide, electrophile, ligand, and nucleophile. Nonetheless, until recently, there was no experimental evidence supporting a Cu(II) intermediate in Ullmann-type reactivity.

In 2012, the first experimental evidence for a Cu(II) radical pathway for Ullmann coupling was discovered. While studying the emissive properties of three-coordinate Cu(I) arylamidophosphine complexes,²⁵ Creutz, Lotito *et al.* observed that the irradiation of $(\text{PPh}_3)_2\text{Cu}(\text{carb})$ (carb = carbazole) in the presence of iodobenzene yielded the C–N coupled product *N*-phenylcarbazole.²⁶ For improved solubility, $[\text{P}(m\text{-tol})_3]_2\text{Cu}(\text{carb})$ (*m*-tol = *meta*-tolyl) was used instead, and showed similar reactivity with a 100-W mercury lamp. C–N coupling product was not observed (< 1%) in the absence of light and copper.²⁶ Unlike previous experiments, when the deuterium-labeled cyclization probe *o*-(allyloxy)iodobenzene was reacted with $[\text{P}(m\text{-tol})_3]_2\text{Cu}(\text{carb})$ with irradiation, the result was a 1:1 *cis*:*trans* diastereomeric mixture of the cyclized product, with no uncyclized product detected (Figure 1.2).²⁷ A competition experiment between 1-bromonaphthalene and 4-chlorobenzonitrile now favored reactivity with the chloride substrate. For the first time in Cu-catalyzed Ullmann coupling, these two mechanistic results are experimentally consistent with an SET pathway for C–N bond formation, instead of a Cu(I)/Cu(III) pathway.

Further evidence to support this mechanistic hypothesis came from an EPR spectrum (77 K) collected upon irradiation of $[\text{P}(m\text{-tol})_3]_2\text{Cu}(\text{carb})$ with iodobenzene at –40 °C; the anisotropic *g*-values of this spectrum suggest metalloradical character on this Cu(II) intermediate. Interestingly, $[\text{P}(m\text{-tol})_3]_2\text{Cu}(\text{carb})$ could also be used to catalytically generate C–N bonds with iodobenzene under UV irradiation.²⁶

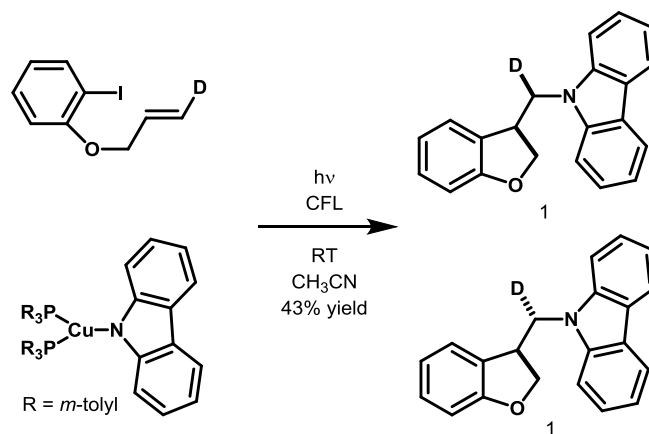


Figure 1.2: Reactivity of $[P(m\text{-tol})_3]_2\text{Cu}(\text{carb})$ with deuterated *o*-(allyloxy)iodobenzene

Soon after the catalytic C–N coupling with aryl iodides and carbazoles was demonstrated, work in the Peters and Fu groups turned to the study of alkyl halide electrophiles ($\text{C}_{\text{sp}^3}\text{–N}$ bonds). Preliminary evidence for productive $\text{C}_{\text{sp}^3}\text{–N}$ coupling had already been demonstrated with the cyclization probe (Figure 1.2).²⁶ Indeed, the photoinduced, copper-catalyzed cross-coupling reaction was feasible with alkyl iodides and bromides.²⁸ This methodology offered milder conditions than typical nucleophilic substitution ($\text{S}_{\text{N}}2$) conditions for $\text{C}_{\text{sp}^3}\text{–N}$ bond formation,²⁹ and proceeded without the addition of any exogenous ligand. The reaction scope was also extended to include functionalized carbazoles, indoles, benzimidazoles, and imidazoles with a variety of aryl halides, alkenyl halides, and an alkynyl bromide (Figure 1.3a).³⁰

Since then, the constructive collaboration between the Peters Group and the Fu group has led to a suite of useful photoinduced, copper-catalyzed methodologies for organic synthesis, both with and without ligands. For nitrogen nucleophiles, these include N-alkylation of amides (Figure 1.3b),³¹ decarboxylative C–N coupling (Figure 1.3c),³² and enantioselective coupling of racemic tertiary alkyl chlorides with carbazoles (Figure 1.3d).³³ Other nucleophiles have also been successful, leading to the development of new

methods for S-arylation of thiols (Figure 1.4a),³⁴ O-arylations of phenols (Figure 1.4b),³⁵ and cyanation of alkyl halides (to be discussed in Chapter 3; Figure 1.4c).³⁶

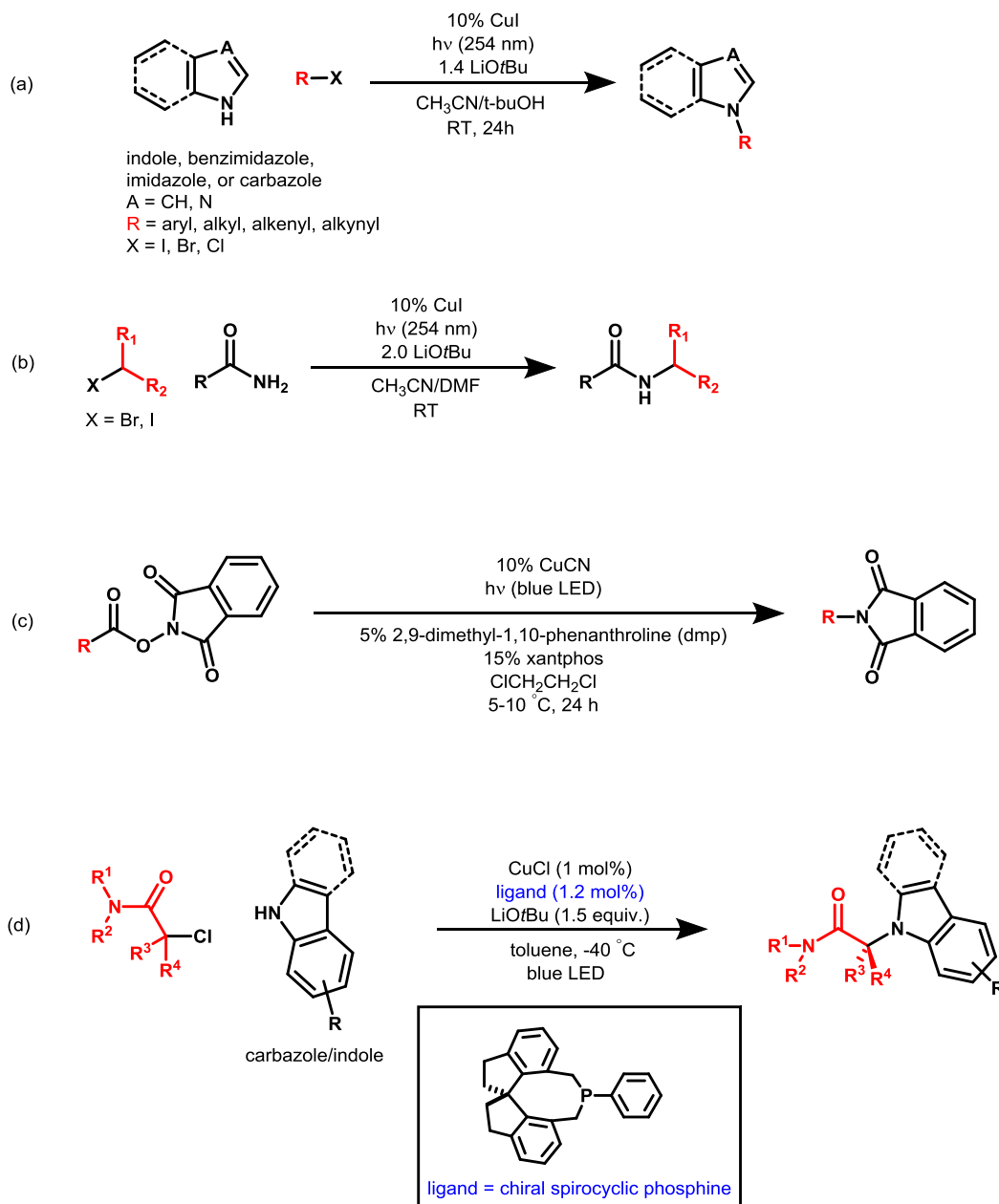


Figure 1.3: The scope of C–N bond forming reactivity accessed with photoinduced, Cu-catalyzed cross coupling reactions.

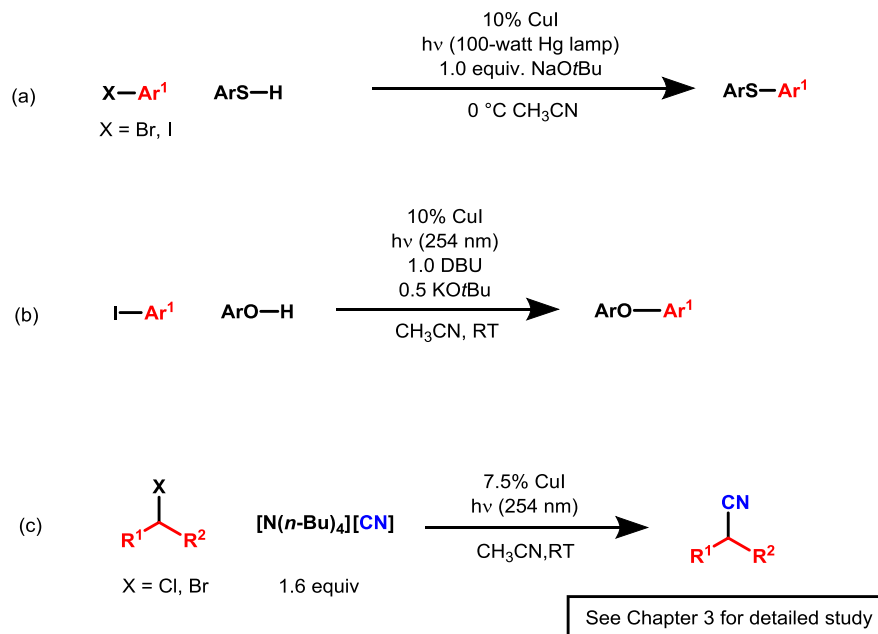
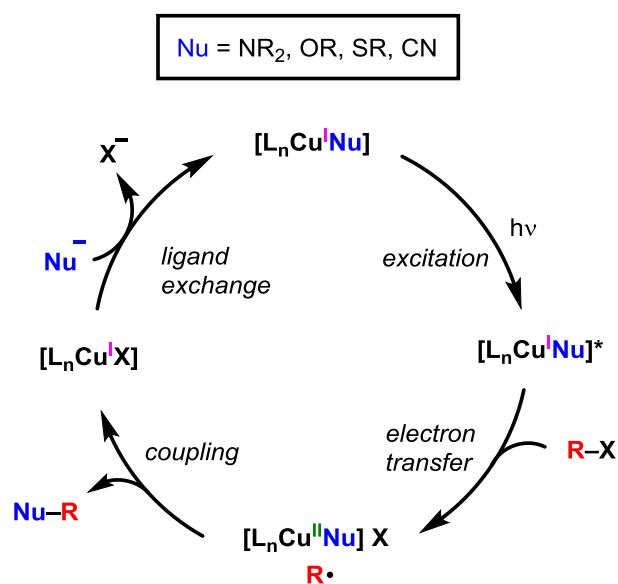


Figure 1.4: Expanding the scope of photoinduced, Cu-catalyzed cross coupling reactions to thiol, alcohol, and cyanide nucleophiles.

While the mechanism of each photoinduced, copper-catalyzed coupling reaction may vary based on nucleophile, electrophile, ligand, and general conditions, the requirement of light and copper in all cases caused us to postulate a general mechanism (Scheme 1.4). We proposed that a Cu(I)-nucleophile complex is irradiated, leading to the formation of an excited state copper complex. This excited species can transfer an electron (SET) to the electrophile to generate an organic radical and a Cu(II)-nucleophile complex. The coupling step between the radical and Cu(II) intermediate occurs at this stage. The Cu(I)-nucleophile species is regenerated upon ligand exchange with excess nucleophile. In 2016, a mechanistic investigation on the stoichiometric coupling of a well-defined copper–thiolate with an aryl iodide yielded results which were consistent with this proposed pathway. The C–S bond formation was found to occur *via* in-cage coupling after the SET step, *i.e.* the Cu(II)–thiolate can capture the aryl radical

intermediate within the solvent cage before it diffuses out.³⁷ In 2017, a detailed mechanistic study on the photoinduced, Cu-catalyzed C–N bond formation of carbazole with alkyl bromides was published, and is the subject of Chapter 2.³⁸

Scheme 1.4: One possible pathway for photoinduced, copper-catalyzed cross-coupling reactions. All Cu complexes are depicted as neutral species, X can be an inner- or outer-sphere group, and L_n represents any ligand(s) coordinated to Cu.



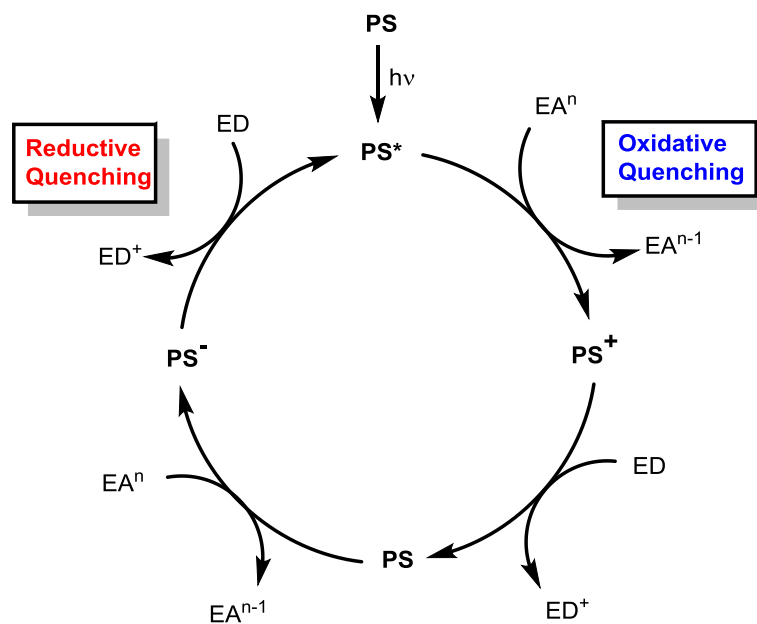
1.3 Photoredox Catalysis for Nitrite Reduction

Chapter 4 of this thesis focuses on a dual catalysis system containing an Ir photosensitizer and a Co co-catalyst for the reduction of nitrite to nitrous oxide. Denitrification processes, which include the reduction of nitrite and nitric oxide to nitrous oxide and dinitrogen, are an integral part of the nitrogen cycle. Buildup in soil of nitrites and nitrates can lead to eutrophication of marine ecosystems, leading to a decrease in the global potable water supply.³⁹ Biological systems (nitrite reductase enzymes) contain hydrogen bonding interactions which are required for nitrite binding and reduction.⁴⁰ We synthesized a macrocyclic ligand with a pendant Lewis acid to emulate these interactions, and have observed selective nitrite binding.⁴¹ This platform has allowed us to explore both electrocatalytic and photocatalytic nitrite reduction to nitrous oxide in the presence of acid. This work discusses the conditions required for successful photoredox catalysis and putative mechanisms for N–N coupling (see Chapter 4).

In the photoinduced copper catalysis, the Cu(I)-nucleophile intermediate functions as the photoreductant and then transforms into the bond-forming species (Cu(II)-nucleophile complex). However, in typical photoredox catalysis, a photosensitizer (PS) does not participate in the bond formation step. While many organic compounds absorb in the UV, photosensitizers provide the ability to use visible light. In these types of photoredox systems, a PS can undergo oxidative or reductive quenching to engage in single electron transfer processes with organic substrates and/or transition metal co-catalysts (Scheme 1.5). In oxidative quenching, the excited photosensitizer transfers an electron to an acceptor, generating PS^+ , and then is reduced back to its original form by an electron donor. In reductive quenching, the excited photosensitizer is

reduced by an electron donor to make PS^- , a highly reducing state which can then transfer its electron to an electron acceptor.⁴² Photosensitizers can also participate in energy transfer pathways, in which decay of the PS excited state promotes another molecule from its ground state to its excited state.^{10a,42,43} Photocatalysts can include both organic dyes, such as eosin Y,⁴⁴ and inorganic transition metal complexes, such as those of Ir, Ru, Cr, and Cu.^{12b,42}

Scheme 1.5: Reductive and oxidative quenching pathways in photoredox chemistry. PS = photosensitizer, EA = electron acceptor, ED = electron donor



1.4 Time-Resolved Laser Spectroscopy

A great advantage with the use of photocatalytic systems is the ability to use phototriggered flash-quench methods with remarkably fast time resolution (femto-, pico-, nanoseconds or slower) to examine the interaction of the excited state with various organic and inorganic substrates. The electron transfer event can be very precisely gated, and electron transfer and subsequent reactions can be monitored by a variety of methods. In this thesis, luminescence, transient absorption, and step-scan time-resolved infrared spectroscopy⁴⁵ are three such methods which were used to study a variety of photochemical reactions.

Flash-quench spectroscopy was first developed for the study of electron transfer in proteins.⁴⁶ In this method, a laser pulse of known duration excites a photoactive compound (PS) nearly instantaneously. The population of the excited state, PS*, decays according to a unimolecular rate law (Equation 1.1):

$$[PS^*]_t = [PS^*]_0 \exp\left(-\frac{t}{\tau_{PS}}\right) = [PS^*]_0 \exp(-k_{PS}t) \quad \text{Eq 1.1}$$

In this equation, τ_{PS} is the excited state lifetime of PS; $[PS^*]_0$ and $[PS^*]_t$ represent the concentration of PS* at time $t = 0$ and t , respectively; and k_{PS} is the rate constant of decay (and the inverse of the lifetime). Typically, the transient absorption or luminescence spectrum of PS* is monitored to determine concentrations of PS* over time. The excited state can decay both by radiative (emission) and non-radiative (thermal relaxation, intersystem crossing) processes.

If the lifetime of the photogenerated excited species is long enough, a reductive or oxidative quencher can be used to deplete the population of the excited state. Quenching of the excited state (PS*) by an electron donor/acceptor competes with the relaxation

processes of the excited state, such that the lifetime of the excited state in the presence and absence of quencher can be measured and analyzed to determine the rate of quenching. In the absence of quencher, the quantum yield of radiative decay of PS* (Φ_r^0) can be represented in terms of its rates of radiative and non-radiative decay (k_r and k_{nr} , respectively; Equation 1.2):

$$\Phi_r^0 = \frac{k_r}{k_r + k_{nr}} \quad \text{Eq 1.2}$$

When quencher is added to the system, there is an additional pathway for excited state decay, and a new expression for quantum yield (Φ_r) can be derived in which k_q is a second order rate constant for quenching and Q is the quencher (Equation 1.3):

$$\Phi_r = \frac{k_r}{k_r + k_{nr} + k_q[Q]} \quad \text{Eq 1.3}$$

By dividing Eq 1.2 by Eq 1.3, we can construct the Stern-Volmer equation (Equation 1.4):

$$\frac{\Phi_r^0}{\Phi_r} = 1 + \frac{k_q[Q]}{k_r + k_{nr}} = 1 + K_{SV}[Q] = \frac{I_0}{I} \quad \text{Eq 1.4}$$

In this equation, K_{SV} is the Stern-Volmer quenching constant, such that $K_{SV} = k_q/(k_r + k_{nr})$. The quantum yield terms can be replaced with emission intensities (I_0/I), though static quenching may also need to be taken into account. When a pulsed laser is used to probe rates of dynamic quenching, lifetimes (τ_0/τ) can replace intensities in the Stern-Volmer relationship (Equations 1.5-1.7):

$$\tau_0 = \frac{1}{k_r + k_{nr}} \quad \text{Eq 1.5}$$

$$\tau = \frac{1}{k_r + k_{nr} + k_q[Q]} \quad \text{Eq 1.6}$$

$$\frac{\tau_0}{\tau} = 1 + \frac{k_q[Q]}{k_r + k_{nr}} = 1 + k_q\tau_0[Q] \quad \text{Eq 1.7}$$

Thus, a plot of I_0/I (with only dynamic quenching) or τ_0/τ as a function of quencher concentration will yield a line with an intercept of 1 and a slope of $K_{sv} = k_q\tau_0$.⁴⁷ This analysis is conducted throughout this thesis to acquire rates of quenching for the excited states of Cu and Ir complexes.

1.5 Chapter Summaries

Chapter 2 discusses a detailed mechanistic study of the photoinduced, copper-catalyzed cross-coupling of carbazole with alkyl bromides. An array of spectroscopic, computational, and reactivity tools are used to investigate this photochemical reaction. Transient absorption and time-resolved luminescence spectroscopy demonstrate that both $[\text{Cu}^{\text{I}}(\text{carb})_2]^-$ and $\text{Li}(\text{carb})$, the nucleophile, are able to serve as photoreductants for the alkyl bromide electrophile. Based on extinction coefficients and relative catalytic concentrations, it is proposed that $\text{Li}(\text{carb})$, not $[\text{Cu}^{\text{I}}(\text{carb})_2]^-$, functions as the major photoreductant to generate a carbazyl radical and an alkyl radical. $[\text{Cu}^{\text{II}}(\text{carb})_3]^-$, which was identified as a persistent radical under catalytic conditions, can couple with the alkyl radical by an out-of-cage process.

Chapter 3 reports the photoinduced, copper-catalyzed carbon-carbon bond formation between unactivated alkyl halides and tetrabutylammonium cyanide (TBACN) at room temperature. This reaction is conducted with 254 nm irradiation, furnishing nitrile products even from hindered alkyl chlorides, which are typically very challenging $\text{S}_{\text{N}}2$ substrates. Initial mechanistic work is consistent with the hypothesis that a $[\text{Cu}(\text{CN})_2]^-$ species can be photoexcited and undergo SET to an alkyl halide. The reaction of iodide with alkyl chlorides under catalytic conditions is also proposed, leading to the transient formation of an alkyl iodide. This method serves as a rare example of a transition-metal catalyzed cyanation of alkyl halides.

Chapter 4 presents a mechanistic study of the photocatalytic reduction of nitrite to nitrous oxide with an Ir photocatalyst ($[\text{Ir}(\text{ppy})_2(\text{phen})][\text{PF}_6]$) and a bimetallic CoMg co-catalyst within a diimine-dioxime ligand platform. This work expands upon previous

work in our group on the electrocatalytic reduction of nitrite to nitrous oxide. Based on step-scan time-resolved infrared spectroscopy, a mechanism for N–N coupling is proposed in which a coordinated and an uncoordinated NO \cdot couple at a single Co center, generating a Co(NONO) intermediate. Characterization of a rare {CoNO} 9 species is also presented. This {CoNO} 9 species is hypothesized to react with free NO \cdot to generate the Co(NONO) intermediate which can release N $_2$ O.

1.6 References

1. Lewis, N. S.; Nocera, D. G. *Proc. Natl. Acad. Sci.* **2006**, *103*, 15729–15735.
2. Intergovernmental Panel on Climate Change (2001), Synthesis Report Summary for Policymakers (Intergovernmental Panel on Climate Change, Washington, DC).
3. Balzani, V.; Credi, A.; Venturi, M. *ChemSusChem* **2008**, *1*, 26–58.
4. Takeda, H.; Ishitani, O. *Coord. Chem. Rev.* **2010**, *254*, 346–354.
5. Kalyanasundaram, K.; Grätzel, M. *Coord. Chem. Rev.* **1998**, *77*, 347–414.
6. (a) Shaw, M. H.; Twilton, J.; Macmillan, D. W. C. *J. Org. Chem.* **2016**, *81*, 6898–6926. (b) Yoon, T. P.; Ischay, M. A.; Du, J. *Nat. Chem.* **2010**, *2*, 527–532.
7. (a) Beletskaya, I. P.; Cheprakov, A. V. *Organometallics* **2012**, *31*, 7753–7808. (b) Ananikov, V. P. *ACS Catal.* **2015**, *5*, 1964–1971. (c) Su, B.; Cao, Z.; Shi, Z. *Acc. Chem. Res.* **2015**, *48*, 886–896.
8. (a) White, M. C. *Adv. Synth. Catal.* **2016**, *358*, 2364–2365. (b) Holland, P. L. *Acc. Chem. Res.* **2015**, *48*, 1696–1702.
9. (a) Chirik, P.; Morris, R. *Acc. Chem. Res.* **2015**, *48*, 2495. (b) Bedford, R. B. *Acc. Chem. Res.* **2015**, *48*, 1485–1493. (c) Tollefson, E. J.; Hanna, L. E.; Jarvo, E. R. *Acc. Chem. Res.* **2015**, *48*, 2344–2353.
10. (a) Skubi, K. L.; Blum, T. R.; Yoon, T. P. *Chem. Rev.* **2016**, *116*, 10035–10074. (b) Twilton, J.; Le, C.; Zhang, P.; Shaw, M. H.; Evans, R. W.; MacMillan, D. W. C. *Nat. Rev. Chem.* **2017**, *1*, 0052.
11. Paria, S.; Reiser, O. *ChemCatChem* **2014**, *6*, 2477–2483.

12. (a) Ye, Y.; Sanford, M. S. *J. Am. Chem. Soc.* **2012**, *134*, 9034. (b) Eckenhoff, W. T.; Eisenberg, R. *Dalton Trans.* **2012**, *41*, 13004.
13. (a) Ullmann, F. *Chem. Ber.*, **1903**, *36*, 2382–2384. (b) Goldberg, I. *Chem. Ber.*, **1906**, *39*, 1691–1692.
14. Ullmann, F.; Sponagel, P. *Chem. Ber.*, **1905**, *38*, 2211–2212.
15. (a) Ullmann, F.; Bielecki, F. *Chem. Ber.*, **1901**, *34*, 2174–2185.
16. For reviews on the development and history of Ullmann-type coupling, see (a) Sambiagio, C.; Marsden, S. P.; Blacker, A. J.; McGowan, P. C. *Chem. Soc. Rev.* **2014**, *43*, 3525–3550. (b) Monnier, F.; Taillefer, M. *Angew. Chem. Int. Ed.* **2009**, *48*, 6954–6971.
17. (a) Zhang, S.; Zhang, D.; Liebeskind, L. S. *J. Org. Chem.* **1997**, *62*, 2312–2313. (b) Marcoux, J.-F.; Doye, S.; Buchwald, S. L. *J. Am. Chem. Soc.* **1997**, *119*, 10539–10540. (c) Kiyomori, A.; Marcoux, J.-F.; Buchwald, S. L. *Tetrahedron Lett.* **1999**, *40*, 2657–2660. (d) Kelkar, A. A.; Patil, N. M.; Chaudhari, R. V. *Tetrahedron Lett.* **2002**, *43*, 7143–7146. (e) Daly, S.; Haddow, M. F.; Orpen, A. G.; Rolls, G. T. A.; Wass, D. F.; Wingad, R. L. *Organometallics* **2008**, *27*, 3196–3202. (f) Gujadhur, R. K.; Bates, C. G.; Venkataraman, D. *Org. Lett.* **2001**, *3*, 4315–4317. (g) Fagan, P. J.; Hauptman, E.; Shapiro, R.; Casalnuovo, A. *J. Am. Chem. Soc.* **2000**, *122*, 5043–5051. (h) Kwong, F. Y.; Klapars, A.; Buchwald, S. L. *Org. Lett.* **2002**, *4*, 581–584. (i) Buck, E.; Song, Z. J.; Tschäen, D.; Dormer, P. G.; Volante, R. P.; Reider, P. J. *Org. Lett.* **2002**, *4*, 1623–1626. (j) Ma, D.; Cai, Q. *Org. Lett.* **2003**, *5*, 3799–3802. (k) Kwong, F. Y.; Buchwald, S. L. *Org. Lett.* **2003**, *5*, 793–796. (l) Zanon, J.; Klapars, A.; Buchwald,

- S. L. *J. Am. Chem. Soc.* **2003**, *125*, 2890–2891. (m) Antilla, J. C.; Baskin, J. M.; Barder, T. E.; Buchwald, S. L. *J. Org. Chem.* **2004**, *69*, 5578–5587. (n) Cristau, H.-J.; Cellier, P. P.; Hamada, S.; Spindler, J.-F.; Taillefer, M. *Org. Lett.* **2004**, *6*, 913–916. (o) Rao, H.; Jin, Y.; Fu, H.; Jiang, Y.; Zhao, Y. *Chem. Eur. J.* **2006**, *12*, 3636–3646.
18. (a) Weingarten, H. *J. Org. Chem.* **1964**, *29*, 3624–3626. (b) Aalten, H. L.; van Koten, G.; Grove, D. M.; Kuilman, T.; Piekstra, O. G.; Hulshof, L. A.; Sheldon, R. A. *Tetrahedron* **1989**, *45*, 5565–5578. (c) Bacon, R. G. R.; Karim, A. *J. Chem. Soc., Perkin Trans. I* **1973**, 272–278. (d) Whitesides, G. M.; Sadowski, J. S.; Lilburn, J. *J. Am. Chem. Soc.* **1974**, *96*, 2829–2835. (e) Yamamoto, T.; Ehara, Y.; Kubota, M.; Yamamoto, A. *Bull. Chem. Soc. Jpn.* **1980**, *53*, 1299–1302. (f) Strieter, E. R.; Blackmond, D. G.; Buchwald, S. L. *J. Am. Chem. Soc.* **2005**, *127*, 4120–4121.
19. Jones, G. O.; Liu, P.; Houk, K. N.; Buchwald, S. L. *J. Am. Chem. Soc.* **2010**, *132*, 6205–6213.
20. Huffman, L. M.; Stahl, S. S. *J. Am. Chem. Soc.* **2008**, *130*, 9196–9197.
21. (a) Casitas, A.; King, A. E.; Parella, T.; Costas, M.; Stahl, S. S.; Ribas, X. *Chem. Sci.* **2010**, *1*, 326. (b) Casitas, A.; Poater, A.; Solà, M.; Stahl, S. S.; Costas, M.; Ribas, X. *Dalton Trans.* **2010**, 39, 10458–10463.
22. (a) Tye, J. W.; Weng, Z.; Johns, A. M.; Incarvito, C. D.; Hartwig, J. F. *J. Am. Chem. Soc.* **2008**, *130*, 9971–9983. (b) Giri, R.; Hartwig, J. F. *J. Am. Chem. Soc.* **2010**, *132*, 15860–15863. (c) Tye, J. W.; Weng, Z.; Giri, R.; Hartwig, J. F. *Angew Chem Int Ed.* **2010**, *49*, 2185–2189. (d) Chen, C.; Weng, Z.; Hartwig, J. F. *Organometallics* **2012**, *31*, 8031–8037.

23. Strieter, E. R.; Bhayana, B.; Buchwald, S. L. *J. Am. Chem. Soc.* **2009**, *131*, 78–88.
24. Yu, H.-Z.; Jiang, Y.-Y.; Fu, Y.; Liu, L. *J. Am. Chem. Soc.* **2010**, *132*, 18078–18091.
25. Lotito, K. J.; Peters, J. C. *Chem. Commun.* **2010**, *46*, 3690–3692.
26. Creutz, S. E.; Lotito, K. J.; Fu, G. C.; Peters, J. C. *Science* **2012**, *338*, 647–651.
27. The deuterium label was used to conclusively rule out a radical-free organometallic mechanism in which the aryl iodide can oxidatively add to Cu(I), β -migratory insert in a *syn* fashion, and reductively eliminate to generate the same cyclized product. If this mechanism were operative, only the (R,R) or (S,S) products would be observed.
28. Bissember, A. C.; Lundgren, R. J.; Creutz, S. E.; Peters, J. C.; Fu, G. C. *Angew. Chem. Int. Ed.* **2013**, *52*, 5129–5133.
29. Schaumann, E. *Sci. Synth.* **2008**, *40a*, 7 – 22
30. Ziegler, D. T.; Choi, J.; Muñoz-Molina, J. M.; Bissember, A. C.; Peters, J. C.; Fu, G. C. *J. Am. Chem. Soc.* **2013**, *135*, 13107–13112.
31. Do, H.-Q.; Bachman, S.; Bissember, A. C.; Peters, J. C.; Fu, G. C. *J. Am. Chem. Soc.* **2014**, *136*, 2162–2167.
32. Zhao, W.; Wurz, R. P.; Peters, J. C.; Fu, G. C. *J. Am. Chem. Soc.* **2017**, *139*, 12153–12156.
33. Kainz, Q. M.; Matier, C. D.; Bartoszewicz, A.; Zultanski, S. L.; Peters, J. C.; Fu, G. C. *Science* **2016**, *351*, 681–685.
34. Uyeda, C.; Tan, Y.; Fu, G. C.; Peters, J. C. *J. Am. Chem. Soc.* **2013**, *135*, 9548–9552.
35. Tan, Y.; Muñoz-Molina, J. M.; Fu, G. C.; Peters, J. C. *Chem. Sci.* **2014**, *5*, 2831–2835.

36. Ratani, T. S.; Bachman, S.; Fu, G. C.; Peters, J. C. *J. Am. Chem. Soc.* **2015**, *137*, 13902–13907.
37. Johnson, M. W.; Hannoun, K. I.; Tan, Y.; Fu, G. C.; Peters, J. C. *Chem. Sci.* **2016**, *7*, 4091–4100.
38. Ahn, J. M.; Ratani, T. S.; Hannoun, K. I.; Fu, G. C.; Peters, J. C. *J. Am. Chem. Soc.* **2017**.
39. Rabalais, N. *Ambio* **2002**, *31*, 102–112.
40. (a) Williams, P. A.; Fülöp, V.; Garman, E. F.; Saunders, N. F. W.; Ferguson, S. J.; Hajdu, J. *Nature* **1997**, *389*, 406–412. (b) Tocheva, E. I.; Rosell, F. I.; Mauk, A. G.; Murphy, M. E. P. *Science* **2004**, *304*, 867–870.
41. Uyeda, C.; Peters, J. C. *J. Am. Chem. Soc.* **2013**, *135*, 12023–12031.
42. Prier, C. K.; Rankic, D. A.; Macmillan, D. W. C. *Chem. Rev.* **2013**, *113*, 5322.
43. Turro, N. J. *Pure Appl. Chem.* **1977**, *49*, 405–429.
44. Fagnoni, M.; Dondi, D.; Ravelli, D.; Albin, A. *Chem. Rev.* **2007**, *107*, 2725–2756.
45. Hartland, G. V.; Xie, W.; Dai, H. L.; Simon, A.; Anderson, M. J. *Rev. Sci. Instrum.* **1992**, *63*, 3261–3267.
46. (a) Chang, I.; Gray, H. B.; Winkler, J. R. *J. Am. Chem. Soc.* **1991**, *113*, 7056–7057.
(b) Liang, N.; Mauk, A. G.; Pielak, G. J.; Johnson, J. A.; Smith, M.; Hoffman, B. M. *Science* **1988**, *240*, 311–313.
47. (a) Fraiji, L. K.; Hayes, D. M.; Werner, T. C. *J. Chem. Educ.* **1992**, *69*, 424–427. (b) Turro, N.J. *Modern Molecular Photochemistry*; University Science Books: Sausalito, 1991.

Chapter 2 : Photoinduced, Copper-Catalyzed Alkylation of Amines: A Mechanistic Study of the Cross-Coupling of Carbazole with Alkyl Bromides

Reproduced in part with permission from:

Ahn, J. M.; [†] **Ratani, T. S.**; [†] Hannoun, K. I.; Fu, G. C.; Peters, J. C. *J. Am. Chem. Soc.* **2017**, *139*, 12716–12723.

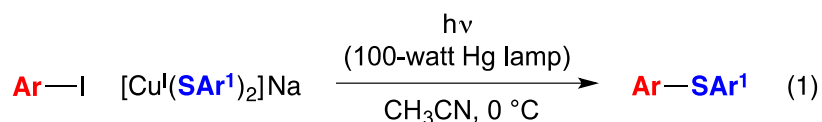
[†]Equal Contributions

© 2017 American Chemical Society

2.1 Introduction

Since our discovery several years ago of a photoinduced, copper-catalyzed Ullmann-type N-arylation process,¹ we have expanded the scope of such photoinduced, copper-catalyzed coupling reactions to a variety of nucleophiles (nitrogen, sulfur, oxygen, and carbon) and electrophiles (aryl, alkyl, alkenyl, and alkynyl halides).^{2,3,4} We have naturally been interested in understanding the mechanisms of these processes, recognizing that different pathways may well be operative, depending on the nucleophile, the electrophile, and the reaction conditions.

In 2016, we described a mechanistic investigation of one such process, specifically, photoinduced reactions of aryl iodides with copper(I)–thiolates (eq 1).⁵ Our observations were consistent with the pathway outlined in Figure 2.1 (**A**→**D**): irradiation of a copper(I)–nucleophile complex (**A**) leads to the formation of an excited-state complex (**B**), which donates an electron to the electrophile (**R**–**X**) to generate an organic radical and a copper(II)–nucleophile complex (**C**), which then combine in-cage to form a carbon–nucleophile bond. Due in part to solubility issues, this mechanistic study of photoinduced S-arylation focused on stoichiometric reactions (**A**→**D**), rather than on catalyzed processes. This pathway, wherein a copper complex serves both as a photoreductant and as a participant in the key bond-forming step, differs from that suggested for most photoredox reactions, wherein a photosensitizer (e.g., Ru(bipy)₃²⁺) generates a radical via reduction or oxidation, but is not itself engaged in the key bond construction.⁶



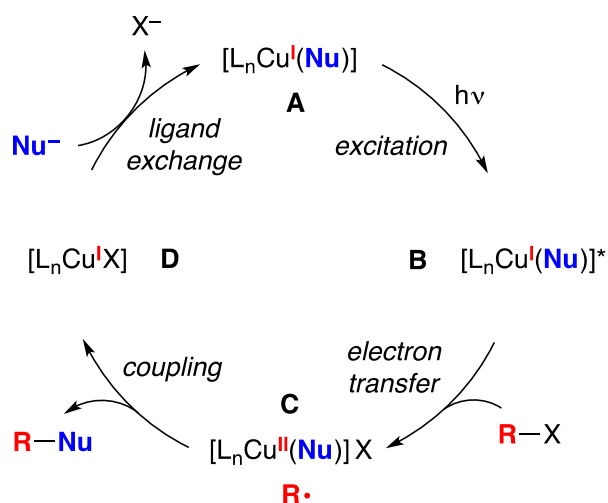
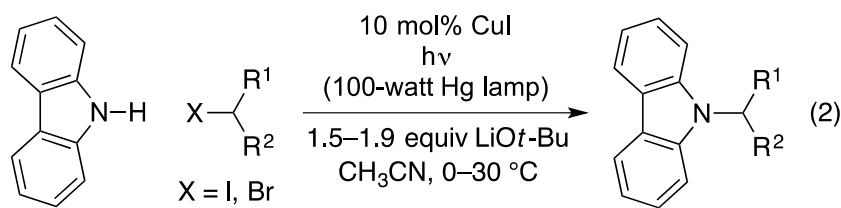


Figure 2.1: Outline of a possible pathway for photoinduced, copper-catalyzed cross-couplings. For simplicity, all copper complexes are illustrated as neutral species, and all processes are depicted as irreversible; X may be an inner- or an outer-sphere group, and L_n denotes additional ligand(s) coordinated to copper.

The development of new methods for the construction of C–N bonds is an important objective, due to the importance of amines in a variety of disciplines, including biology, chemistry, and materials science.⁷ Because classical S_N2 reactions of nitrogen nucleophiles with alkyl halides have rather limited scope, the discovery of catalyzed variants is of substantial interest, and in recent years the first systematic studies of transition-metal catalysis have been described.^{2a,d,g,8} For example, in 2013 we reported that alkylations of carbazoles by unactivated primary and secondary alkyl halides can be achieved under mild conditions in the presence of copper and light (eq 2).^{2a}

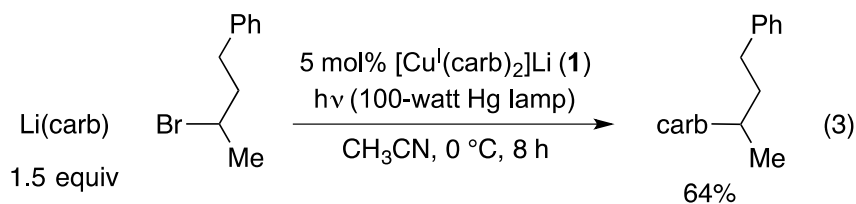


Complementing our recent study of the photoinduced arylation of copper–thiolates,⁵ we have turned our attention to elucidating the mechanism of the photoinduced, copper-catalyzed alkylation of carbazole by alkyl halides. These processes differ in the nucleophile (sulfur vs. nitrogen) and in the electrophile (aryl vs. alkyl halide), while keeping the reaction conditions (light source, solvent, and temperature) constant; furthermore, in the present investigation, we examine not only stoichiometric reactions, but also catalyzed couplings.

2.2 Results and Discussion

2.2.1 Background

In our original report of photoinduced, copper-catalyzed alkylations of carbazoles, we described preliminary mechanistic studies that employed alkyl iodides as electrophiles.^{2a} In the present investigation, we have chosen to focus instead on alkyl bromides, in order to reduce potential complications due to undesired photoinduced side reactions. Furthermore, we have utilized discrete reaction components $[\text{Cu}^{\text{I}}(\text{carb})_2]\text{Li}$ (**1**)⁹ as the catalyst and $\text{Li}(\text{carb})$ as the nucleophile; carb = carbazolide), rather than the mixture of CuI , carbazole, and LiOt-Bu that was described in our original study. Under the new conditions, carbazole is alkylated by 2-bromo-4-phenylbutane in 64% yield at 0 °C in the presence of 5 mol% of catalyst **1** (eq 3). In the absence of light, no coupling (<1%) is observed.



2.2.2 Stoichiometric coupling of $[\text{Cu}^{\text{I}}(\text{carb})_2]\text{Li}$ with an alkyl bromide (Figure 2.2, A'→D')

In an initial study, we examined the stoichiometric reaction of $[\text{Cu}^{\text{I}}(\text{carb})_2]\text{Li}$ with 2-bromo-4-phenylbutane (1:1), and we have determined that N-alkylation proceeds in 96% yield (eq 4). This is consistent with the mechanism outlined in Figures 2.1 and 2.2.

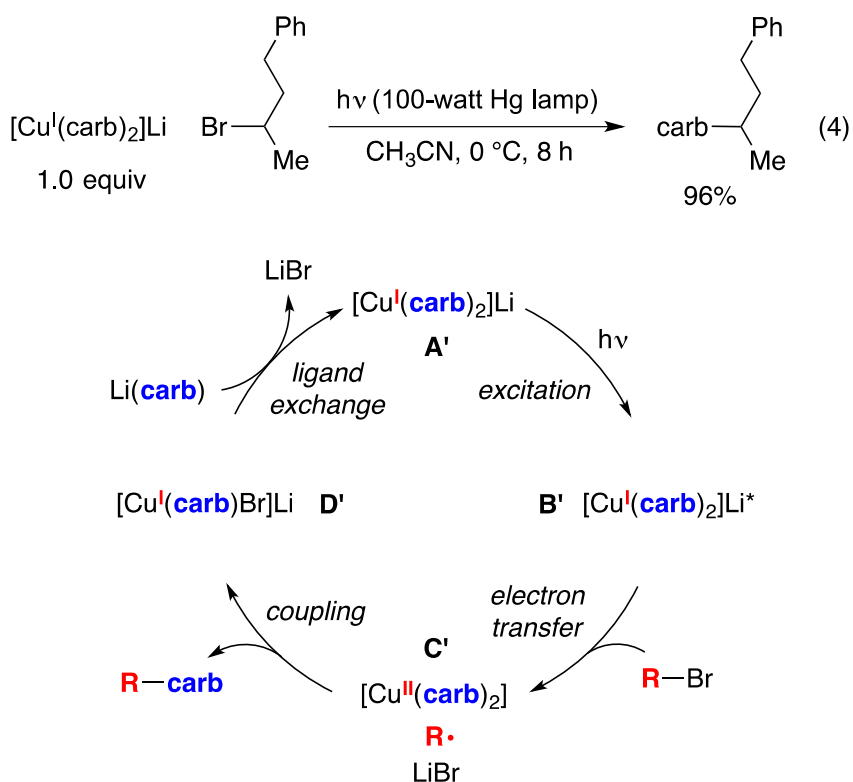


Figure 2.2: Outline of a possible pathway for the photoinduced, copper-catalyzed cross-coupling of Li(carb) with an alkyl bromide.

2.2.3 Excitation of $[\text{Cu}^{\text{I}}(\text{carb})_2]\text{Li}$ (Figure 2.2, A'→B')

The UV–vis spectrum of $[\text{Cu}^{\text{I}}(\text{carb})_2]\text{Li}$ in CH_3CN exhibits an absorption at 365 nm with $\epsilon = 4300 \text{ M}^{-1} \text{ cm}^{-1}$, which overlaps with the highest-energy emission band of the medium-pressure Hg lamp used for the catalytic reactions. This absorption profile has enabled us to probe the photophysical properties of the excited-state copper complex, $[\text{Cu}^{\text{I}}(\text{carb})_2]\text{Li}^*$, by transient absorption spectroscopy using a Nd:YAG laser source with excitation at 355 nm. For a 1.7 mM solution of $[\text{Cu}^{\text{I}}(\text{carb})_2]\text{Li}$ (as under the catalysis conditions of eq 3), we observe a non-emissive excited state with a maximum absorption at 580 nm and a lifetime of 910 ns (Figure 2.3a).¹⁰

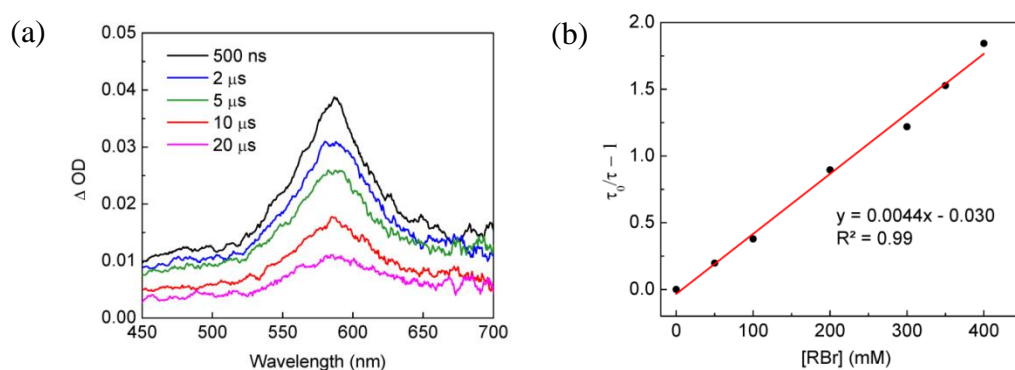


Figure 2.3: (a) Difference absorption spectra of $[\text{Cu}^{\text{I}}(\text{carb})_2]\text{Li}^*$ at selected time delays (excitation of $[\text{Cu}^{\text{I}}(\text{carb})_2]\text{Li}$ in CH_3CN at 355 nm). (b) Quenching of $[\text{Cu}^{\text{I}}(\text{carb})_2]\text{Li}^*$ by 2-bromo-4-phenylbutane (RBr) in CH_3CN observed by time-resolved transient absorption spectroscopy ($\lambda_{\text{exc}} = 355$ nm; $\lambda_{\text{obs}} = 580$ nm; room temperature).

2.2.4 Single electron transfer (SET) from $[\text{Cu}^{\text{I}}(\text{carb})_2]\text{Li}^*$ to an alkyl bromide

(Figure 2.2, B' \rightarrow C')

To determine the viability of photoinduced SET from $[\text{Cu}^{\text{I}}(\text{carb})_2]\text{Li}^*$ to 2-bromo-4-phenylbutane, we have studied the excited-state quenching kinetics by examining the dependence of the lifetime of the transient-absorption signal at 580 nm on the concentration of the alkyl bromide. The lifetime of $[\text{Cu}^{\text{I}}(\text{carb})_2]\text{Li}^*$ in CH_3CN decreases as the concentration of the alkyl bromide increases (Figure 2.3b), and the second-order rate constant for quenching is $4.8 \times 10^6 \text{ M}^{-1} \text{ s}^{-1}$. In view of the lowest-energy excited state of the alkyl bromide, electron transfer, rather than energy transfer, from $[\text{Cu}^{\text{I}}(\text{carb})_2]\text{Li}^*$ to the alkyl bromide is the more likely mechanism of quenching.¹¹

Because SET from $[\text{Cu}^{\text{I}}(\text{carb})_2]\text{Li}^*$ to an alkyl bromide should lead to the formation of a paramagnetic Cu(II) complex, we have employed electron paramagnetic resonance (EPR) spectroscopy to probe for an $S = 1/2$ copper photoproduct. When a

freezing mixture of $[\text{Cu}^{\text{I}}(\text{carb})_2]\text{Li}$ and 2-bromo-4-phenylbutane (5 equiv) in butyronitrile is irradiated at 350 nm, a pseudo-axial EPR signal is observed (Figure 2.4, black trace). A similar spectrum is obtained by treating $[\text{Cu}^{\text{I}}(\text{carb})_2]\text{Li}$ with tris(4-bromophenyl)aminium hexachloroantimonate (Magic Blue; 0.2 equiv) in butyronitrile at $-80\text{ }^\circ\text{C}$ (Figure 2.4, red trace). Although hyperfine coupling is unresolved in these spectra, strong g anisotropy indicates the presence of a copper-containing metalloradical.

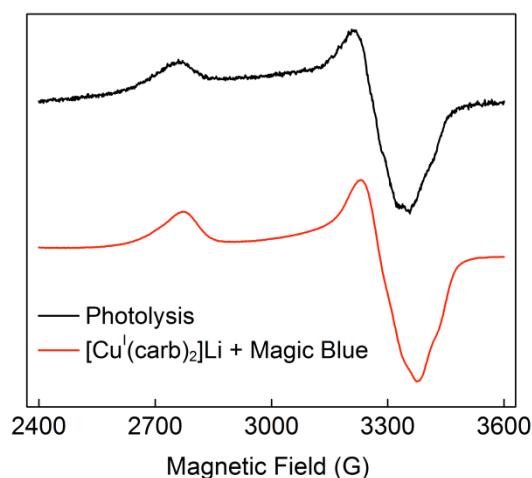


Figure 2.4: EPR spectra (9.4 GHz, 77 K). Black trace: mixture of $[\text{Cu}^{\text{I}}(\text{carb})_2]\text{Li}$ and 2-bromo-4-phenylbutane (5 equiv) in freezing butyronitrile upon irradiation at 350 nm; red trace: mixture of $[\text{Cu}^{\text{I}}(\text{carb})_2]\text{Li}$ and Magic Blue (0.2 equiv) in butyronitrile at $-80\text{ }^\circ\text{C}$. Simulated g -values (see SI): $g = [2.445, 2.060, 1.994]$.

2.2.5 SET from $[\text{Li}(\text{carb})]^*$ to an alkyl bromide

In a control reaction, $\text{Li}(\text{carb})$ and 2-bromo-4-phenylbutane do not couple in the absence of light (8 h at $0\text{ }^\circ\text{C}$); the alkyl bromide can be recovered quantitatively. However, when a mixture of $\text{Li}(\text{carb})$ and 2-bromo-4-phenylbutane is irradiated with a Hg lamp, a small amount of the C–N coupling product is generated (5% yield), although

this N-alkylation is much less efficient than in the presence of a copper catalyst (Figure 2.5). In the copper-free reaction, side products E (32%), F (4%), and G (3%)¹² are also observed (eq 5).

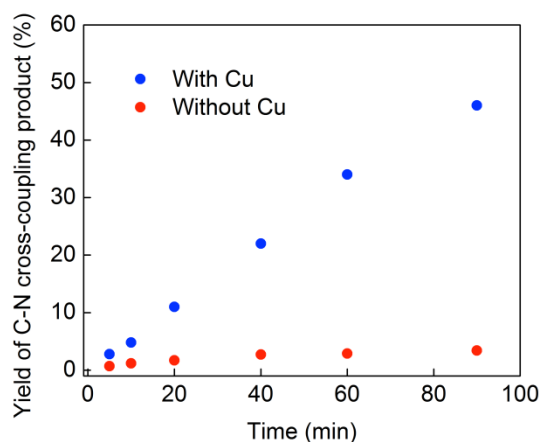
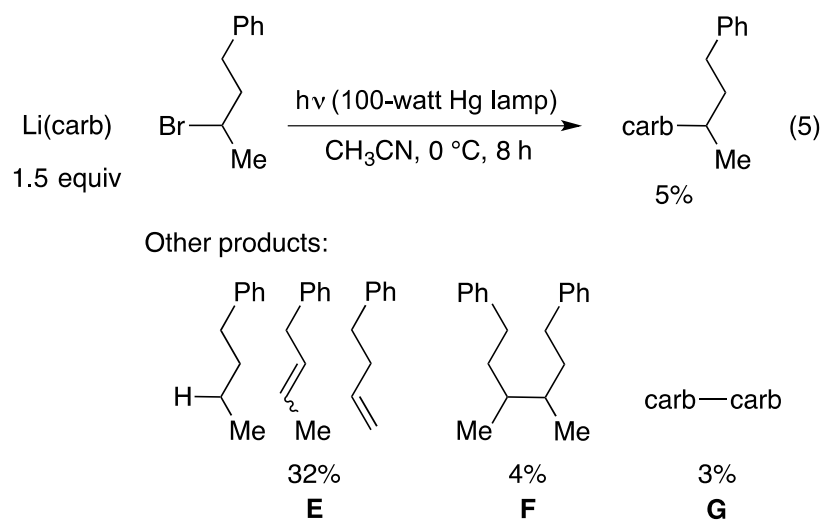


Figure 2.5: Impact of a copper catalyst on C–N cross-coupling: Photoinduced reaction of Li(carb) (1.5 equiv) with 2-bromo-4-phenylbutane (100-watt Hg lamp, CH₃CN, 0 °C) in the presence of 5 mol% [Cu^I(carb)₂Li and in the absence of copper.

Because compounds **E–G** likely form via bimolecular reactions of alkyl or carbazyl radicals,¹³ we decided to investigate a possible role for photoinduced SET from $[\text{Li}(\text{carb})]^*$, the excited state of $\text{Li}(\text{carb})$, to the alkyl bromide under our reaction conditions. The UV–vis spectra of solutions of $\text{Li}(\text{carb})$ in CH_3CN show concentration-dependent molar absorptivity. At concentrations below 0.4 mM, $\text{Li}(\text{carb})$ does not absorb appreciably at 365 nm (Figure 2.6, black trace); however, at concentrations above 0.4 mM, absorption bands near 365 nm that feature molar absorptivity that is concentration-dependent begin to appear and are pronounced at 3.1 mM (Figure 2.6, blue trace). At 49 mM, which is the concentration of $\text{Li}(\text{carb})$ that is present under our catalysis conditions (eq 3), the molar absorptivity of $\text{Li}(\text{carb})$ at 365 nm is $2200 \text{ M}^{-1} \text{ cm}^{-1}$.

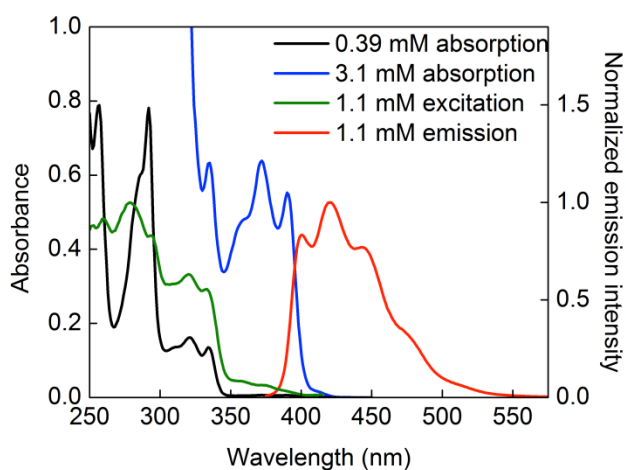


Figure 2.6: All data were collected in CH_3CN at room temperature. (a) Black trace: absorption spectrum for $[\text{Li}(\text{carb})] = 0.39 \text{ mM}$; blue trace: absorption spectrum for $[\text{Li}(\text{carb})] = 3.1 \text{ mM}$; green trace: excitation spectrum for $[\text{Li}(\text{carb})] = 1.1 \text{ mM}$ ($\lambda_{\text{em}} = 420 \text{ nm}$); red trace: emission spectrum for $[\text{Li}(\text{carb})] = 1.1 \text{ mM}$ ($\lambda_{\text{exc}} = 365 \text{ nm}$).

This dependence of the molar absorptivity on the concentration of Li(carb) is likely due to changes in aggregation.¹⁴ ^7Li NMR and ^1H NMR spectroscopic data support the hypothesis that the aggregation of Li(carb) is concentration-dependent in CH_3CN . For example, the ^7Li and ^1H NMR chemical shifts of Li(carb) vary with concentration. Furthermore, ^1H diffusion ordered spectroscopy (^1H DOSY) reveals that, at low concentrations (<2 mM) of Li(carb), a species with a hydrodynamic volume comparable to that of carbazole is observed.¹⁵ When the concentration of Li(carb) is increased to 49 mM (as under the catalysis conditions of eq 3), the volume triples, consistent with a significant change in aggregation.

Upon photoexcitation of a 49 mM solution of Li(carb) by a Nd:YAG laser at 355 nm, the excited state of Li(carb) emits at 420 nm with a lifetime of 31 ns (see SI). Stern–Volmer analysis establishes that the luminescent state of $[\text{Li}(\text{carb})]^*$ is quenched by 2-bromo-4-phenylbutane with a second-order rate constant of $4.9 \times 10^8 \text{ M}^{-1} \text{ s}^{-1}$ at room temperature (Figure 2.7). Thus, the UV–vis and Stern–Volmer data, combined with the higher concentration of Li(carb) compared with $[\text{Cu}^{\text{I}}(\text{carb})_2]\text{Li}$ under the catalysis conditions, suggest that $[\text{Li}(\text{carb})]^*$ may be the primary photoreductant during catalysis.

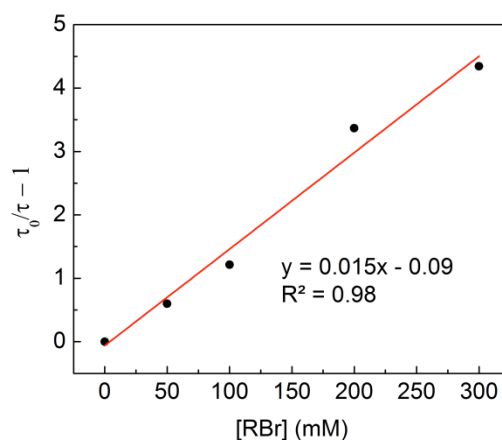


Figure 2.7: Quenching of $[\text{Li}(\text{carb})]^*$ by 2-bromo-4-phenylbutane (RBr) in CH_3CN observed by time-resolved luminescence spectroscopy ($\lambda_{\text{exc}} = 355 \text{ nm}$; $\lambda_{\text{obs}} = 420 \text{ nm}$; room temperature).

On the basis of these observations, we propose an additional, dominant pathway for the photoinduced, copper-catalyzed coupling of carbazole with alkyl bromides (Figure 2.8). In this mechanism, $\text{Li}(\text{carb})$ is photoexcited to generate $[\text{Li}(\text{carb})]^*$, which transfers an electron to the alkyl bromide, resulting in the formation of a carbazyl radical and an alkyl radical. These radicals diffuse away from one another faster than they couple. The carbazyl radical reacts with $[\text{Cu}^{\text{I}}(\text{carb})_2]\text{Li}$ (**1**) to generate a copper(II) complex, $[\text{Cu}^{\text{II}}(\text{carb})_3]\text{Li}$ (**2**), which then couples with an alkyl radical to afford the N-alkylation product. As in the case of the original mechanism (Figure 2.2),¹⁶ the key C–N bond-forming step is the reaction of an alkyl radical with a Cu(II)–carbazolide complex, but the pathway for forming these intermediates is different.

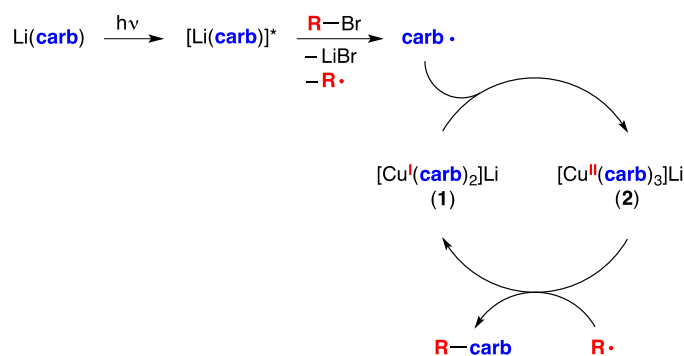


Figure 2.8: Outline of a new possible pathway for photoinduced, copper-catalyzed cross-coupling of Li(carb) with an alkyl bromide.

In order for this catalytic cycle to be viable and for side products (e.g., **E**, **F**, and **G** in the copper-free reaction illustrated in eq 5) to be minimized, the concentration of complexes **1** and **2** should be higher than the concentration of carbazyl and alkyl radicals that are being generated by photolysis. Accordingly, we sought evidence for $[\text{Cu}^{\text{I}}(\text{carb})_2]\text{Li}$ (**1**) and for $[\text{Cu}^{\text{II}}(\text{carb})_3]\text{Li}$ (**2**), the postulated persistent radical,¹⁷ under catalysis conditions.¹⁸

2.2.6 Evidence for the presence of $[\text{Cu}^{\text{I}}(\text{carb})_2]\text{Li}$ (**1**) under catalysis conditions

Previously, we have crystallographically characterized $[\text{Cu}^{\text{I}}(\text{carb})_2]\text{Li}$ and observed its presence via ESI-MS during a photoinduced, copper-catalyzed alkylation of carbazole by an alkyl iodide.^{2a} We have now determined that, for the coupling of an alkyl bromide (eq 3), we also observe signals at m/z of 395 and 397, which correspond to the masses of $[\text{Cu}^{\text{I}}(\text{carb})_2]^-$ and $[\text{Cu}^{\text{II}}(\text{carb})_3]^-$, respectively, after 60 minutes of irradiation.

2.2.7 Evidence for the presence of $[\text{Cu}^{\text{II}}(\text{carb})_3]\text{Li}$ (**2**) under catalysis conditions

As indicated above, the efficient operation of the catalytic cycle outlined in Figure 2.8 requires that the concentration of $[\text{Cu}^{\text{II}}(\text{carb})_3]\text{Li}$ (**2**) be higher than the concentration

of the alkyl radical that is being generated through photolysis of Li(carb). This suggested that it might be possible to characterize this proposed intermediate via spectroscopy and perhaps even crystallography.

Since $[\text{Cu}^{\text{II}}(\text{carb})_3]\text{Li}$ would have a d^9 configuration, we undertook an EPR investigation of a catalyzed cross-coupling. Specifically, a reaction mixture under the model conditions (eq 3) was irradiated at $0\text{ }^\circ\text{C}$ for 60 minutes and then freeze-quenched at $-196\text{ }^\circ\text{C}$, leading to the observation of a strong, pseudo-axial EPR signal that shows an unpaired spin coupled to $^{63/65}\text{Cu}$ ($I = 3/2$) (Figure 2.9, black trace; a 4-line coupling pattern is evident in g_z). This EPR spectrum is different from that observed upon irradiation of a mixture of $[\text{Cu}^{\text{I}}(\text{carb})_2]\text{Li}$ (**1**) and this alkyl bromide in the absence of added Li(carb) (Figure 2.4, black trace).

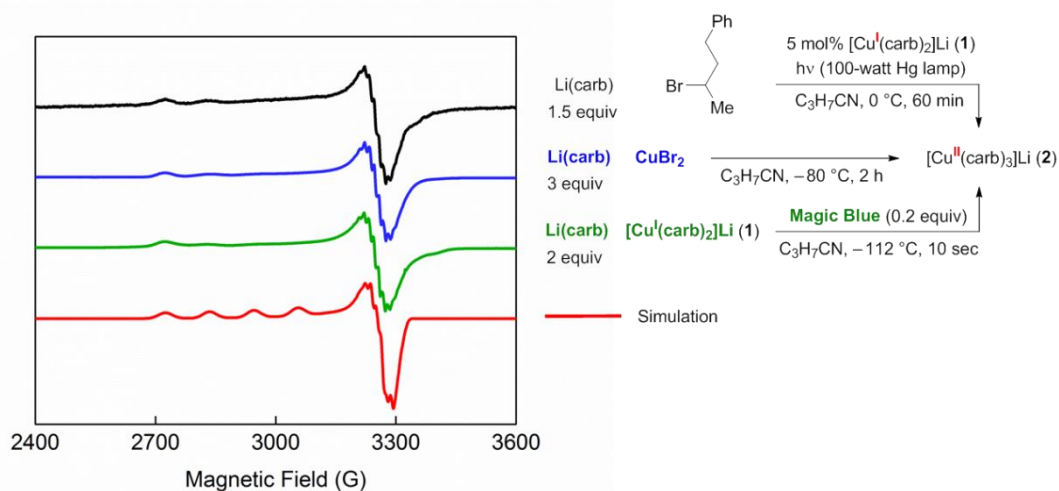


Figure 2.9: EPR evidence for $[\text{Cu}^{\text{II}}(\text{carb})_3]\text{Li}$ (**2**), generated through three independent pathways. Black trace: catalysis mixture; blue trace: mixture of Li(carb) and CuBr₂; green trace: mixture of Li(carb), $[\text{Cu}^{\text{I}}(\text{carb})_2]\text{Li}$ (**1**), and Magic Blue; red trace: simulated

EPR spectrum ($g = [2.318, 2.058, 2.050]$) displaying hyperfine to Cu and three ^{14}N atoms.

The same EPR-active compound can be generated through low temperature treatment of CuBr_2 with 3 equivalents of $\text{Li}(\text{carb})$ (Figure 2.9, blue trace) and through reaction of $[\text{Cu}^{\text{I}}(\text{carb})_2]\text{Li}$ (**1**) with $\text{Li}(\text{carb})$ and Magic Blue (Figure 2.9, green trace). These EPR signals are modeled well as a monomeric $\text{Cu}(\text{II})$ species coordinated by three equivalent nitrogen ($I = 1$) atoms (Figure 2.9, red trace), consistent with its assignment as the homoleptic $[\text{Cu}^{\text{II}}(\text{carb})_3]^-$ complex.

We have carried out corresponding studies using UV-vis spectroscopy (Figure 2.10). When a reaction mixture is irradiated under the standard catalysis conditions (eq 3), the solution turns deep-blue; this color diminishes when irradiation is discontinued or when the solution is allowed to warm to room temperature. Similarly, under the standard conditions but in butyronitrile at $-80\text{ }^\circ\text{C}$, irradiation results in an intense blue color. The UV-vis spectrum of this solution displays an absorption maximum at 580 nm (Figure 2.10, black trace); this feature is not observed when the same experiment is conducted in the absence of $[\text{Cu}^{\text{I}}(\text{carb})_2]\text{Li}$.¹⁹ Likewise, when CuBr_2 is treated with 3 equiv of $\text{Li}(\text{carb})$ in butyronitrile at $-80\text{ }^\circ\text{C}$, a deep-blue solution with an absorption band centered around 580 nm is observed (Figure 2.10, blue trace). Finally, when a mixture of $[\text{Cu}^{\text{I}}(\text{carb})_2]\text{Li}$ and $\text{Li}(\text{carb})$ (2 equiv) is oxidized by Magic Blue (0.3 equiv) in butyronitrile at $-80\text{ }^\circ\text{C}$, the same absorption feature is evident (green trace). We hypothesize that the absorption band at 580 nm correlates with the EPR-active $\text{Cu}(\text{II})$ species shown in Figure 2.9.

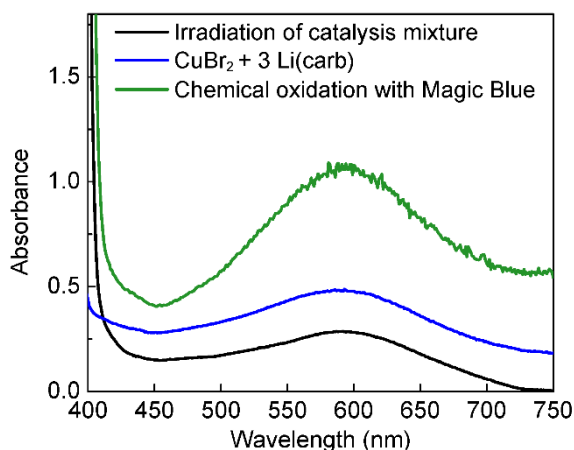


Figure 2.10: UV-vis spectra. Black trace: catalyzed reaction mixture irradiated in butyronitrile at $-80\text{ }^{\circ}\text{C}$; blue trace: mixture of CuBr_2 and $\text{Li}(\text{carb})$ (3 equiv) in butyronitrile at $-80\text{ }^{\circ}\text{C}$; green trace: mixture of $[\text{Cu}^{\text{I}}(\text{carb})_2]\text{Li}$ (1) and $\text{Li}(\text{carb})$ (2 equiv) treated with Magic Blue (0.3 equiv) in butyronitrile at $-80\text{ }^{\circ}\text{C}$.

Although we have been unable to crystallographically characterize a lithium salt of $[\text{Cu}^{\text{II}}(\text{carb})_3]^-$, due in part to its thermal instability, crystals of two potassium salts, $[\text{Cu}^{\text{II}}(\text{carb})_3][\text{K}(\text{THF})_6]$ and $[\text{Cu}^{\text{II}}(\text{carb})_3][\text{K}(\text{benzo-15-crown-5})_2]$,²⁰ have been obtained by layering Et_2O onto a solution that contained $\text{Cu}(\text{OTf})_2$, $\text{K}(\text{carb})$, and benzo-15-crown-5 in THF at $-78\text{ }^{\circ}\text{C}$ (Figure 2.11a). This complex represents a rare example of a structurally characterized homoleptic three-coordinate copper(II) complex.²¹ The powder and glass EPR spectra of $[\text{Cu}^{\text{II}}(\text{carb})_3][\text{K}(\text{benzo-15-crown-5})_2]$ are consistent with the spectra illustrated in Figure 2.9.

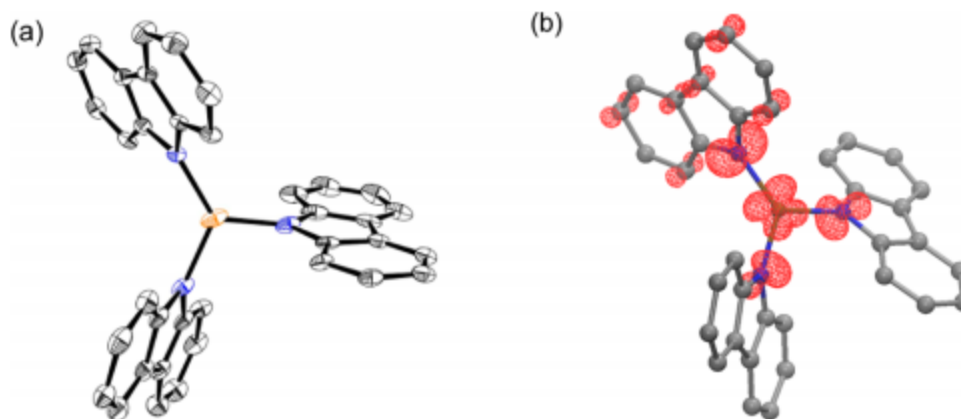


Figure 2.11: (a) X-ray crystal structure of [Cu^{II}(carb)₃][K(THF)₆] (thermal ellipsoids at 30% probability; hydrogen atoms and [K(THF)₆]⁺ are omitted for clarity). (b) DFT-computed spin-density plot of [Cu^{II}(carb)₃]⁻; 27% of the total spin resides on the three nitrogen atoms. See Appendix A for details.

The quality of the X-ray diffraction data for [Cu^{II}(carb)₃][K(THF)₆] is modest, and structural metrics should therefore be viewed with caution. Nevertheless, the N–Cu–N bond angles (two large and one small: 126.7(2)°, 124.4(2)°, 108.8(2)°) indicate a significant distortion from a trigonal planar geometry, as anticipated for an ²E electronic state that is Jahn-Teller active. DFT computations show significant spin delocalization, with 0.43 e⁻ on Cu and 0.27 e⁻ distributed between the three nitrogen atoms of the carbazolid ligands (Figure 2.11b).²²

Given the appreciable predicted spin density on nitrogen, [Cu^{II}(carb)₃]⁻ might display reactivity characteristic of a carbazyl radical. For example, the key bond-forming step in these photoinduced, copper-catalyzed reactions might occur through direct C–N coupling, rather than through a copper(III) intermediate. Previously, Warren and coworkers have observed the reaction between trityl radical (Ph₃C·) and a Cu(II)–anilido

complex to furnish a C–N bond ($\text{Ph}_3\text{C–NHAr}$) and Cu(I) .²³ While the addition of trityl radical did not yield C–N coupled product, addition of TEMPO–H to a solution of $[\text{Cu}^{\text{II}}(\text{carb})_3]\text{Li}$ generates $[\text{Cu}^{\text{I}}(\text{carb})_2]\text{Li}$ and $\text{TEMPO}\cdot$ as the only EPR-active species (TEMPO = 2,2,6,6-tetramethylpiperidine 1-oxyl). This reactivity is consistent with hydrogen atom abstraction of TEMPO–H by $[\text{Cu}^{\text{II}}(\text{carb})_3]^-$.²⁴

As outlined in Figure 2.8, we hypothesize that $[\text{Cu}^{\text{II}}(\text{carb})_3]\text{Li}$ (**2**) is generated through the coupling of $\text{carb}\cdot$ with $[\text{Cu}^{\text{I}}(\text{carb})_2]\text{Li}$ (**1**). DFT calculations support the viability of this elementary step, indicating that it is exergonic by $\sim 9 \text{ kcal mol}^{-1}$.²⁵ In contrast, the potential coupling of $[\text{Cu}^{\text{I}}(\text{carb})_2]\text{Li}$ (**1**) with $\text{R}\cdot$, the other radical that is produced upon excitation of $\text{Li}(\text{carb})$ and subsequent reaction with R–Br , to form $[\text{Cu}^{\text{II}}\text{R}(\text{carb})_2]^-$ is endergonic by $\sim 3 \text{ kcal mol}^{-1}$.

Next, using UV–vis spectroscopy, we have examined the build-up of the persistent radical, $[\text{Cu}^{\text{II}}(\text{carb})_3]\text{Li}$ (**2**), under our standard conditions for a catalyzed coupling (eq 3). When a reaction mixture is irradiated in a quartz cuvette at $0 \text{ }^\circ\text{C}$, an absorption band for $[\text{Cu}^{\text{II}}(\text{carb})_3]\text{Li}$ ($\lambda_{\text{max}} = 580 \text{ nm}$) is observed within a few seconds (Figure 2.12a). On the basis of an extinction coefficient of $\sim 1100 \text{ M}^{-1} \text{ cm}^{-1}$ for $[\text{Cu}^{\text{II}}(\text{carb})_3]\text{Li}$, a concentration of $[\text{Cu}^{\text{II}}(\text{carb})_3]\text{Li}$ corresponding to $\sim 50\%$ of the original amount of copper is reached within three minutes (Figure 2.12b).

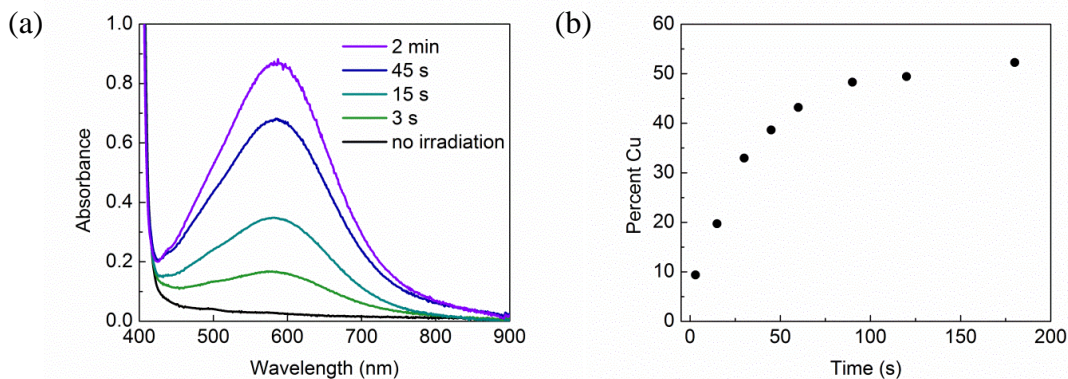


Figure 2.12: (a) Appearance of an absorption band ($\lambda_{\text{max}} = 580 \text{ nm}$) for $[\text{Cu}^{\text{II}}(\text{carb})_3]\text{Li}$ upon irradiation of a reaction mixture containing $[\text{Cu}^{\text{I}}(\text{carb})_2]\text{Li}$, $\text{Li}(\text{carb})$, and 2-bromo-4-phenylbutane in CH_3CN in a quartz cuvette at 0°C . (b) Concentration of $[\text{Cu}^{\text{II}}(\text{carb})_3]\text{Li}$ as a function of time.

According to our mechanistic hypothesis, at the outset of a photoinduced, copper-catalyzed C–N coupling, when the concentration of the persistent radical, $[\text{Cu}^{\text{II}}(\text{carb})_3]\text{Li}$ (2), is still low, a higher proportion of products derived from undesired side reactions of $\text{R}\cdot$ (e.g., E in eq 5) is expected; as the concentration of $[\text{Cu}^{\text{II}}(\text{carb})_3]\text{Li}$ builds up upon irradiation of the catalysis mixture, the proportion of the C–N cross-coupling product should increase. This is indeed observed (Figure 2.13).

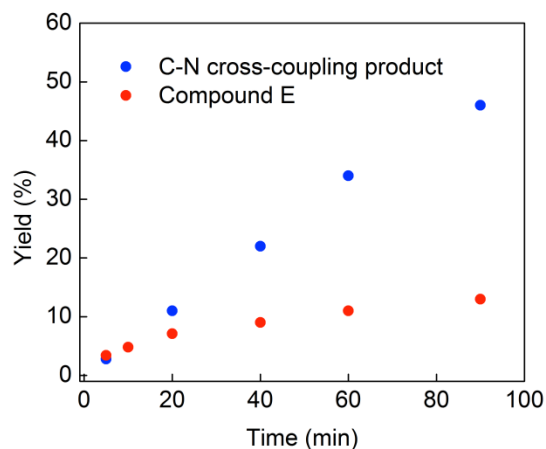


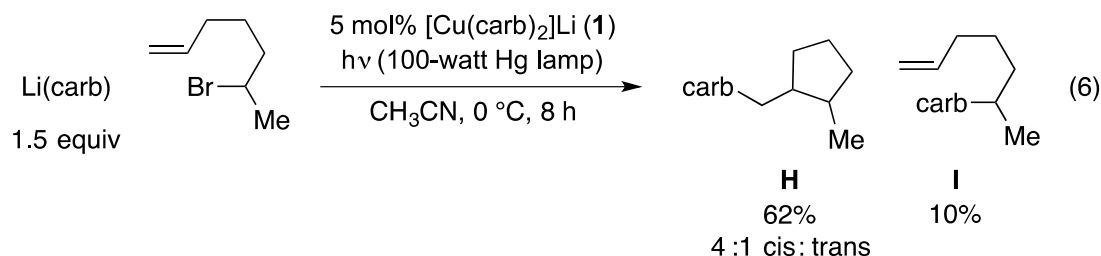
Figure 2.13: Product distribution in the photoinduced, copper-catalyzed coupling of Li(carb) with 2-bromo-4-phenylbutane (eq 3).

2.2.8 Evidence for out-of-cage C–N bond formation via a free-radical intermediate under catalysis conditions (Figure 2.8, 2→1)

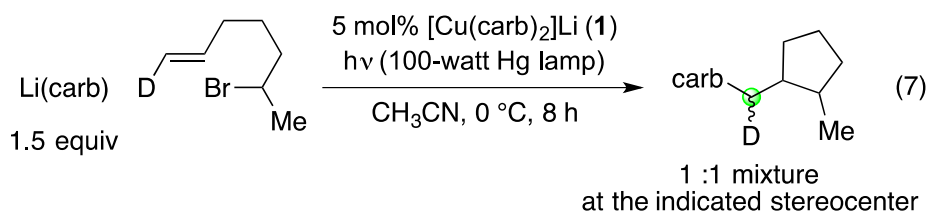
The mechanism outlined in Figure 2.8 suggests that the coupling of R· and carb· is an out-of-cage process mediated by copper. We have turned to a radical-cyclization probe to gain insight into the C–N bond-forming step of the catalytic cycle. Because the reaction of secondary bromides is the focus of the present study, we chose 6-bromo-1-heptene as the substrate. The derived secondary alkyl radical cyclizes with a rate constant of $1.0 \times 10^5 \text{ s}^{-1}$ at 25 °C,²⁶ furnishing a primary alkyl radical with 4:1 cis/trans diastereoselectivity.²⁷

When 6-bromo-1-heptene is subjected to our standard reaction conditions, the cyclization/coupling product (**H**) is formed in 62% yield with 4:1 diastereoselectivity, along with 10% of the direct-coupling product (**I**) (eq 6). Because the rate of diffusion (typically $>10^8 \text{ s}^{-1}$)²⁸ is significantly higher than the rate of cyclization of the derived

secondary radical, predominant generation of cyclized product **H** suggests that, if ring formation is occurring through radical cyclization, then C–N bond construction is proceeding primarily through an out-of-cage pathway.

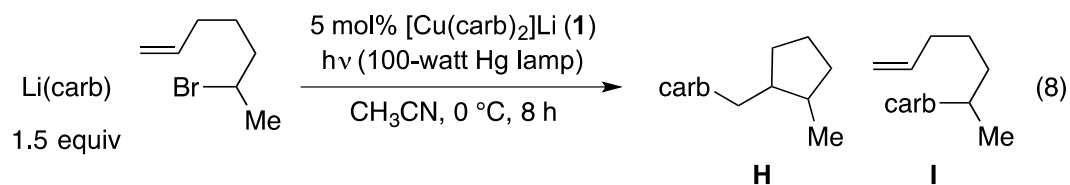


The 4:1 cis/trans stereoselectivity that we observe is identical to that previously reported for the cyclization of this putative secondary alkyl radical at 0 °C.²⁶ To provide further support for a radical, rather than an organometallic, pathway for ring formation, we have examined the photoinduced, copper-catalyzed coupling of the deuterium-labeled analogue of 6-bromo-1-heptene that is illustrated in eq 7. Analysis via NMR spectroscopy (60% yield) revealed a 1:1 mixture at the indicated stereocenter, which is inconsistent with a radical-free organometallic mechanism that involves uninterrupted oxidative addition, β -migratory insertion, and reductive elimination.²⁹



To further explore the question of out-of-cage coupling, we have investigated the effect of the concentration of the reaction on the ratio of cyclized (**H**) to uncyclized (**I**) product (eq 8; Table 2.1).³⁰ If all of the cross-coupling is occurring in-cage, then the ratio should not depend on concentration. The trend that we observe—a greater preference for cyclization at lower concentration—is that expected if out-of-cage coupling is occurring.

Table 2.1: Effect of reaction concentration on ratio of cyclized (H) to uncyclized (I) product.



[alkyl bromide] (mM)	ratio of products (H/I)
11	11
22	7.6
33	6.1
44	5.5
55	5.1

2.2.9 Evaluation of a radical chain mechanism under catalysis conditions

A recent report by Yoon serves as a reminder of the need to consider the possibility of radical chain pathways during photoredox processes.^{31,32} In the present study, we have determined that the total quantum yield (Φ) for all processes that consume 2-bromo-4-phenylbutane under the standard catalysis conditions (eq 3) is 0.10 ± 0.01 ,³³ a value that is consistent both with a non-chain pathway and with a chain process with rapid chain termination. We have also measured the Stern–Volmer quenching fraction (Q) to be 0.33, which suggests that at most 33% of all excited states of lithium carbazolidine that are generated are quenched by the electrophile. The chain length (Φ/Q ; the number of molecules of product formed per photoinduced electron-transfer event) is therefore 0.30, indicating that every quenching event of Li(carb)* leads to the consumption of 0.30 equivalents of electrophile. This low chain length, which represents a lower limit (see Appendix A), is suggestive of a non-chain pathway.

2.3 Conclusions

Using a wide range of tools, we have investigated the mechanism of the photoinduced, copper-catalyzed coupling of carbazole with an alkyl bromide, which is one of the first examples of transition-metal catalysis of the alkylation of an amine by an alkyl halide. In addition to the originally proposed pathway, we suggest that a second mechanism is operative and dominant, wherein photoexcited Li(carb) serves as a reductant of the alkyl bromide, generating an alkyl radical and a carbazyl radical, which combine via an out-of-cage, copper-catalyzed pathway in which $[\text{Cu}^{\text{I}}(\text{carb})_2]^-$ (**1**) and $[\text{Cu}^{\text{II}}(\text{carb})_3]^-$ (**2**) are key intermediates (Figure 2.8).

Using ESI-MS, we have obtained evidence for the presence of $[\text{Cu}^{\text{I}}(\text{carb})_2]^-$ (**1**) under catalysis conditions. With the aid of UV-vis and luminescence spectroscopy, we have established that, upon irradiation, Li(carb) can undergo excitation and then electron transfer to an alkyl bromide, thereby affording a carbazyl radical and an alkyl radical. Using EPR spectroscopy, we have obtained evidence for the formation of a Cu(II) complex during catalysis; we postulated this intermediate to be $[\text{Cu}^{\text{II}}(\text{carb})_3]^-$ (**2**); generated by the reaction of a carbazyl radical with $[\text{Cu}^{\text{I}}(\text{carb})_2]^-$ (**1**), which we then independently synthesized and structurally characterized. Through the use of UV-vis spectroscopy, we have monitored the buildup of this complex, the persistent radical that is responsible for effective cross-coupling, during a reaction. Radical-cyclization, stereochemical, and reactivity probes are consistent with the generation of an alkyl radical, which engages in out-of-cage coupling with $[\text{Cu}^{\text{II}}(\text{carb})_3]^-$ (**2**). The chain length for the coupling reaction is relatively low (0.3), as expected for a non-chain process.

The additional pathway illustrated in Figure 2.8 highlights the opportunity to achieve photoinduced, copper-catalyzed coupling reactions not only through excitation of copper–nucleophile complexes, but also of nucleophiles themselves. Regardless of the photoreductant under catalytic conditions, copper appears to play a critical role in the key bond construction step via coupling of a copper(II)–nucleophile complex with an organic radical. Ongoing studies are directed at further expanding the scope of such processes, as well as exploring their mechanisms.

2.4 References

1. Creutz, S. E.; Lotito, K. J.; Fu, G. C.; Peters, J. C. *Science* **2012**, *338*, 647–651.
2. (a) Alkylation of nitrogen nucleophiles: Bissember, A. C.; Lundgren, R. J.; Creutz, S. E.; Peters, J. C.; Fu, G. C. *Angew. Chem. Int. Ed.* **2013**, *52*, 5129–5133. (b) Arylation of sulfur nucleophiles: Uyeda, C.; Tan, Y.; Fu, G. C.; Peters, J. C. *J. Am. Chem. Soc.* **2013**, *135*, 9548–9552. (c) Arylation, alkenylation, and alkynylation of nitrogen nucleophiles: Ziegler, D. T.; Choi, J.; Munoz-Molina, J. M.; Bissember, A. C.; Peters, J. C.; Fu, G. C. *J. Am. Chem. Soc.* **2013**, *135*, 13107–13112. (d) Alkylation of nitrogen nucleophiles: Do, H.-Q.; Bachman, S.; Bissember, A. C.; Peters, J. C.; Fu, G. C. *J. Am. Chem. Soc.* **2014**, *136*, 2162–2167. (e) Arylation of oxygen nucleophiles: Tan, Y.; Munoz-Molina, J. M.; Fu, G. C.; Peters, J. C. *Chem. Sci.* **2014**, *5*, 2831–2835. (f) Alkylation of carbon nucleophiles: Ratani, T. S.; Bachman, S.; Fu, G. C.; Peters, J. C. *J. Am. Chem. Soc.* **2015**, *137*, 13902–13907. (g) Enantioconvergent alkylation of nitrogen nucleophiles: Kainz, Q. M.; Matier, C. M.; Bartoszewicz, A.; Zultanski, S. L.; Peters, J. C.; Fu, G. C. *Science* **2016**, *351*, 681–684.
3. For independent early work, see: Sagadevan, A.; Hwang, K. C. *Adv. Synth. Catal.* **2012**, *354*, 3421–3427.
4. For an overview of copper in photocatalysis, see: Paria, S.; Reiser, O. *ChemCatChem* **2014**, *6*, 2477–2483.
5. Johnson, M. W.; Hannoun, K. I.; Tan, Y.; Fu, G. C.; Peters, J. C. *Chem. Sci.* **2016**, *7*, 4091–4100.

6. For leading reviews on photoredox catalysis, see: (a) Prier, C. K.; Rankic, D. A.; MacMillan, D. W. C. *Chem. Rev.* **2013**, *113*, 5322–5363. (b) Skubi, K. L.; Blum, T. R.; Yoon, T. P. *Chem. Rev.* **2016**, *116*, 10035–10074.
7. For example, see: Lawrence, S. A. *Amines: Synthesis, Properties, and Applications*; Cambridge University Press: Cambridge, U.K., 2004.
8. Peacock, D. M.; Roos, C. B.; Hartwig, J. F. *ACS Cent. Sci.* **2016**, *2*, 647–652.
9. For simplicity, we write “[Cu^I(carb)₂Li”, although the lithium is in fact solvated by CH₃CN. For example, see Reference 2a.
10. A luminescent state of [Cu^I(carb)₂Li* with a lifetime of 590 ps was also observed.
11. A concentrated sample of the alkyl bromide in CH₃CN shows no absorption beyond 300 nm, whereas the Nd:YAG laser is pumping the sample at 355 nm.
12. Compound **G** is the N–N coupled product.
13. Alfassi, Z. B. In *General Aspects of the Chemistry of Radicals*; Alfassi, Z. B., Ed.; Wiley: Chichester, U.K., 1999; pp 139–173.
14. For examples of aggregation of carbazolide anions, see: (a) Dinnebier, R.; Esbak, H.; Olbrich, F.; Behrens, U. *Organometallics* **2007**, *26*, 2604–2608. (b) Bock, H.; Arad, C.; Näther, C.; Havlas, Z. *J. Organomet. Chem.* **1997**, *548*, 115–120.
15. The expected value for the diffusion coefficient for carbazole is 24.2×10^{10} m²/s, which leads to a hydrodynamic radius of 2.6 Å; the measured value is 22.7×10^{10} m²/s, which gives a hydrodynamic radius of 2.8 Å.

16. Correspondingly, with respect to the C–N coupling pathway that proceeds via excitation of $[\text{Cu}^{\text{I}}(\text{carb})_2]\text{Li}$ (Figure 2.2), $\text{R}\cdot$ may react with $[\text{Cu}^{\text{II}}(\text{carb})_3]\text{Li}$ (**2**), rather than with $\text{Cu}^{\text{II}}(\text{carb})_2$.
17. For leading references, see: (a) Studer, A. *Chem. Eur. J.* **2001**, *7*, 1159–1164. (b) Fischer, H. *Chem. Rev.* **2001**, *101*, 3581–3610.
18. We use this term loosely to include reactions conducted according to eq 3, but where irradiation has been stopped (e.g., to allow spectroscopic studies).
19. The absorption profiles shown in Figure 2.3a (the transient absorption spectrum of $[\text{Cu}^{\text{I}}(\text{carb})_2]\text{Li}$ in the absence of added electrophile) and Figure 2.10 (the absorption spectrum of $[\text{Cu}^{\text{II}}(\text{carb})_3]^-$) are similar. The $[\text{Cu}^{\text{I}}(\text{carb})_2]\text{Li}^*$ excited state detected in Figure 2.3a presumably has MLCT character with some degree of admixed ligand-to-ligand charge transfer (i.e., MLLCT), reflecting a degree of copper(II)-carbazolide character. MLCT character in $[\text{Cu}^{\text{I}}(\text{carb})_2]\text{Li}^*$ is consistent with a molar extinction coefficient of $4300 \text{ M}^{-1} \text{ cm}^{-1}$ for this transition of $[\text{Cu}^{\text{I}}(\text{carb})_2]^-$ at 365 nm.
20. The X-ray diffraction data for $[\text{Cu}^{\text{II}}(\text{carb})_3][\text{K}(\text{benzo-15-crown-5})_2]$ was of poor quality and hence were only sufficient for establishing overall atomic connectivity.
21. Homoleptic monomeric three-coordinate Cu(II) anions have only been crystallographically characterized in the case of alkoxide ligands: (a) Purdy, A. P.; George, C. F. *Inorg. Chem.* **1991**, *30*, 1969–1970. (b) Hannigan, S. F.; Lum, J. S.; Bacon, J. W.; Moore, C.; Golen, J. A.; Rheingold, A. L.; Doerrer, L. H. *Organometallics* **2013**, *32*, 3429–3436.

22. For examples of other copper(II)–amido complexes wherein significant spin density is believed to reside on nitrogen, see: (a) Mankad, N. P.; Antholine, W. E.; Szilagyi, R. K.; Peters, J. C. *J. Am. Chem. Soc.* **2009**, *131*, 3878–3880. (b) Wiese, S.; Badiei, Y. M.; Gephart, R. T.; Mossin, S.; Varonka, M. S.; Melzer, M. M.; Meyer, K.; Cundari, T. R.; Warren, T. H. *Angew. Chem. Int. Ed.* **2010**, *49*, 8850–8855. (c) Wagner, C. L.; Tao, L.; Thompson, E. J.; Stich, T. A.; Guo, J.; Fettingner, J. C.; Berben, L. A.; Britt, R. D.; Nagase, S.; Power, P. P. *Angew. Chem. Int. Ed.* **2016**, *55*, 10444–10447.
23. Jang, E. S.; McMullin, C. L.; Käß, M.; Meyer, K.; Cundari, T. R.; Warren, T. H. *J. Am. Chem. Soc.* **2014**, *136*, 10930–10940.
24. For examples of other copper(II)–amido complexes that abstract hydrogen atoms, see refs 22a and 23.
25. The computed activation barrier is less than 8 kcal/mol.
26. Lusztyk, J.; Maillard, B.; Deycard, S.; Lindsay, D. A.; Ingold, K. U. *J. Org. Chem.* **1987**, *52*, 3509–3514.
27. This diastereoselectivity (4:1 cis/trans) has previously been observed for the cyclization of this radical at 0 °C: Reference 26.
28. Anslyn, E. V.; Dougherty, D. A. *Modern Physical Organic Chemistry*; University Science Books: Sausalito, CA, 2006; p 156.
29. When a photoinduced, copper-catalyzed cross-coupling is run in the presence of TEMPO, a considerable amount of the TEMPO adducts (derived from trapping of the uncyclized secondary radical or the cyclized primary radical) is observed.

30. For leading references on radical clocks, see: Newcomb, M. In *Encyclopedia of Radicals in Chemistry, Biology and Materials*; Chatgililoglu, C., Studer, A., Eds.; John Wiley & Sons, Chichester, U.K., 2012; Vol 1, pp 107–124.
31. Cismesia, M. A.; Yoon, T. P. *Chem. Sci.* **2015**, 6, 5426–5434.
32. For reviews of photoinduced SRN1 reactions, see: (a) Buden, M. E.; Martin, S. E.; Rossi, R. A. *CRC Handbook of Organic Photochemistry and Photobiology*; Griesbeck, A., Oelgemoller, M., Ghetti, F., Eds.; CRC Press: Boca Raton, Florida, 2012; pp 347–368. (b) Penenory, A. B.; Argüello, J. E. *Handbook of Synthetic Photochemistry*; Albini, A., Fagnoni, M., Eds.; Wiley–VCH: Weinheim, Germany, 2010; Chapter 10.
33. The Hatchard–Parker method was employed. See: (a) Murov, S. L.; Carmichael, I.; Hug, G. L. *Handbook of Photochemistry*; CRC Press: New York, 1993; pp 298–313. (b) Bolton, J. R.; Stefan, M. I.; Shaw, P.-S.; Lykke, K. R. *J. Photochem. Photobiol. A: Chem.* **2011**, 222, 166–169.

Chapter 3 : Photoinduced, Copper-Catalyzed Carbon–Carbon Bond Formation with Alkyl Electrophiles: Cyanation of Unactivated Secondary Alkyl Chlorides at Room Temperature

Reproduced in part with permission from:

Ratani, T.S.;[†] Bachman, S.;[†] Fu, G. C.; Peters, J. C. *J. Am. Chem. Soc.* **2015**, *137*, 13902–13907.

[†]Equal Contributions

© 2015 American Chemical Society

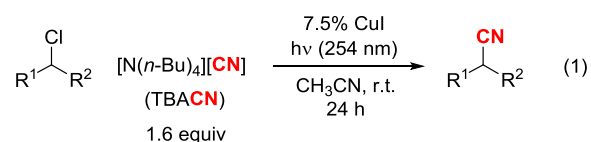
3.1 Introduction

The development of metal-catalyzed cross-coupling reactions has had a profound impact on the synthesis of organic molecules.¹ The use of catalysts based on earth-abundant metals is attractive, and remarkable progress has been described in achieving a wide variety of bond constructions with the aid of copper catalysts.² Elevated temperatures and added ligands are typically required.

We have recently established that, with the aid of light, an array of copper-catalyzed cross-couplings can be achieved under unusually mild conditions (−40 to 30 °C) without the need for an added ligand. In the case of couplings with aryl electrophiles, we have demonstrated the viability of nitrogen, sulfur, and oxygen nucleophiles as reaction partners,^{3,4} and, in the case of alkyl electrophiles, we have described the use of nitrogen nucleophiles.^{5,6} On the basis of one of our working mechanistic hypotheses for these processes (see below), the photophysical properties of a copper–nucleophile complex may play a key role in determining the feasibility of such transformations. Consequently, it was not clear at the outset whether the expansion of this mode of reactivity to the alkylation of carbon-based nucleophiles would be possible.

Organic compounds that bear a cyano group serve as important intermediates and endpoints in organic chemistry.^{7,8} Nucleophilic substitution of an alkyl electrophile with cyanide anion through an S_N2 pathway is an attractive approach to the synthesis of nitriles, although undesired side reactions such as elimination can intervene, especially in the case of less reactive electrophiles. For unactivated secondary alkyl chlorides, we are not aware of cyanations that proceed efficiently at a temperature below 75 °C.⁹

Although a few studies have described the use of transition metals to catalyze the cyanation of alkyl halides, to the best of our knowledge these methods have been limited to benzylic chlorides.¹⁰ We therefore decided to investigate the possibility that a copper catalyst in combination with light could expand the scope of such metal-catalyzed cyanations to include challenging substrates such as unactivated secondary alkyl chlorides. In this report, we establish that copper and light do indeed enable cyanations of these electrophiles at room temperature (eq 1), thus expanding the scope of photoinduced, copper-catalyzed bond formation to include the alkylation of carbon-centered nucleophiles as well as the use of secondary chlorides as electrophiles.

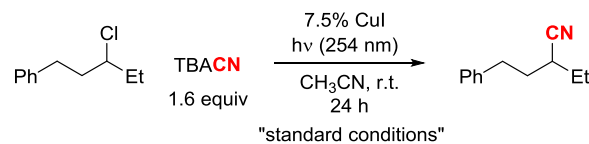


3.2 Results and Discussion

3.2.1 Optimization and Scope

Upon investigating a variety of reaction parameters, we have determined that the cyanation of an unactivated secondary alkyl chloride proceeds in good yield at room temperature with $[N(n\text{-Bu})_4][\text{CN}]$ (TBACN) as the cyanide source, CuI as the catalyst, and irradiation with 15-watt UVC compact fluorescent light bulbs¹¹ (Table 3.1, entry 1).¹² This photoinduced, copper-catalyzed cyanation can even be achieved at 0 °C (entry 2; 60 h), whereas the thermal (no CuI and no light) cyanation of this substrate with TBACN in CH_3CN requires heating to 92 °C (82% yield after 24 h). Under our standard conditions but in the absence of CuI and/or light, essentially no carbon–carbon bond formation is observed (entries 3–5). Use of a photoreactor establishes that irradiation at 254 nm is more effective than at 300 or 350 nm (entries 6–8). Substituting CuI with a variety of other Cu(I) or Cu(II) complexes, as well as with Cu nanopowder, leads to a significantly lower yield (entries 9–14), as does replacement of TBACN with other cyanide sources (entries 15–17). The amount of CuI can be reduced to 2.5% (but not to 1.0%; entries 18–20), and the reaction time can be shortened to 12 h (entry 21), without substantially diminishing product formation. Use of a smaller excess of TBACN results in a small loss in yield (entry 22). Although the cyanation method is somewhat sensitive to air (entry 23), it is not sensitive to moisture (entry 24).

Table 3.1: Photoinduced, copper-catalyzed cyanation of an unactivated secondary alkyl chloride: Effect of reaction parameters^a



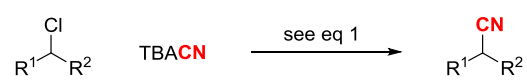
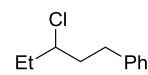
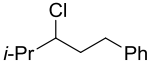
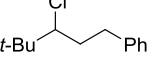
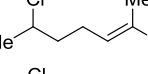
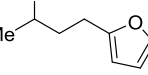
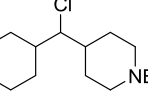
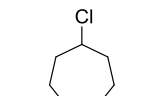
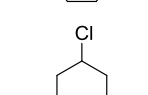
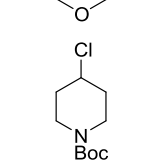
entry	change from the "standard conditions"	yield (%) ^b
1	none	88
2	0 °C (60 h)	85 ^c
3	no CuI	<1
4	no hv	<1
5	no CuI and no hv	<1
6	hv (photoreactor at 254 nm)	86
7	hv (photoreactor at 300 nm)	15
8	hv (photoreactor at 350 nm)	12
9	CuBr, instead of CuI	42
10	CuCl, instead of CuI	48
11	Cu ₂ O, instead of CuI	32
12	CuCl ₂ , instead of CuI	44
13	Cu(OTf) ₂ , instead of CuI	42
14	Cu nanopowder (60-80 nm), instead of CuI	23
15	NaCN, instead of TBACN	25
16	KCN, instead of TBACN	27
17	K ₄ [Fe(CN) ₆], instead of TBACN	<1
18	5.0% CuI	83
19	2.5% CuI	78
20	1.0% CuI	47
21	12 h	82
22	1.2, instead of 1.6, equiv TBACN	75
23	under an atmosphere of air, instead of nitrogen	32
24	0.1 equiv H ₂ O added	87

^aAll data are the average of two or more experiments. ^bThe yield was determined through GC analysis with the aid of a calibrated internal standard. ^cYield of purified product: 85% (average of two runs).

Under our standard conditions, photoinduced, copper-catalyzed cyanation of an array of unactivated secondary alkyl chlorides proceeds in generally good yield at room temperature (Table 3.2).¹³ Both acyclic (entries 1–6) and cyclic (entries 7–9) electrophiles are suitable coupling partners. This method is remarkably effective in the case of very hindered electrophiles, including a secondary alkyl chloride that bears a *t*-butyl substituent (entry 3; substantially more sterically demanding than neopentyl chloride) and one in which both substituents are α -branched (entry 6); an attempted cyanation of the latter substrate under thermal conditions (1.6 equiv TBACN, DMF, 80

°C, 24 h) was unsuccessful (<5% yield at 90% conversion). Functional groups such as an olefin, a furan, a carbamate, and a dialkyl ether are compatible with the coupling conditions (entries 4–6, 8, and 9). Furthermore, when additives (1.0 equiv) that contain a terminal alkyne, a *cis*-disubstituted olefin (4-decene), or an ester (ethyl heptanoate) are introduced to the reaction mixture, cross-coupling occurs smoothly; on the other hand, the presence of certain nitrogen heterocycles impedes carbon–carbon bond formation. On a gram-scale (1.3 g of product), the cross-coupling illustrated in entry 1 of Table 3.2 proceeds in 94% yield.

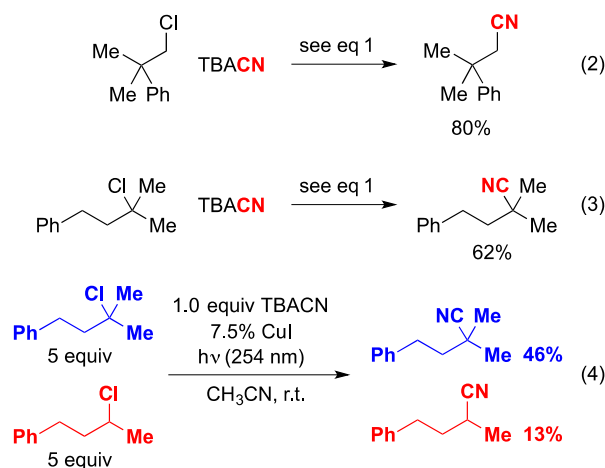
Table 3.2: Photoinduced, copper-catalyzed cyanation of unactivated secondary alkyl chlorides: Scope

		
entry	electrophile	yield (%) ^a
1		93
2		84
3		84
4		84
5		74
6		93
7		79
8		68
9		86

^aYield of purified product (average of two experiments).

This new pathway for carbon–carbon bond formation is not limited to the cyanation of unactivated secondary alkyl chlorides. For example, under our standard conditions, neophyl chloride, a poor substrate for S_N2 reactions, can be converted to the target nitrile in 80% yield (eq 2); no product formation (<1%) was observed in the absence of light or of copper, or under thermal conditions (DMF, 80 °C, 24 h). We have also determined that an unactivated *tertiary* alkyl chloride can serve as a useful coupling

partner, thereby generating an all-carbon quaternary center (eq 3);¹⁴ an effort to accomplish this transformation under thermal conditions failed to furnish the desired product (<1% yield; DMF, 80 °C, 24 h).¹⁵ In a competition experiment, we have established that a tertiary alkyl chloride undergoes cyanation more rapidly than a secondary alkyl chloride, likely due to the greater stability of the more highly substituted radical (eq 4; see the mechanistic discussion below).



The conditions that we have developed for the photoinduced, copper-catalyzed cyanation of alkyl chlorides can be applied without modification to unactivated secondary alkyl *bromides* (Table 3.3);¹⁶ for these electrophiles, under our standard conditions but in the absence either of copper or of light, a small amount of cyanation occurs (the catalyzed process is at least five times faster). A nitrile, an ester, and a carbamate are compatible with the coupling method. In a competition study, we have determined that an alkyl bromide reacts much more rapidly than does an alkyl chloride (eq 5).

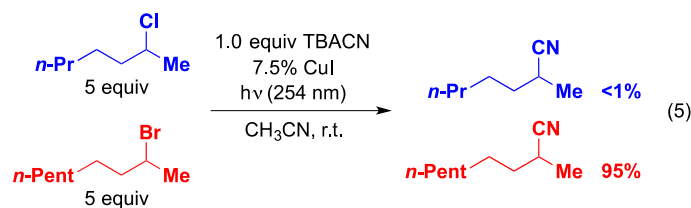


Table 3.3: Photoinduced, copper-catalyzed cyanation of unactivated secondary alkyl bromides: Scope

entry	electrophile	yield (%) ^a
1		84
2		82
3		82
4		92
5		84

^aYield of purified product (average of two experiments).

3.2.2 Mechanistic Observations

Figure 3.1 provides an outline of one of the possible pathways for photoinduced, copper-catalyzed cyanations of unactivated secondary alkyl chlorides.^{3,5,17} In this scenario, a Cu(I)-cyanide adduct (**A**) undergoes photoexcitation to afford an excited-state complex (**B**) that engages in an electron-transfer reaction with the alkyl halide to furnish a Cu(II)-cyanide adduct (**C**) and an alkyl radical, which next combine to provide the nitrile and a Cu(I)-halide complex (**D**).¹⁷ Reaction of Cu(I)-halide complex **D** with TBACN then regenerates Cu(I)-cyanide adduct **A**.

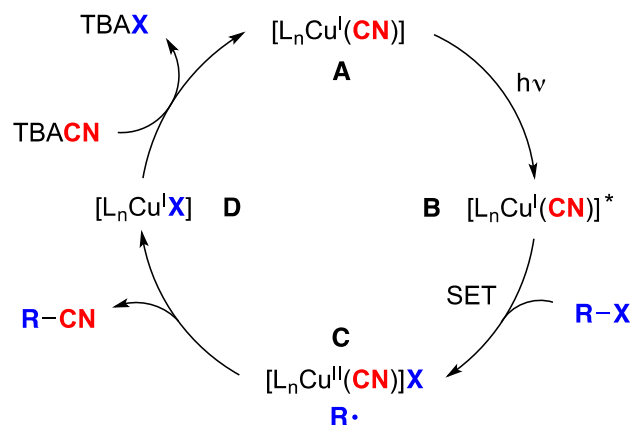
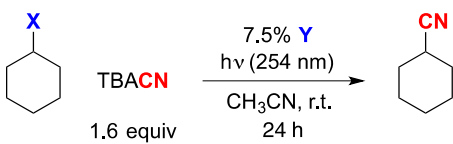


Figure 3.1: Outline of one of the possible pathways for photoinduced, copper-catalyzed cyanations of unactivated secondary alkyl chlorides (for the sake of simplicity, the copper complexes are illustrated as neutral species).

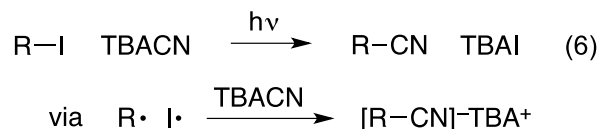
During our reaction-development efforts, we determined that, while CuCl displays activity as a catalyst for the photoinduced cyanation of a secondary alkyl chloride, carbon–carbon bond formation is more efficient in the presence of CuI (Table 3.1, entries 1 and 10). We have confirmed that similar behavior is observed when cyclohexyl chloride is employed as the electrophile (Table 3.4, entries 1 and 2); the addition of TBAI to CuCl furnishes results that are comparable to CuI alone (entries 2 and 3).¹⁸ Because copper(I) halides undergo ligand substitution in the presence of TBACN (see below), we hypothesized that the enhanced effectiveness of CuI relative to CuCl might arise from the transient formation of an alkyl iodide through the reaction of iodide anion with the alkyl chloride,¹⁹ which could provide a pathway for carbon–carbon bond formation that parallels direct reaction of the alkyl chloride.

Table 3.4: Cyanation of cyclohexyl halides


entry	X	Y	yield (%) ^a
1	Cl	CuCl	34
2	Cl	CuI	82
3	Cl	CuCl + TBAI	78
4	I	none	26
5	I	none (no light)	<1
6	Cl	TBAI	5
7	Cl	[Cu(CN) ₂]TBA	26
8	Cl	[Cu(CN) ₂]TBA + TBAI	76

^aThe yield was determined through GC analysis with the aid of a calibrated internal standard (average of two runs).

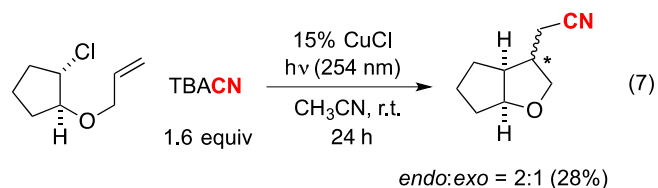
The in situ generation of an alkyl iodide could enhance the efficiency of the pathway outlined in Figure 3.1 by, for example, facilitating electron transfer from excited-state complex **B** to the alkyl halide. At the same time, we also considered the possibility that the transient formation of an alkyl iodide might open the door to a copper-free cyanation pathway (e.g., eq 6), since homolysis of an alkyl–I bond can occur upon irradiation at 254 nm.^{20,21,22,23}



Indeed, we have determined that, upon irradiation, cyclohexyl iodide reacts with TBACN to generate the corresponding nitrile in modest yield (26%; Table 3.4, entry 4); a control reaction in the absence of light demonstrates that this cyanation does not arise from a simple S_N2 displacement (Table 3.4, entry 5).²⁴ However, we have also established that, under our standard conditions for photoinduced cyanation, replacement of CuI with TBAI does not lead to a substantial quantity of the nitrile (Table 3.4, entry 6 vs. entry 2),²⁵ thereby confirming the critical role of copper. Thus, in situ formation of an

alkyl iodide, followed by copper-free, photoinduced formation of the nitrile (eq 6), is likely at most a minor contributor to the enhanced catalytic activity of CuI relative to CuCl (Table 3.4, entries 1 and 2).

We decided to explore the possible intermediacy of an organic radical in photoinduced, copper-catalyzed cyanations (e.g., Figure 3.1). To avoid complications that might arise from the formation and direct photochemistry of an alkyl iodide, we chose to employ CuCl as a catalyst in our investigation, while recognizing that it would afford a modest yield. In particular, we have examined the cyanation of the unactivated secondary alkyl chloride illustrated in eq 7;²⁶ the radical derived from this electrophile has been reported to furnish a 2:1 *endo:exo* mixture of [3.3.0] bicyclic compounds upon cyclization.²⁷ When we subject this electrophile to photoinduced, copper-catalyzed cyanation, we also obtain a 2:1 *endo:exo* mixture of products, consistent with a common radical intermediate.

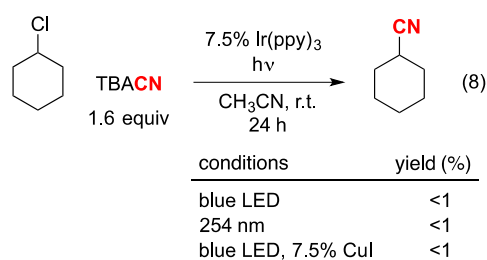


Although our working mechanistic hypothesis (Figure 3.1) does not invoke a radical-chain pathway, a variety of photoinitiated nucleophilic substitution processes have been described that are believed to proceed through a chain mechanism.²³ To gain insight into whether a chain process might be operative under our cyanation conditions, we determined the quantum yield for the reaction of cyclohexyl chloride with TBACN.²⁸ The observed value of 0.030 (.002) does not suggest a chain pathway.

To obtain information about what copper complexes might be present under our standard coupling conditions, we have analyzed by electrospray ionization mass spectrometry (ESI–MS) the cyanation of cyclohexyl chloride. After 30 min of irradiation, anionic species were detected with $m/z = 115$ and 117 , which can be assigned to $^{63}\text{Cu}^{\text{I}}(\text{CN})_2^-$ and $^{65}\text{Cu}^{\text{I}}(\text{CN})_2^-$, respectively. When a mixture of CuI (or CuCl) and TBACN (1:10) was independently analyzed by ESI–MS, the same two species were observed.

The absorption spectrum of $[\text{Cu}(\text{CN})_2]\text{TBA}^{29}$ reveals stronger absorbance at 254 nm ($\epsilon_{254} = 1.5 \times 10^3 \text{ M}^{-1} \text{ cm}^{-1}$) than at 300 and 350 nm (Figure 3.2). In view of our observation that irradiation at 254 nm leads to more effective coupling than does irradiation at 300 or 350 nm (Table 3.1, entries 6–8), this spectrum is consistent with the hypothesis that excitation of $[\text{Cu}(\text{CN})_2]^-$ may play a key role in the photoinduced, copper-catalyzed process, for example by serving as a reductant (Figure 3.1).³⁰ Under a variety of conditions, a common photoredox catalyst, $\text{Ir}(\text{ppy})_3$,^{3e,31} does not facilitate cyanation (eq 8, Table 3.5), consistent with the hypothesis (Figure 3.1) that the role of copper may extend beyond electron transfer.³²

Table 3.5: Attempted use of an Ir photoredox catalyst for cyanation of cyclohexyl chloride



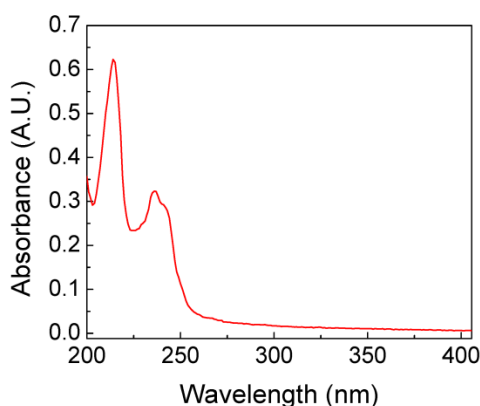
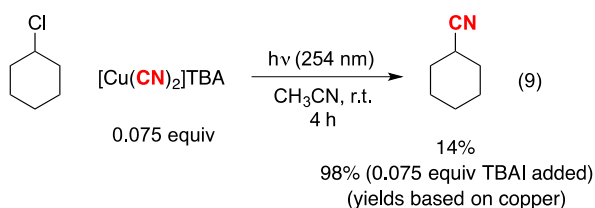


Figure 3.2: Absorption spectrum of $[\text{Cu}(\text{CN})_2]\text{TBA}$ in CH_3CN at room temperature.

Finally, we have examined the chemical competence of $[\text{Cu}(\text{CN})_2]\text{TBA}$ under our coupling conditions by irradiating it in the presence of cyclohexyl chloride. Cyanation proceeds in 14% yield in the absence of TBAI, whereas the addition of TBAI leads to a substantial improvement in coupling efficiency (98% yield) (eq 9); no product is formed in the absence of light. These data for stoichiometric reactions of $[\text{Cu}(\text{CN})_2]\text{TBA}$ are consistent with our observation that the presence of iodide anion is beneficial, although not absolutely required, for copper-catalyzed cyanations of alkyl chlorides (Table 3.4, entries 1 and 2). Similarly, photoinduced cyanations in which $[\text{Cu}(\text{CN})_2]\text{TBA}$ is employed as a catalyst are less effective under iodide-free conditions than when iodide is added (Table 3.4, entries 7 and 8; cf., entries 1 and 3).



3.3 Conclusion

We have expanded the scope of photoinduced, copper-catalyzed cross-couplings of alkyl electrophiles: with respect to the nucleophile, we have shown for the first time that a carbon nucleophile can be employed; with respect to the electrophile, we have provided the first examples of the use of secondary alkyl chlorides as electrophiles. More specifically, we have established that, with a combination of light and a copper catalyst, the cyanation of a variety of unactivated secondary alkyl chlorides, including very sterically demanding substrates, proceeds in good yield under unusually mild conditions (room temperature) to generate nitriles, a useful class of organic molecules. An inexpensive pre-catalyst (CuI) and light source are used, no added ligand is necessary, the method is versatile (e.g., secondary alkyl bromides, a very hindered primary alkyl chloride, and an unactivated tertiary alkyl chloride serve as suitable electrophiles under the same conditions), and the cyanation can even be achieved at 0 °C. Initial mechanistic observations are consistent with possible roles for $[\text{Cu}(\text{CN})_2]^-*$, alkyl iodides, and alkyl radicals as intermediates. Further efforts are underway to exploit the unusual reactivity provided by copper and light to accomplish new families of bond constructions for organic synthesis.

3.4 References

1. For recent monographs with leading references, see: (a) *New Trends in Cross-Coupling*; Colacot, T., Ed.; RSC: Cambridge, UK, 2015. (b) *Metal-Catalyzed Cross-Coupling Reactions and More*; de Meijere, A., Oestreich, M., Eds.; Wiley-VCH: Weinheim, Germany, 2014.
2. For a recent monograph, see: *Copper-Mediated Cross-Coupling Reactions*; Evano, G., Blanchard, N., Eds.; John Wiley & Sons: Hoboken, NJ, 2013.
3. (a) C–N: Creutz, S. E.; Lotito, K. J.; Fu, G. C.; Peters, J. C. *Science* **2012**, *338*, 647–651. (b) C–S: Uyeda, C.; Tan, Y.; Fu, G. C.; Peters, J. C. *J. Am. Chem. Soc.* **2013**, *135*, 9548–9552. (c) C–N: Ziegler, D. T.; Choi, J.; Muñoz-Molina, J. M.; Bissember, A. C.; Peters, J. C.; Fu, G. C. *J. Am. Chem. Soc.* **2013**, *135*, 13107–13112. (d) C–O: Tan, Y.; Muñoz-Molina, J. M.; Fu, G. C.; Peters, J. C. *Chem. Sci.* **2014**, *5*, 2831–2835. (e) For a related study, see: Yoo, W.-J.; Tsukamoto, T.; Kobayashi, S. *Org. Lett.* **2015**, *17*, 3640–3642.
4. For independent work by Hwang, see: Sagadevan, A.; Hwang, K. C. *Adv. Synth. Catal.* **2012**, *354*, 3421–3427.
5. (a) Carbazoles as nucleophiles: Bissember, A. C.; Lundgren, R. J.; Creutz, S. E.; Peters, J. C.; Fu, G. C. *Angew. Chem., Int. Ed.* **2013**, *52*, 5129–5133. (b) Amides as nucleophiles: Do, H.-Q.; Bachman, S.; Bissember, A. C.; Peters, J. C.; Fu, G. C. *J. Am. Chem. Soc.* **2014**, *136*, 2162–2167.

6. For recent overviews of photoinduced, copper-catalyzed reactions, see: (a) Majek, M.; von Wangelin, A. J. *Angew. Chem., Int. Ed.* **2013**, *52*, 5919–5921. (b) Paria, S.; Reiser, O. *ChemCatChem* **2014**, *6*, 2477–2483.
7. For leading references, see: (a) *Science of Synthesis*; Murahashi, S.-I., Ed.; Georg Thieme Verlag: Stuttgart, Germany, 2004; Vol 19. (b) Fleming, F. F.; Yao, L.; Ravikumar, P. C.; Funk, L.; Shook, B. C. *J. Med. Chem.* **2010**, *53*, 7902–7917.
8. Vildagliptin and verapamil are two examples of alkyl nitriles that serve as pharmaceutical drugs.
9. For example, see: (a) Smiley, R. A.; Arnold, C. *J. Org. Chem.* **1960**, *25*, 257–258 (reflux; DMSO). 2-Chlorobutane and 2-chlorooctane were cyanated in 69% and 70% yield, respectively. (b) Cook, F. L.; Bowers, C. W.; Liotta, C. L. *J. Org. Chem.* **1974**, *39*, 3416–3418 (83 °C; CH₃CN/18-crown-6). 2-Chlorooctane was cyanated in 78% yield (based on recovered starting material; 10 days), whereas cyclohexyl chloride did not furnish any of the desired product. (c) Shaw, J. E.; Hsia, D. Y.; Parries, G. S.; Sawyer, T. K. *J. Org. Chem.* **1978**, *43*, 1017–1018 (80 °C; HMPA). 2-Chlorooctane was cyanated in 87% yield. (d) Reddy, M. S.; Rajan, S. T.; Eswaraiah, S.; Satyanarayana, R. Improved Process for Manufacture of Pregabalin. Patent WO 2009/001372 A2, Dec 31, 2008. A secondary alkyl chloride was cyanated in ~70% yield.
10. For example, see: (a) Nickel catalyst/60 °C: Satoh, Y.; Obora, Y. *RSC Adv.* **2014**, *4*, 15736–15739. (b) Copper catalyst/180 °C: Ren, Y.; Dong, C.; Zhao, S.; Sun, Y.; Wang, J.; Ma, J.; Hou, C. *Tetrahedron Lett.* **2012**, *53*, 2825–2827. (c) Palladium

- catalyst/140 °C: Ren, Y.; Yan, M.; Zhao, S.; Sun, Y.; Wang, J.; Yin, W.; Liu, Z. *Tetrahedron Lett.* **2011**, *52*, 5107–5109. (d) Titanium catalyst/0 °C (benzhydryl chloride): Zieger, H. E.; Wo, S. *J. Org. Chem.* **1994**, *59*, 3838–3840.
11. The UVC bulbs can be purchased from a retailer such as Amazon.com (\$15).
 12. Notes: (a) The temperature of the reaction mixture during the course of the cross-coupling has been determined to be ≤ 25 °C. (b) A very small amount (~2%) of reduction of the alkyl chloride (Cl→H) is observed.
 13. An *aryl* halide (iodide) can also undergo cyanation, albeit in modest yield. The use of a bis(imine) ligand on Cu has since been shown to significantly improve yields: Kim, K.; Hong, S. H. *Adv. Synth. Catal.* **2017**, *359*, 2345–2351.
 14. Notes: (a) In the absence of light and/or CuI, no cyanation was observed. (b) This method is not yet general: under the current conditions, more hindered tertiary alkyl chlorides react more slowly. We have not yet pursued optimization of this process.
 15. The cyanation of a tertiary alkyl chloride under S_N1 conditions has been described. For example, see: Reetz, M. T.; Chatziosifidis, I. *Angew. Chem., Int. Ed.* **1981**, *20*, 1017–1018.
 16. In preliminary studies under our standard conditions, an unactivated secondary alkyl fluoride and an unactivated secondary alkyl tosylate did not serve as suitable coupling partners.
 17. Note: We are also considering mechanisms that incorporate features such as out-of-cage chemistry of the alkyl radical, including carbon–carbon bond formation via reaction of an alkyl radical with a Cu(I)–CN complex.

18. Cyclohexyl chloride can be a challenging substrate for cyanation, including under “naked nucleophile” conditions (Reference 9b).
19. During the course of a catalyzed cyanation, we have observed the accumulation of only a trace (<1%) of the alkyl iodide.
20. Photolysis (254 nm) of cyclohexyl iodide in CH₃CN leads to its gradual disappearance over 24 hours. In contrast, under the same conditions, cyclohexyl chloride can be recovered quantitatively after 24 hours (in the presence of TBAI (1.0 equiv), some cyclohexyl chloride is consumed (~25%)).
21. For an example and leading references, see: Kropp, P. J.; Poindexter, G. S.; Pienta, N. J.; Hamilton, D. C. *J. Am. Chem. Soc.* **1976**, 98, 8135–8144. These authors report that, under certain conditions, a sequence of homolysis and then electron transfer can generate carbocationic intermediates.
22. The cyanation of alkyl iodides by diethylphosphoryl cyanide via a radical pathway has been described: Cho, C. H.; Lee, J. Y.; Kim, S. *Synlett* **2009**, 81–84.
23. For reviews of photoinduced S_{RN}1 reactions, see: (a) Buden, M. E.; Martin, S. E.; Rossi, R. A. *CRC Handbook of Organic Photochemistry and Photobiology*; Griesbeck, A., Oelgemoller, M., Ghetti, F., Eds.; CRC Press: Boca Raton, Florida, 2012; pp 347–368. (b) Penenory, A. B.; Argüello, J. E. *Handbook of Synthetic Photochemistry*; Albini, A., Fagnoni, M., Eds.; Wiley–VCH: Weinheim, Germany, 2010; Chapter 10. (c) Bowman, W. R. *Photoinduced Electron Transfer*; Fox, M. A., Chanon, M., Eds.; Elsevier: Amsterdam, 1990; pp 487–552.

24. In contrast, in the case of an acyclic secondary alkyl iodide, we have observed cyanation under the same conditions.
25. When entry 6 of Table 3.4 was conducted in the absence of light, essentially no cyanation (<1%) was observed.
26. Notes: (a) This alkyl chloride is stable to irradiation at 254 nm. (b) If CuI is employed as the catalyst, at partial conversion we observe a trace of the two diastereomers of the [3.3.0] bicyclic primary alkyl iodide, which could be formed through Cl→I transhalogenation of the starting electrophile, homolysis of the C–I bond, radical cyclization, and then radical–radical recombination to generate a C–I bond.
27. Pandey, G.; Rao, K. S. S. P.; Palit, D. K.; Mittal, J. P. *J. Org. Chem.* **1998**, *63*, 3968–3978.
28. The Hatchard–Parker method was employed. See: (a) Murov, S. L.; Carmichael, I.; Hug, G. L. *Handbook of Photochemistry*; CRC Press: New York, 1993; pp 298–313. (b) Bolton, J. R.; Stefan, M. I.; Shaw, P.-S.; Lykke, K. R. *J. Photochem. Photobiol. A: Chem.* **2011**, *222*, 166–169.
29. Nilsson, M. *Acta Chem. Scand. B* **1982**, *36*, 125–126.
30. For examples of studies of the reactivity of $[\text{Cu}(\text{CN})_2]^-*$ in aqueous solution, see: (a) Formation of an exciplex with halide ions: Horváth, A.; Stevenson, K. L. *Inorg. Chem.* **1993**, *32*, 2225–2227. (b) Electron transfer: Kemecci, F.; Wood, C. E.; Horváth, A.; Stevenson, K. L. *J. Photochem. Photobiol. A: Chem.* **1995**, *89*, 121–125.
31. For a recent review of photoredox catalysis, see: Prier, C. K.; Rankic, D. A.; MacMillan, D. W. C. *Chem. Rev.* **2013**, *113*, 5322–5363.

32. For a recent example, see: Bagal, D. B.; Kachkovskyi, G.; Knorn, M.; Rawner, T.; Bhanage, B. M.; Reiser, O. *Angew. Chem., Int. Ed.* **2015**, *54*, 6999–7002.

**Chapter 4 : Photocatalytic Nitrite Reduction on
Heterobimetallic Cobalt-Magnesium Complexes:
Mechanistic Insights into N–N Bond Formation**

4.1 Introduction

The reduction of nitric oxide ($\cdot\text{NO}$) is essential in biological denitrification as well as in controlling NO_x emissions from automotive exhausts. In biological systems, nitric oxide reductase (NOR) and flavodiiron nitric oxide reductase (FDP) play key enzymatic roles in the reduction and protonation of nitric oxide to nitrous oxide (N_2O) and water.^{1,2} However, the order of addition of electron and proton equivalents, the coordination mode of the hyponitrite intermediate which results from N–N bond-formation, and the N–O bond cleavage step within the di-iron active sites to generate the observed products are still mechanistically contested.² Mechanistic studies of functional model complexes of NOR can be used to complement enzymatic studies, with the advantage over natural systems that protons and electrons can be delivered systematically to trap potential intermediates.^{1a,2a,3} However, in synthetic Fe model complexes for NOR which have been successfully able to model the reductive coupling of $\cdot\text{NO}$, only the initial binding of NO to the active-site mimic or the production of N_2O could be experimentally confirmed, with no examples of an N–N coupled intermediate before release of product.³ Only one example of a heme-based hyponitrite intermediate on a model complex has been observed thus far, and it derives from *trans*-hyponitrous acid rather than the reductive coupling of two NO molecules.⁴

While both heme and non-heme Fe model complexes of NOR have demonstrated some success in N–N coupling, our group⁵ and, more recently, Hung and coworkers,⁶ have also observed NOR-like activity with the use of non-porphyrin Co compounds. These complexes implicate the generation of a $\{\text{CoNO}\}$ ⁹ intermediate to allow for N_2O production. The system developed by the Hung group is thought to proceed *via* a neutral

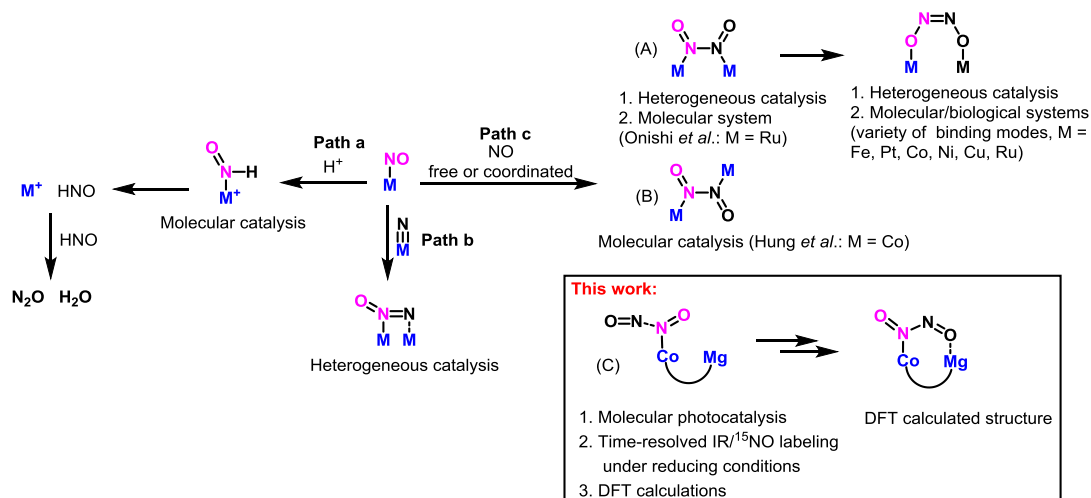
hyponitrite intermediate which bridges two reduced Co centers (Scheme 4.1, path c). Their system is able to undergo five conversion cycles of NO to N₂O with reloading of NO at the beginning of each cycle.⁶ Our group has employed a heterobimetallic CoMg platform to facilitate nitrite binding and promote *selective* electrocatalytic reduction to nitrous oxide, a 4 electron, 6 proton process.⁵ Unlike biological denitrification (and most molecular catalysts), in which ·NO is released from nitrite reductase into the cytoplasmic membrane for further reduction by a different NOR catalyst,⁷ this CoMg platform is able to reduce nitrite to nitric oxide and then reductively couple two ·NO to generate N₂O (and H₂O).

Other monometallic complexes that catalyze N–O bond cleavage of nitrite to generate transition metal nitrosyl intermediates and release N₂O include Van Eldik's Fe phthalocyanine⁸ and Ford's heme⁹ systems. However, the mechanism of N–N bond formation on the phthalocyanine platform is unexplored, and the ferrous heme nitrosyl complex was shown to release free HNO upon protonation which can dimerize to form N₂O (Scheme 4.1, Path a). Meyer and coworkers have shown that heme complexes are also capable of electrochemical reduction of nitrite to ammonia and nitrous oxide. However, the mechanism of N–N coupling is similarly unknown.¹⁰

There are also a variety of heterogeneous systems which can catalyze the reduction of ·NO to N₂O. One generally accepted mechanism for N–N coupling on surfaces is through NO dissociation to an oxide and a nitride, followed by the surface-bound nitride interacting with a neighboring adsorbed NO (Scheme 4.1, Path b).¹¹ Computational and experimental results also suggest an alternative mechanism in which two NO molecules couple to generate adsorbed (NO)₂ (a hyponitrite intermediate)

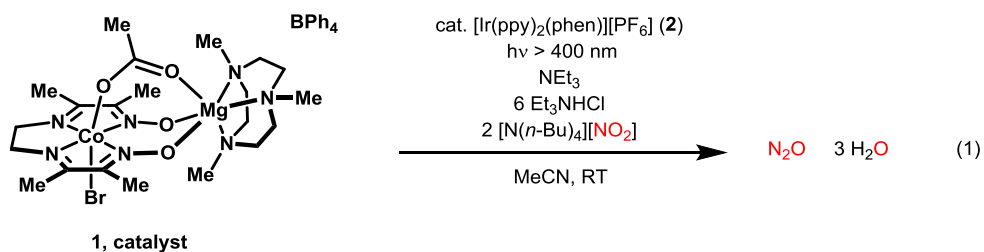
without requiring NO dissociation (Scheme 4.1, Path c).^{12,34a} Considering the mechanistic uncertainties surrounding NO_x reduction catalysis in biological, molecular, and surface systems, there is a need for fundamental studies on the nature of the N–N bond formation step.

Scheme 4.1: Possible pathways for N–N reductive coupling of NO during molecular (homogeneous) and heterogeneous catalysis. Charges omitted for clarity.



To address these mechanistic questions, in this work we describe a photocatalytic variant of our electrocatalytic system that employs the same acid, triethylammonium chloride (NEt₃HCl), and CoMg macrocyclic platform (*vide supra*), [(Br)(μ-OAc)Co(^{Me}doen)Mg(Me₃TACN)][BPh₄] (**1**), but with [(phen)Ir(ppy)₂][PF₆] (**2**) as a photosensitizer and triethylamine (NEt₃) as a sacrificial reductant (Eq 1) in place of an electrode. This is the first example of a homogeneous photocatalytic system for the reduction of nitrite and, to the best of our knowledge, the only photocatalytic system which is selective for nitrous oxide instead of more reduced products such as dinitrogen or ammonia.¹³ By using a host of spectroscopic and computational methods, including

step-scan time-resolved FTIR spectroscopy with nanosecond time resolution, we were able to gain some mechanistic insight into the N–N coupling step. Time resolved IR data, corroborated by DFT calculations, supports the transient generation of a neutral *cis* NO dimer species (Co(NONO)) akin to the neutral *trans* hyponitrite proposed in the Hung system.⁶ We propose that the ability of this system to selectively produce N₂O from NO₂[−] lies in its ability to bind both nitrite and hyponitrite intermediates on Co with cooperative Lewis acid (Mg²⁺) coordination.



4.2 Results and Discussion

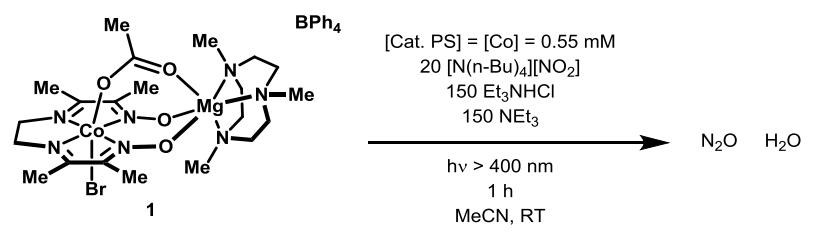
4.2.1 Photocatalysis with [(Br)(μ -OAc)Co(^{Me}doen)Mg(Me₃TACN)][BPh₄] (**1**)

The bimetallic complex **1** was prepared according to a previously reported procedure.⁵ The complex was shown to function as a pre-catalyst for the electrochemical reduction of nitrite to N₂O by electrolysis at -1.2 V vs SCE with the acid NEt₃HCl. During electrocatalysis, 11 electron equivalents were passed per pre-catalyst equivalent, resulting in 2.75 turnovers. We have developed a photocatalytic system for the selective conversion of nitrite to nitrous oxide with greater efficiency (Table 4.1, Entry 1) than that of reported for the electrocatalytic system. The photosensitizer, [(phen)Ir(ppy)₂][PF₆] (**2**), was initially chosen because the reduction potential ($E_{1/2}(\mathbf{2}^-/\mathbf{2}^*) = -1.42$ V vs SCE) provided a driving force similar to the electrocatalytic system. The sources of nitrite and acid were unchanged from those used for electrocatalysis, and triethylamine was used as a sacrificial reductant because it is also the conjugate base of the acid, and thus least likely to disrupt the functionality of the overall system. An important advantage offered by the photochemical system over the electrochemical system is faster time resolution for the observation of potential intermediates.¹⁴

Following the discovery that nitrite reduction could occur photocatalytically on our bimetallic CoMg system, initial efforts were directed toward the screening of photosensitizers (PS) based on their reduction potentials¹⁵ to maximize the turnover number (Table 4.1). Satisfyingly, the most efficient photosensitizer was found to be [(phen)Ir(ppy)₂][PF₆], which when added at a concentration equal to that of **1** produced 5.8 turnovers of N₂O (Table 4.1, Entry 1). Because the absorption bands of **1** and **2** overlap between 400 and 450 nm (see Appendix C), the catalytic turnover might be

inhibited by a competition for photons between the PS and the Co catalyst **1**. To determine the maximum efficiency for nitrite reduction, the concentration of PS was increased, with constant [**1**], until the turnover plateaued; at this point, all the light can be assumed to be absorbed by the PS (See Appendix C). The concentration of **2** at which the catalysis maximized at 9.8 turnovers (0.67 mL N₂O) is 4.0 mM (Table 4.1, Entry 2). Of special note is entry 7, which highlights the necessity of a Lewis acid interaction for productive photocatalysis. The Mg²⁺ cation is known to be essential for nitrite binding,⁵ which was our first indication that the coordination of nitrite was a requirement for turnover (*vide infra*).

Table 4.1: Photocatalytic Nitrite Reduction with a Co co-catalyst



Entry	Conditions	E _{1/2} (M/M ⁺) ^a	TON/Co ^c
1	PS = 2	-1.42	5.8 ± 0.3
2	PS = 4.0 mM 2	-1.42	9.8 ± 0.1
3	PS = Ir(ppy) ₃	-2.19	1.7 ± 0.1
4	PS = [(tpy)Pt(CCPPh)][PF ₆]	-1.21 ^b	1.3 ± 0.1
5	PS = [Ru(bpy) ₃][PF ₆] ₂	-1.33	1.7 ± 0.1
6	PS = 2 , no Co	-1.42	0.7 ± 0.1
7	PS = 2 , [(Br) ₂ Co(^{Me} doen)][BPh ₄] instead of 1	-1.42	0.8 ± 0.1

^a All potentials are given in V vs. SCE.

^b This value is for an excited state reduction potential (E_{1/2} (M^{*}/M⁺)).

^c All TON are the average of 2 or more experiments.

4.2.2 Identification of (NO₂)Co(^{Me}doen)Mg(Me₃TACN) complex under photochemical conditions

After optimization of the reaction condition for photocatalysis, we sought to observe reaction intermediates to gain insight into the molecular reaction mechanism(s)

for the nitrite reduction/protonation reaction. Previously, based on in situ spectroelectrochemical data for a putative $\{\text{CoNO}\}^9$ complex and stoichiometric reactivity of the corresponding complexes, we proposed that the electrocatalytic system proceeded through formation of a variety of Co-NO₂ and Co-NO complexes (Figure 4.1). All of the compounds shown in Figure 4.1 were isolated and thoroughly characterized.⁵ It was proposed that the Co(III)-acetate pre-catalyst is able to ligand exchange the acetate for a nitrite and be reduced to Co(I) to make $(\mu\text{-NO}_2)\text{Co}(\text{Me}^e\text{doen})\text{Mg}(\text{Me}_3\text{TACN})$ (**3**). The first N–O bond cleavage step in **3** could generate $[(\text{Cl})(\text{NO})\text{Co}(\text{Me}^e\text{doen})\text{Mg}(\text{Me}_3\text{TACN})(\text{H}_2\text{O})][\text{BPh}_4]$ (**4**).

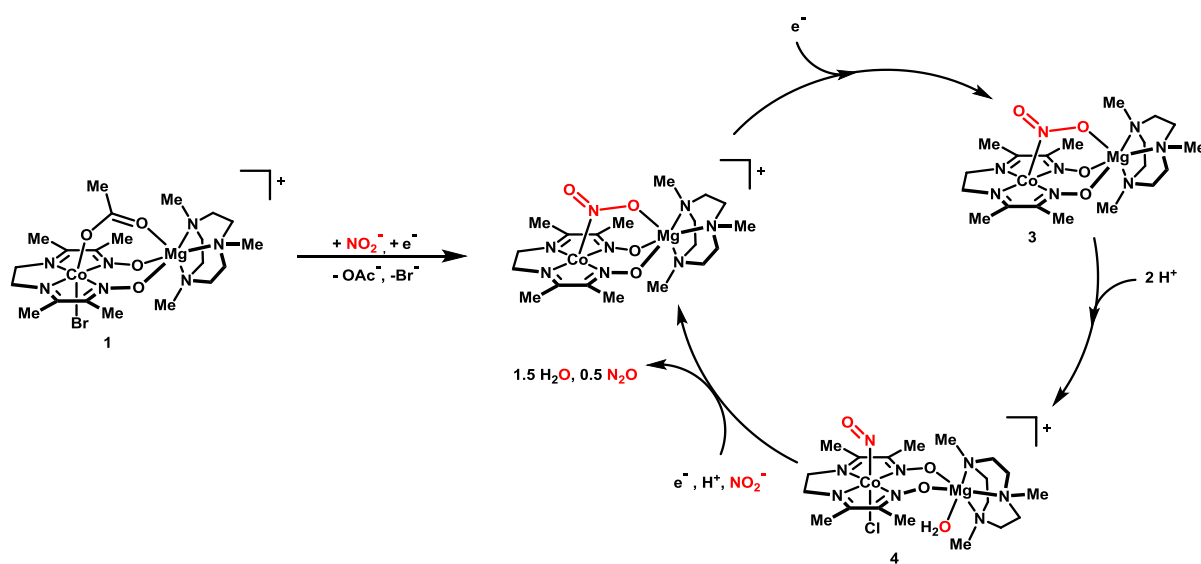


Figure 4.1: Initially proposed mechanism of electrocatalytic nitrite reduction using complex **1**.

We first turned to optical spectroscopy to identify which, if any, of the complexes in the proposed mechanism in Figure 4.1 were being generated during photocatalysis. When a catalytic reaction mixture containing **1**, **2**, triethylamine, triethylammonium chloride, and $[(n\text{-BuN})_4][\text{NO}_2]$ was irradiated with visible light, an absorption band at

574 nm was observed (Figure 4.2a). However, this band could be observed even when only **2** and triethylamine were irradiated, and was not visible when only **2** was present; thus, this band was assigned to a reduced Ir species. This band is also suggestive of a reductive quenching mechanism,^{15a} wherein the excited state of **2**, **2***, can be reduced by triethylamine to generate the corresponding Ir(II) complex. While **2** can be quenched by both NEt₃ and **1**, the catalytic reaction mixture contains much higher concentrations of NEt₃ and thus should favor a reductive quenching mechanism (see Appendix C for Stern-Volmer experiment).

When the catalytic reaction mixture was irradiated without NEt₃HCl, a new band at 700 nm was detected; this band was assigned to the previously-characterized **3** (Figure 4.2b). When NEt₃HCl is added to this mixture, the band at 700 nm disappears and generates a red solution, as would be expected if **3** were reacting with the acid to generate the {CoNO}⁸ complex **4**.¹⁶ ESI-MS of the reaction mixture upon addition of acid indicated the presence of a {CoNO}⁸ complex similar to **4**, with an acetate displacing the chloride ligand, [(OAc)(NO)Co(^{Me}doen)Mg(Me₃TACN)][BPh₄] (m/z = 567). Thus, under photolysis conditions, compound **1** can access the reduced Co(I)-NO₂ species **3**. In the presence of acid, the N–O bond is cleaved to generate {CoNO}⁸, which is consistent with the stoichiometric reactivity of **3**.

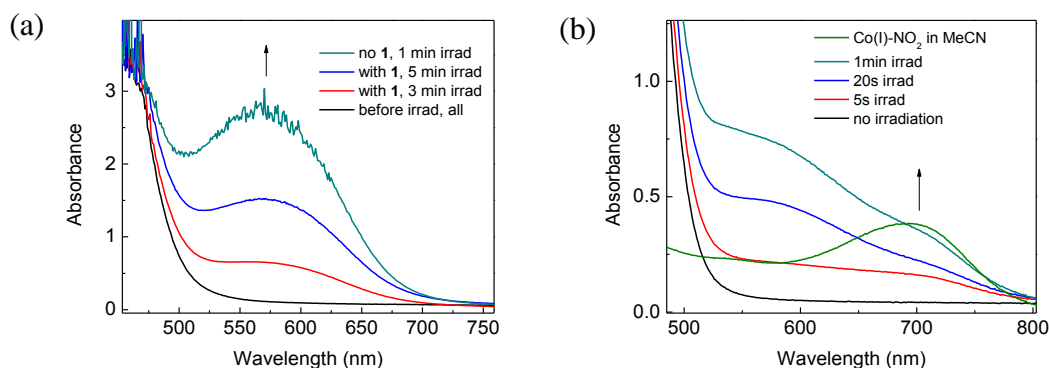


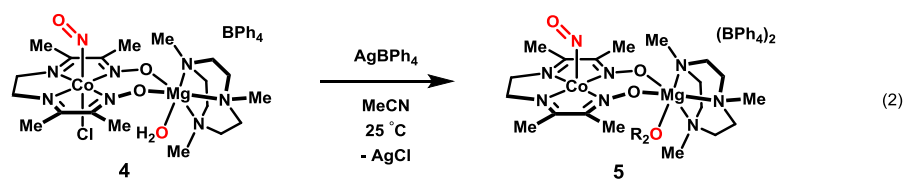
Figure 4.2: (a) Appearance of band at 574 nm upon irradiation of the catalytic reaction mixture with **1** (red and blue traces) and without **1** (teal trace). (b) Appearance of bands at 574 nm and 700 nm upon irradiation of a mixture containing **1**, **2**, [(*n*-BuN)₄][NO₂], and triethylamine (red, blue, and teal traces). An authentic sample of (μ -NO₂)Co(^{Me}doen)Mg(Me₃TACN) is in green.

4.2.3 Characterization and reactivity of a {CoNO}⁹ complex

While optical spectroscopy provided evidence for the generation of **3** and **4** during catalysis, the reduction and protonation steps of **4**, leading to the N–N bond-forming and N–O bond-cleaving steps, were not understood. Therefore, we first studied the behavior of the {CoNO}⁹ complex which results from reduction of **4** as this complex is competent for N₂O generation in the presence of acid. While {CoNO}⁹ could not be isolated due to its high reactivity even at –80 °C, EPR, IR, UV-Vis spectroscopy along with DFT calculations were used for the full characterization of this complex. Co–NO compounds with this Enemark-Feltham number are rare, and thus understanding the electronic structure of this compound is of great interest.^{6, 17}

Counterintuitively, upon reduction of complex **4**, {CoNO}⁸, the frequency of the IR band assigned to the N–O bond increases from 1636 cm⁻¹ to 1695 cm⁻¹ (Figure 4.3,

black trace); this stretching frequency is identical to that observed by IR spectroelectrochemistry during electrocatalysis, and shifts to the expected value of 1665 cm^{-1} when the ^{15}NO analog of **4** is prepared (see Appendix C). The binding of a ligand *trans* to a NO ligand is known to weaken the metal–nitrosyl σ -bond, leading to greater electron density in the NO π^* orbital and reduced NO vibrational frequencies.¹⁸ Thus, the increase in NO stretching frequency upon reduction can be ascribed to the loss of the *trans* ligand to NO. Based on this logic, we hypothesized that the unexpected increase in frequency was due to a change in coordination number upon reduction, in particular the loss of Cl^- from the coordination sphere. To test our hypothesis, we synthesized a 5-coordinate $\{\text{CoNO}\}^8$ complex $[(\text{NO})\text{Co}^{\text{Me}}\text{doen})\text{Mg}(\text{Me}_3\text{TACN})][(\text{BPh}_4)_2]$ (**5**) through halide abstraction of **4** (Eq 2)¹⁹ followed by reduction. The resulting $\{\text{CoNO}\}^9$ exhibits an identical stretching frequency (1695 cm^{-1}) to the one formed from reduction of **4** (Figure 4.3a, red trace).



Compound **5** has an NO stretching frequency of 1703 cm^{-1} which shifts to 1672 cm^{-1} when ^{15}NO is used (expected 1672 cm^{-1}). The $<10\text{ cm}^{-1}$ shift in the NO frequency upon reduction of **5** implies a Co-centered reduction (Figure 4.3a); direct reduction of the NO moiety when bound to transition metals such as Fe leads to red-shifts in the NO frequency which are $\sim 100\text{--}300\text{ cm}^{-1}$ in magnitude.²⁰

The EPR spectrum obtained upon reduction of **4** to the $\{\text{CoNO}\}^9$ complex is also consistent with a Co-centered reduction. The reduction of both **4** and **5** yielded identical EPR spectra (Figure 4.3b), demonstrating that reduction is accompanied by the loss of the

chloride ligand.²¹ The EPR spectrum was simulated ($g_{\perp} = 2.043, 2.044$, and $g_{\parallel} = 2.209$ and $A(\text{Co})_{\perp} = 148, 156$ and $A(\text{Co})_{\parallel} = 363.8$ MHz) and displayed coupling primarily to ^{59}Co ($I = 7/2$), with little observable hyperfine coupling to either the macrocyclic ligand or the NO ligand. Replacement of ^{14}NO with ^{15}NO (see Appendix C) sharpened the line widths associated with the minor NO hyperfine coupling, but the spectrum was essentially unchanged. The EPR spectra indicate that the $\{\text{CoNO}\}^9$ complex is a Co(II)-centered paramagnet, and not a nitroxyl radical bound to a diamagnetic Co(I) center. In other low-spin Co(II) centers, the unpaired electron can be found in the d_{z^2} orbital, leading to $g_{\perp} > g_{\parallel}$ and small values of A_{\perp} .²² However, parameters similar to those for our $\{\text{CoNO}\}^9$ were recently observed by Harrop and coworkers on a comparable ligand platform and were attributed to the unpaired electron in the Co-centered $d_{x^2-y^2}$ orbital based on EPR spectroscopy, XAS spectroscopy, and DFT calculations.^{17e} The electronic structure assigned to their $\{\text{CoNO}\}^9$ system was an $S = 3/2$ Co(II) antiferromagnetically coupled to an $S = 1$ NO^- . Based on the similarity of the EPR spectra for these two compounds, as well as our DFT-predicted spin-density (65% on Co, 35% on NO; see Appendix C for broken symmetry calculations), we believe that our $\{\text{CoNO}\}^9$ complex features a similar electronic structure.

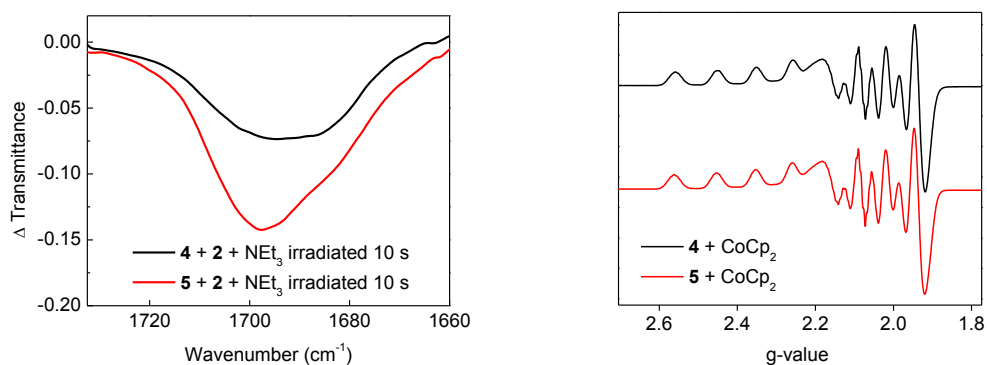


Figure 4.3: (a) FT-IR spectrum of **4**, **2**, and NET_3 in CD_3CN (black trace) and **5**, **2**, and NET_3 (red trace) in CD_3CN after irradiation with a blue LED. (b) EPR spectrum in butyronitrile of **4** (black trace) and **5** (red trace) reduced by cobaltocene. The simulated EPR spectrum ($g = [2.043, 2.044, 2.209]$) displays hyperfine to Co ($A_{\text{Co}} = [148\ 156\ 363.8]$).

In the presence of nitrite, the UV-Vis spectrum of the reduction of **4** (Co(III)) to the $\{\text{CoNO}\}^9$ species reveals the appearance of the Co(I)- NO_2 intermediate **3**, which has a signature peak at 700 nm (Figure 4.4). Regardless of whether one equivalent of CoCp_2 or excess photosensitizer/ NET_3 is used as the reductant, the appearance of this band is observed. These data suggest that $\text{NO}\cdot$ can be labilized from the Co(II) coordination sphere (ascertained by EPR spectroscopy) with concomitant reduction to Co(I). This behavior can also explain the difficulty in obtaining a crystal structure of the $\{\text{CoNO}\}^9$. Furthermore, upon reduction, the band does not appear until nitrite is added to the reaction mixture, which is inconsistent with an NO disproportionation pathway in which nitrogen dioxide is generated and reduced. Further evidence for the loss of NO from $\{\text{CoNO}\}^9$ is the detection of trace amounts of free NO when **4** is reduced with 1 equiv CoCp_2 . This NO disappears with concomitant appearance of a substoichiometric amount

of N_2O (0.07 equiv). When acid is added to this mixture, the amount of N_2O released increases to 0.33 equiv per Co center.²³

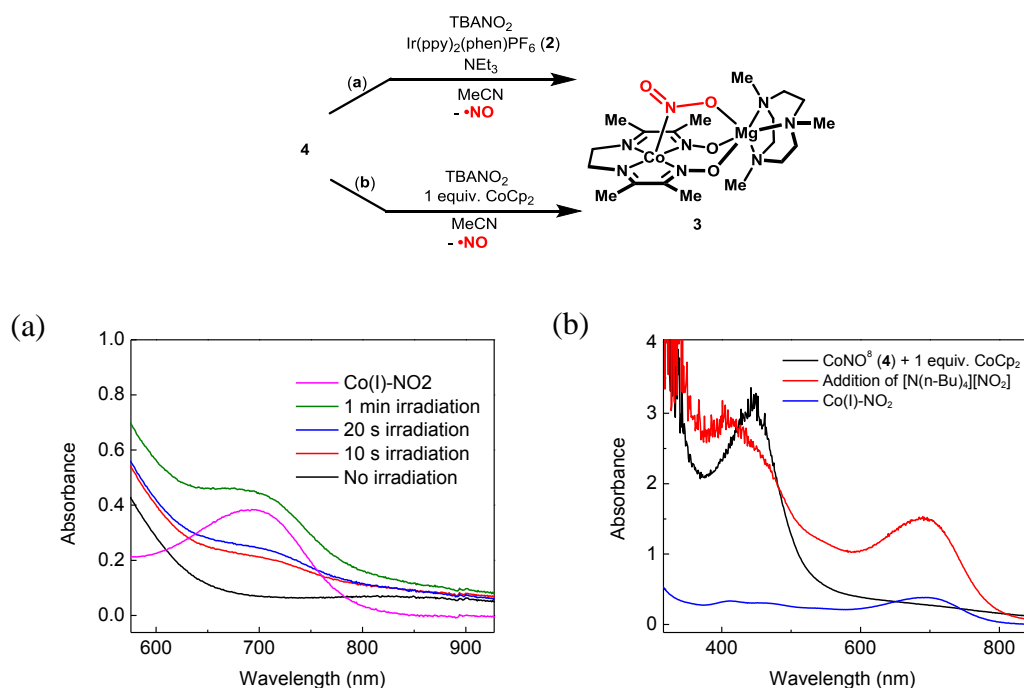


Figure 4.4: (a) Appearance of **3** upon irradiation of a reaction containing **4**, **2**, NEt_3 , and $[\text{N}(n\text{-Bu})_4][\text{NO}_2]$ in MeCN . (b) Appearance of **3** upon reduction of **4** with cobaltocene, and then addition of $[\text{N}(n\text{-Bu})_4][\text{NO}_2]$. An authentic sample of **3** in MeCN is included in both figures for comparison.

The products of the reduction and protonation of **4** were determined to be N_2O and H_2O .²⁴ To measure the amount of water generated as a product, deuterated acid (NEt_3DCl) was used and D_2O was measured by ^2H NMR spectroscopy relative to an internal C_6D_6 calibrated standard. Because **4** is an aquo complex, the protons can exchange for ^2H . Thus, to know whether additional D_2O was generated during the reduction and protonation of **4**, a known amount of **4** was reduced with 1 equivalent CoCp_2 and protonated with NEt_3DCl . The resulting reaction was measured to have 1.29

equivalents of D₂O, indicating that more D₂O was being generated than just what is on the complex.²⁵ The presence of water and the absence of NO₂ are indicative of a reductive coupling mechanism and are inconsistent with a dominant NO disproportionation pathway which would generate NO₂ and N₂O from free NO.²⁶

4.2.4 N–N Coupling Step

To determine whether free nitroxyl (HNO) is formed during catalysis which can bimolecularly couple to form N₂O and H₂O,²⁷ triphenylphosphine was used as a nitroxyl trap.²⁸ The reaction of HNO with PPh₃ has been shown to generate OPPh₃ and HNPPPh₃. The {CoNO}⁹ complexes synthesized by Walter *et al.* were shown to release free nitroxyl upon addition of acid.^{17e} However, the {CoNO}⁹ complex which results from reduction of **4** with CoCp₂ forms neither OPPh₃ nor HNPPPh₃ upon protonation; it also forms no oxidized triphenylphosphine products under photocatalytic conditions.²⁹ If nitroxyl were being formed in solution, we would expect the rate of trapping by PPh₃ to be faster than bimolecular reactivity. While this result by itself does not rule out the generation of nitroxyl as the main source of N₂O, failure to observe oxidized PPh₃ products led us to investigate other pathways for N–N bond formation.

We sought to determine the intermediate(s) responsible for N–N bond formation during photocatalysis. To do so, step-scan time-resolved FT-IR laser spectroscopy at the nanosecond time scale was used to monitor a mixture containing **4**, **2**, and NEt₃ after irradiation with a 460 nm laser pulse (Figure 4.5).³⁰ To simplify the experiment, nitrite was not included so that only the reduction step was probed and not the regeneration of **4**.³¹ Upon laser excitation of the mixture, a bleach at 1635 cm⁻¹, corresponding to the disappearance **4**, was observed along with appearance of a peak at 1690 cm⁻¹, which has

been previously characterized as the $\{\text{CoNO}\}^9$ intermediate. In addition to these peaks of known identity, two new peaks at 1723 and 1666 cm^{-1} also appeared and disappeared together (Figure 4.5); when the ^{15}N -labeled $\{\text{CoNO}\}^8$ compound was used, the peaks at 1635 (due to **4**), 1690 (due to $\{\text{CoNO}\}^9$), 1723 (new), and 1666 (new) cm^{-1} shifted to 1609, 1671, 1699, and 1643 cm^{-1} , respectively (see Supporting Information).³² These two new peaks are tentatively assigned to a neutral hyponitrite (*cis* NO dimer) intermediate with a weak bonding interaction between the two nitrosyl moieties. Shifts observed in well-characterized neutral hyponitrite bridges originating from $\{\text{Co}_2(\text{NO})_2\}^{18}$ (1622 cm^{-1})⁶ and $\{\text{Ru}_2(\text{NO})_2\}^{14}$ (1605 cm^{-1})^{33,17c,34} are lower than the values we have observed, indicating greater activation of NO radical and a stronger N–N interaction in these species. In these compounds and in ours, the high-energy hyponitrite shift indicates a substantial degree of neutral nitrosyl radical character on the N=O groups. In the case of the neutral Co hyponitrite observed by Chuang *et al.*, the frequency of the N=O vibration increased by 90 cm^{-1} compared with the monometallic $\{\text{CoNO}\}^9$.⁶ We assign the peak at 1723 cm^{-1} as the one with a weakly bonding interaction with the Co, and thus less electron density in the π^* antibonding orbital. A withdrawal of electron density by the oxophilic Mg^{2+} ion can also have the effect of increasing the N-O stretch, though the data do not require this type of chelating interaction.

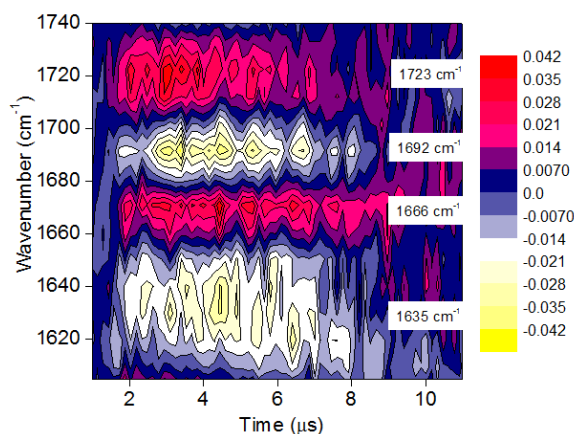
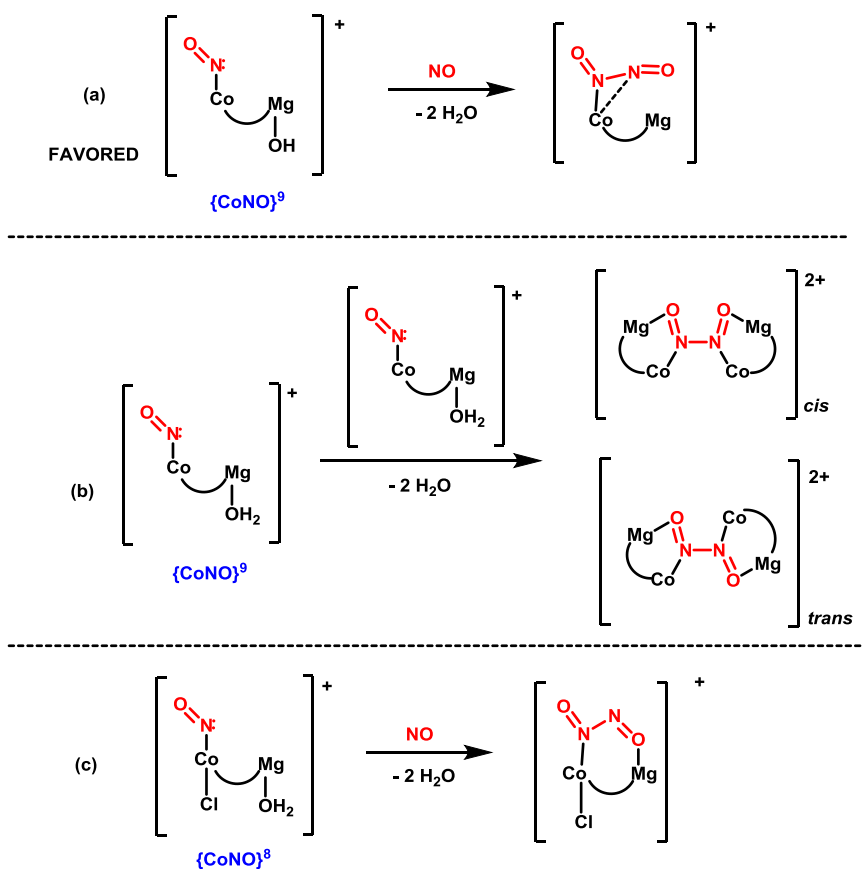


Figure 4.5: TRIR data collected after phototriggering ($\lambda_{\text{exc}} = 460 \text{ nm}$) a reaction mixture containing **4**, **2**, and NEt_3 .

The similarity of the NONO frequencies observed experimentally in this photocatalytic system to the $\{\text{CoNO}\}^9$ character indicates that this species likely arises from the interaction of the $\{\text{CoNO}\}^9$ intermediate with free NO rather than $\{\text{CoNO}\}^8$ **4** with free NO (Scheme 4.2a vs 4.2c), especially under the reducing conditions of catalysis.³⁵ A bimolecular mechanism in which two $\{\text{CoNO}\}^9$ complexes or a $\{\text{CoNO}\}^8$ and a $\{\text{CoNO}\}^9$ complex come together to reductively generate N_2O and H_2O can also not be ruled out (Scheme 4.2b), though release of NO from the $\{\text{CoNO}\}^9$ intermediate suggests a monometallic pathway.³⁶ Furthermore, in previous examples of bimetallic hyponitrite intermediates, only one NO stretching frequency was observed, so observing two stretching frequencies can rule out a symmetric bimetallic intermediate (Scheme 4.2b). Another possible geometry one could postulate for this intermediate is a 6-coordinate *cis*-dinitrosyl intermediate on Co ($\{\text{Co}(\text{NO})_2\}^{10}$). However, other Co complexes with this configuration are four-coordinate tetrahedral compounds with higher

IR frequencies than are observed in our experiments. The lowest NO asymmetric and symmetric frequencies observed for *cis*-dinitrosyl complexes on Co are 1769 and 1699 cm^{-1} , respectively;^{37a,b} the majority of stretches range from 1730-1798 and 1809-1876 for the symmetric and asymmetric stretches, respectively.³⁷ This makes it unlikely that the intermediate we observe would be stable as a six-coordinate dinitrosyl complex. While these frequencies would also be consistent with a *trans*-dinitrosyl complex, this puts the NO in an unfavorable conformation for intramolecular N–N bond formation and N–O bond cleavage. It is also worth noting that there are no examples of *trans* dinitrosyl compounds on Co in the literature.

Scheme 4.2: Possible mechanistic scenarios in which the observed $\{\text{CoNO}\}^9$ intermediate can react either with (a) the NO released from another $\{\text{CoNO}\}^9$ (generates Co(I) upon NO release, which is not shown here; favored pathway), (b) with another $\{\text{CoNO}\}^9$ or (c) the released NO can react with **4** to generate a hyponitrite intermediate that can react with 2 equivalents of NEt_3HCl to make N_2O and H_2O .



To help resolve the identity of the observed intermediate, DFT calculations³⁸ were performed on several $\{\text{Co}(\text{NO})_2\}^{10}$ isomers. To this end, *cis*-dinitrosyl, *trans*-dinitrosyl and neutral hyponitrite complexes were optimized (Figure 4.6). Comparison of the predicted N–O stretching frequencies to experimental values from TRIR experiments suggest that a *trans*-dinitrosyl is unlikely, given the relatively low energies predicted (ν_{NO}

= 1650 cm^{-1} ; 1587 cm^{-1}). Similarly, the stretching modes predicted for a CoMg-bridged neutral hyponitrite complex ($\nu_{\text{NO}} = 1536 \text{ cm}^{-1}$; 1467 cm^{-1}) are also too low in energy to account for the observed bands (Co-hyponitrite-B; Figure 4.6). Attempts to optimize a cis-dinitrosyl led to stretching frequencies most consistent with the observed data, with predicted stretches of 1746 cm^{-1} and 1646 cm^{-1} . Interestingly, this species optimizes to a minimum that appears to be electronically in between a true dinitrosyl complex and a neutral hyponitrite structure (cis- $\{\text{CoNONO}\}^{10}$; Figure 4.6). The long Co–N (1.80 Å and 2.78 Å) and N–N distances (2.04 Å) are consistent with an intermediate structure in which the NO is weakly bound to both the Co center and a second NO unit. The N–N bond length is longer than Arikawa *et al.*'s Ru hyponitrite, which has a bond length of 1.861 Å, but shorter than that of a solid-state *cis*-NO dimer at low temperature (2.18 Å), indicative of the weak bonding interaction between the two NO molecules.

It is possible that this structure represents a metastable intermediate that either loses one equivalent of $\text{NO}\cdot_{(\text{g})}$, to regenerate the $\{\text{CoNO}\}^9$, or couples the NO units to form the hyponitrite species Co-hyponitrite-A (Figure 4.6). Furthermore, while NO coupling to form a hyponitrite intermediate in which H_2O remains bound to magnesium (Co-hyponitrite-A; Figure 4.6) is predicted to be thermoneutral with this putative cis- $\{\text{CoNONO}\}^{10}$ species, formation of a chelated species (Co-hyponitrite-B; Figure 4.6), with loss of H_2O , is predicted to be exergonic by 8.3 kcal/mol. The combined DFT data is therefore consistent with a mechanism in which $\text{NO}\cdot_{(\text{g})}$ equilibration with the $\{\text{CoNO}\}^9$ intermediate, to form a cis- $\{\text{CoNONO}\}^{10}$ species, is followed by “irreversible” formation of a chelated hyponitrite species (Co-hyponitrite-B; Figure 4.6).

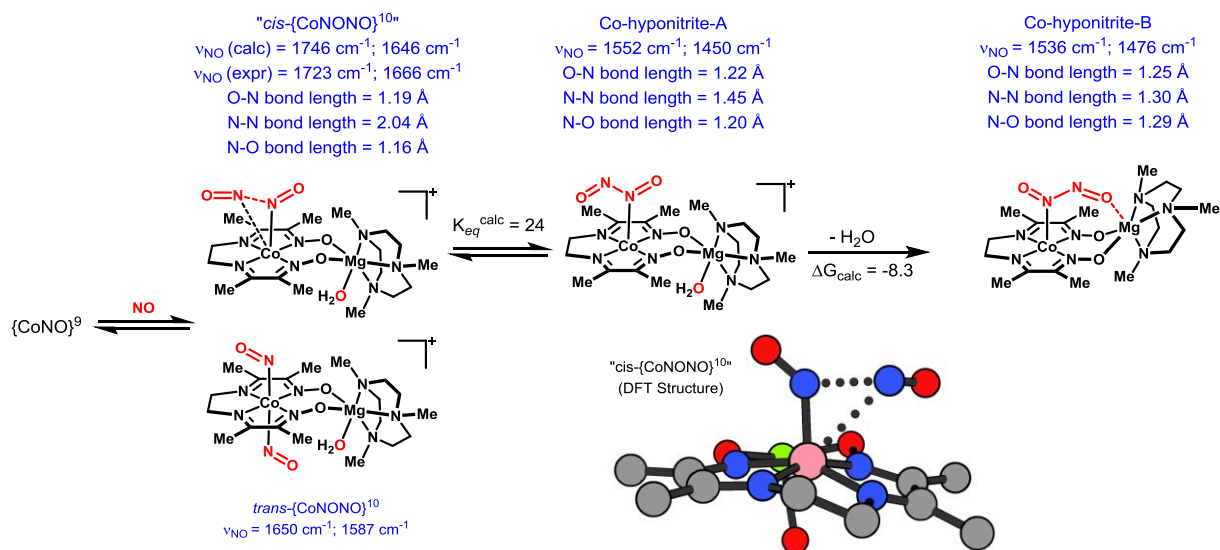
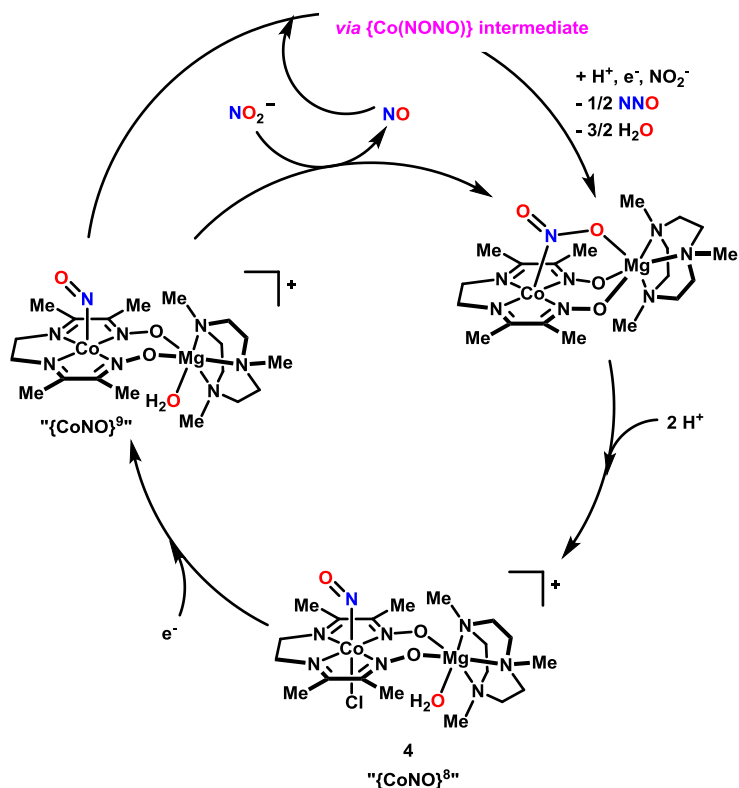


Figure 4.6: Summary of DFT data obtained via optimization of three $\{\text{Co}(\text{NO})_2\}^{10}$ isomers. Bottom right, DFT optimized structure of “cis- $\{\text{CoNONO}\}^{10}$ ” (hydrogen atoms and Me_3TACN omitted for clarity). ΔG_{calc} values are reported in kcal/mol.

4.3 Conclusions

Scheme 4.3: Outline of a viable mechanistic cycle proposed for photocatalytic nitrite reduction to nitrous oxide.



In summary, we have discovered the first homogeneous system for photocatalytic nitrite reduction, as well as the only photocatalytic system which is selective for nitrous oxide. Mechanistic work on this system suggests that the proposed pathway in Scheme 4.3 is viable. A Co(I)-nitrite species can react with two equivalents of triethylammonium chloride to generate a $\{\text{CoNO}\}^8$ complex **4** which needs to be further reduced and protonated to generate N_2O . The $\{\text{CoNO}\}^9$ product which results from reduction of **4** was characterized by EPR and IR spectroscopy, and found to be a 5-coordinate, $S = 3/2$ Co(II) metal center coupled to a $S = 1$ NO^- ligand. This complex is able to release free NO and, in the presence of acid, generate 0.33 equiv N_2O . Using TRIR spectroscopy, we observed

a Co(NONO) intermediate which has been tentatively assigned as a metastable neutral hyponitrite intermediate with a weak N–N bond that can eventually bridge the CoMg platform with loss of the aquo ligand from Mg. This complex can generate N₂O upon protonation and subsequent N–O cleavage. The order of bond cleavage and protonation is still under investigation. Future work will focus on reducing catalyst and photosensitizer loading, and employing non-noble metals as photosensitizers.

4.4 References

1. (a) Wasser, I. M.; Vries, S. De; Moe, P.; Schro, I.; Karlin, K. D. *Chem. Rev.* **2002**, *102*, 1201–1234. (b) Hayashi, T.; Caranto, J. D.; Matsumura, H.; Kurtz, D. M.; Moënne-Loccoz, P. *J. Am. Chem. Soc.* **2012**, *134*, 6878–6884. (c) Moënne-Loccoz, P. *Nat. Prod. Rep.* **2007**, *24*, 610–620. (d) Girsch, P.; De Vries, S. *Biochim. Biophys. Acta - Bioenerg.* **1997**, *1318*, 202–216. (e) Hendriks, J.; Oubrie, A.; Castresana, J.; Urbani, A.; Gemeinhardt, S.; Saraste, M. *Biochim. Biophys. Acta - Bioenerg.* **2000**, *1459*, 266–273. (f) Suharti, S.; Strampraad, M. J.; Schröder, I.; De Vries, S. *Biochemistry* **2001**, *40*, 2632–2639. (g) Silaghi-Dumitrescu, R.; Coulter, E. D.; Das, A.; Ljungdahl, L. G.; Jameson, G. N. L.; Huynh, B. H.; Kurtz, D. M. *Biochemistry* **2003**, *42*, 2806–2815. (h) Varotsis, C.; Ohta, T.; Kitagawa, T.; Soulimane, T.; Pinakoulaki, E. *Angew. Chem. Int. Ed.* **2007**, *46*, 2210–2214.
2. (a) Schopfer, M. P.; Wang, J.; Karlin, K. D. *Inorg. Chem.* **2010**, *49*, 6267–6282. (b) Kurtz, Jr., D. M. *Dalton Trans.* **2007**, 4115–4121. (c) Blomberg, L. M.; Blomberg, M. R. A.; Siegbahn, P. E. M. *J. Biol. Inorg. Chem.* **2007**, *12*, 79–89. (d) Moënne-Loccoz, P. *Nat. Prod. Rep.* **2007**, *24*, 610–620. (e) Hayashi, T.; Caranto, J. D.; Wampler, D. A.; Kurtz, D. M.; Moënne-Loccoz, P. *Biochemistry* **2010**, *49*, 7040–7049. (f) Ohta, T.; Kitagawa, T.; Varotsis, C. *Inorg. Chem.* **2006**, *45*, 3187–3190. (g) Daskalakis, V.; Ohta, T.; Kitagawa, T.; Varotsis, C. *Biochem. Biophys. Acta* **2015**, *1847*, 1240–1244.
3. (a) Berto, T. C.; Speelman, A. L.; Zheng, S.; Lehnert, N. *Coord. Chem. Rev.* **2012**, *257*, 244–259. (b) Collman, J. P.; Dey, A.; Decréau, R. A.; Yang, Y.; Hosseini, A.; Solomon, E. I.; Eberspacher, T. A. *Proc. Natl. Acad. Sci. U. S. A.* **2008**, *105*, 9892–

9896. (c) Collman, J. P.; Yang, Y.; Dey, A.; Decréau, R. A.; Ghosh, S.; Ohta, T.; Solomon, E. I. *Proc. Natl. Acad. Sci.* **2008**, *105*, 15660–15665. (d) Collman, J. P.; Dey, A.; Yang, Y.; Decréau, R. A.; Ohta, T.; Solomon, E. I. *J. Am. Chem. Soc.* **2008**, *130*, 16498–16499. (e) Yeung, N.; Lin, Y.-W.; Gao, Y.-G.; Zhao, X.; Russell, B. S.; Lei, L.; Miner, K. D.; Robinson, H.; Lu, Y. *Nature* **2009**, *462*, 1079–1082. (f) Lin, Y.; Yeung, N.; Gao, Y.; Miner, K. D.; Tian, S.; Robinson, H.; Lu, Y. *Proc. Natl. Acad. Sci. U. S. A.* **2010**, *107*, 8581–8586. (g) Zheng, S.; Berto, T. C.; Dahl, E. W.; Hoffman, M. B.; Speelman, A. L.; Lehnert, N. *J. Am. Chem. Soc.* **2013**, *135*, 4902–4905.
4. Xu, N.; Campbell, A. L. O.; Powell, D. R.; Khandogin, J.; Richter-Addo, G. B. *J. Am. Chem. Soc.* **2009**, *131*, 2460–2461.
5. Uyeda, C.; Peters, J. C. *J. Am. Chem. Soc.* **2013**, *135*, 12023–12031.
6. Chuang, C. H.; Liaw, W. F.; Hung, C. H. *Angew. Chem., Int. Ed.* **2016**, *55*, 5190–5194.
7. Averill, B. A. *Chem. Rev.* **1996**, *96*, 2951–2964.
8. Kudrik, E. V.; Makarov, S. V.; Zahl, A.; Eldik, R. Van. *Inorg. Chem.* **2005**, *44*, 6470–6475.
9. Heinecke, J. L.; Khin, C.; Pereira, J. C. M.; Suárez, S. A.; Iretskii, A. V.; Doctorovich, F.; Ford, P. C. *J. Am. Chem. Soc.* **2013**, *135*, 4007–4017.
10. (a) Barley, M. H.; Takeuchi, K. J.; Meyer, T. J. *J. Am. Chem. Soc.* **1986**, *108*, 5876–5885. (b) Barley, M. H.; Rhodes, M. R.; Meyer, T. J. *Inorg. Chem.* **1987**, *26*, 1746–1750.
11. Granger, P.; Parvulescu, V. I. *Chem. Rev.* **2011**, *111*, 3155–3207.

12. (a) Brown, W. A.; King, D. A. *J. Phys. Chem. B* **2000**, *104*, 2578–2595. (b) Gao, W.; Chen, J.; Guan, X.; Jin, R.; Zhang, F.; Guan, N. *Catal. Today* **2004**, *93–95*, 333–339. (c) Rosca, V.; Duca, M.; Groot, M. T. De; Koper, M. T. M. *Chem. Rev.* **2009**, *109*, 2209–2244.
13. For examples of photocatalytic nitrite reduction to N₂ or NH₃ on a variety of solid supports, see: (a) Halmann, M.; Zuckerman, K. *J. Chem. Soc. Chem. Commun.* **1986**, 455. (b) Ranjit, K. T.; Varadarajan, T. K.; Viswanathan, B. *J. Photochem. Photobiol. A Chem.* **1995**, *89*, 67–68. (c) Zhang, F.; Jin, R.; Chen, J.; Shao, C.; Gao, W.; Li, L.; Guan, N. *J. Catal.* **2005**, *232*, 424–431. (d) Ranjit, K. T.; Viswanathan, B. *J. Photochem. Photobiol. A* **1997**, *108*, 73–78. (e) Kominami, H.; Nakaseko, T.; Shimada, Y.; Furusho, A.; Inoue, H.; Murakami, S.; Kera, Y.; Ohtani, B. *Chem. Commun.* **2005**, *3*, 2933–2935.
14. Electrochemical systems probed by *in situ* spectroscopy have a maximum time resolution of 10 μs which is limited by the formation of a charged double layer on a microelectrode; in typical electrodes, this time constant is much slower and limits time resolution to hundreds of microseconds. For details and examples, see: (a) *Diffraction and Spectroscopic Methods in Electrochemistry*; Alkire, R. C.; Kolb, D. M.; Lipkowsky, J. Ross, P. A., Eds.; Wiley–VCH: Weinheim, Germany, 2006. (b) *In-situ Spectroscopic Studies of Adsorption at the Electrode and Electrocatalysis*; Sun, S.-G.; Christensen, P. A.; Wieckowski, A., Eds.; Elsevier: Amsterdam, Netherlands, 2007. (c) Zhou, Z.-Y.; Lin, S.-C.; Chen, S.-P.; Sun, S.-G. *Electrochem. Commun.* **2005**, *7*, 490–495. (d) Iwasita, T.; Nart, F. *Prog. Surf. Sci.* **1997**, *55*, 271–340. (e)

- Zhou, Z.-Y.; Sun, S.-G. *Electrochim. Acta* **2005**, *50*, 5163–5171. (f) Nesselberger, M.; Ashton, S. J.; Wiberg, G. K. H.; Arenz, M. *Rev. Sci. Instrum.* **2013**, *84*. (g) Farias, M. J. S.; Camara, G. A.; Feliu, J. M. *J. Phys. Chem. C* **2015**, *119*, 20272–20282. (h) Pathirathna, P.; Samaranayake, S.; Atcherley, C. W.; Parent, K. L.; Heien, M. L.; McElmurry, S. P.; Hashemi, P. *Analyst* **2014**, *139*, 4673.
15. (a) Prier, C. K.; Rankic, D. A.; Macmillan, D. W. C. *Chem. Rev.* **2013**, *113*, 5322. (b) Eckenhoff, W. T.; Eisenberg, R. *Dalton Trans.* **2012**, *41*, 13004. (c) Luong, J. C.; Nadjo, L.; Wrighton, M. S. *J. Am. Chem. Soc.* **1978**, *100*, 5790–5795.
16. For a discussion of Enemark-Feltham notation, see Enemark, J. H.; Feltham, R. D. *Coord. Chem. Rev.* **1974**, *13*, 339–406.
17. For examples of known {CoNO}⁹ complexes, see (a) Blanchard, A.; Rafter, J. R.; Adams, W. B. *J. Am. Chem. Soc.* **1934**, *56*, 16–17. (b) Di Vaira, M.; Ghilardi, C. A.; Sacconi, L. *Inorg. Chem.* **1976**, *15*, 1555–1561. (c) Thyagarajan, S.; Incarvito, C. D.; Rheingold, A. L.; Theopold, K. H. *Inorganica Chim. Acta* **2003**, *345*, 333–339. (d) Tomson, N. C.; Crimmin, M. R.; Petrenko, T.; Rosebrugh, L. E.; Sproules, S.; Boyd, W. C.; Bergman, R. G.; Debeer, S.; Toste, F. D.; Wieghardt, K. *J. Am. Chem. Soc.* **2011**, *133*, 18785–18801. (e) Walter, M. R.; Dzul, S. P.; Rodrigues, A. V.; Stemmler, T. L.; Telser, J.; Conradie, J.; Ghosh, A.; Harrop, T. C. *J. Am. Chem. Soc.* **2016**, *138*, 12459–12471.
18. For examples of the effect of *trans* ligands on NO frequencies, see (a) Kurtikyan, T. S.; Hovhannisyan, A. A.; Ford, P. C. *Inorg. Chem.* **2016**, *55*, 9517–9520. (b) Kurtikyan, T. S.; Gulyan, G. M.; Dalaloyan, A. M.; Kidd, B. E.; Goodwin, J. A.

- Inorg. Chem.* **2010**, *49*, 7793–7798. (c) Praneeth, V. K. K.; Näther, C.; Peters, G.; Lehnert, N. *Inorg. Chem.* **2006**, *45*, 2795–2811.
19. While a crystal structure of **5** confirms the 5-coordinate structure of the Co–nitrosyl complex, the identity of the Mg-coordinated species is unclear. There is some disorder on the O-containing species on Mg which been modeled as 63% acetic acid and 37% H₂O. Numerous attempts to grow crystals have led to this same structure and disorder.
20. (a) Serres, R. G.; Grapperhaus, C. A.; Bothe, E.; Bill, E.; Neese, F.; Wieghardt, K. *J. Am. Chem. Soc.* **2004**, *126*, 5138–5153. (b) Hu, B.; Li, J. *Angew. Chemie. Int. Ed.* **2015**, *54*, 10579–10582. (c) Chalkley, M. J.; Peters, J. C. *Angew. Chemie. Int. Ed.* **2016**, *55*, 11995–11998.
21. Using either the photosensitizer/triethylamine combination or cobaltocene as the reducing agent resulted in the same EPR spectrum.
22. (a) Little, R. G.; Hoffman, B. M.; Ibers, J. A. *Bioinorg. Chem.* **1974**, *3*, 207–215. (b) Wayland, B. B.; Abd-Elmageed, M. E. *J. Am. Chem. Soc.* **1974**, *96*, 4809–4814. (c) Wayland, B. B.; Minkiewicz, J. V. *J. Am. Chem. Soc.* **1972**, *13*, 2795–2801. (d) McGarvey, B. R. *Can. J. Chem.* **1975**, *53*, 2498–2511.
23. Without acid, 0.07 equivalents of N₂O can be observed, presumably because H₂O can dissociate from two equivalents of **4** and be used as an acid in this reaction to generate dechelated (TACN)Mg(OH)₂; the generation of an intermediate oxo species has not been observed, though it cannot be ruled out.
24. Free NO₂ was not detected in the headspace of the reaction mixture.

25. This experiment was done in the absence of nitrite because it would not be possible to distinguish between water that was being generated from catalysis and which was exchanging its aquo ligand with deuterated acid upon formation of **4** from **3**.
26. (a) Ford, P. C.; Lorkovic, I. M. *Chem. Rev.* **2002**, *102*, 993–1017. (b) Brozek, C. K.; Miller, J. T.; Stoian, S. A.; Dinca, M. *J. Am. Chem. Soc.* **2015**, *137*, 7495–7501.
27. Shafirovich, V.; Lymar, S. V. *Proc. Natl. Acad. Sci.* **2002**, *99*, 7340–7345.
28. (a) Reisz, J. A.; Zink, C. N.; King, S. B. *J. Am. Chem. Soc.* **2011**, *133*, 11675–11685. (b) Abucayon, E. G.; Khade, R. L.; Powell, D. R.; Zhang, Y.; Richter-Addo, G. B. *J. Am. Chem. Soc.* **2016**, *138*, 104–107.
29. Compared with a photocatalytic reaction mixture without PPh₃, adding triphenylphosphine reduced catalytic efficiency from 18 turnovers to 6 turnovers. One reason for this is that PPh₃ competes with nitrite for Co(I).
30. The acquired spectra had the same features in the presence and absence of acid.
31. Addition of acid and no nitrite yielded comparable results, suggesting that the event observed is due to the reduction step and not the protonation step.
32. Because of some variation in photon flux and flow rates in between samples, the {CoNO}⁹ intermediate could be seen as both a rise or a bleach, based on whether it was being generated by reduction of **4** or whether the NO was being photochemically labilized.
33. For an example of a neutral hyponitrite ligand on Ru, see: (a) Arikawa, Y.; Asayama, T.; Moriguchi, Y.; Agari, S.; Onishi, M. *J. Am. Chem. Soc.* **2007**, *129*, 14160–14161.

34. For examples of dianionic hyponitrite ligands bound to Co and other transition metal hyponitrite complexes, see (a) Wright, A. M.; Hayton, T. W. *Inorg. Chem.* **2015**, *35*. (b) Arikawa, Y.; Onishi, M. *Coord. Chem. Rev.* **2012**, *256*, 468–478. (c) Hoskins, B. F.; Whillans, F. D.; Dale, D. H.; Hodgkin, D. C. *J. Chem. Soc. Chem. Commun.* **1969**, 69–70. (d) Hoskins, B. F.; Whillans, F. D. *J. Chem. Soc. Trans.* **1973**, 607–611. (e) Mercer, E. E.; McAllister, W. A.; Durig, J. R. *Inorg. Chem.* **1967**, *6*, 1816–1821. (f) Okamura, H.; Miki, E.; Mizumachi, K.; Ishimori, T. *Chem. Lett.* **1974**, *3*, 103–106. (g) Okamura, H.; Miki, E.; Mizumachi, K.; Ishimori, T. *Bull. Chem. Soc. Jpn.* **1976**, *49*, 666–670. (h) Bau, R.; Sabherwal, I. H.; Burg, A. B. *J. Am. Chem. Soc.* **1971**, *93*, 4926–4928.
35. Reaction of free NO with **4** under argon atmosphere resulted in formation of a complex mixture of NO₂, N₂O, and N₂ which was dependent on the concentration of NO used. Complex **4** is presumably a catalyst for NO disproportionation.
36. The rate-determining step of the photocatalytic reaction is the reduction step, which is first order in **4**, zero order in acid, and zero order in nitrite. The slow reaction of **4** and NO to generate N₂O was first order in NO and first order in **4**, and zero order in acid; triethylamine was one possible source of electrons in this reaction. As might be expected, at high NO concentrations, NO disproportionation to NO₂ and N₂O was also observed.
37. (a) Tennyson, A. G.; Dhar, S.; Lippard, S. J. *J. Am. Chem. Soc.* **2008**, *130*, 15087–15098. (b) Kozhukh, J.; Lippard, S. J. *J. Am. Chem. Soc.* **2012**, *134*, 11120–11123. (c) Franz, K. J.; Singh, N.; Spingler, B.; Lippard, S. J. *Inorg. Chem.* **2000**, *39*, 4081–4092.

(d) Martin, R. L.; Taylor, D. *Inorg. Chem.* **1976**, *15*, 2970–2976. (e) Hendrickson, A. R.; Ho, R. K. Y.; Martin, R. L. *Inorg. Chem.* **1974**, *13*, 1279–1281. (f) Aresta, M.; Ballivet-Tkatchenko, D.; Bonnet, M. C. *J. Am. Chem. Soc.* **1985**, *107*, 2994–2995. (g) Roustan, J.-L.; Ansari, N.; Le Page, Y.; Charland, J.-P. *Can. J. Chem.* **1992**, *70*, 1650–1657. (h) Kaduk, J. A.; Ibers, J. A. *Inorg. Chem.* **1977**, *16*, 3283–3287. (i) Haymore, B. L.; Huffman, J. C.; Butler, N. E. *Inorg. Chem.* **1983**, *22*, 168–170. (j) Lim, M. H.; Kuang, C.; Lippard, S. J. *ChemBioChem* **2006**, *7*, 1571–1576. (k) Franz, K. J.; Singh, N.; Lippard, S. J. *Angew. Chem., Int. Ed.* **2000**, *39*, 2120–2122. (l) Tonzetich, Z. J.; Héroguel, F.; Do, L. H.; Lippard, S. J. *Inorg. Chem.* **2011**, *50*, 1570–1579.

38. DFT calculations were performed the TPSS functional with a def2-TZVP basis set on Co and a def2-SVP basis set on all other atoms. Calculated stretching frequencies were referenced to the experimental stretching frequency of {CoNO}⁸. See SI for full computational details: (a) Tao, J. M.; Perdew, J. P.; Staroverov, V. N.; Scuseria, G. E. *Phys. Rev. Lett.* **2003**, *91*, 146401. (b) Weigend, F.; Ahlrichs, R. Balanced Basis Sets of Split Valence, Triple Zeta Valence and Quadruple Zeta Valence Quality for H to Rn: Design and Assessment of Accuracy. *Phys. Chem. Chem. Phys.* **2005**, *7*, 3297–3305.

Appendix A : Supplementary Information for Chapter 2

A.1 General Information

Chemicals. Unless otherwise noted, all materials were purchased from commercial suppliers and used as received. All manipulations of air-sensitive materials were carried out in oven-dried glassware using standard Schlenk or glovebox techniques under an N₂ atmosphere. Solvents were deoxygenated and dried by thoroughly sparging with argon followed by passage through an activated column in a solvent purification system. Silicycle *SiliaFlash*[®] P60 Silica gel (particle size 40–63 nm) was used for flash chromatography. Analytical thin layer chromatography was conducted with glass TLC plates (silica gel 60 F254) and spots were visualized under UV light or after treatment with standard TLC stains. Carbazole (carbH) was recrystallized from hot ethanol. Mesitylcopper¹ and 2-bromo-4-phenylbutane,² were prepared following a reported procedure. Note: herein carbazolide = carb and they are used interchangeably.

EPR, Infrared, and UV-vis Spectroscopy. X-band EPR measurements were made with a Bruker EMX spectrometer at 77 K. Simulation of EPR data was conducted using the software EasySpin.³ IR measurements were recorded on a Bruker ALPHA Diamond ATR. Absorbance spectra were acquired on a Cary 50 UV-vis spectrophotometer with a Unisoku Scientific Instruments cryostat to maintain temperature.

NMR spectroscopy. ¹H, ²H, ¹³C, ⁷Li, ³¹P NMR, and DOSY spectra were recorded on a Bruker Ascend 400, a Varian 300 MHz, a Varian 400 MHz, a Varian 500 MHz, or a Varian 600 MHz spectrometer, and referencing was done using either the proteo impurity in a deuterated solvent, or to the deuterium lock signal. Multiplicity and qualifier

abbreviations are as follows: s = singlet, d = doublet, t = triplet, q = quartet, m = multiplet, br = broad, app = apparent.

Gas chromatography. Calibrated GC yields were obtained on an Agilent 6890 Series system with an HP-5 column (length 30 m, I.D. 0.25 mm, FID Detector) using dodecane as an internal standard.

X-ray crystallography. XRD studies were carried out at the Beckman Institute Crystallography Facility (<http://www.its.caltech.edu/~xray/index.html>) on a Bruker D8 Venture kappa duo photon 100 CMOS instrument (Mo K α radiation). Structures were solved using SHELXT and refined against F^2 by full-matrix least squares with SHELXL and OLEX2. Hydrogen atoms were added at calculated positions and refined using a riding model. The crystals were mounted on a glass fiber or a nylon loop with Paratone N oil.

Photolytic reactions. Photolytic reactions were performed using a 100-W Blak-Ray Long Wave Ultraviolet Lamp (Hg), 100-W Blak-Ray B-100Y High Intensity Inspection Lamp (Hg), or a Luzchem LZC-4V photoreactor equipped with LZC-UVA lamps centered at 350 nm (Figure A.1). Temperature control was maintained with an isopropanol bath cooled by an SP Scientific cryostat. For reactions using mercury lamps, the light source was placed approximately 20 cm above the sample and the reaction mixture was stirred vigorously using a magnetic stir bar.

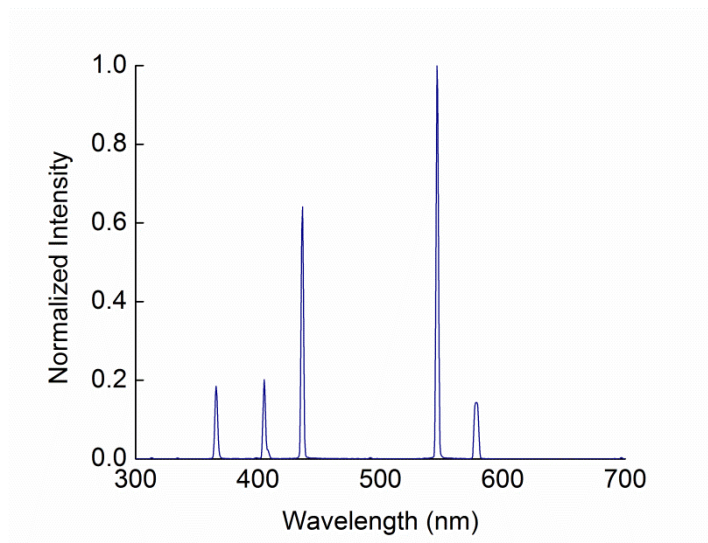


Figure A.1: Emission spectrum of 100-W Blak-Ray Long Wave Ultraviolet Lamp

Photophysical methods. Steady-state fluorimetry and time-resolved transient absorption and luminescence measurements were performed in the Beckman Institute Laser Resource Center (BILRC; California Institute of Technology). Samples for room temperature transient absorption and luminescence measurements were prepared in dry (passage through alumina three times), degassed (three freeze-pump-thaw cycles) acetonitrile inside a nitrogen-filled glovebox, and transferred to a 1-cm or 1-mm pathlength fused quartz or glass cuvette (Starna Cells) which was sealed with a high-vacuum Teflon valve (Kontes), or a Harrick demountable liquid flow cell (DLC-S25) with quartz windows and 100 μm path length Teflon spacers. Steady-state emission spectra were collected on a Jobin S4 Yvon Spec Fluorolog-3-11 with a Hamamatsu R928P photomultiplier tube detector with photon counting.

For luminescence and transient absorption at the nanosecond to microsecond time scale, a Q-switched Nd:YAG laser (Spectra-Physics Quanta-Ray PRO-Series; 355 nm; pulse duration 8 ns, operating at 10 Hz) was used as the source of the excitation pulse,

with laser power at 0.5 mJ/pulse. Probe light for transient absorption kinetics measurements was provided by a 75-W arc lamp (PTI Model A 1010) which was operated in continuous wave or pulsed modes. The laser light was aligned so as to be collinear with the arclamp beam, and the scattered excitation light was rejected with appropriate long pass and short pass filters. Transmitted light from the sample was detected with a photomultiplier tube (Hamamatsu R928). All instruments and electronics in these systems were controlled by software written in LabVIEW (National Instruments).

Transient absorption difference spectra were collected using the same excitation source ($\lambda_{\text{ex}} = 355 \text{ nm}$), and a white light flash lamp source with nanosecond durations. All instruments and electronics in these systems were controlled by software written in LabVIEW (National Instruments). Data manipulation was performed with MatlabR2014B.

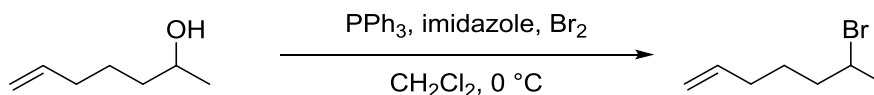
Fluorescence decay measurements at the picosecond time scale were performed as previously described.⁴ A mode-locked Nd:YAG laser (Vanguard 2000-HM532; Spectra-Physics) provided 10 ps pulses that were regeneratively amplified (Continuum) and frequency tripled (355 nm excitation). Laser power was reduced to 0.5 mJ/pulse. Fluorescence from the sample was focused onto the entrance slit of a spectrograph (Acton Research Corp SpectraPro 275) through a 355 nm dielectric mirror to reject scattered excitation light. Fluorescence decays were obtained at a spectrograph center wavelength of 420 nm. Decays were collected using a streak camera (C5680; Hamamatsu Photonics) in photon counting mode over a 50 ns window. Samples were prepared in the glove box using a flow cell apparatus with quartz windows to allow for UV penetration.

A sample path length of 100 μm was used by inserting Teflon spacers in between the two quartz windows. A syringe pump was used to flow sample in between two gas-tight 10 mL syringes (Hamilton) under inert atmosphere.

A.2 Preparation of Substrates

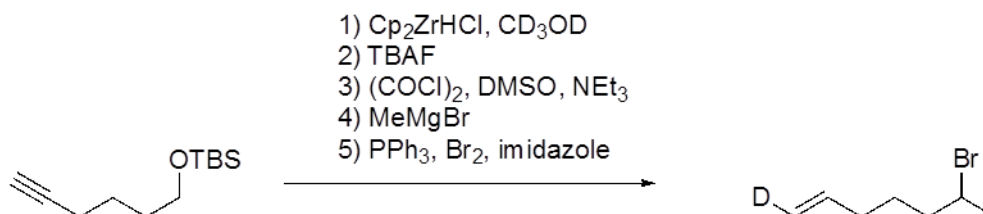
Yields have not been optimized.

6-bromohept-1-ene [38334-98-4]:



A 500 mL round-bottomed flask was charged with triphenylphosphine (14.5 g, 55 mmol), imidazole (3.7 g, 55 mmol), and a magnetic stir bar. CH_2Cl_2 (300 mL) was added under a nitrogen atmosphere and the mixture was cooled to 0 °C. Br_2 (2.6 mL, 51 mmol) was added dropwise. The resulting mixture was stirred for 30 minutes at 0 °C before a solution of hept-6-en-2-ol⁵ (5 g, 44 mmol) in 10 mL CH_2Cl_2 was added dropwise at 0 °C. The mixture was stirred at 0 °C for 2 hours and allowed to warm to ambient temperature overnight. The mixture was concentrated under reduced pressure on a rotary evaporator to an approximate volume of 25 mL, and diluted with hexanes. The resulting solid was filtered, and the filtrate was concentrated and purified by column chromatography (hexanes) to yield 6.1 g (78 % yield) of colorless liquid. Spectroscopic data match those reported in the literature.⁶

(E)-6-bromohept-1-ene-1-*d*:



In the glovebox under nitrogen atmosphere, Cp_2ZrHCl (12 g, 47 mmol) was suspended in THF (200 mL) in a 500 mL round-bottomed flask. *tert*-butyl(hex-5-yn-1-

xyloxy)dimethylsilane (8.7 g, 41 mmol) in THF was then added dropwise to the stirring suspension at ambient temperature. After overnight stirring, excess D₂O (9 mL) was added to the brown solution in one portion at ambient temperature via syringe. The resulting yellow solution was allowed to stir at ambient temperature for 6 h and diluted with Et₂O (~ 250 mL). The suspension was filtered through a pad of silica over MgSO₄, and concentrated under reduced pressure on a rotary evaporator. The oily residue was dissolved in anhydrous THF. This solution was added to a solution of tetrabutylammonium fluoride (30 mL, 1 M in THF) at ambient temperature over 5 min. After stirring for 2 h, the mixture was extracted with diethyl ether and washed with water (50 mL). The organic layer was dried over Na₂SO₄, filtered and concentrated on a rotary evaporator. The oily residue was passed through a plug of silica gel eluting with diethyl ether, and the material with the same R_f value on the TLC plate as the commercially available hex-5-en-1-ol was collected. The ¹H NMR spectrum of the oil matched that of hex-5-en-1-ol except for the resonances corresponding to the deuterated vinylic proton. The filtrate was concentrated under reduced pressure on a rotary evaporator. The residue was dissolved in dichloromethane (10 mL). In a separate flask, DMSO (5.7 mL) in dichloromethane (5 mL) was added dropwise to a cold solution of oxalyl chloride (4.1 mL) in dichloromethane (150 mL) at -78 °C. After stirring for 15 min, the dichloromethane solution of the oily residue was added dropwise. Excess trimethylamine (28 mL) was added after 1 h at 78 °C, and the mixture was allowed to warm to ambient temperature. 1 M HCl_(aq) (100 mL) was added to the mixture, and the aqueous layer was extracted with dichloromethane (2 x 50 mL). The organic layer was dried over Na₂SO₄, filtered, and concentrated on a rotary evaporator. The oily residue was dissolved in

anhydrous Et₂O and added slowly to a cold solution of methylmagnesium bromide (20 mL, 3 M in Et₂O at -10 °C). The solution was allowed to warm to room temperature overnight and quenched with NH₄Cl_(aq). The aqueous layer was extracted with Et₂O (2 x 50 mL), and the organic layer was dried over Na₂SO₄, filtered, and concentrated under reduced pressure on a rotary evaporator. The crude material was purified by column chromatography (70% Et₂O/hexanes), affording 2 g of colorless oil that had the same R_f value on the TLC plate as hept-6-en-2-ol. The ¹H NMR spectrum of the oil matched that of hept-6-en-2-ol except for the resonances corresponding to the deuterated vinylic proton. This oil was subjected to the standard bromination conditions using triphenylphosphine (5.8 g), imidazole (1.5 g), and bromine (1 mL) to yield 1.2 g of (E)-6-bromohept-1-ene-1-d as colorless oil (16% yield over 5 steps). The ²H NMR spectrum of this material shows approximately 9.5:1 selectivity of hydrozirconation versus over-reduction of the alkyne. The hydrozirconation proceeded in 13:1 selectivity to afford the desired *E*-isotopomer.

¹H NMR (300 MHz, Chloroform-*d*): δ 5.96–5.71 (m, 1H), 5.03–4.96 (m, 1H), 3.86–3.73 (m, 1H), 2.11–1.97 (m, 2H), 1.40–1.49 (m, 4H), 1.19 (d, J = 6.2 Hz, 3H).

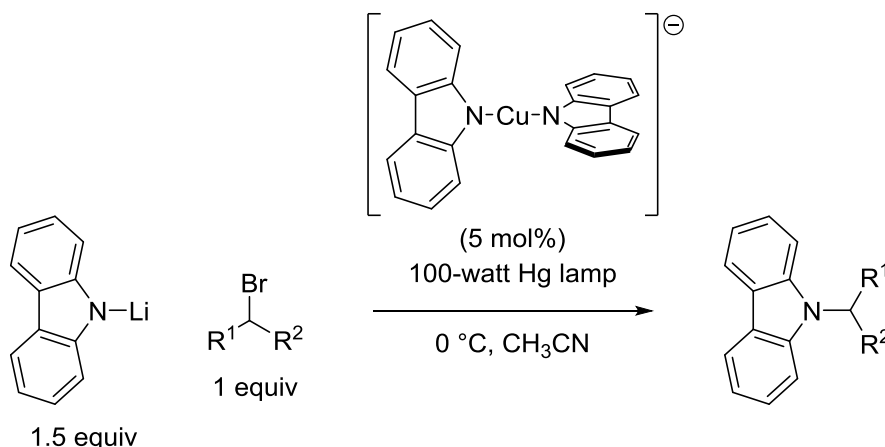
¹³C NMR (75 MHz, Chloroform- *d*): δ 138.08, 114.64 (t), 51.58, 40.47, 32.96, 26.96, 26.46.

²H NMR (61 MHz, Chloroform): δ 5.01.

MS (EI) m/z (M-Br⁺) calc for C₇H₁₂DBr: 98, found: 98.

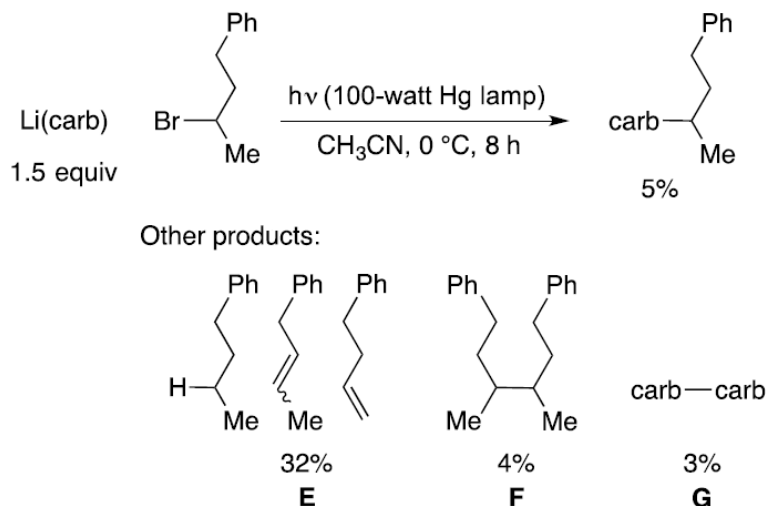
A.3 Procedures for Photoinduced Cross-Couplings

A.3.1 General procedure for the coupling of alkyl bromides



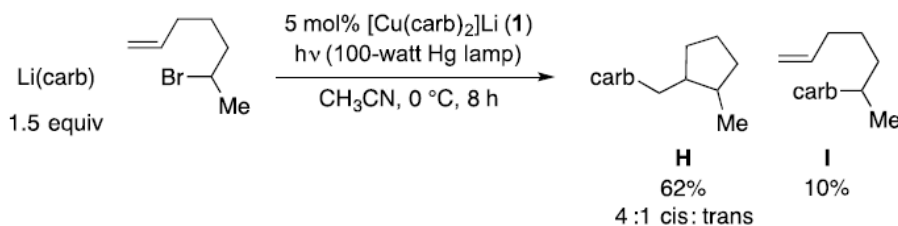
[Li(MeCN)_n][Cu(carbazolide)₂] (0.0067 mmol), lithium carbazolide (0.2 mmol), and alkyl bromide (0.13 mmol) were added to a 4 mL borosilicate vial in the glovebox under a nitrogen atmosphere. A magnetic stir bar and 4 mL acetonitrile were added to the vial. The mixture was capped and stirred for 5 minutes and the reaction vessel was fully submerged in an isopropanol bath kept at 0 °C with a cryostat. The mixture was irradiated with a 100-watt Hg lamp while stirring for 8 hours, after which time it was diluted with a solution of dodecane in diethyl ether or ethyl acetate. An aliquot was filtered through a short pad of silica gel (ethyl acetate eluent) and the sample was injected for GC analysis. Products were isolated after removing the solvent *in vacuo* and loading the crude on silica gel and eluting with hexanes.

A.3.2 Procedure for the photolytic reaction in the absence of copper



Lithium carbazolidide (0.2 mmol) and alkyl bromide (0.13 mmol) were added to a 4 mL borosilicate vial in the glovebox under nitrogen atmosphere. A magnetic stir bar and 4 mL acetonitrile were added to the vial. The mixture was capped and stirred for 5 minutes and the reaction vessel was fully submerged in an isopropanol bath kept at 0 °C with a cryostat. The mixture was irradiated with 100-watt Hg lamp while stirring for 8 hours, after which time it was diluted with a solution of dodecane in diethyl ether or ethyl acetate. An aliquot was filtered through a short pad of silica gel (ethyl acetate eluent) and the sample was analyzed by GC. Typical calibrated GC yields of products are shown in the scheme above. 9,9'-bicarbazyl (1.2 mg, 3% yield) was quantified by preparative TLC with hexanes.

A.3.3 Procedure for standard photolytic reactions at varying reaction concentrations



Stock solutions of [Li(MeCN)_n][Cu(carbazolide)₂], lithium carbazolide, and 6-bromohept-1-ene were prepared in acetonitrile. Desired amounts of each were transferred to a 4 mL borosilicate vial, and the mixture was diluted to a total volume of 4 mL with acetonitrile. The vial was subjected to the standard photolytic conditions, and the products were analyzed by GC. Five reaction concentrations were tested: 0.011 M, 0.022 M, 0.033 M, 0.044 M, and 0.055 M in a total of 4 mL of acetonitrile using 6-bromohept-1-ene as the limiting reagent. The data are summarized in the table below. **H/I** values were calculated prior to rounding of yields of products **H** and **I**.

Table A.1: Variation of yields of H and I as a function of alkyl bromide concentration.

Alkyl bromide [mM]	Product H (dr)	Product I	H/I
11	70% (4:1)	6.7%	11
22	68% (4:1)	9.1%	7.6
33	62% (4:1)	10%	6.1
44	55% (4:1)	10%	5.5
55	51% (4:1)	10%	5.1

A.3.4 Procedure for stoichiometric coupling of [Cu^I(carb)₂]Li* with 2-bromo-4-phenylbutane (Eq 4 in Chapter 2)

(0.0067 mmol/mL) of [Li(MeCN)_n][Cu(carbazolide)₂] and 2-bromo-4-phenylbutane were prepared in acetonitrile. Then, 0.0067 mmol of each reactant was added to a 4 mL vial

containing a magnetic stir bar. The mixture was diluted to a total of 4 mL with acetonitrile. The mixture was capped and stirred for 5 minutes and the reaction vessel was fully submerged in an isopropanol bath kept at 0 °C with a cryostat. The mixture was irradiated with 100-watt Hg lamp while stirring for 8 hours, after which time it was diluted with a solution of dodecane in diethyl ether or ethyl acetate. An aliquot was filtered through a short pad of silica gel (ethyl acetate eluent) and the sample was analyzed by GC. Run 1: 95% yield. Run 2: 96% yield.

A.3.5 Procedure for the time-course analysis of reactions with and without

$[\text{Li}(\text{MeCN})_n][\text{Cu}(\text{carbazolide})_2]$

Stock solutions of $[\text{Li}(\text{MeCN})_n][\text{Cu}(\text{carbazolide})_2]$, lithium carbazolidine, and 2-bromo-4-phenylbutane were prepared in acetonitrile. Desired amounts of each were transferred to a 4 mL borosilicate vial as outlined in the general procedure, and the vial was diluted to a total of 4 mL with acetonitrile. The vial was subjected to the standard photolytic conditions for the specified amount of time, and the products were analyzed by GC.

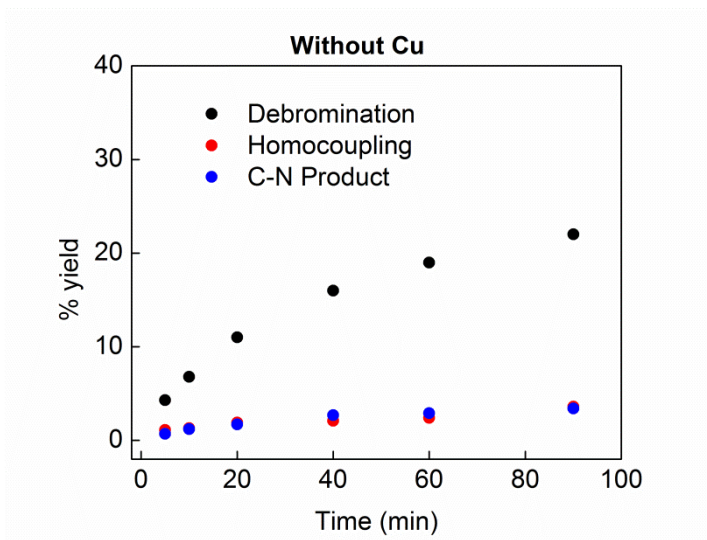


Figure A.2: Time-course analysis of the standard reaction mixture in the absence of Cu.

Table A.2: Yields of debromination, homocoupling, and C–N cross-coupled product over time in the absence of Cu.

Time (min)	Debromination (%)	Homocoupling (%)	C–N cross-coupled product (%)
5	4.3	1.1	0.7
10	6.8	1.3	1.2
20	11	1.9	1.7
40	16	2.1	2.7
60	19	2.4	2.9
90	22	3.6	3.4

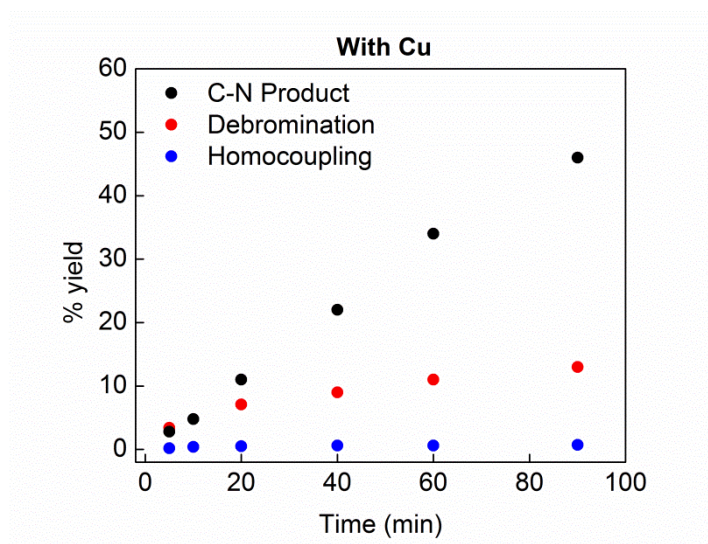


Figure A.3: Time-course analysis of the standard catalysis reaction mixture.

Table A.3: Yields of debromination, homocoupling, and C–N cross-coupled product over time under catalysis conditions.

Time (min)	Debromination (%)	Homocoupling (%)	C-N cross-coupled product (%)
5	3.4	0.2	2.8
10	4.8	0.4	4.8
20	7.1	0.5	11
40	9	0.6	22
60	11	0.6	34
90	13	0.7	46

A.4 Preparation of Metal Carbazolides

A.4.1 Preparation of $[\text{Li}(\text{MeCN})_n][\text{Cu}(\text{carbazolide})_2]$

Mesitylcopper (183 mg, 1 mmol), carbazole (167 mg, 1 mmol), and lithium carbazolidate (1 mmol) were added to a 20 mL scintillation vial in a nitrogen atmosphere glovebox. 10 mL of acetonitrile was added to the vial, and the mixture was stirred overnight at ambient temperature. The solution was filtered through a pad of Celite and the volatiles were removed *in vacuo*. Benzene (1 mL) was added to dissolve the oil and the residue was triturated with pentane (5 mL). The supernatant was decanted and benzene was added again. Benzene (1 mL) was added to the solid residue followed by pentane (5 mL) to precipitate the product. This process was repeated until a free-flowing, off-white powder was obtained. This powder was isolated atop a sintered glass frit and washed with benzene (3 x 5 mL) and pentane (3 x 5 mL). The title compound can be further dried under vacuum overnight to yield the title compound (400 mg) as an acetonitrile adduct as determined by ^1H NMR analysis. Spectroscopic data match the literature report.⁷

A.4.2 Preparation of Li(carbazolide) (13390-92-6)

Carbazole (3.6 g, 22 mmol) was suspended in 150 mL of diethyl ether in a 250 mL flask in a nitrogen-atmosphere glovebox. After cooling to $-78\text{ }^\circ\text{C}$, butyllithium (1.6 M in hexanes, 15 mL) was added dropwise. The mixture was stirred at $-78\text{ }^\circ\text{C}$ for 3 h and allowed to warm to room temperature overnight. The white solid was collected atop a sintered glass frit, washed with cold diethyl ether and pentane, and then recrystallized in cold THF. The crystals were then dissolved in minimal acetonitrile and the solution was dried *in vacuo* to afford the title compound (2.9 g, 76% yield). Spectroscopic data match those reported in the literature.⁸

A.4.3 Preparation of $[\text{K}(\text{benzo-15-crown-5})_2][\text{Cu}^{\text{II}}(\text{carbazolide})_3]$

A $-70\text{ }^\circ\text{C}$ suspension of $\text{Cu}(\text{OTf})_2$ (36 mg, 0.05 mmol) in 2 mL THF was added dropwise to a pre-chilled stirring solution of potassium carbazolidate (3 equiv, 64 mg, 0.15 mmol) in 2 mL at $-70\text{ }^\circ\text{C}$. The blue solution was allowed to stir for 5 h. The EPR spectrum of the crude mixture showed complete conversion of CuBr_2 to the $\text{Cu}^{\text{II}}(\text{carbazolide})_3^-$ anion (Figure A.4). The solution was then filtered through a PTFE syringe filter, and a THF solution of benzo-15-crown-5 (2 equiv, 26 mg, 0.1 mmol) in 1 mL THF was added at $-70\text{ }^\circ\text{C}$. The mixture was allowed to stand overnight at $-70\text{ }^\circ\text{C}$ to give a deep blue suspension containing a deep blue precipitate. The precipitate was collected while cold atop a sintered glass frit and washed with cold Et_2O to yield $[\text{K}(\text{benzo-15-crown-5})_2][\text{Cu}^{\text{II}}(\text{carbazolide})_3]$ (30 mg, 26% yield). Crystals were grown by layering Et_2O onto the solution in THF at $-70\text{ }^\circ\text{C}$. The blue solid was stored at $-30\text{ }^\circ\text{C}$.

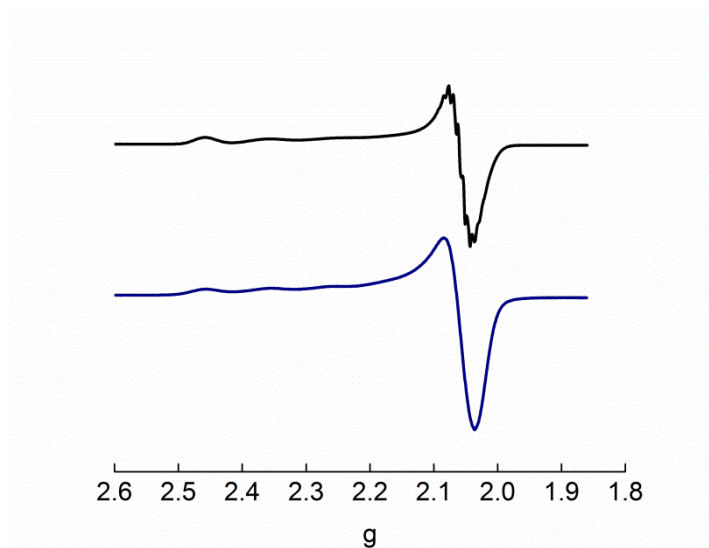


Figure A.4: X-Band EPR spectra of $[\text{K}(\text{benzo-15-crown-5})_2][\text{Cu}^{\text{II}}(\text{carbazolide})_3]$ in butyronitrile glass (black trace, 77 K) and in the solid-state (blue trace, 77 K).

A.5 Procedures for Freeze-Quench EPR Studies

A.5.1 Stoichiometric reaction between $[\text{Li}(\text{MeCN})][\text{Cu}(\text{carb})_2]$ and 2-bromo-4-phenylbutane under irradiation

$[\text{Li}(\text{MeCN})][\text{Cu}(\text{carbazolide})_2]$ (4.4 mg, 0.01 mmol) and 2-bromo-4-phenylbutane (10 mg, 0.05 mmol) were added to a 4 mL vial. The mixture was dissolved in 0.3 mL butyronitrile, and the resulting solution was transferred to an EPR tube. The EPR tube was sealed and cooled to $-78\text{ }^\circ\text{C}$. The EPR tube was irradiated in the Luzchem photoreactor (350 nm) while being introduced to a quartz Dewar filled with liquid nitrogen. Irradiation of the freezing solution proceeded for approximately 15 seconds.

A.5.2 Detection of EPR active $[\text{Li}(\text{CH}_3\text{CN})_n][\text{Cu}^{\text{II}}(\text{carb})_3]$ in a catalytic reaction mixture

A 4 mL solution of the standard reaction mixture containing $[\text{Li}(\text{MeCN})_n][\text{Cu}(\text{carbazolide})_2]$ (0.0067 mmol), lithium carbazolidide (0.2 mmol), and alkyl bromide (0.13 mmol) was prepared in a 4 mL borosilicate glass vial according to the standard procedure using butyronitrile as the solvent. A portion of the resulting solution (300 μL) was transferred to an EPR tube. The tube was sealed and cooled to $0\text{ }^\circ\text{C}$, and irradiated with a 100-watt Hg lamp at $0\text{ }^\circ\text{C}$. Alternatively, an aliquot (0.1 mL) of the standard reaction mixture in acetonitrile in a 4 mL borosilicate vial that was irradiated for 1 h was transferred to a pre-cooled EPR tube containing butyronitrile (0.2 mL) under N_2 . The EPR tube was briefly shaken and cooled to 77 K. Simulation parameters are as follows: $g = [2.318, 2.058, 2.050]$; $H_{\text{Strain}} (\text{MHz}) = [120, 5, 5]$; $A_{\text{Cu}} (\text{MHz}) = [350, 25, 21]$ $A_{3\text{N}} (\text{MHz}) = [50, 35, 35]$.

A.5.3 Generation and detection of EPR active $[\text{Li}(\text{CH}_3\text{CN})_n][\text{Cu}^{\text{II}}(\text{carb})_3]$ via metallation

A pre-chilled solution of CuBr_2 (2.2 mg, 0.01 mmol) in 1 mL acetonitrile was added dropwise to a pre-chilled slurry of lithium carbazolidide (5.3 mg, 0.03 mmol) in the glovebox. The deep blue solution was allowed to stir for 5 min before transferring an aliquot to a solution of butyronitrile in acetone/dry ice bath. The solution was then transferred to an EPR tube.

A.5.4 Detection of EPR active $[\text{Li}(\text{CH}_3\text{CN})_n][\text{Cu}^{\text{II}}(\text{carb})_3]$ via oxidation of $[\text{Li}(\text{MeCN})][\text{Cu}(\text{carb})_2]$

$[\text{Li}(\text{MeCN})][\text{Cu}(\text{carbazolidide})_2]$ (10.0 mg, 0.023 mmol) and lithium carbazolidide (8 mg, 0.046 mmol) were mixed in 200 μL of butyronitrile, added to an EPR tube, and frozen at 77 K. To this frozen layer was added a 200 μL solution of tris(4-bromophenyl)ammoniumyl hexachloroantimonate ("Magic Blue", 3.4 mg, 0.0042 mmol) in butyronitrile. The solutions were allowed to mix briefly (~5 s) in thawing butyronitrile and frozen again.

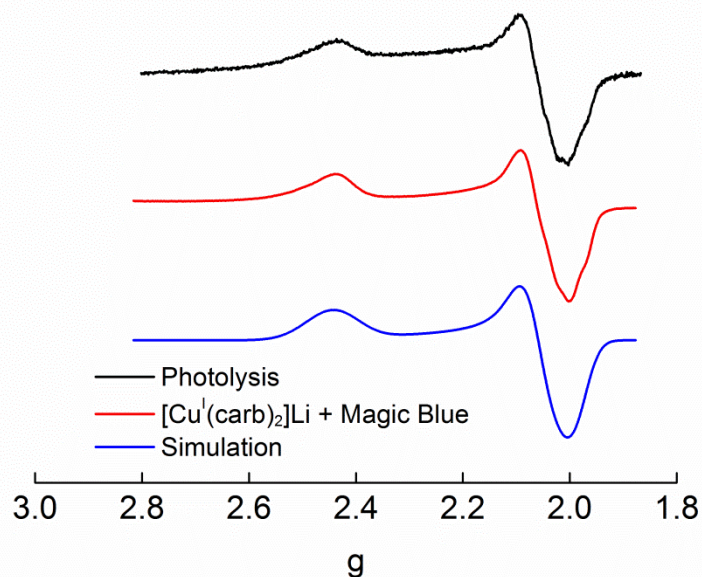


Figure A.5: EPR spectra (9.4 GHz, 77 K). Black trace: mixture of $[\text{Cu}^{\text{I}}(\text{carb})_2]\text{Li}$ and 2-bromo-4-phenylbutane (5 equiv) in freezing butyronitrile upon irradiation at 350 nm; red trace: mixture of $[\text{Cu}^{\text{I}}(\text{carb})_2]\text{Li}$ and Magic Blue (0.2 equiv) in butyronitrile at $-80\text{ }^\circ\text{C}$; blue trace: simulation of red trace. Simulation parameters: $g = [2.445, 2.060, 1.994]$; isotropic linewidth (Gaussian lineshape, FWHM = 10 mT). Coupling to one Cu nucleus was included with $A = [75, 1, 1]$.

A.6 Procedures for UV-vis studies

A.6.1 Molar absorptivity of $[\text{Li}(\text{CH}_3\text{CN})_n][\text{Cu}^{\text{II}}(\text{carb})_3]$ at 580 nm

A 20 mL vial was charged with lithium carbazolid (5.5 mg, 0.030 mmol) and a magnetic stir bar. Acetonitrile (9.0 mL) was added to the vial, and the solution was cooled to thawing acetonitrile temperature. A separate vial was charged with CuBr_2 (6.6 mg, 0.030 mmol) and acetonitrile (3.0 mL). 1 mL of the resulting green solution of CuBr_2 (0.010 mmol) was added dropwise to the thawing acetonitrile solution of lithium carbazolid. After completed addition, the deep blue solution was allowed to stir vigorously at thawing acetonitrile temperature for approximately 30 minutes. The solution was transferred into a prechilled 1 cm pathlength quartz cuvette. The cuvette was capped and quickly inserted into the $-40\text{ }^\circ\text{C}$ UV-vis sample holder. The average molar absorptivity at 580 nm was found to be $1100\text{ M}^{-1}\text{ cm}^{-1}$.

Table A.4: Measured molar absorptivity (580 nm) of $[\text{Li}(\text{CH}_3\text{CN})_n][\text{Cu}^{\text{II}}(\text{carb})_3]$ at various concentrations.

Concentration (mM)	Absorbance	Molar Absorptivity ($\text{M}^{-1}\text{ cm}^{-1}$)
0.103	1.170	1140
0.100	1.092	1092
0.083	1.028	1233
0.050	0.608	1216

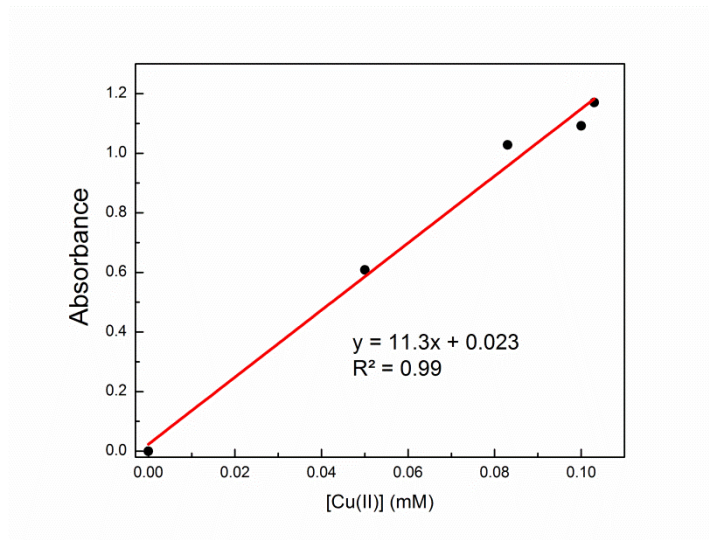


Figure A.6: Absorbance at 580 nm as a function of concentration of Cu(II); path length = 1 cm.

A.6.2 Detection of $[\text{Li}(\text{CH}_3\text{CN})_n][\text{Cu}^{\text{II}}(\text{carb})_3]$ during catalysis

A 4 mL acetonitrile solution of the standard reaction mixture containing $[\text{Li}(\text{MeCN})_n][\text{Cu}(\text{carbazolide})_2]$ (2.9 mg, 0.0067 mmol), lithium carbazolidate (34 mg, 0.19 mmol), and 2-bromo-4-phenylbutane (28 mg, 0.13 mmol) was prepared in a quartz cuvette with a stirbar. The reaction mixture was allowed to cool for 10 minutes in the dark at 0 °C in an ice bath. Then the mixture was irradiated with a 100-watt Hg lamp while stirring, and UV-vis spectra were collected at 0 °C at various times after irradiation until the Cu(II) absorption at 580 nm was maximized.

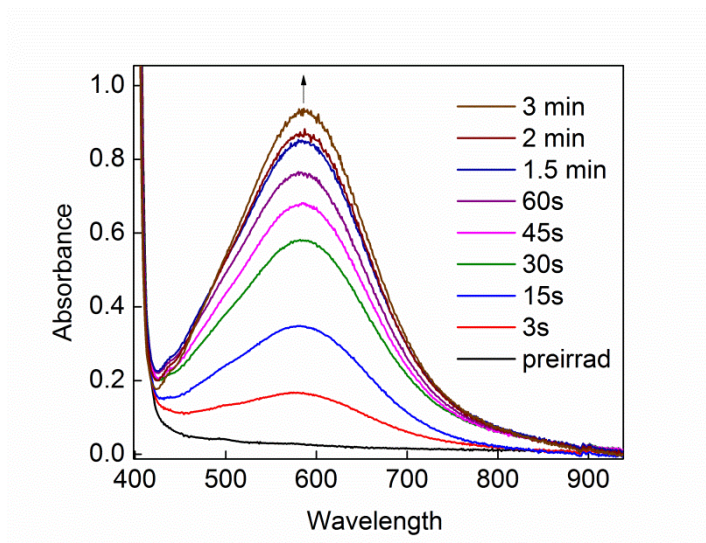


Figure A.7: Appearance of Cu(II) absorption band at short irradiation times of reaction mixture.

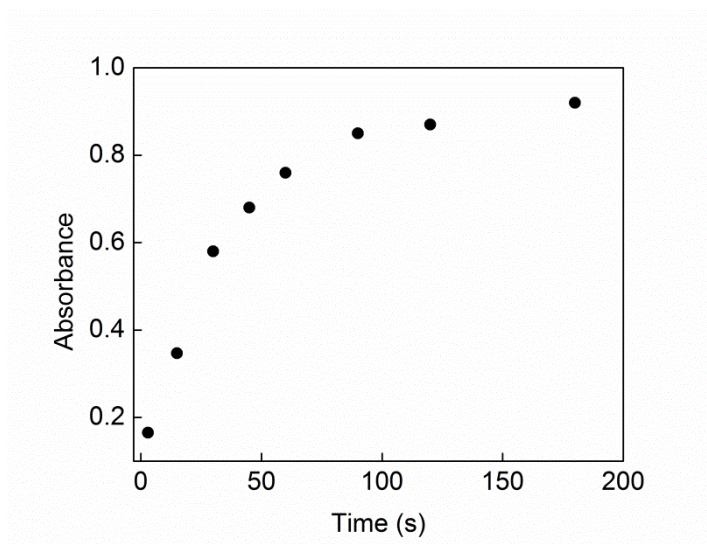


Figure A.8: Absorbance at 580 nm at short irradiation times of reaction mixture.

A.6.3 Generation and detection of $[\text{Li}(\text{CH}_3\text{CN})_n][\text{Cu}^{\text{II}}(\text{carb})_3]$ via oxidation of $[\text{Li}(\text{MeCN})][\text{Cu}(\text{carb})_2]$

In a glovebox atmosphere, a 4 mL butyronitrile solution containing $[\text{Li}(\text{MeCN})_n][\text{Cu}(\text{carbazolide})_2]$ (0.037 mmol) and lithium carbazolidide (0.074 mmol) was

prepared in a quartz cuvette with a stirbar and sealed with a septum. Another solution containing tris(4-bromophenyl)ammoniumyl hexachloroantimonate (“Magic Blue”, 0.012 mmol) was dissolved in 0.2 mL butyronitrile and taken up into a 1 mL Hamilton sample locked syringe, and the needle was pierced through a septum to prevent the introduction of air. The cuvette was cooled to -80 °C in the UV-vis sample holder, and the syringe with Magic Blue was pierced through the cuvette septum. The sample lock was opened and the solution of Magic Blue was introduced into the mixture with vigorous stirring. The stirring was stopped and the sample was allowed to stabilize before a spectrum was acquired.

A.6.4 Molar absorptivity of [Li(MeCN)][Cu(carbazolide)₂] at 365 nm

A 1.9 mM solution of [Li(MeCN)][Cu(carbazolide)₂] was made by dissolving 4.2 mg (0.0095 mmol) in 5 mL acetonitrile, and this solution was used as a stock to generate lower concentration solutions of the complex. Each solution was pipetted into a 1 mm path length cuvette and absorption spectra were acquired at room temperature for each concentration. The molar absorptivity for [Li(MeCN)][Cu(carbazolide)₂] at 365 nm was found to be 4300 M⁻¹ cm⁻¹.

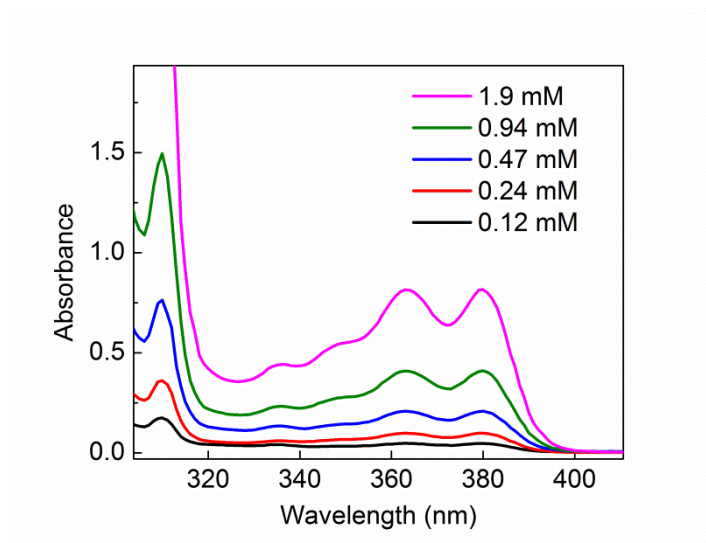


Figure A.9: UV-vis spectra of $[\text{Li}(\text{MeCN})][\text{Cu}(\text{carbazolide})_2]$ at various concentrations in CH_3CN at room temperature in 1 mm cuvette.

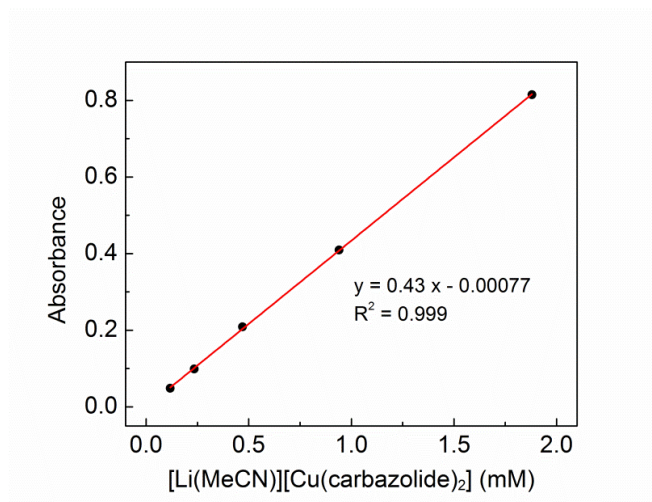


Figure A.10: Absorbance at 365 nm as a function of $[\text{Li}(\text{MeCN})][\text{Cu}(\text{carbazolide})_2]$ concentration; path length = 1 mm.

A.6.5 Molar absorptivity of lithium carbazolidate at 365 nm

A 10 mM solution of lithium carbazolidate was made, and this solution was used as a stock to generate lower concentration solutions of the complex. Each solution was pipetted

into a 1 mm path length cuvette and absorption spectra were acquired at room temperature for each concentration. The molar absorptivity at 365 nm for concentrations of lithium carbazolidate greater than 0.4 mM was found to be $2200 \text{ M}^{-1} \text{ cm}^{-1}$.

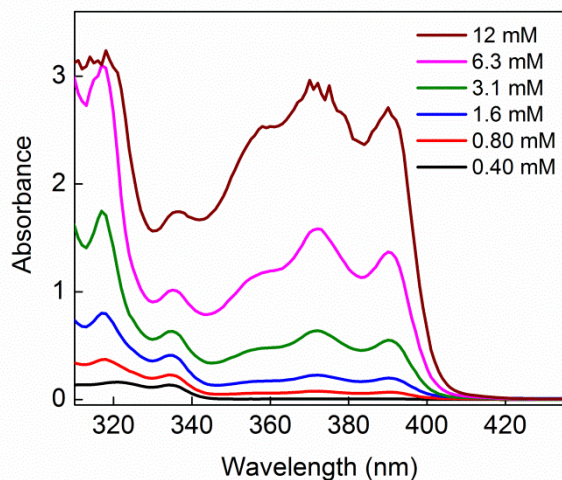


Figure A.11: UV-vis spectra of lithium carbazolidate at various concentrations in CH_3CN at room temperature in 1 mm cuvette.

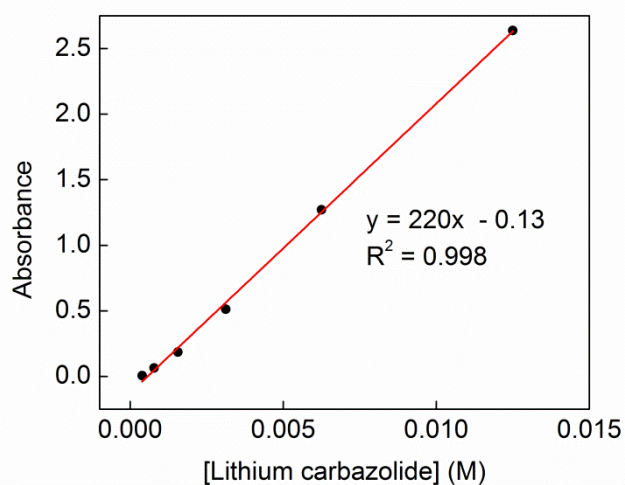


Figure A.12: Absorbance at 365 nm as a function of lithium carbazolidate concentration; path length = 1 mm.

A.7 Procedures for DOSY Analysis

Equimolar quantities of lithium carbazolidine and 1,3,5-trimethoxybenzene (as an internal standard) were dissolved in 500 μL CD_3CN at concentrations ranging from 0.8 mM to 150 mM lithium carbazolidine/1,3,5-trimethoxybenzene. A DOSY spectrum was acquired on a Varian 500 MHz spectrometer with a probe temperature of 25.0 $^\circ\text{C}$, and the diffusion constants were calculated by an exponential fit for each of the four lithium carbazolidine resonances in the ^1H NMR spectrum. Average hydrodynamic radii were calculated from each of the four diffusion constants using the Stokes-Einstein equation. The hydrodynamic radius for 1,3,5-trimethoxybenzene was similarly calculated as an average for both of its ^1H NMR resonances.

Table A.5: Measured hydrodynamic radii and volumes.

[Lithium carbazolidine] (mM)	Lithium carbazolidine R_h (\AA), average of 4	Lithium carbazolidine vol. (\AA^3)	1,3,5-trimethoxybenzene R_h (\AA)	1,3,5-trimethoxybenzene vol. (\AA^3)	MeCN R_h (\AA)	MeCN vol. (\AA^3)
0.8	3.07	121.2	3.03	116.5	1.61	17.5
2	3.10	124.8	2.96	108.6	1.58	16.5
4	3.52	157.5	3.06	118.8	1.68	19.9
8	3.66	205.4	2.95	107.5	1.62	17.8
49	4.61	410.4	3.21	138.5	1.73	21.7
98	4.77	454.6	3.26	145.1	1.79	24.0
150	4.81	466.1	3.3	150.5	1.76	22.8
carbazole (4.8 mM)	2.79	91.0	3.13	128.4	1.61	17.5

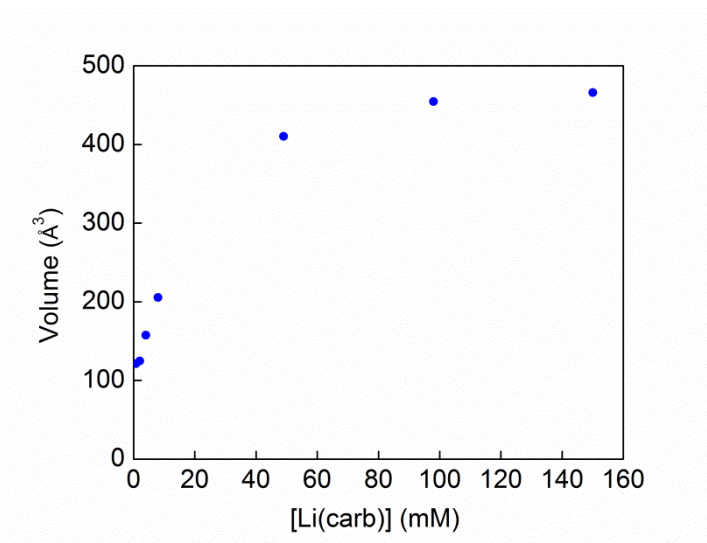


Figure A.13: The hydrodynamic volume of lithium carbazolidine increases as a function of increasing lithium carbazolidine concentration.

A.8 Actinometric Studies

A.8.1 Determination of light intensity

The Hatchard-Parker method was used to make a 0.006 M potassium ferrioxalate solution in 0.1 N H₂SO₄.⁹ A 4 mL ferrioxalate solution in a quartz cuvette was then irradiated at 0 °C for 40 s in three separate runs using a 365 nm LED (Thorlabs, M365L2) and a focusing lens.

Sample photon flux calculation for 40 s photolysis:

$$I = \frac{AV_2V_3}{\epsilon d\Phi_\lambda tV_1}$$

where I is the intensity in einsteins/min, A is the absorbance (at 510 nm) of irradiated actinometer solution, V_2 is the volume (in L) of actinometer irradiated, V_3 is the volume (10 mL) of the volumetric flask used for the dilution of the irradiated aliquot, ϵ is the extinction coefficient of the ferrous 1,10-phenanthroline complex at 510 nm (1.11×10^4 L mol⁻¹ cm⁻¹), d is the path length (in cm) of the cuvette used to measure the absorbance, Φ_λ is the quantum yield of ferrous production at 365 nm (1.21), t is the time of irradiation (in min), and V_1 is the volume (in mL) of irradiated actinometer solution withdrawn.

$$I = \frac{(0.19)(0.004 \text{ L})(10 \text{ mL})}{(1.11 \times 10^4 \text{ M}^{-1}\text{cm}^{-1})(1 \text{ cm})(1.21) \left(\frac{40\text{s}}{60\text{s}/\text{min}}\right) (0.5 \text{ mL})}$$

$$I = 1.7 \times 10^{-6} \text{ Einsteins/minute}$$

A photon flux of $1.7(5) \times 10^{-6}$ Einsteins/minute was calculated by averaging all runs.

A.8.2 Determination of quantum yield for stoichiometric model reaction

A 4 mL acetonitrile solution of the standard reaction mixture containing [Li(MeCN)][Cu(carbazolide)₂] (0.0067 mmol), lithium carbazolide (0.2 mmol), and alkyl

bromide (0.13 mmol) was prepared in a 1 cm path length quartz cuvette with a stirbar. The reaction mixture was allowed to cool to 0 °C with an internal cooling loop in a cuvette holder. Then, the mixture was irradiated with the 365 nm LED while stirring. After irradiation, the reaction mixture was diluted with diethyl ether and dodecane as an internal standard. An aliquot was filtered through a short pad of silica gel (ethyl acetate eluent) and the sample was injected for GC analysis. The quantum yield (Φ) was then determined by the following equation:

$$\Phi = \frac{\text{moles of electrophile consumed}}{\text{Light intensity} * \text{time irradiated (min)}}$$

The quantum yield was determined to be 0.099.

A.9 Stern-Volmer Quenching and Determining Quenching Efficiency

A.9.1 Quenching of [Li(MeCN)][Cu(carbazolide)₂] with electrophile

[Li(MeCN)][Cu(carbazolide)₂] was diluted in acetonitrile to make a 0.00335 M solution. (3-bromobutyl)benzene was also diluted in acetonitrile to make 100, 200, 400, 600, 700, and 800 mM solutions. In 4 mL vials, a 250 μ L aliquot of the solution containing [Li(MeCN)][Cu(carbazolide)₂] was mixed with a 250 μ L aliquot of either acetonitrile or one of the solutions containing electrophile, such that the concentration of the copper catalyst in each solution was equal to the standard reaction concentration, 0.0017 M. The solutions were pipetted into cuvettes with a path length of 1 mm. The lifetime of a non-emissive excited state of [Li(MeCN)][Cu(carbazolide)₂] as a function of electrophile concentration was measured by transient absorbance spectroscopy ($\lambda_{\text{pump}} = 355$ nm, $\lambda_{\text{probe}} = 580$ nm) (Figure A.13). The lifetime of the short-lived, emissive excited state of [Li(MeCN)][Cu(carbazolide)₂] was measured at the picosecond time scale using luminescence spectroscopy, and was found to be 590 ps (Figure A.14). Data were analyzed using Matlab R2014A with the default curve fitting function. The rate of electron transfer was calculated to be $4.8 \times 10^6 \text{ M}^{-1} \text{ cm}^{-1}$.

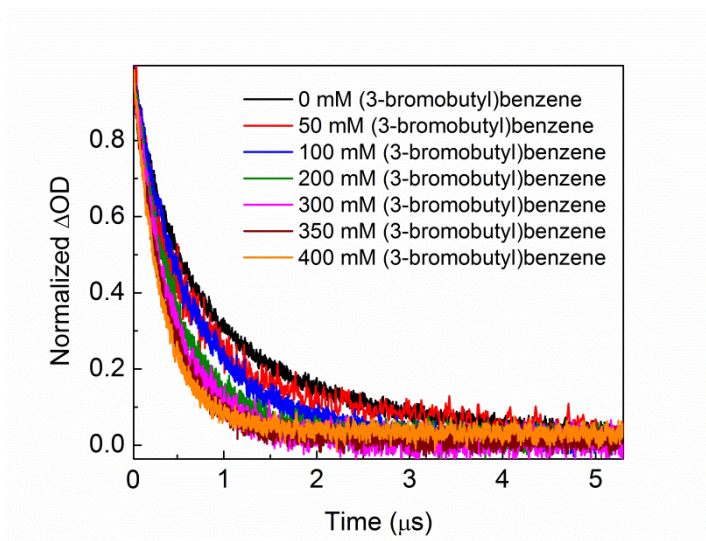


Figure A.14: Transient absorbance decays for $[\text{Li}(\text{MeCN})][\text{Cu}(\text{carbazolide})_2]$ with varying electrophile concentrations.

Table A.6: Excited state lifetime of $[\text{Li}(\text{MeCN})][\text{Cu}(\text{carbazolide})_2]$ as a function of electrophile concentration.

[(3-bromobutyl)benzene] (mM)	Lifetime (ns)
0	910
50	760
100	660
200	481
300	410
350	370
400	320

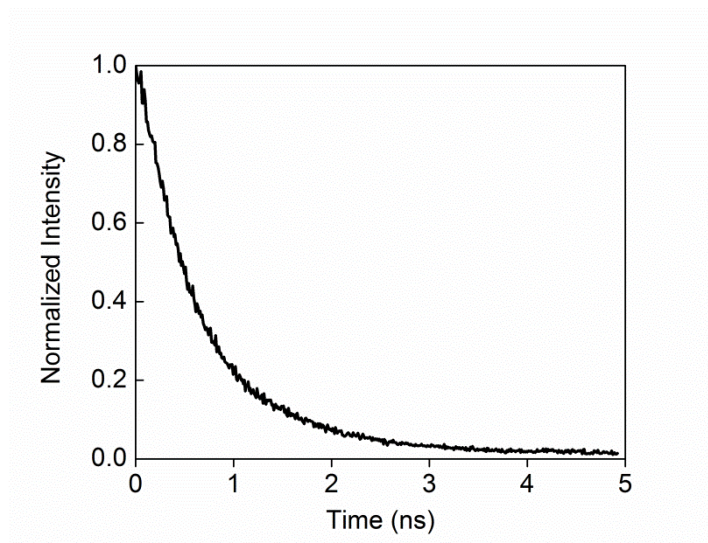


Figure A.15: Luminescence decay of the emissive excited state of [Li(MeCN)][Cu(carbazolide)₂].

A.9.2 Quenching of lithium carbazolidine with electrophile

Lithium carbazolidine (86.6 mg, 0.5 mmol) was diluted in a 10 mL volumetric flask with acetonitrile to make 10 mL of a 0.05 M solution (the concentration in the catalytic reactions). In four other volumetric flasks, the same amount of lithium carbazolidine was weighed out, but only ~5 mL of acetonitrile was added. Then, (3-bromobutyl)benzene was added to the lithium carbazolidine solutions *via* syringe to make 50, 100, 200, or 400 mM solutions of electrophile in 10 mL acetonitrile, and acetonitrile was added to the mark. For each run, one of these solutions was syringed into the Harrick flow cell described above (100 μm path length) until there were no gas bubbles, and flowed through with a syringe pump while fluorescence measurements were being collected. After each run, the flow cell was cleaned and dried under vacuum, and the next solution was syringed into the cell. The rate of electron transfer was calculated to be $4.9 \times 10^8 \text{ M}^{-1} \text{ s}^{-1}$.

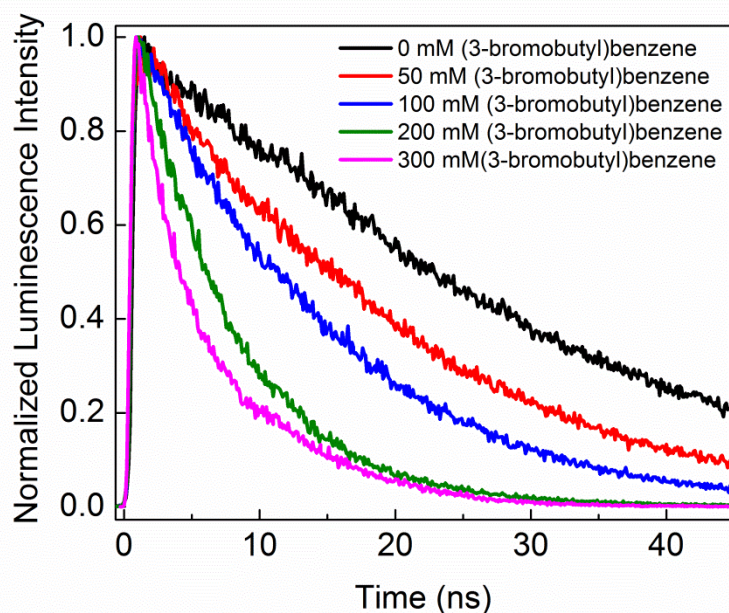


Figure A.16: Luminescence decays for lithium carbazolidate with varying electrophile concentrations.

Table A.7: Excited state lifetime of lithium carbazolidate as a function of electrophile concentration.

[(3-bromobutyl)benzene] (mM)	Lifetime (ns)
0	31
50	19.4
100	14
200	7.1
300	5.8

A.9.3 Self-quenching of [Li(MeCN)][Cu(carbazolidate)₂]

[Li(MeCN)][Cu(carbazolidate)₂] (4.2 mg, 0.0094 mmol) was diluted in 5 mL acetonitrile to make a 1.9 mM stock solution. This solution was serially diluted to make 0.94, 0.47, and 0.12 mM solutions. The solutions were pipetted into cuvettes with a path length of 1 mm.

The excited state lifetime of $[\text{Li}(\text{MeCN})][\text{Cu}(\text{carbazolide})_2]$ as a function of electrophile concentration was measured by transient absorbance spectroscopy ($\lambda_{\text{pump}} = 355 \text{ nm}$, $\lambda_{\text{probe}} = 580 \text{ nm}$). Logarithmically compressed data were analyzed using Matlab R2014A with the default curve fitting function. The rate of self-quenching was found to be $2.9 \times 10^8 \text{ M}^{-1} \text{ s}^{-1}$.

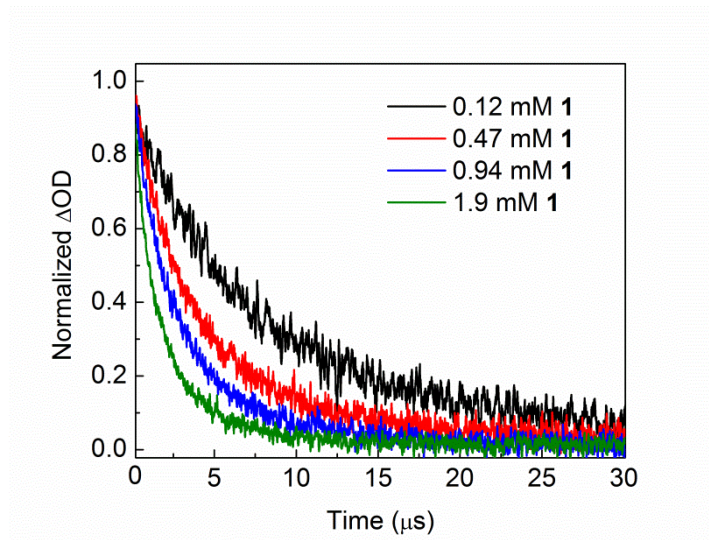


Figure A.17: Transient absorbance decays for $[\text{Li}(\text{MeCN})][\text{Cu}(\text{carbazolide})_2]$ at varying concentrations.

Table A.8: Excited state lifetime of $[\text{Li}(\text{MeCN})][\text{Cu}(\text{carbazolide})_2]$ as a function of concentration.

$[[\text{Li}(\text{MeCN})][\text{Cu}(\text{carbazolide})_2]$ (mM)	Lifetime (μs)
0.12	7.5
0.47	3.6
0.94	2.6
1.9	1.51

A.9.4 Self-quenching of lithium carbazolidide

Lithium carbazolidide (43.3 mg, 0.25 mmol) was diluted in 5 mL of acetonitrile to make a 0.05 M solution (the concentration in the catalytic reactions). This solution was serially diluted to make 4.3, 2.2, 1.1, and 0.50 mM solutions. The solutions were pipetted into cuvettes with a path length of 1 mm. The excited state lifetime of lithium carbazolidide as a function of electrophile concentration was measured by transient absorbance spectroscopy ($\lambda_{\text{pump}} = 355 \text{ nm}$, $\lambda_{\text{probe}} = 580 \text{ nm}$). Data were analyzed using Matlab R2014A with the default curve fitting function. The rate of self-quenching was found to be $2.0 \times 10^7 \text{ M}^{-1} \text{ s}^{-1}$. It is important to note that in the presence of electrophile quencher, this long-lived, non-emissive excited state was not observed, and S.E.T. seemed to proceed from the fluorescent state at a rate faster than that of intersystem crossing.

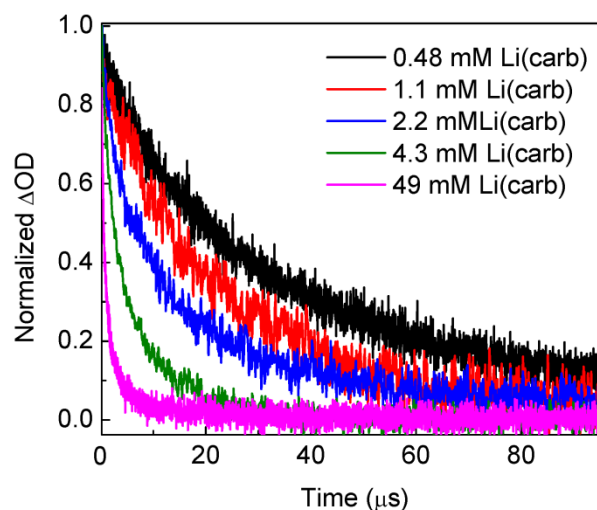


Figure A.18: Transient absorbance decays for lithium carbazolidide at varying concentrations.

Table A.9: Excited state lifetime of Li(carb) as a function of concentration

[Li(carb)] (mM)	Lifetime (μs)
0.5	33
1.1	22
2.2	14
4.3	5.8
49	1.0

A.9.5 Quenching efficiency of lithium carbazolid

The quenching fraction (Q) can be defined as the ratio of the rate at which the excited state photocatalyst (lithium carbazolid) is quenched productively (by electrophile) to the sum of the rates of all the other relaxation processes which are available to the excited state. In the case of lithium carbazolid, in addition to being quenched, the excited state can luminesce and also self-quench (after intersystem crossing to a lower-energy state; there is no evidence of self-quenching from the shorter-lived, emissive state). However, since the rate of self-quenching is only measured in the absence of electrophile, it is unclear what role self-quenching plays in the presence of electrophile. Thus, we can only estimate an upper limit for the quenching fraction.

$$Q \leq \frac{k_q * [\text{electrophile}]}{\frac{1}{\tau_{0, Li}} + k_q * [\text{electrophile}]}$$

$$\leq \frac{(4.9 \times 10^8 \text{ M}^{-1}\text{s}^{-1})(0.0325 \text{ M})}{\frac{1}{3.1 \times 10^{-8} \text{ s}} + (4.9 \times 10^8 \text{ M}^{-1}\text{s}^{-1})(0.0325 \text{ M})} \leq \mathbf{0.33}$$

This value for the quenching fraction implies that 33% of all lithium carbazolid excited states generated are quenched by electrophile. The remainder may be self-quenched or quenched by other species in solution.

The chain length is the ratio of the quantum yield to the quenching fraction, and a lower limit can be calculated:

$$\text{Chain length} \geq \frac{\Phi}{Q} \geq \frac{0.099}{0.33} \geq 0.30$$

This low value for chain length may be due to unproductive back electron transfer. In principle, the true chain length could be higher than 0.30 if, for example, Q is less than 0.33 due to self-quenching effects that we are unable to measure. Auto-quenching was observed for the excited state of $[\text{Cu}^{\text{II}}(\text{carb})_3]\text{Li}$ with a rate constant of $5 \times 10^7 \text{ M}^{-1} \text{ s}^{-1}$ from the long-lived, non-emissive state. However, this state is not accessible in the presence of electrophile, possibly because the rate of quenching is greater than the rate of intersystem crossing. Thus, the auto-quenching rate does not apply to a solution in which the electrophile is present. On the basis of our flash-quench analysis, we have calculated the upper limit for the quenching fraction to be 0.33.

A.10 Reactivity of $[\text{Li}(\text{CH}_3\text{CN})_n][\text{Cu}^{\text{II}}(\text{carb})_3]$

A.10.1 Decomposition of $[\text{Li}(\text{CH}_3\text{CN})_n][\text{Cu}^{\text{II}}(\text{carb})_3]$

A freshly prepared acetonitrile solution of $[\text{Li}(\text{CH}_3\text{CN})_n][\text{Cu}^{\text{II}}(\text{carb})_3]$ in dry-ice/acetone bath was allowed to warm to room temperature overnight. The mixture was then concentrated in vacuo and the residue was loaded on a 20 cm x 20 cm Merck TLC plate. Two of many UV-active bands after developing the TLC in hexanes were identified as the commercially available 9,9-bicarbazyl and 3,3'-bicarbazole.

A.10.2 Decomposition of $[\text{Li}(\text{CH}_3\text{CN})_n][\text{Cu}^{\text{II}}(\text{carb})_3]$ in the presence of TEMPO-H

A freshly prepared solution of $[\text{Li}(\text{CH}_3\text{CN})_n][\text{Cu}^{\text{II}}(\text{carb})_3]$ was prepared in thawing MeCN. A cold solution of 2,2,6,6-tetramethylpiperidin-1-ol¹⁰ (TEMPO-H, 1 equiv) in MeCN was added to the cold solution of $[\text{Li}(\text{CH}_3\text{CN})_n][\text{Cu}^{\text{II}}(\text{carb})_3]$, and the mixture was allowed to stir in thawing MeCN temperature for 30 min. A portion of the reaction mixture was transferred to an EPR tube and diluted with butyronitrile for X-band EPR measurement at 77 K. The only EPR active signal was that of 2,2,6,6-Tetramethylpiperidine 1-oxyl, and signals corresponding to a Cu^{II} species were absent. The analogous reaction conducted in CD_3CN at $-45\text{ }^\circ\text{C}$ shows the appearance of $[\text{Cu}^{\text{I}}(\text{carb})_2]^-$ signal by ^1H NMR spectroscopy, consistent with the delivery of an H atom.

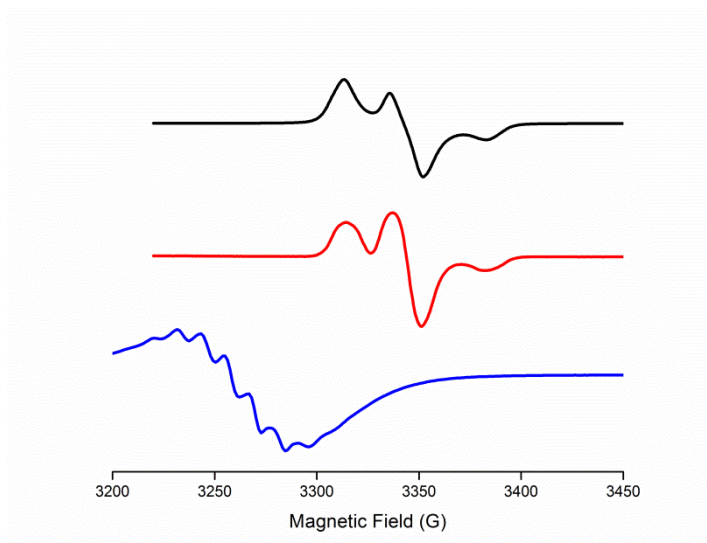


Figure A.19: EPR spectra (9.4 GHz, 77 K, butyronitrile) of freshly made $\text{Li}[\text{Cu}^{\text{II}}(\text{carb})_3]$ (blue trace), reaction of $\text{Li}[\text{Cu}^{\text{II}}(\text{carb})_3]$ with TEMPO–H (red trace), and TEMPO (black).

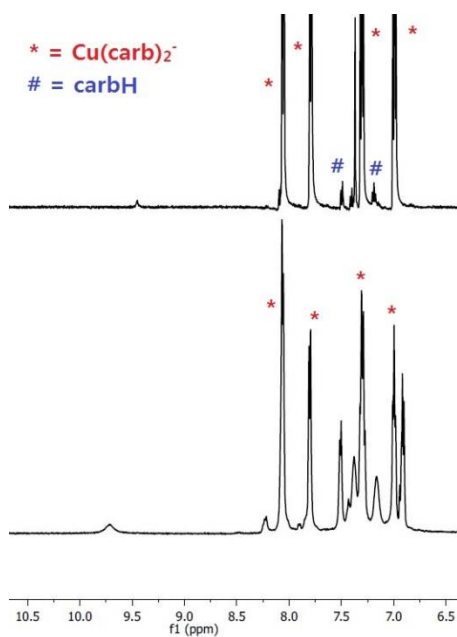


Figure A.20: ^1H NMR spectra (500 MHz, $-40\text{ }^\circ\text{C}$, CD_3CN) of a mixture of carbH and $[\text{Li}(\text{CH}_3\text{CN})][\text{Cu}^{\text{I}}(\text{carb})_2]$ (top) and of a mixture of $[\text{Li}(\text{CH}_3\text{CN})_n][\text{Cu}^{\text{II}}(\text{carb})_3]$ and TEMPOH (bottom).

A.11 Computational Methods

General considerations. The Orca 3.0.1 program was used for all calculations.¹¹ All optimizations and energy calculations were conducted with tight convergence criteria using the M06-l functional¹² and def2-TZVP basis set.¹³ Open- and closed-shell species were modeled within the unrestricted and restricted Kohn-Sham formalisms, respectively. All geometry optimizations were conducted without symmetry constraints using gradient methods. Ground state geometries were verified as true minima by the absence of imaginary frequencies. All energies reported are Gibbs free energies at 298.15 K and include translational, rotational, vibrational, and solvation energy contributions. Solvation was treated with the conductor-like screening model, using default parameters for acetonitrile in all cases.¹⁴ For $[\text{Cu}^{\text{II}}(\text{carb})_3]^-$, the Loewdin spin density shown in Figure 2.11 was derived from a constrained optimization where the N-Cu-N angles and the C(1)-C(9a)-N-Cu dihedrals along each carbazole were constrained to match that of the experimentally determined solid-state crystal structure. The energy was derived from an unconstrained optimization. Time-dependent DFT calculations were performed using the M06l functional within the Tamm–Dancoff approximation employing the def2-TZVP basis set. The 50 lowest-lying excited states were calculated, based on the same constrained optimized geometry used for the spin density calculation. Solvation was treated with the conductor-like screening model, using values of $\epsilon = 20$ and $\eta = 1.38$ for butyronitrile.

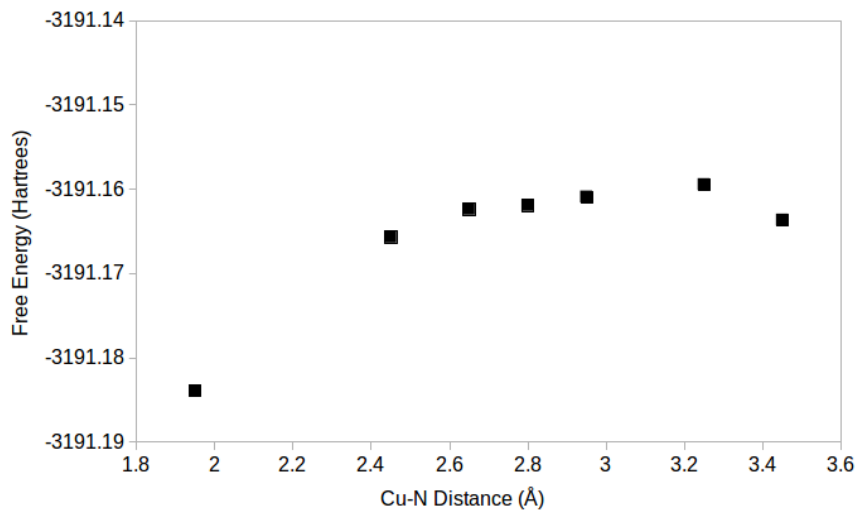


Figure A.21: Relaxed surface scan for the reaction between $[\text{Cu}^{\text{I}}(\text{carb})_2]^-$ and carb radical. Due to the shallow nature of the potential energy surface, a precise transition state could not be located.

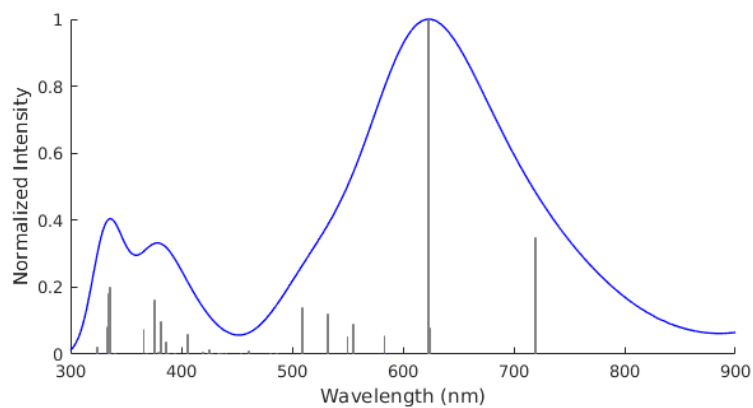


Figure A.22: Absorbance spectrum of $[\text{Cu}^{\text{II}}(\text{carb})_3]^-$ calculated by TD-DFT.

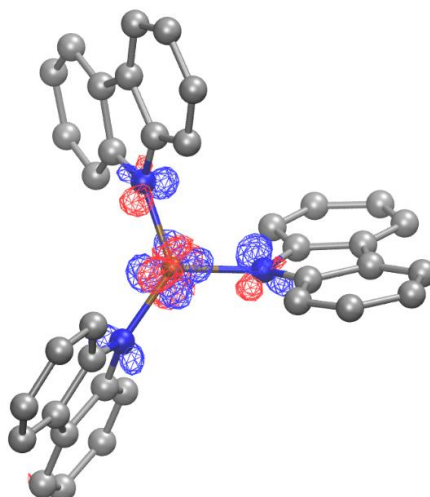


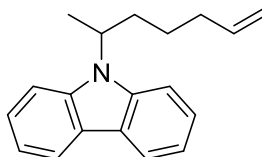
Figure A.23: Difference density plot for the most intense calculated absorption band of $[\text{Cu}^{\text{II}}(\text{carb})_3]^-$ at 623 nm. The donor orbital is shown in red, and the acceptor orbital is shown in blue.

Table A.10: Free Energies of computed molecules

Compound	Gibbs Free Energy (Hartrees)
$[\text{Cu}^{\text{I}}(\text{carb})_2]^-$	-2674.3593
$\text{Cu}^{\text{II}}(\text{carb})_2$	-2674.2012
$[\text{Cu}^{\text{II}}(\text{carb})_3]^-$	-3191.1839
$[\text{Cu}^{\text{II}}(\text{carb})_2(^1\text{Pr})]^-$	-2792.7926
$[\text{carb}]^-$	-516.9644
$(\text{carb})\cdot$	-516.8096
$(^1\text{Pr})\cdot$	-118.4381

A.12 Characterization data for new coupling products

9-(hept-6-en-2-yl)-9H-carbazole:



Following the general coupling procedure for 6-bromohept-1-ene, the title compound can be obtained after column chromatography (hexanes \rightarrow 1% ethyl acetate/hexanes) as a colorless oil. A typical run produces 10% of the coupling product according to calibrated GC analysis.

^1H NMR (300 MHz, Chloroform-*d*): δ 8.11 (d, $J = 7.7$ Hz, 2H), 7.65–7.34 (m, 4H), 7.20 (d, $J = 7.6$ Hz, 2H), 5.86–5.56 (m, 1H), 5.02–4.85 (m, 2H), 4.83–4.71 (m, 1H), 2.38–2.25 (m, 1H), 2.03–1.92 (m, 3H), 1.68 (d, $J = 7.0$ Hz, 3H), 1.49–1.29 (m, 1H), 1.25–1.13 (m, 1H).

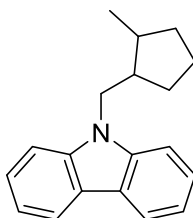
^{13}C NMR (101 MHz, Benzene-*d*₆): δ 139.87, 138.14, 125.38, 123.55, 120.48, 118.76, 114.51, 110.00, 50.88, 34.00, 33.29, 25.97, 18.83.

MS (EI) m/z (M^+) calc for $\text{C}_{19}\text{H}_{21}\text{N}$: 263, found: 263.

FT-IR (film): 2931, 1640, 1625, 1594, 1482, 1451, 1331, 1316, 1223, 1157, 746, 721 cm^{-1}

1

9-((2-methylcyclopentyl)methyl)-9H-carbazole:



Following the general coupling procedure for 6-bromohept-1-ene, the title compound can be obtained as the mixture of diastereomers after column chromatography (hexanes \rightarrow 1% ethyl acetate/hexanes) as a colorless solid. A typical run produces 60% of the coupling product according to calibrated GC analysis. NMR resonances of the major diastereomer are as follows.

^1H NMR (400 MHz, Chloroform-*d*): δ 8.13 (d, $J = 7.7$ Hz, 2H), 7.54–7.38 (m, 4H), 7.27–7.21 (m, 2H), 4.40 (dd, $J = 14.6, 4.6$ Hz, 1H), 4.20 (dd, $J = 14.6, 10.9$ Hz, 1H), 2.74–2.45 (m, 1H), 2.28–2.22 (m, 1H), 1.96–1.72 (m, 2H), 1.53–1.38 (m, 4H), 1.15 (d, $J = 7.1$ Hz, 3H).

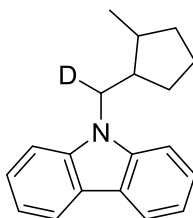
^{13}C NMR (126 MHz, Chloroform-*d*): δ 140.64, 125.48, 122.85, 120.31, 118.64, 108.88, 43.91, 42.94, 36.06, 33.19, 28.85, 22.53, 15.48.

FT-IR (film): 2954, 2870, 1597, 1484, 1461, 1452, 1326, 1218, 1153, 748, 722 cm^{-1}

MS (EI) m/z (M^+) calc for $\text{C}_{19}\text{H}_{21}\text{N}$: 263, found: 263.

^1H NMR resonances were assigned for major and minor diastereomers based on COSY data. Stereochemistry of the major diastereomer was assigned based on NOESY analysis.

9-((2-methylcyclopentyl)methyl-*d*)-9H-carbazole:



Following general coupling procedure with (E)-6-bromohept-1-ene-1-*d*, the title compound can be obtained as the mixture of diastereomers after column chromatography (hexanes \rightarrow 1% ethyl acetate/hexanes) as colorless solid. A typical run produces 60% of

the coupling product according to calibrated GC analysis. NMR resonances of the major diastereomer are as follows.

^1H NMR (400 MHz, Benzene- d_6): δ 8.10-8.06 (m, 2H), 7.41-7.45 (m, 2H), 7.28-7.23 (m, 4H), 3.92-3.86 (m, 0.5H) 3.77-3.67 (m, 0.5H) 2.29-2.21 (m, 1H) 1.88-1.78 (m, 1H) 1.58-1.49 (m, 2H) 1.28-1.11 (m, 4H) 0.81 (d, $J = 7.1$ Hz, 3H)

^{13}C NMR (126 MHz, Benzene- d_6): δ 141.11, 125.83, 123.57, 120.82, 119.19, 109.27, 43.56 (t, $J = 20.4$ Hz), 42.99, 36.18, 33.31, 28.94, 22.74, 15.38.

^2H NMR (61 MHz, Benzene): δ 3.86, 3.70.

MS (EI) m/z (M^+) calc for $\text{C}_{19}\text{H}_{20}\text{DN}$: 264, found: 264.

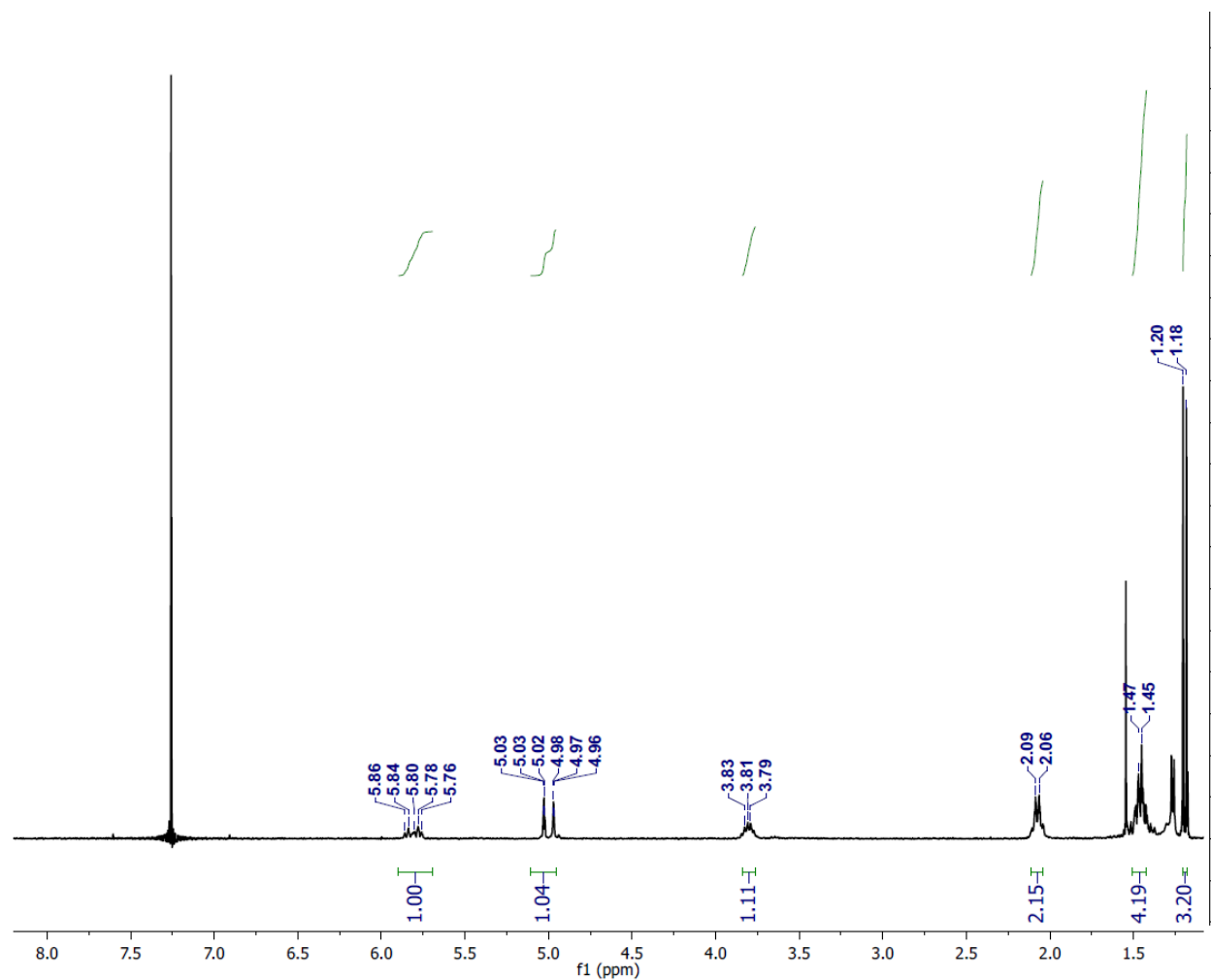
A.13 ^1H , ^2H , and ^{13}C NMR spectra of new compounds

Figure A.24: ^1H NMR spectrum of (E)-6-bromohept-1-ene-1-d (CDCl_3 , 300 MHz, rt).

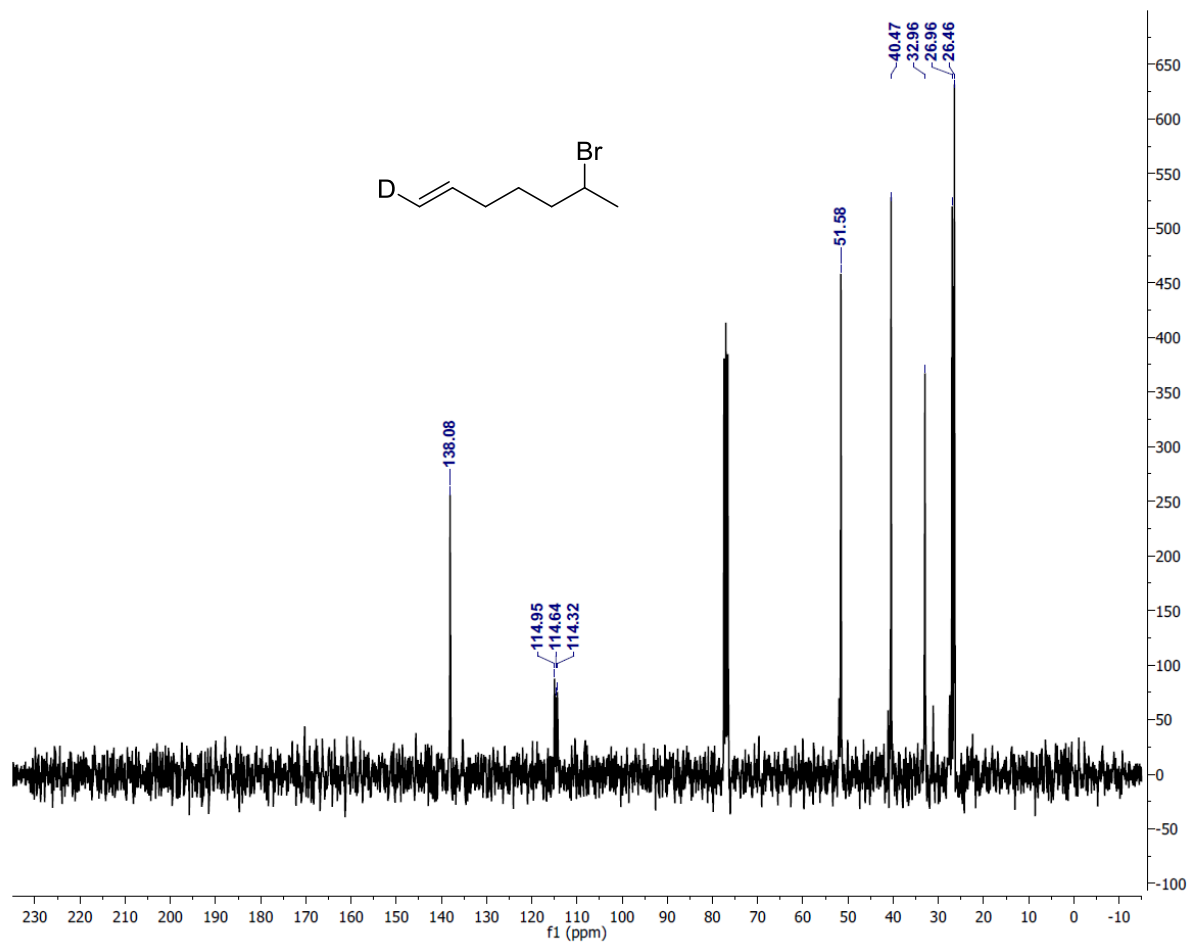


Figure A.25: $^{13}\text{C}\{^1\text{H}\}$ NMR spectrum of (E)-6-bromohept-1-ene-1-d (CDCl_3 , 75 MHz, rt).

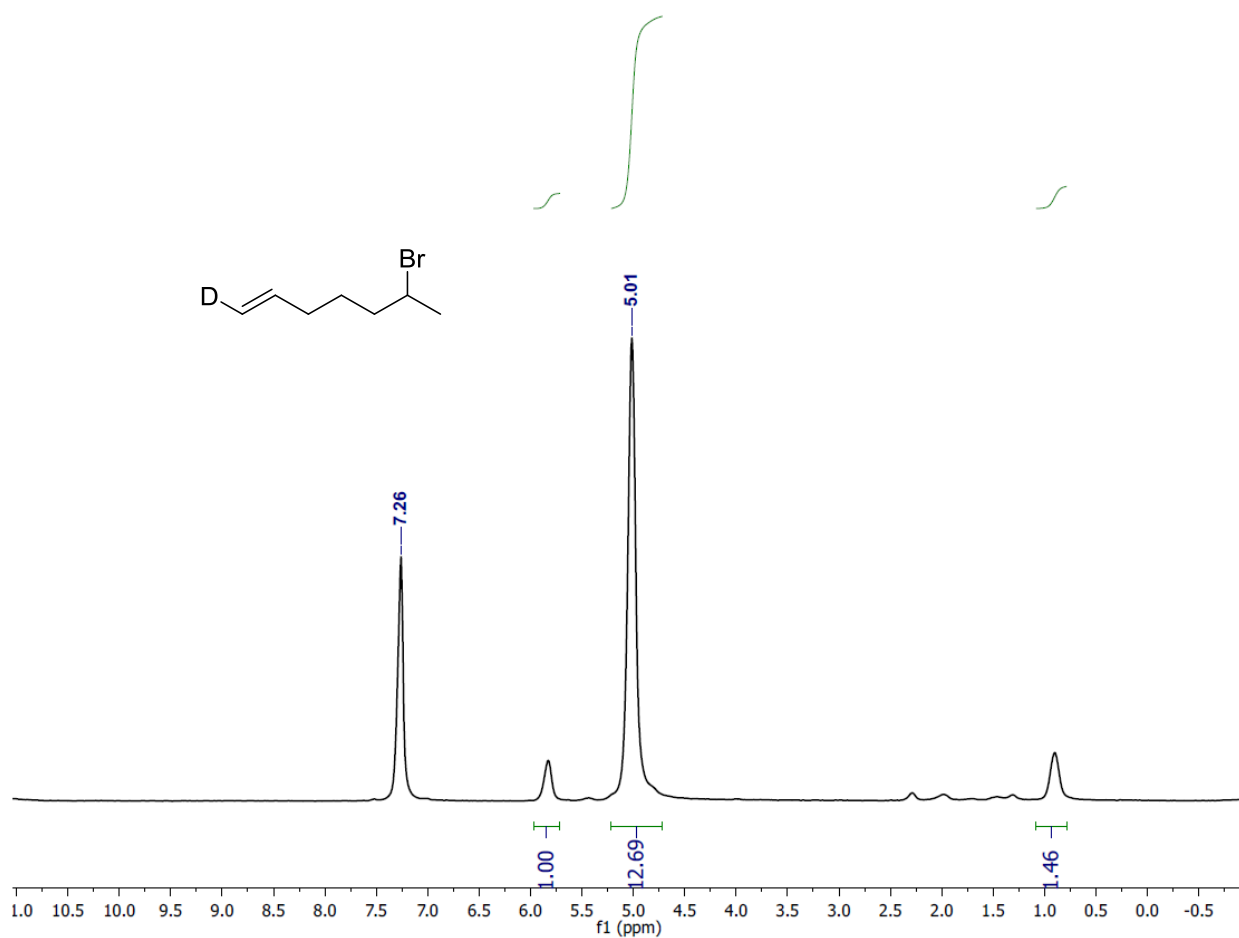


Figure A.26: ^2H NMR spectrum of (E)-6-bromohept-1-ene-1-d (CHCl_3 , 61 MHz, rt).

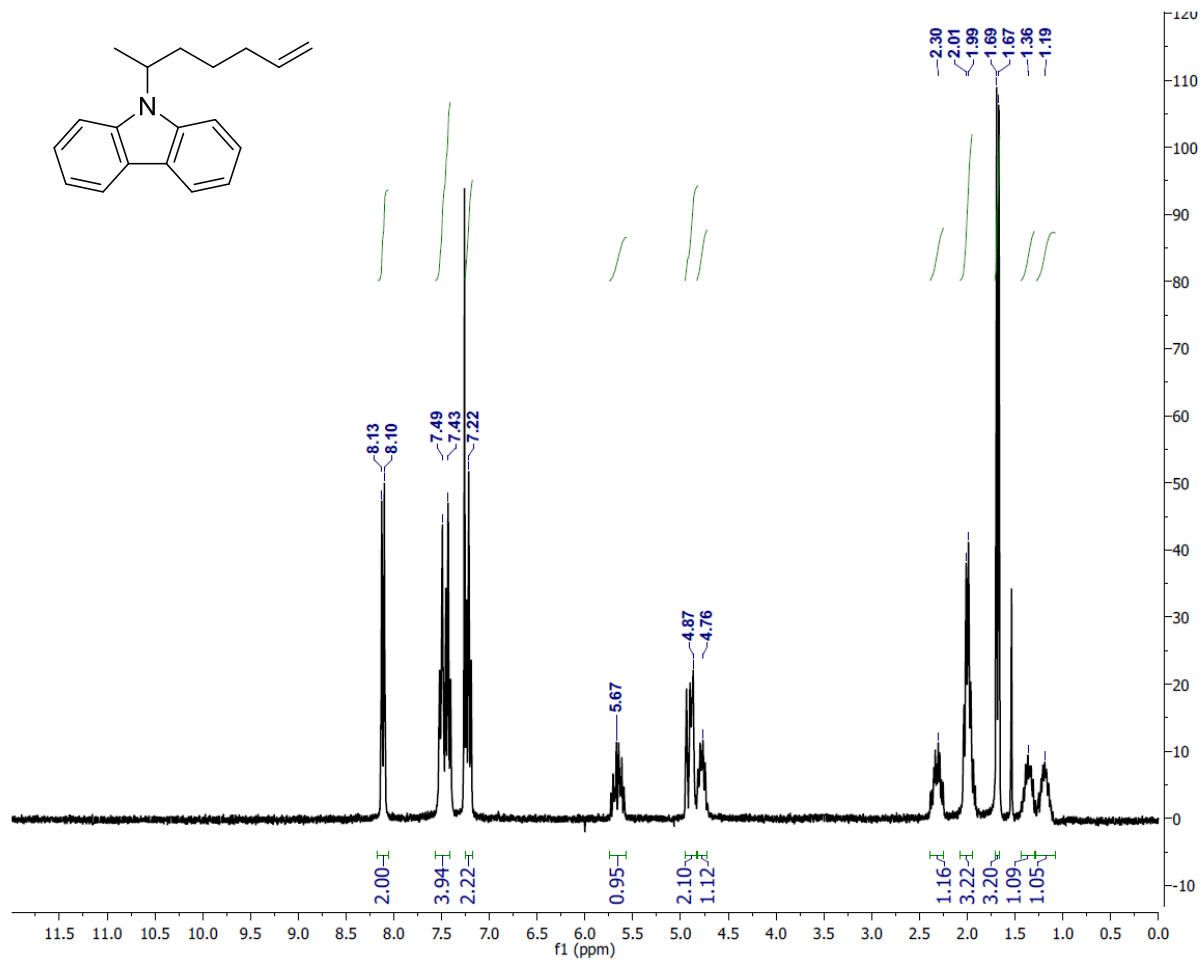


Figure A.27: ^1H NMR spectrum of 9-(hept-6-en-2-yl)-9H-carbazole (CDCl_3 , 300 MHz, rt).

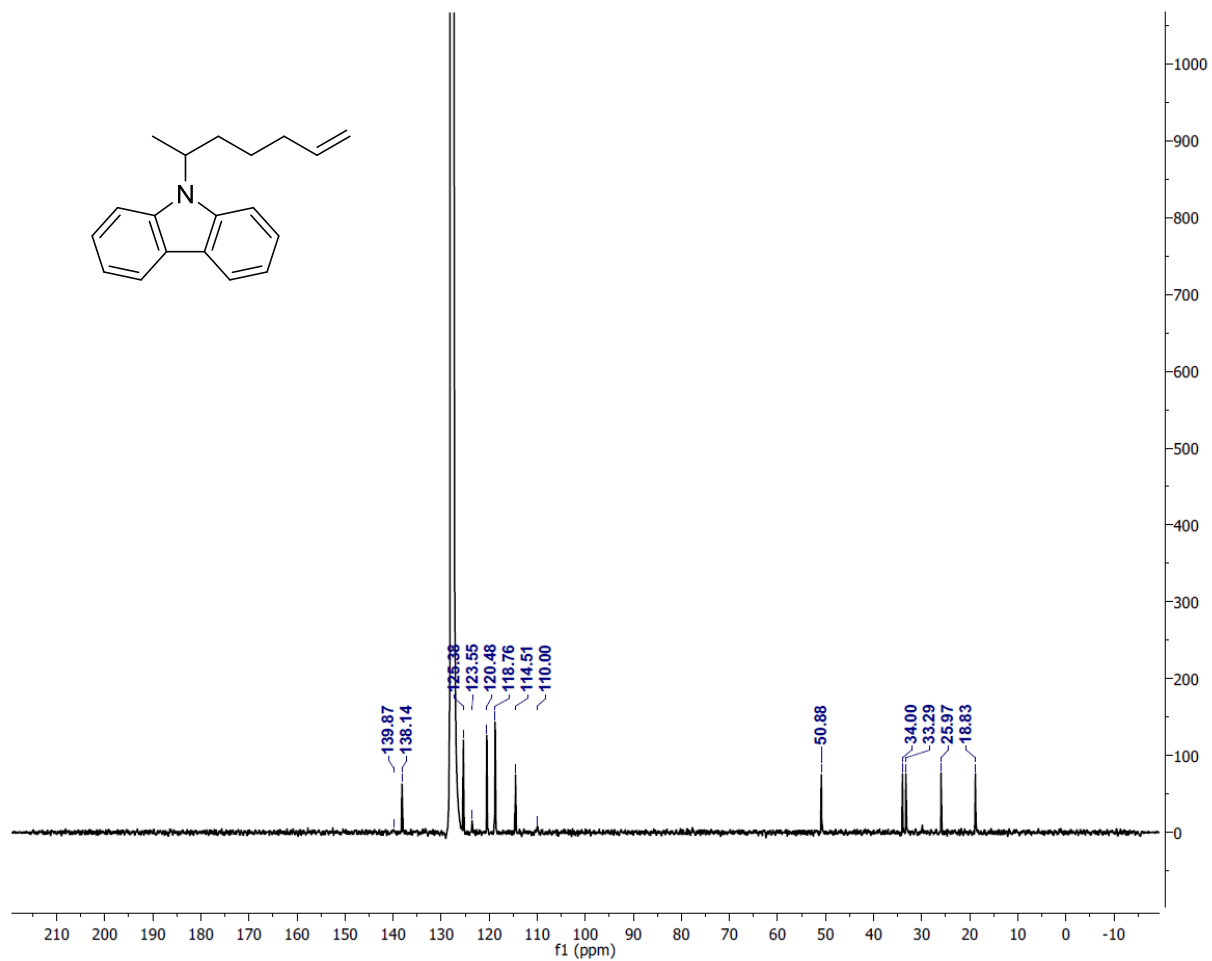


Figure A.28: $^{13}\text{C}\{^1\text{H}\}$ NMR spectrum of 9-((2-methylcyclopentyl)methyl-d)-9H-carbazole (C_6D_6 , 126 MHz, rt).

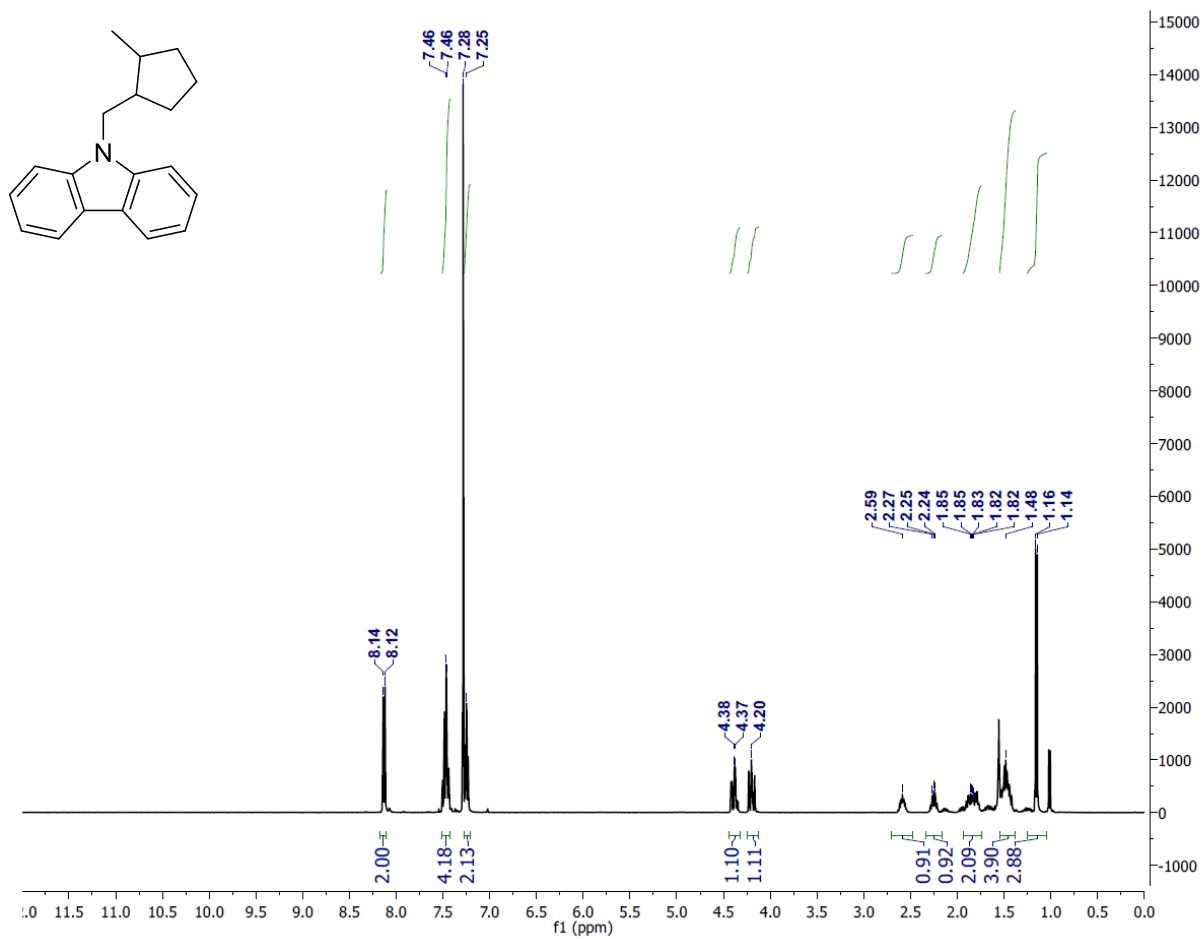


Figure A.29: ¹H NMR spectrum of 9-((2-methylcyclopentyl)methyl)-9H-carbazole (CDCl₃, 400 MHz, rt).

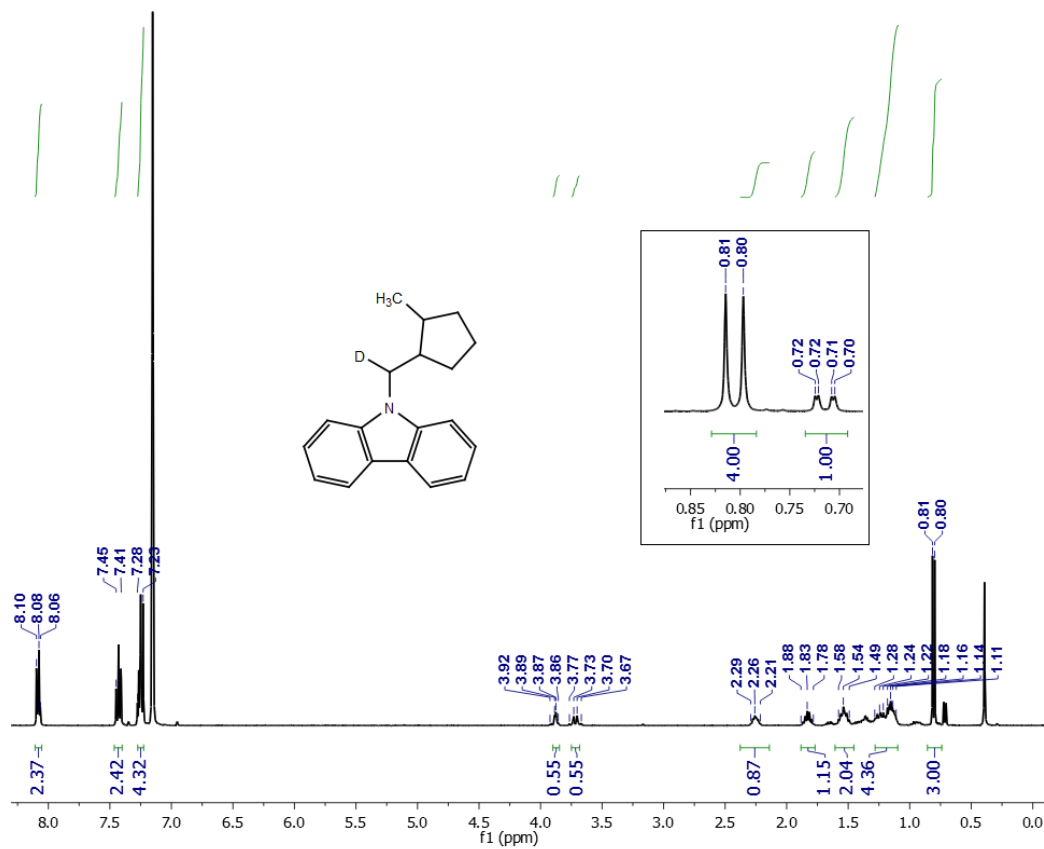


Figure A.30: ^1H NMR spectrum of 9-((2-methylcyclopentyl)methyl-d)-9H-carbazole (C_6H_6 , 400 MHz, rt).

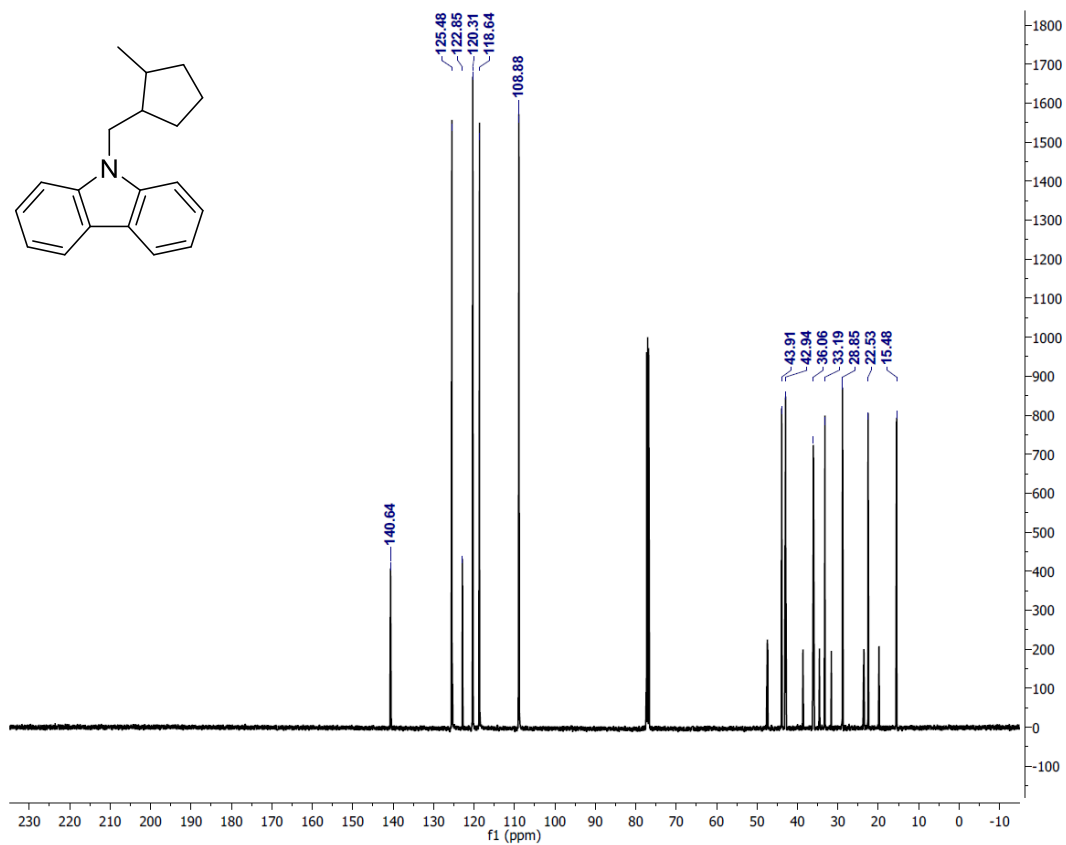


Figure A.31: $^{13}\text{C}\{^1\text{H}\}$ NMR spectrum of 9-((2-methylcyclopentyl)methyl-d)-9H-carbazole (C_6D_6 , 126 MHz, rt).

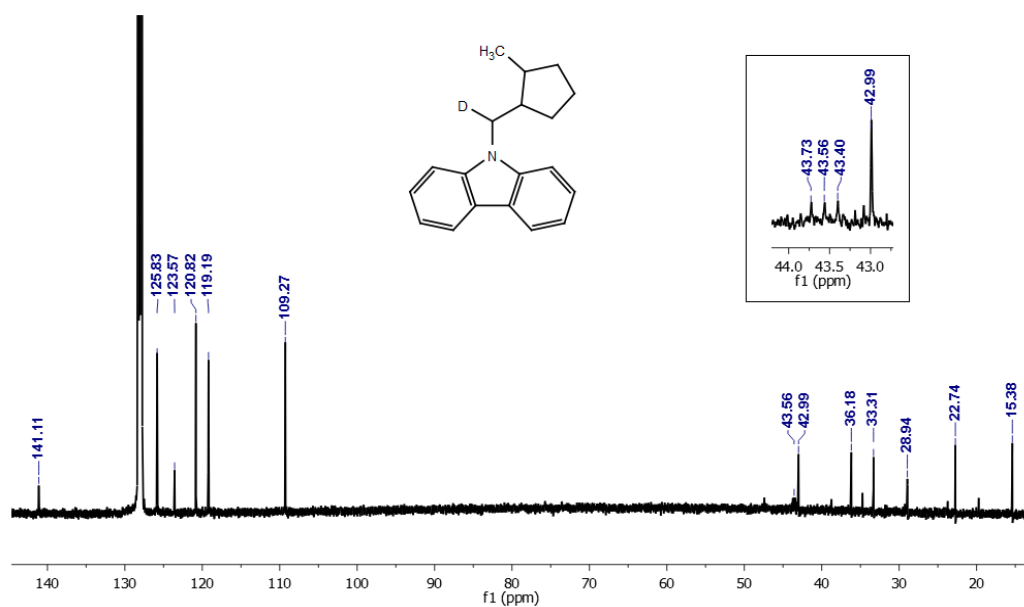


Figure A.32: $^{13}\text{C}\{^1\text{H}\}$ NMR spectrum of 9-((2-methylcyclopentyl)methyl-d)-9H-carbazole (C_6D_6 , 126 MHz, rt).

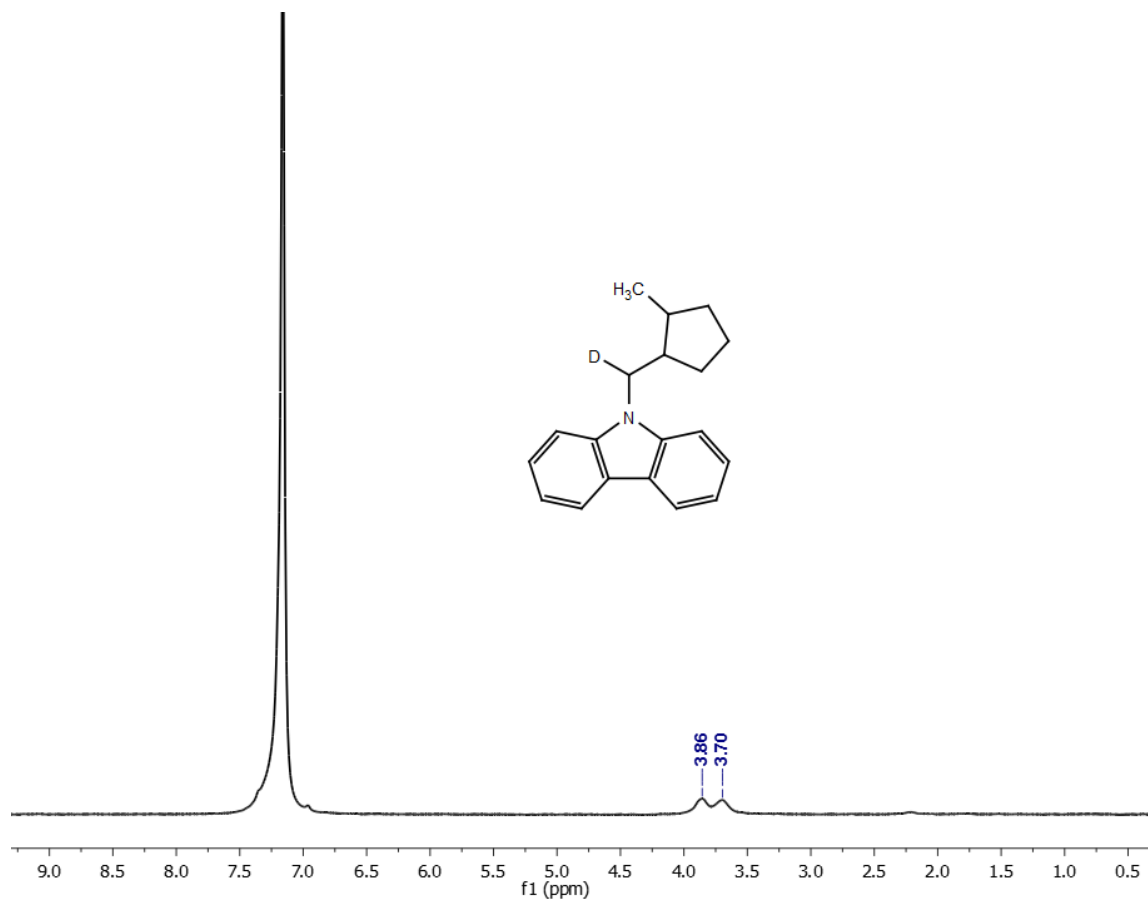


Figure A.33: ^2H NMR spectrum of 9-((2-methylcyclopentyl)methyl-d)-9H-carbazole (C_6H_6 , 61 MHz, rt).

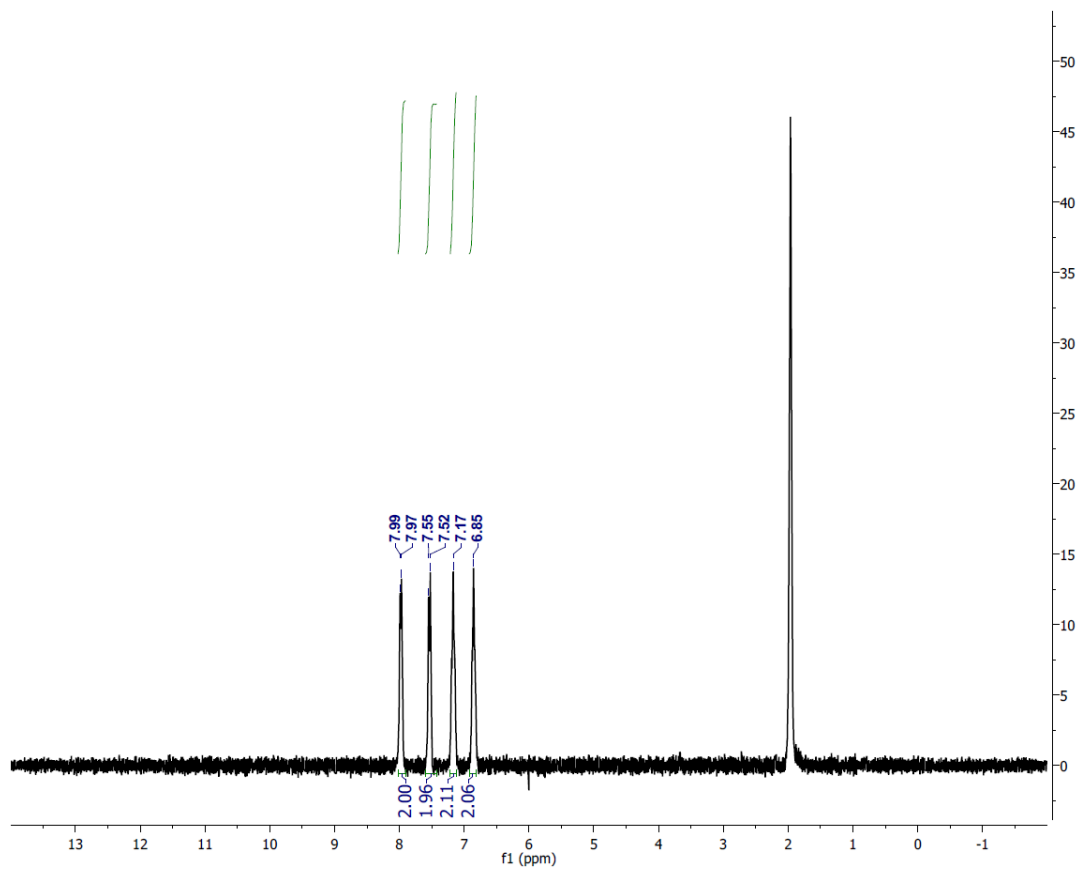


Figure A.34: ^1H NMR spectrum lithium carbazolidine (CD_3CN , 300 MHz, rt).

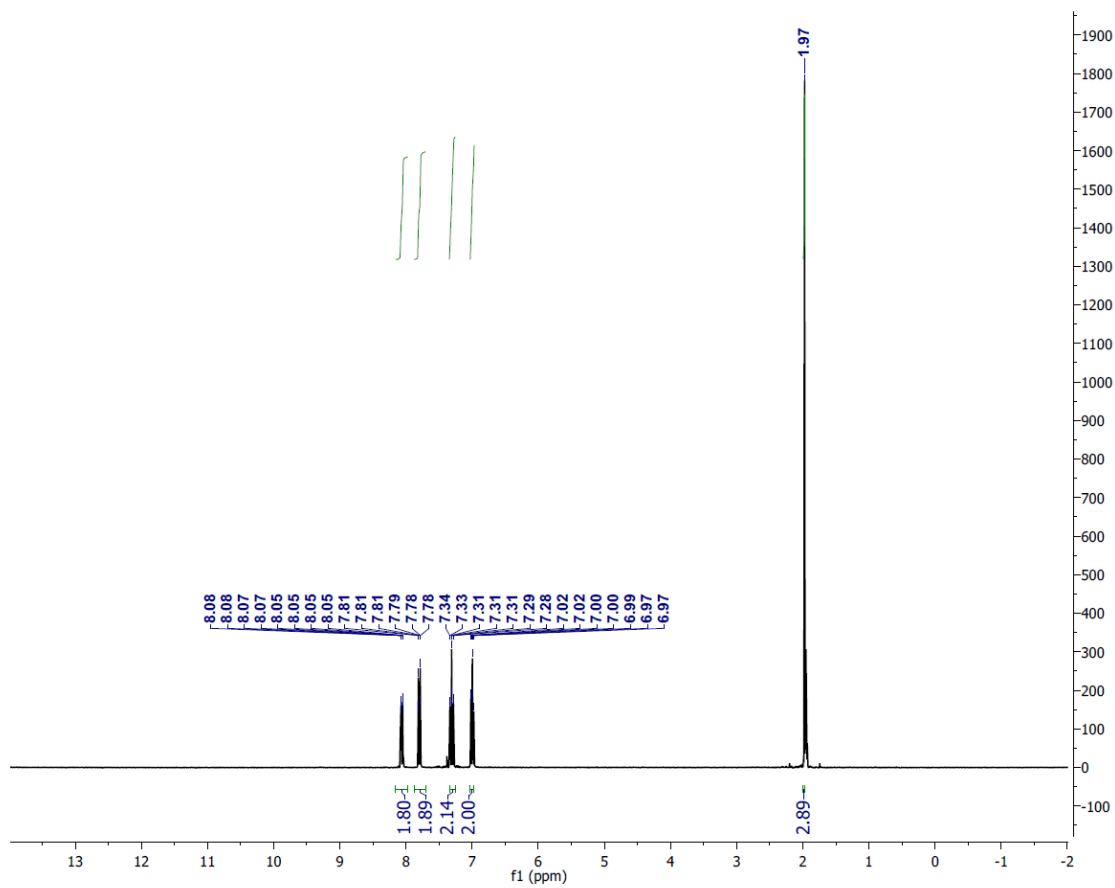


Figure A.35: ^1H NMR spectrum $\text{Li}(\text{MeCN})[\text{Cu}(\text{carbazolide})_2]$ (CD_3CN , 300 MHz, rt).

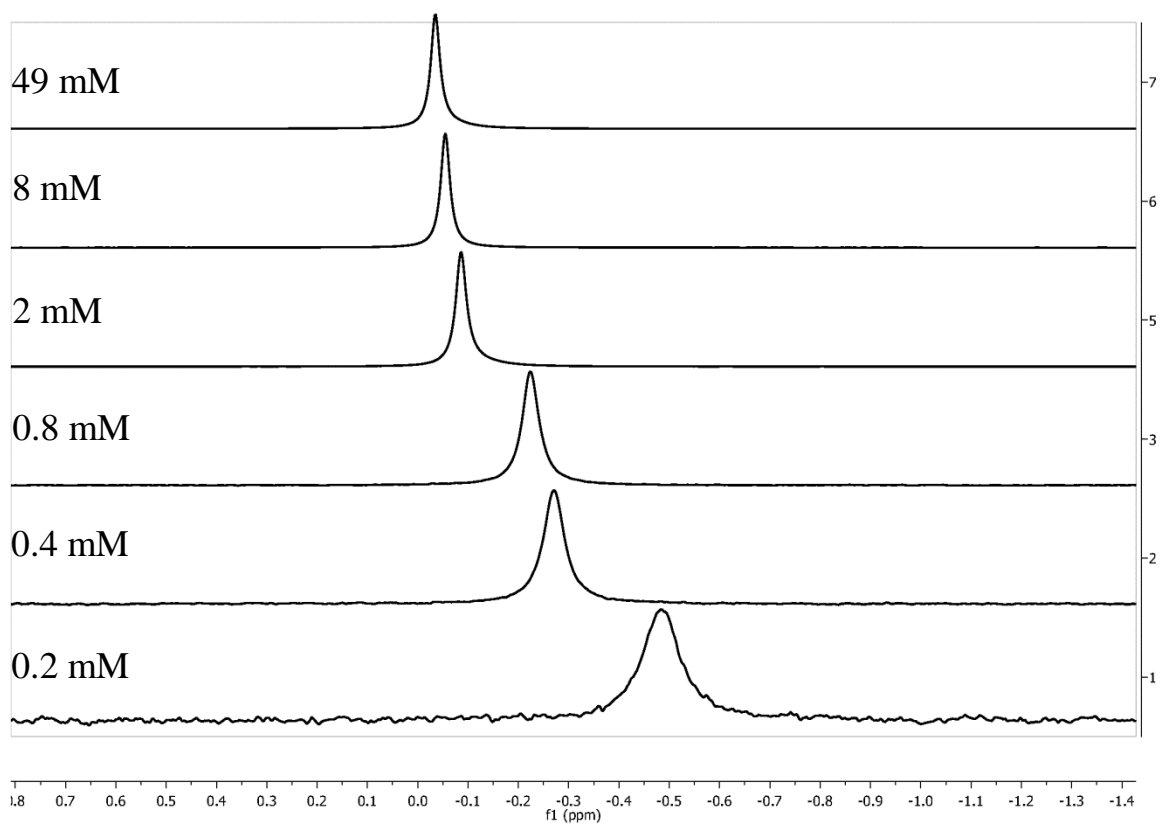


Figure A.36: ^7Li NMR of lithium carbazolid at various concentrations (CD_3CN , rt, 194 MHz).

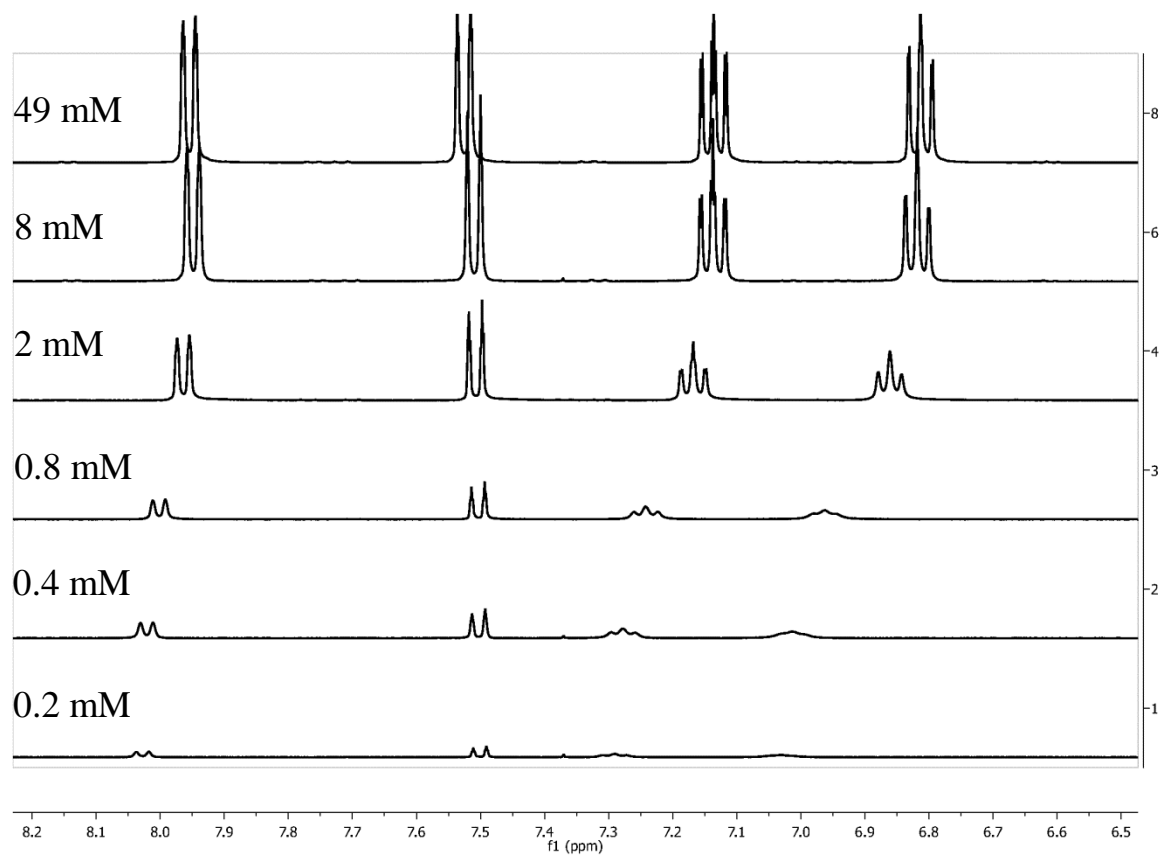


Figure A.37: ^1H NMR of lithium carbazolidine at various concentrations (CD_3CN , rt, 500 MHz).

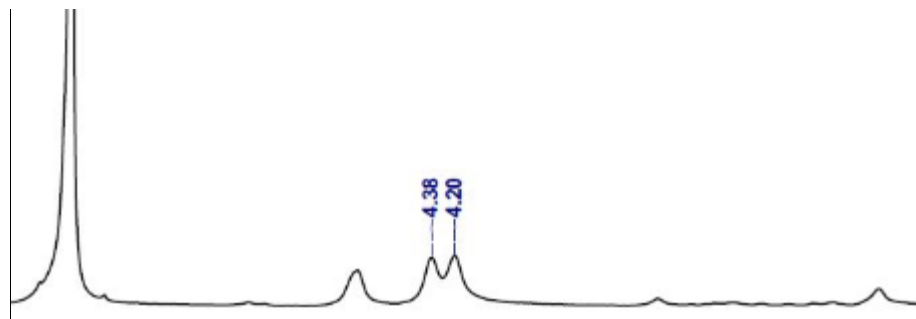


Figure A.38: ^2H NMR spectrum of a crude reaction mixture of the reaction between (E)-6-bromohept-1-ene-1-d and Li(carb) as depicted in eq 7 of Chapter 2 (CHCl_3 , rt, 61 MHz).

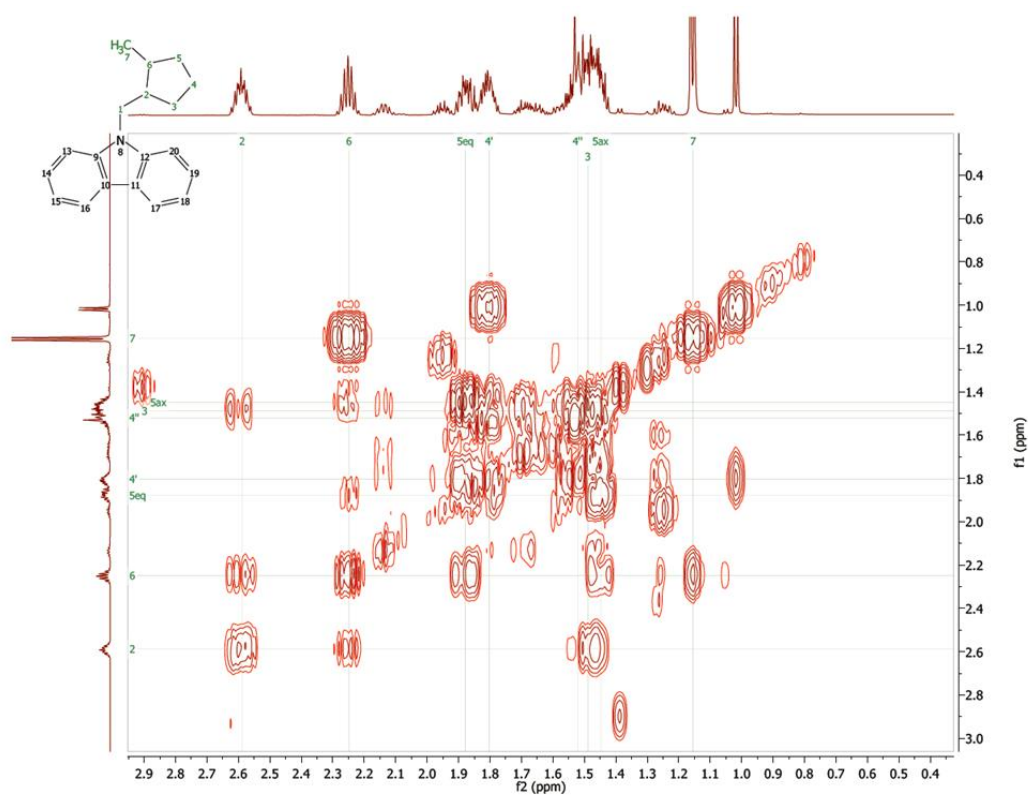


Figure A.39: ^1H - ^1H COSY trace of the major diastereomer (CDCl_3 , rt, 600 MHz) referencing eq 6 of Chapter 2.

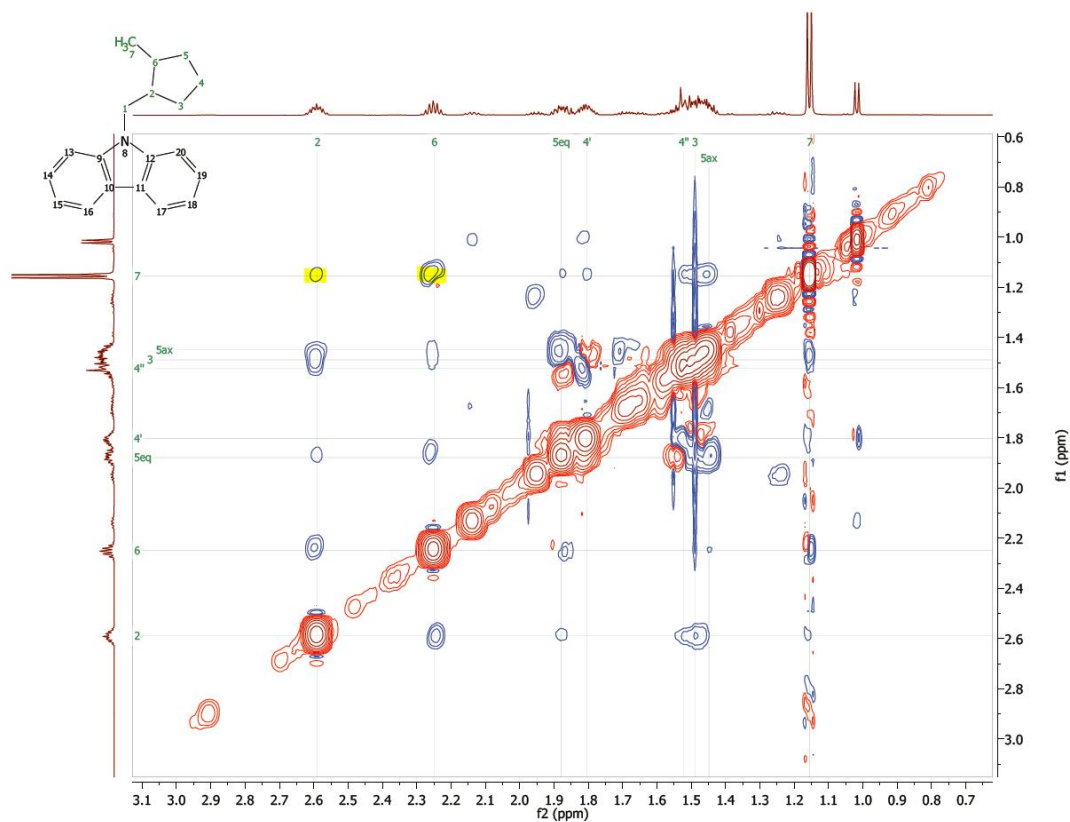


Figure A.40: ^1H - ^1H NOESY trace of the major (*cis*) diastereomer referencing eq 6 of Chapter 2. (CDCl_3 , rt, 600 MHz). Couplings of the methyl resonances to the methine resonances are highlighted in yellow. The difference in the magnitude of correlation is consistent with the *cis* configuration in a 5-membered ring.

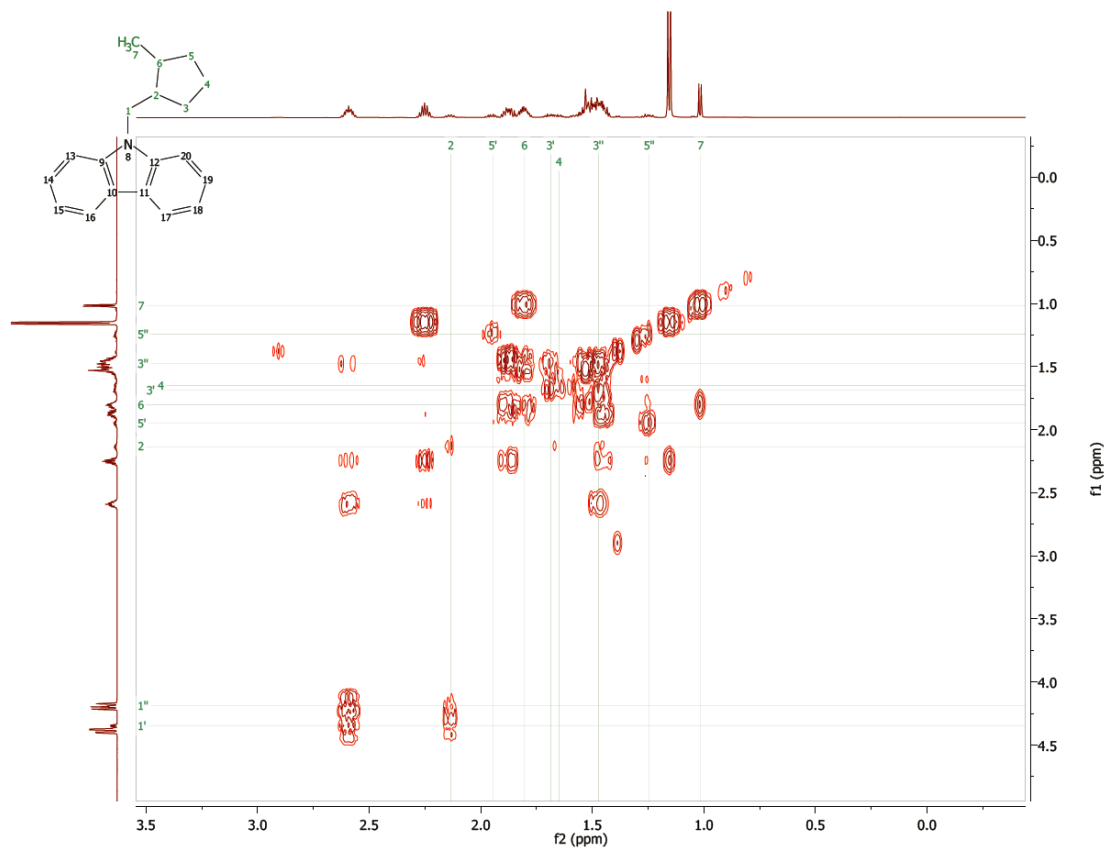


Figure A.41: ^1H - ^1H COSY trace of the minor diastereomer (CDCl_3 , rt, 600 MHz) referencing eq 6 of Chapter 2.

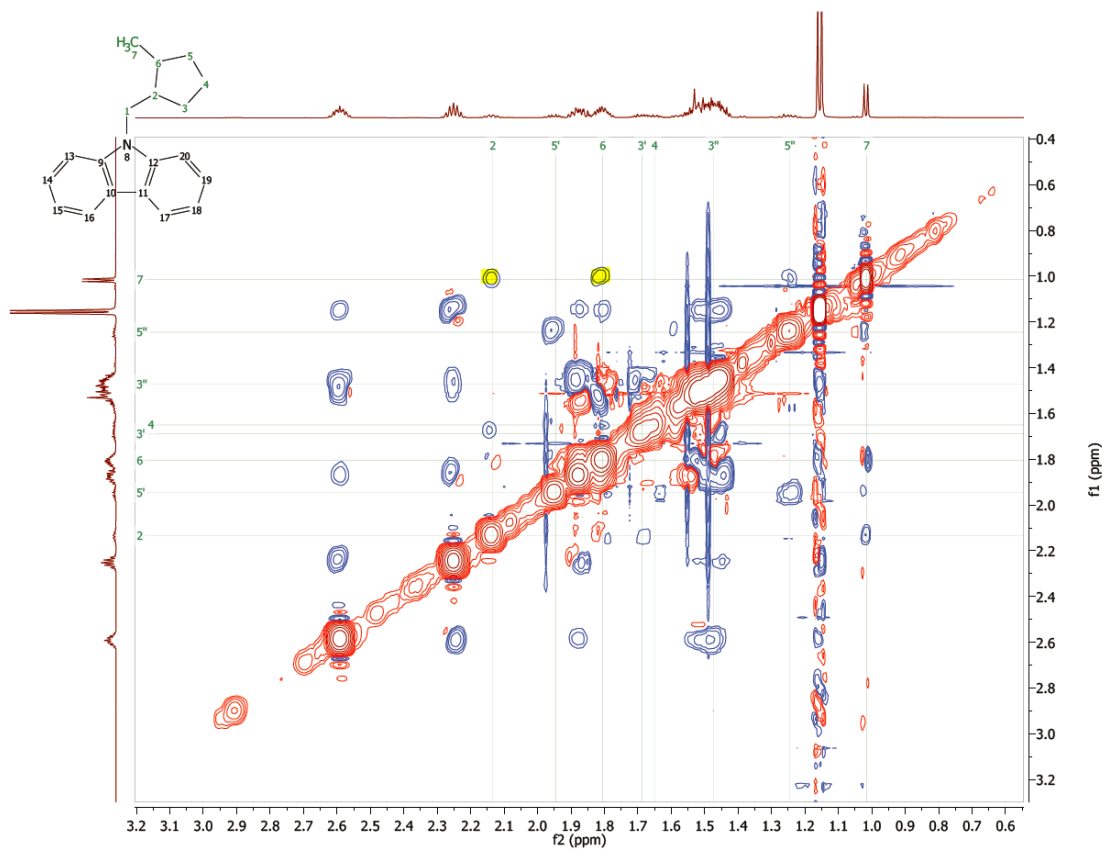


Figure A.42: ^1H - ^1H NOESY trace of the minor (*trans*) diastereomer (CDCl_3 , rt, 600 MHz) referencing eq 6 of Chapter 2. Couplings of the methyl resonances to the methane resonances are highlighted in yellow. Approximately equal magnitude of correlation is consistent with the *trans* configuration in a 5-membered ring.

A.14 X-Ray Crystallography Data

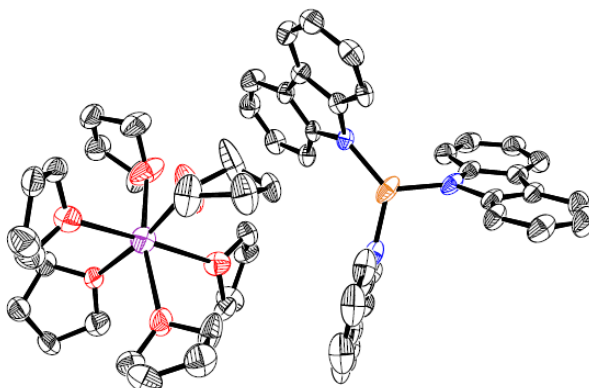


Table A.11: Crystal data and structure refinement for [K(THF)₆][Cu(carbazolide)₃]

Identification code	[K(THF) ₆][Cu(carbazolide) ₃]
Empirical formula	C ₄₀ H ₄₄ Cu _{0.67} K _{0.67} N ₂ O ₄
Formula weight	685.20
Temperature/K	100.05
Crystal system	monoclinic
Space group	P2 ₁ /n
a/Å	12.9317(5)
b/Å	22.3762(9)
c/Å	18.9484(6)
α/°	90
β/°	104.763(2)
γ/°	90
Volume/Å ³	5301.9(3)
Z	6
ρ _{calc} /cm ³	1.288
μ/mm ⁻¹	1.709
F(000)	2172.0
Radiation	CuKα (λ = 1.54178)
2θ range for data collection/°	6.234 to 136.854
Index ranges	-15 ≤ h ≤ 14, -26 ≤ k ≤ 26, -22 ≤ l ≤ 22
Reflections collected	57323
Independent reflections	9697 [R _{int} = 0.1553, R _{sigma} = 0.1076]
Data/restraints/parameters	9697/0/650
Goodness-of-fit on F ²	1.043
Final R indexes [I ≥ 2σ (I)]	R ₁ = 0.1065, wR ₂ = 0.2568

Final R indexes [all data] $R_1 = 0.1845$, $wR_2 = 0.3014$
 Largest diff. peak/hole / $e \text{ \AA}^{-3}$ 1.19/-0.99

Table A.12: Fractional atomic coordinates ($\times 10^4$) and equivalent isotropic displacement parameters ($\text{\AA}^2 \times 10^3$) for $[\text{K}(\text{THF})_6][\text{Cu}(\text{carbazolide})_3]$. U_{eq} is defined as 1/3 of the trace of the orthogonalised U_{IJ} tensor.

Atom	x	y	z	$U(\text{eq})$
Cu01	4786.3(8)	5173.8(6)	2403.2(5)	46.4(4)
K002	155.6(14)	6827.8(8)	2586.4(10)	56.2(5)
N003	3640(4)	4749(2)	2613(2)	27.6(12)
O004	2166(4)	6796(2)	3057(3)	48.4(13)
O005	-1816(4)	6897(2)	1959(3)	53.1(14)
O006	724(4)	7682(2)	1949(3)	55.6(15)
N007	4909(4)	6011(3)	2337(3)	43.7(16)
O008	-10(4)	7497(2)	3587(4)	72.9(19)
N009	6048(4)	4818(3)	2281(3)	38.9(14)
O00A	213(5)	5984(3)	3441(3)	75(2)
C00B	3364(5)	4737(3)	3280(3)	28.4(14)
C00C	2868(5)	4412(3)	2140(3)	29.5(14)
C00D	5478(5)	6373(3)	2893(3)	37.1(17)
C00E	2100(5)	4189(3)	2483(3)	30.7(14)
O00F	158(6)	6072(3)	1667(3)	91(2)
C00G	2432(5)	4405(3)	3231(3)	32.1(15)
C00H	6513(5)	4868(3)	1692(3)	38.1(17)
C00I	6795(6)	4508(3)	2805(4)	38.6(17)
C00J	2802(5)	4274(3)	1414(3)	34.4(16)
C00K	6090(5)	6201(3)	3587(3)	36.5(16)
C00L	6561(5)	6641(3)	4072(4)	39.3(17)
C00M	5390(5)	6980(3)	2709(4)	37.2(17)
C00N	6450(5)	7238(4)	3895(4)	41.1(18)
C00O	7509(6)	4587(3)	1832(4)	40.1(18)
C00P	4714(5)	7000(4)	1960(3)	42.6(19)
C00Q	7705(6)	4357(3)	2562(4)	39.4(17)
C00R	4451(5)	6403(4)	1776(4)	49(2)
C00S	3891(5)	5008(3)	3936(3)	33.5(16)
C00T	1966(6)	3931(3)	1042(4)	43.2(18)
C00U	5877(5)	7407(3)	3205(4)	40.4(17)
C00V	3472(6)	4940(3)	4531(4)	42.9(18)
C00W	1264(5)	3840(3)	2100(4)	41.3(17)
C00X	6067(6)	5129(4)	1004(3)	41.9(18)
C00Y	2023(6)	4343(3)	3844(4)	46.3(19)
C00Z	2561(6)	4608(4)	4480(4)	48(2)

C010	8071(7)	4574(4)	1294(4)	50(2)
C011	8445(6)	3869(3)	3700(4)	48.9(19)
C012	1198(6)	3711(3)	1378(4)	43.5(18)
C013	6630(7)	5103(4)	489(4)	53(2)
C014	8528(6)	4036(3)	3013(4)	49.1(19)
C015	2794(6)	6294(3)	3376(4)	43.3(18)
C016	6724(6)	4345(3)	3504(4)	45.4(19)
C017	-2539(6)	6409(3)	1671(4)	46.6(19)
C018	2827(6)	7310(4)	3272(4)	46.6(19)
C019	7544(7)	4032(4)	3943(4)	53(2)
C01A	-273(6)	8494(3)	3917(5)	56(2)
C01B	3448(6)	6519(3)	4137(4)	49.0(19)
C01C	-1312(6)	8185(3)	3617(4)	50(2)
C01D	-3206(6)	6635(4)	921(4)	51(2)
C01E	3795(6)	6253(5)	1082(4)	58(2)
C01F	4340(6)	7451(4)	1465(4)	57(2)
C01G	7615(7)	4828(4)	625(4)	59(2)
C01H	310(7)	8261(4)	1768(4)	52(2)
C01I	-2981(7)	7298(4)	924(5)	64(2)
C01J	3402(7)	7182(4)	4060(4)	57(2)
C01K	538(7)	8046(4)	3803(5)	58(2)
C01L	3700(7)	7298(5)	781(4)	64(3)
C01M	3441(7)	6724(5)	600(4)	65(3)
C01N	-460(7)	5480(4)	3290(5)	68(3)
C01O	-1150(7)	5547(4)	3839(5)	59(2)
C01P	174(7)	8314(4)	953(4)	59(2)
C01Q	-471(7)	5874(4)	4459(4)	60(2)
C01R	-1045(6)	7537(4)	3727(5)	58(2)
C01S	-2412(7)	7433(4)	1704(4)	61(2)
C01T	1012(8)	7904(5)	813(4)	69(3)
C01U	546(7)	5956(5)	555(4)	70(3)
C01V	-285(7)	6185(5)	905(4)	69(3)
C01W	1496(7)	7605(5)	1518(4)	73(3)
C01X	526(7)	6049(5)	4223(4)	69(3)
C01Y	925(10)	5623(6)	1747(5)	107(5)
C01Z	963(18)	5441(9)	1012(7)	54(6)
C01{	1510(30)	5740(18)	1300(20)	64(12)

Table A.13: Anisotropic displacement parameters ($\text{\AA}^2 \times 10^3$) for $[\text{K}(\text{THF})_6][\text{Cu}(\text{carbazolide})_3]$. The anisotropic displacement factor exponent takes the form: $-2\pi^2[h^2a^*{}^2U_{11}+2hka^*b^*U_{12}+\dots]$.

Atom	U_{11}	U_{22}	U_{33}	U_{23}	U_{13}	U_{12}
------	----------	----------	----------	----------	----------	----------

Cu01	38.7(6)	79.6(9)	24.3(5)	-9.1(5)	13.8(4)	-23.1(6)
K002	48.5(10)	57.0(11)	63.9(12)	1.4(9)	15.6(9)	0.1(8)
N003	26(3)	38(3)	19(2)	0(2)	7(2)	1(2)
O004	44(3)	52(3)	43(3)	-2(3)	-2(2)	-7(2)
O005	56(3)	50(3)	53(3)	-1(3)	12(3)	0(3)
O006	57(3)	61(4)	59(3)	19(3)	34(3)	14(3)
N007	28(3)	74(5)	29(3)	-15(3)	7(2)	-13(3)
O008	52(3)	37(3)	147(6)	-23(3)	56(4)	-6(3)
N009	43(3)	53(4)	25(3)	-6(3)	16(3)	-20(3)
O00A	92(5)	96(5)	50(3)	-21(3)	39(3)	-49(4)
C00B	25(3)	35(4)	26(3)	4(3)	8(3)	9(3)
C00C	29(3)	33(4)	24(3)	3(3)	2(3)	6(3)
C00D	20(3)	66(5)	29(3)	-5(3)	14(3)	-2(3)
C00E	26(3)	37(4)	28(3)	7(3)	3(3)	2(3)
O00F	113(5)	126(6)	36(3)	5(3)	23(3)	73(5)
C00G	26(3)	39(4)	30(3)	4(3)	6(3)	5(3)
C00H	43(4)	46(4)	29(4)	-14(3)	16(3)	-23(4)
C00I	44(4)	41(4)	33(4)	-12(3)	14(3)	-19(3)
C00J	31(4)	43(4)	28(3)	1(3)	7(3)	13(3)
C00K	26(3)	56(5)	29(3)	-5(3)	9(3)	-8(3)
C00L	26(4)	61(5)	29(4)	2(3)	3(3)	-1(3)
C00M	21(3)	57(5)	34(4)	-5(4)	8(3)	6(3)
C00N	26(4)	60(5)	37(4)	-12(4)	6(3)	5(3)
C00O	46(4)	45(4)	33(4)	-19(3)	18(3)	-20(3)
C00P	21(3)	82(6)	24(4)	-6(4)	5(3)	12(4)
C00Q	46(4)	41(4)	32(4)	-16(3)	12(3)	-15(4)
C00R	28(4)	91(7)	30(4)	4(4)	11(3)	6(4)
C00S	26(3)	45(4)	27(3)	2(3)	3(3)	7(3)
C00T	49(4)	44(4)	31(4)	-7(3)	-1(3)	10(4)
C00U	31(4)	49(4)	43(4)	0(4)	11(3)	9(3)
C00V	49(4)	55(5)	23(3)	-1(3)	6(3)	9(4)
C00W	33(4)	48(5)	44(4)	0(4)	11(3)	-1(3)
C00X	39(4)	63(5)	25(3)	-8(3)	12(3)	-13(4)
C00Y	55(5)	55(5)	32(4)	5(4)	18(3)	-9(4)
C00Z	50(5)	60(5)	41(4)	13(4)	22(4)	6(4)
C010	58(5)	59(5)	39(4)	-11(4)	25(4)	-3(4)
C011	51(5)	45(5)	50(5)	-6(4)	10(4)	-11(4)
C012	35(4)	43(4)	46(4)	-3(4)	-1(3)	3(3)
C013	60(5)	72(6)	28(4)	-8(4)	15(4)	-23(5)
C014	57(5)	47(5)	49(5)	-13(4)	23(4)	-8(4)
C015	42(4)	46(4)	41(4)	1(4)	7(3)	11(3)
C016	60(5)	47(5)	34(4)	-5(4)	22(4)	-10(4)

C017	48(4)	47(5)	50(4)	-4(4)	23(4)	-5(4)
C018	35(4)	57(5)	49(4)	5(4)	13(3)	-8(4)
C019	71(6)	54(5)	38(4)	-4(4)	18(4)	-23(4)
C01A	53(5)	36(4)	80(6)	-10(4)	19(4)	7(4)
C01B	41(4)	51(5)	51(5)	0(4)	4(4)	-12(4)
C01C	50(5)	48(5)	54(5)	6(4)	17(4)	7(4)
C01D	40(4)	60(5)	58(5)	4(4)	21(4)	6(4)
C01E	35(4)	105(7)	32(4)	-22(5)	5(3)	-1(4)
C01F	37(4)	94(7)	39(4)	-1(5)	11(4)	21(4)
C01G	70(6)	82(6)	37(4)	-18(4)	34(4)	-16(5)
C01H	58(5)	51(5)	48(5)	2(4)	15(4)	-5(4)
C01I	76(6)	58(6)	61(6)	8(4)	20(5)	10(5)
C01J	66(5)	55(5)	42(4)	-3(4)	0(4)	3(4)
C01K	54(5)	56(5)	64(5)	-4(4)	16(4)	-4(4)
C01L	51(5)	107(8)	30(4)	4(5)	2(4)	29(5)
C01M	45(5)	122(9)	26(4)	0(5)	4(4)	24(5)
C01N	76(6)	74(6)	62(5)	-41(5)	32(5)	-39(5)
C01O	52(5)	62(5)	71(6)	-16(5)	32(4)	-13(4)
C01P	79(6)	48(5)	42(5)	3(4)	-1(4)	6(4)
C01Q	67(6)	66(6)	57(5)	-5(4)	31(4)	-9(5)
C01R	51(5)	55(5)	79(6)	12(5)	37(4)	6(4)
C01S	73(6)	55(5)	60(5)	-12(4)	25(5)	-3(5)
C01T	84(7)	83(7)	46(5)	18(5)	28(5)	6(5)
C01U	79(6)	100(8)	37(4)	-2(5)	24(4)	28(6)
C01V	53(5)	121(9)	34(4)	2(5)	9(4)	14(5)
C01W	49(5)	132(9)	47(5)	29(5)	27(4)	17(5)
C01X	48(5)	116(9)	45(5)	-17(5)	13(4)	-17(5)
C01Y	142(10)	140(11)	38(5)	12(6)	23(6)	111(9)
C01Z	71(12)	55(10)	37(8)	-3(7)	17(7)	22(9)
C01{	48(19)	50(20)	100(30)	10(20)	31(19)	25(15)

Table A.14: Hydrogen atom coordinates ($\text{\AA}\times 10^4$) and isotropic displacement parameters ($\text{\AA}^2\times 10^3$) for $[\text{K}(\text{THF})_6][\text{Cu}(\text{carbazolide})_3]$.

Atom	x	y	z	U(eq)
H00J	3325	4415	1183	41
H00K	6176	5791	3719	44
H00L	6976	6528	4543	47
H00N	6765	7532	4246	49
H00S	4524	5234	3971	40
H00T	1905	3839	543	52
H00U	5819	7817	3073	49
H00V	3816	5125	4981	51

H00W	744	3691	2330	50
H00X	5387	5318	903	50
H00Y	1387	4123	3817	56
H00Z	2298	4561	4902	58
H010	8756	4392	1387	59
H011	9001	3642	4009	59
H012	626	3472	1107	52
H013	6338	5279	25	63
H014	9143	3932	2853	59
H01A	3275	6166	3073	52
H01B	2330	5953	3429	52
H016	6114	4451	3670	54
H01C	-3007	6319	1999	56
H01D	-2136	6043	1614	56
H01E	2390	7677	3232	56
H01F	3341	7355	2968	56
H019	7507	3922	4421	64
H01G	-168	8586	4442	67
H01H	-231	8870	3649	67
H01I	3119	6386	4528	59
H01J	4195	6374	4247	59
H01K	-1598	8277	3092	60
H01L	-1845	8305	3883	60
H01M	-2982	6434	519	62
H01N	-3978	6560	864	62
H0BA	3604	5851	950	69
H1BA	4515	7857	1587	68
H2BA	7985	4814	252	71
H01O	812	8568	2033	63
H01P	-385	8310	1890	63
H01Q	-2523	7394	593	77
H01R	-3654	7529	770	77
H01S	4132	7352	4177	68
H01T	3007	7358	4393	68
H01U	874	8188	3419	69
H01V	1105	7991	4260	69
H3BA	3440	7604	434	77
H4BA	3002	6638	128	78
H01W	-219	5084	3145	82
H01X	-1810	5775	3621	71
H01Y	-1349	5151	3995	71
H01Z	-549	8185	680	71

H	294	8730	814	71
H01	-283	5616	4899	72
HA	-846	6233	4572	72
H0AA	-1197	7318	4150	69
H1AA	-1927	7780	1733	74
HB	-2930	7520	1995	74
H2AA	689	7606	435	83
HC	1560	8133	645	83
H3AA	228	5835	42	85
HD	1110	6258	568	85
HE	804	6273	278	85
HF	277	5615	226	85
H4AA	-1025	6029	697	83
H5AA	2249	7723	1762	88
H6AA	1256	5931	4515	83
H7AA	599	5273	1939	128
H8AA	1706	5350	995	65
HG	514	5083	852	65
H9AA	1897	5381	1194	76
HH	2029	6064	1480	76

Table A.15: Bond angles for [K(THF)₆][Cu(carbazolide)₃].

Atom Atom Atom	Angle/°	Atom Atom Atom	Angle/°
N007 Cu01 N003	126.7 (2)	N007 C00D C00M	112.7 (6)
N009 Cu01 N003	124.4 (2)	C00M C00D C00K	119.4 (6)
N009 Cu01 N007	108.8 (2)	C00C C00E C00G	105.4 (5)
O004 K002 O005	172.63 (17)	C00W C00E C00C	120.4 (6)
O004 K002 C01N	99.0 (2)	C00W C00E C00G	134.2 (6)
O004 K002 C01R	112.86 (19)	C01V O00F K002	121.7 (6)
O004 K002 C01V	103.31 (19)	C01Y O00F K002	123.8 (6)
O004 K002 C01W	66.16 (18)	C01Y O00F C01V	109.1 (6)
O004 K002 C01X	77.03 (18)	C00B C00G C00E	106.0 (5)
O004 K002 C01Y	75.3 (3)	C00B C00G C00Y	119.9 (6)
O005 K002 C01N	86.1 (2)	C00Y C00G C00E	134.1 (6)
O005 K002 C01R	72.44 (19)	N009 C00H C00X	127.7 (7)
O005 K002 C01V	71.19 (19)	C00O C00H N009	112.0 (6)
O005 K002 C01W	106.87 (19)	C00O C00H C00X	120.1 (6)
O005 K002 C01X	110.06 (19)	N009 C00I C00Q	112.0 (6)
O005 K002 C01Y	102.0 (2)	N009 C00I C016	127.4 (7)
O006 K002 O004	77.68 (18)	C016 C00I C00Q	120.6 (7)
O006 K002 O005	96.48 (18)	C00T C00J C00C	118.4 (6)
O006 K002 O00A	161.2 (2)	C00L C00K C00D	118.4 (7)

O006 K002 C01N	170.4 (2)	C00N C00L C00K	122.0 (7)
O006 K002 C01R	101.11 (19)	C00D C00M C00P	105.2 (6)
O006 K002 C01V	82.5 (2)	C00U C00M C00D	120.7 (6)
O006 K002 C01W	21.1 (2)	C00U C00M C00P	134.2 (7)
O006 K002 C01X	146.3 (2)	C00L C00N C00U	119.6 (7)
O006 K002 C01Y	103.0 (3)	C00H C00O C00Q	105.8 (6)
O008 K002 O004	91.64 (18)	C010 C00O C00H	119.9 (7)
O008 K002 O005	92.87 (19)	C010 C00O C00Q	134.3 (7)
O008 K002 O006	90.1 (2)	C00R C00P C00M	105.0 (7)
O008 K002 O00A	87.3 (2)	C01F C00P C00M	134.5 (8)
O008 K002 C01N	99.1 (2)	C01F C00P C00R	120.5 (7)
O008 K002 C01R	22.38 (19)	C00I C00Q C00O	105.7 (6)
O008 K002 C01V	161.4 (2)	C014 C00Q C00I	119.8 (7)
O008 K002 C01W	107.5 (2)	C014 C00Q C00O	134.4 (7)
O008 K002 C01X	68.8 (2)	N007 C00R C00P	112.6 (6)
O008 K002 C01Y	158.8 (2)	N007 C00R C01E	126.9 (9)
O00A K002 O004	83.75 (19)	C00P C00R C01E	120.6 (8)
O00A K002 O005	102.3 (2)	C00V C00S C00B	118.4 (6)
O00A K002 C01N	19.58 (19)	C00J C00T C012	121.5 (7)
O00A K002 C01R	83.2 (2)	C00M C00U C00N	119.9 (7)
O00A K002 C01V	105.1 (2)	C00Z C00V C00S	120.7 (7)
O00A K002 C01W	146.3 (2)	C012 C00W C00E	118.8 (7)
O00A K002 C01X	20.2 (2)	C013 C00X C00H	118.6 (7)
O00A K002 C01Y	74.8 (2)	C00Z C00Y C00G	118.4 (7)
O00F K002 O004	92.6 (2)	C00Y C00Z C00V	122.0 (7)
O00F K002 O005	83.7 (2)	C01G C010 C00O	118.8 (8)
O00F K002 O006	97.7 (2)	C014 C011 C019	120.5 (8)
O00F K002 O008	171.8 (2)	C00W C012 C00T	120.4 (7)
O00F K002 O00A	86.1 (2)	C00X C013 C01G	121.5 (7)
O00F K002 C01N	73.3 (2)	C00Q C014 C011	119.3 (7)
O00F K002 C01R	151.0 (2)	O004 C015 C01B	104.6 (6)
O00F K002 C01V	21.0 (2)	C019 C016 C00I	118.9 (7)
O00F K002 C01W	80.7 (3)	O005 C017 C01D	104.6 (6)
O00F K002 C01X	105.4 (2)	O004 C018 K002	36.1 (3)
O00F K002 C01Y	19.9 (2)	O004 C018 C01J	103.7 (6)
C01N K002 C01X	38.4 (2)	C01J C018 K002	119.5 (5)
C01R K002 C01N	88.5 (2)	C016 C019 C011	120.9 (7)
C01R K002 C01V	143.6 (2)	C01C C01A C01K	103.2 (6)
C01R K002 C01W	121.5 (2)	C01J C01B C015	103.5 (6)
C01R K002 C01X	69.2 (2)	C01A C01C C01R	104.2 (6)
C01R K002 C01Y	155.7 (3)	C01I C01D C017	104.9 (6)
C01V K002 C01N	89.6 (2)	C01M C01E C00R	116.7 (9)

C01V K002 C01W	69.7 (2)	C00P C01F C01L	118.4 (9)
C01V K002 C01X	125.0 (3)	C010 C01G C013	121.1 (7)
C01WK002 C01N	149.5 (2)	O006 C01H C01P	105.0 (6)
C01WK002 C01X	143.0 (2)	C01S C01I C01D	104.3 (7)
C01Y K002 C01N	67.3 (3)	C01B C01J C018	106.4 (6)
C01Y K002 C01V	39.5 (2)	O008 C01K K002	33.8 (3)
C01Y K002 C01W	82.8 (3)	O008 C01K C01A	107.6 (6)
C01Y K002 C01X	91.7 (2)	C01A C01K K002	128.5 (5)
C00B N003 Cu01	126.6 (4)	C01MC01L C01F	121.5 (9)
C00C N003 Cu01	127.9 (4)	C01L C01MC01E	122.3 (8)
C00C N003 C00B	105.5 (5)	O00A C01N K002	36.1 (4)
C015 O004 K002	126.5 (4)	O00A C01N C01O	102.6 (6)
C015 O004 C018	106.2 (5)	C01O C01N K002	113.8 (6)
C018 O004 K002	124.4 (4)	C01Q C01O C01N	105.0 (6)
C017 O005 K002	127.4 (4)	C01T C01P C01H	103.5 (6)
C01S O005 K002	126.7 (5)	C01O C01Q C01X	105.7 (6)
C01S O005 C017	105.2 (6)	O008 C01R K002	41.0 (4)
C01H O006 K002	133.5 (4)	O008 C01R C01C	103.2 (6)
C01H O006 C01W	104.1 (6)	C01C C01R K002	119.7 (5)
C01WO006 K002	121.1 (5)	O005 C01S C01I	104.3 (6)
C00D N007 Cu01	124.7 (5)	C01WC01T C01P	106.0 (7)
C00D N007 C00R	104.6 (7)	C01V C01U C01{	101.0 (11)
C00R N007 Cu01	130.7 (5)	C01Z C01U C01V	101.9 (9)
C01K O008 K002	127.5 (5)	O00F C01V K002	37.3 (4)
C01K O008 C01R	108.2 (6)	O00F C01V C01U	103.9 (7)
C01R O008 K002	116.6 (5)	C01U C01V K002	126.4 (6)
C00H N009 Cu01	128.7 (5)	O006 C01WK002	37.8 (4)
C00I N009 Cu01	126.3 (4)	O006 C01WC01T	105.1 (7)
C00I N009 C00H	104.4 (6)	C01T C01WK002	126.6 (6)
C01N O00AK002	124.3 (5)	O00A C01X K002	36.4 (4)
C01N O00AC01X	106.7 (6)	O00A C01X C01Q	103.8 (6)
C01X O00AK002	123.4 (5)	C01Q C01X K002	117.2 (6)
N003 C00B C00G	111.4 (5)	O00F C01Y K002	36.3 (4)
C00S C00B N003	128.1 (6)	O00F C01Y C01Z	107.1 (8)
C00S C00B C00G	120.4 (6)	C01Z C01Y K002	138.5 (8)
N003 C00C C00E	111.7 (5)	C01{ C01Y K002	116 (2)
N003 C00C C00J	127.9 (6)	C01{ C01Y O00F	107.5 (14)
C00J C00C C00E	120.3 (6)	C01U C01Z C01Y	104.4 (11)
N007 C00D C00K	127.9 (7)	C01Y C01{ C01U	100 (2)

A.15 References

1. Tsuda, T.; Yazawa, T.; Watanabe, K.; Fujii, T.; Saegusa, T. *J. Org. Chem.* **1981**, *46*, 192–194.
2. González-Bobes, F.; Fu, G. C. *J. Am. Chem. Soc.* **2006**, *128*, 5360–5361.
3. Stoll, S.; Schweiger, A. *J. Magn. Reson.* **2006**, *178*, 42–55.
4. (a) Kimura, T.; Lee, J. C.; Gray, H. B.; Winkler, J. R. *Proc. Natl. Acad. Sci. U. S. A.* **2009**, *106*, 7834–7839. (b) Yamada, S.; Bouley Ford, N. D.; Keller, G. E.; Ford, W. C.; Gray, H. B.; Winkler, J. R. *Proc. Natl. Acad. Sci. U. S. A.* **2013**, *110*, 1606–1610.
5. Leijondahl, K.; Borén, L.; Braun, R.; Bäckvall, J.-E. *J. Org. Chem.* **2009**, *74*, 1988–1993.
6. Sargent, B. T.; Alexanian, E. J. *J. Am. Chem. Soc.* **2016**, *138*, 7520–7523.
7. Bissember, A. C.; Lundgren, R. J.; Creutz, S. E. Peters, J. C. Fu, G. C. *Angew. Chem. Int. Ed.* **2013**, *52*, 5129–5133.
8. Dinnebier, R.; Esbak, H.; Olbrich, F.; Behrens, U. *Organometallics* **2007**, *26*, 2604–2608.
9. (a) Murov, S. L.; Carmichael, I.; Hug, G. L. *Handbook of Photochemistry*; CRC Press: New York, 1993; pp 298–313. (b) Bolton, J. R.; Stefan, M. I.; Shaw, P.-S.; Lykke, K. *R. J. Photochem. Photobiol., A* **2011**, *222*, 166–169.
10. Wu, A.; Mader, E. A.; Datta, A.; Hrovat, D. A.; Borden, W. T.; Mayer, J. M. *J. Am. Chem. Soc.* **2009**, *131*, 11985–11997.
11. Neese, F. *Wiley Interdiscip. Rev. Comput. Mol. Sci.* **2012**, *2*, 73–78.
12. Zhao, Y.; Truhlar, D.G. *J. Chem. Phys.* **2006**, *125*, 194101.

13. Weigend, F.; Furche, F.; Ahlrichs, R. *J. Chem. Phys.* **2003**, *119*, 12753.
14. Klamt, A; Schüürmann, G. *J. Chem. Soc. Perkin Trans. 2* **1993**, *2*, 799–805.

Appendix B : Supplementary Information for Chapter 3

B.1 General Information

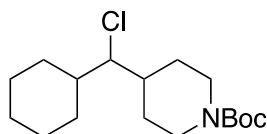
The following reagents were purchased and used as received: Copper(I) iodide (Aldrich; 99.999%), tetrabutylammonium cyanide (Aldrich; 95%), 4-chlorotetrahydro-2*H*-pyran (Acros), *tert*-butyl 4-bromopiperidine-1-carboxylate (Aldrich), (1-chloro-2-methylpropan-2-yl)benzene (Aldrich). CH₃CN was deoxygenated and dried by sparging with nitrogen followed by passage through an activated alumina column (S. G. Water) prior to use.

¹H and ¹³C spectroscopic data were collected on a Varian 500 MHz spectrometer or a Varian 400 MHz spectrometer at ambient temperature. GC analyses were carried out on an Agilent 6890 series system with an HP-5 column (length 30 m, I.D. 0.25 mm). All photoreactions were carried out in oven-dried quartz test tubes or a quartz flask, under an inert atmosphere, with the use of 15W, 120V, UV Germicidal Compact Lamps (Norman Lamps, Inc.) and a Fantec 172 x 150 x 51 mm Dual Ball Bearing AC high speed fan (240 CFM).

B.2 Preparation of Electrophiles

These procedures have not been optimized.

General Procedure for the Chlorination of Secondary Alcohols. To an oven-dried 500-mL round-bottom flask containing a stir bar was added dry CH_2Cl_2 (0.2 M) and the alcohol (1.00 equiv). The mixture was cooled to 0 °C in an ice bath, and PPh_3 (1.00 equiv) and NCS (1.00 equiv) were slowly added in turn. The round-bottom flask was then capped with a rubber septum and placed under a nitrogen atmosphere with the use of a needle attached to a vacuum manifold. The reaction was allowed to warm to room temperature as it remained in the water bath. After 5–8 hours, the reaction was quenched by the addition of saturated aqueous NH_4Cl . The organic phase was separated, dried over anhydrous Na_2SO_4 , and then concentrated carefully by rotary evaporator (careful concentration was important for volatile products). The product was purified by column chromatography (hexanes or Et_2O /hexanes).



***tert*-Butyl 4-(chloro(cyclohexyl)methyl)piperidine-1-carboxylate.**

Cyclohexylmagnesium chloride (2.0 M in Et_2O ; 23.5 mL, 46.9 mmol) was added dropwise to a solution of *tert*-butyl 4-formylpiperidine-1-carboxylate (10.0 g, 46.9 mmol) in THF (230 mL) at -78 °C (dry ice/acetone bath). The resulting solution was allowed to warm to room temperature while remaining in the acetone bath and stirring for 6 h. Next, the reaction was quenched by the addition of saturated aqueous NH_4Cl (100 mL), and the resulting mixture was extracted with Et_2O . The combined organic phases were dried over

anhydrous Na_2SO_4 and concentrated by rotary evaporator. The residue was passed through a plug of silica gel (60% Et_2O /hexanes), and the resulting filtrate was concentrated by rotary evaporator and used in the next step without further purification.

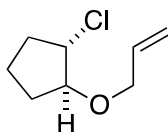
The title compound was prepared according to the general procedure for chlorination of secondary alcohols, using the unpurified *tert*-butyl 4-(cyclohexyl(hydroxy)methyl)piperidine-1-carboxylate. The product was purified by flash chromatography (5%→30% Et_2O /hexanes). Off-white solid (1.05 g, 7% over two steps).

^1H NMR (500 MHz, CDCl_3) δ 4.21–4.12 (m, 2H), 3.58 (dd, 1H, $J = 6.8, 5.5$ Hz), 2.73–2.62 (m, 2H), 1.96–1.75 (m, 5H), 1.73–1.65 (m, 2H), 1.65–1.57 (m, 2H), 1.47 (s, 9H), 1.45–1.17 (m, 7H).

^{13}C NMR (126 MHz, CDCl_3) δ 155.1, 79.8, 74.7, 40.8, 39.9, 31.5, 28.8, 26.6, 26.2.

ATR-IR (neat) 2928, 2848, 1682, 1445, 1417, 1368, 1284, 1265, 1246, 1163, 1121, 773 cm^{-1} .

HRMS (ESI) m/z [$\text{M}-(\text{isobutylene})+\text{H}$] $^+$ calcd for $\text{C}_{13}\text{H}_{23}\text{ClNO}_2$: 260.1, found: 260.1.



(1*S*,2*S*)-1-(allyloxy)-2-chlorocyclopentane. This procedure was adapted from a literature procedure.¹ Cyclopentene (5.00 mL, 56.6 mmol) was added dropwise over 30 minutes to a suspension of *N*-chlorosuccinimide (7.60 g, 56.6 mmol) in dry CH₂Cl₂ (100 mL). The resulting suspension was stirred at room temperature for 2 h, and then allyl alcohol (7.70 mL, 113.2 mmol) was added dropwise by syringe pump over 2 h. The reaction mixture was stirred at room temperature for 6 h. The solvent was then removed by rotary evaporator, and the crude residue was poured into a separatory funnel containing H₂O (100 mL). The mixture was extracted with Et₂O (3 x 50 mL), and the combined organic phases were washed with water (50 mL), dried over MgSO₄, filtered, and concentrated by rotary evaporator. The product was purified by column chromatography (100% hexanes). Clear oil (695 mg, 4% yield).

¹H NMR (400 MHz, CDCl₃) δ 5.90 (ddt, 1H, *J* = 17.2, 10.4, 5.6 Hz), 5.28 (dq, 1H, *J* = 17.2, 1.7 Hz), 5.21–5.16 (m, 1H), 4.22–4.17 (m, 1H), 4.08–4.01 (m, 2H), 4.00–3.95 (m, 1H), 2.27–2.06 (m, 2H), 1.93–1.72 (m, 3H), 1.70–1.60 (m, 1H).

¹³C NMR (100 MHz, CDCl₃) δ 134.6, 117.0, 87.2, 70.5, 63.1, 34.2, 29.9, 21.4.

ATR-IR (neat) 3100, 2960, 2861, 1651, 1463, 1433, 1341, 1256, 1082, 1013, 922, 793, 702, 655, 560 cm⁻¹.

MS (EI) *m/z* (M⁺) calcd for C₈H₁₃ClO: 160.1, found: 160.1.

B.3 Photoinduced, Copper-Catalyzed Cyanation Reactions

Four 15 watt, 120 volt UV Germicidal Compact Lamps were suspended from a ring clamp on a ring stand (Figure B.1). The lamps were spaced approximately evenly around the circumference of the ring clamp with a diameter of ~14 cm. In a second clamp below the ring clamp, the top of a wire test tube rack was placed interior to the lamps.

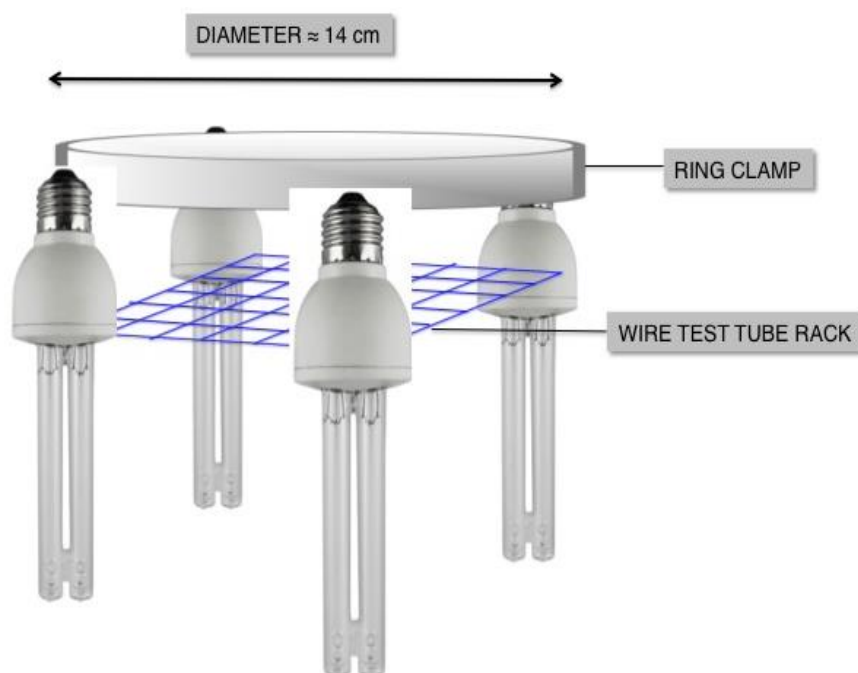


Figure B.1: Placement of UV Germicidal Compact Lamps around a ring clamp

A stir plate covered in aluminum foil was placed underneath the lamps (Figure B.2). A cardboard box lined with aluminum foil was placed over the ring stand, lamps, and stir plate. In one side of the cardboard box, a space was cut out, and a 172 x 150 x 51 mm high-speed (240 CFM) fan was fitted into this side of the box. In the side of the box directly opposite the fan, a vent was cut out. Photoreactions were carried out in quartz tubes or a quartz flask placed approximately in the center of the wire test tube rack,

ensuring that the reaction vessels were within the line of airflow from the fan and did not touch the lamps.

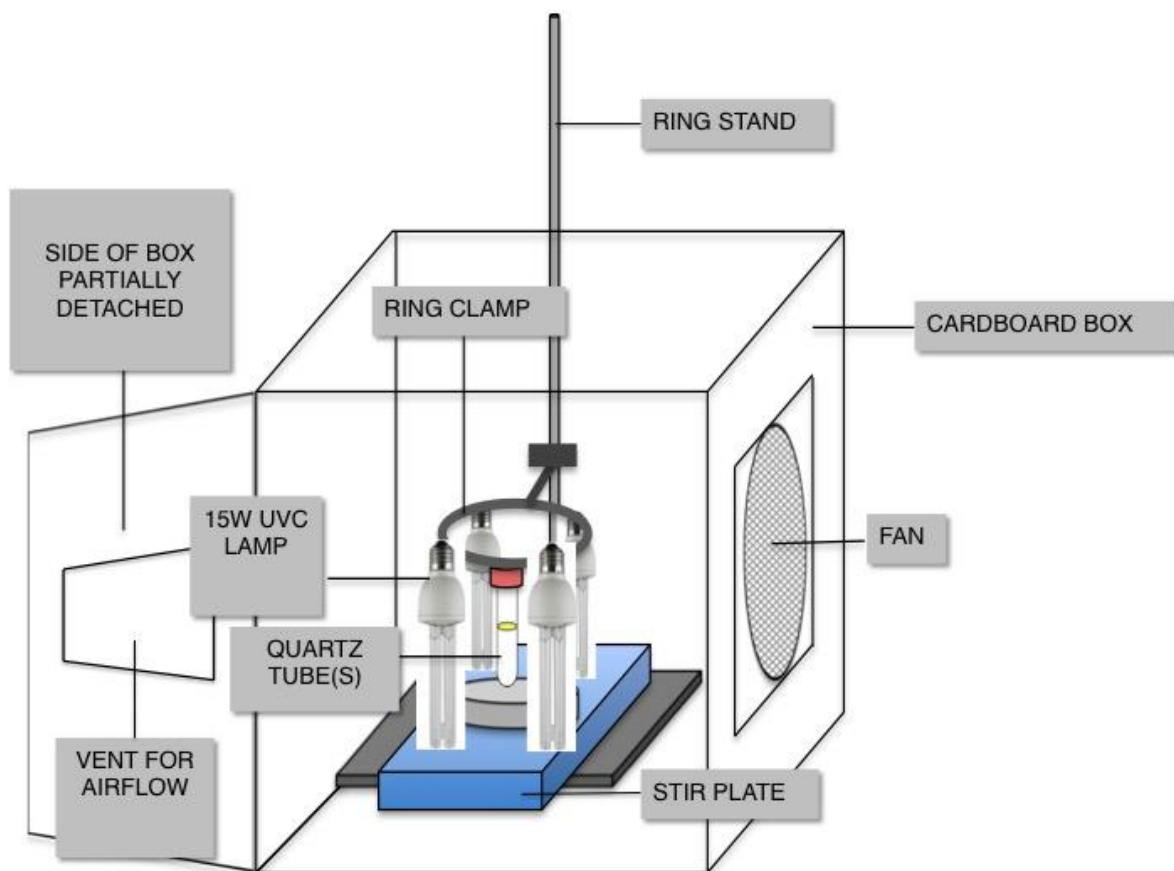
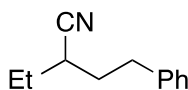


Figure B.2: Placement of cardboard box and fan relative to the UV lamps

General Procedure. Inside a glovebox, an oven-dried 20-mL vial equipped with a stir bar was charged with TBACN (*Caution: Highly toxic!* 601 mg, 2.24 mmol, 1.60 equiv) and capped with a PTFE-lined pierceable cap sealed with electrical tape. The vial was then removed from the glovebox, and MeCN (18.0 mL) was added via syringe. The mixture was vigorously stirred for 5 minutes, resulting in a colorless suspension. An oven-dried 20-mL quartz tube containing a stir bar was then charged with CuI (20.0 mg, 0.105 mmol, 0.0750 equiv), capped with a rubber septum, and sealed with electrical tape. The tube was evacuated and backfilled with nitrogen three times (through a needle attached to a vacuum manifold), and the TBACN suspension was added via syringe,

followed by the electrophile (1.40 mmol, 1.00 equiv) via microsyringe (if the electrophile is a solid, then it was added immediately after the addition of CuI). The reaction mixture was stirred vigorously for one minute. The quartz tube was then removed from the manifold, and the resulting mixture was then stirred vigorously and irradiated in the center of four, 15 watt UVC compact fluorescent light bulbs at room temperature for 24 h. Then, the reaction mixture was transferred to a 100-mL round-bottom flask and concentrated using a rotary evaporator in a well-ventilated fume hood. The residue was purified by column chromatography.

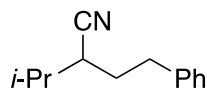


2-Ethyl-4-phenylbutanenitrile (Table 3.2, Entry 1) [1126479-77-3]. The title compound was prepared according to the General Procedure from (3-chloropentyl)benzene (258 μ L, 1.40 mmol) as the electrophile. The product was purified by column chromatography on silica gel (5 \rightarrow 10% EtOAc/hexanes). Tan oil. First run: 223 mg (92% yield). Second run: 227 mg (94% yield).

Gram-scale reaction. In a glove box, a 200-mL quartz flask was charged with TBACN (3.44 g, 12.8 mmol, 1.60 equiv), and a stir bar was added. The flask was capped with a rubber septum and sealed with electrical tape and then removed from the glove box. A separate 250-mL flask (borosilicate glass) was then charged with CuI (114 mg, 0.600 mmol, 0.0750 equiv), and acetonitrile (110 mL) and a stir bar were added. The CuI/acetonitrile solution was vigorously stirred for 1 minute under a nitrogen atmosphere, after which the homogeneous solution was cannula transferred to the quartz flask containing TBACN. Then, the alkyl chloride (1.50 mL, 8.00 mmol, 1.00 equiv) was

added via syringe. The reaction mixture was irradiated for 24 h using the same irradiation set-up as described above. Then, the stir bar was removed, and the reaction mixture was concentrated using a rotary evaporator in a well-ventilated fume hood. The product was purified by column chromatography on silica gel (10→20% Et₂O/hexanes). Tan oil. 1.30 g, 94% yield.

¹H NMR (500 MHz, CDCl₃) δ 7.34–7.30 (m, 2H), 7.26–7.19 (m, 3H), 2.91 (ddd, 1H, *J* = 14.2, 9.1, 5.2 Hz), 2.75 (ddd, 1H, *J* = 13.8, 8.9, 7.6 Hz), 2.49–2.43 (m, 1H), 2.01–1.92 (m, 1H), 1.90–1.82 (m, 1H), 1.70–1.63 (m, 2H), 1.09 (t, 3H, *J* = 7.4 Hz).



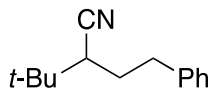
2-Isopropyl-4-phenylbutanenitrile (Table 3.2, Entry 2). The title compound was prepared according to the General Procedure from (3-chloro-4-methylpentyl)benzene (280 μL, 1.40 mmol) as the electrophile. The product was purified by column chromatography on silica gel (5→10% EtOAc/hexanes). Tan oil. First run: 220 mg (84% yield). Second run: 222 mg (85% yield).

¹H NMR (500 MHz, CDCl₃) δ 7.33–7.29 (m, 2H), 7.25–7.19 (m, 3H), 2.92 (ddd, 1H, *J* = 14.1, 9.2, 5.0 Hz), 2.71 (ddd, 1H, *J* = 13.8, 9.0, 7.6 Hz), 2.40 (dt, 1H, *J* = 10.4, 5.0 Hz), 1.96 (dddd, 1H, *J* = 13.9, 10.7, 9.0, 5.0 Hz), 1.89–1.78 (m, 2H), 1.08–1.02 (m, 6H).

¹³C NMR (126 MHz, CDCl₃) δ 140.6, 129.0, 128.8, 126.7, 121.3, 38.8, 33.9, 32.2, 30.4, 21.3, 19.0.

ATR-IR (neat) 3028, 2964, 2932, 2900, 2874, 2236, 1603, 1497, 1455, 1391, 1373, 751, 701 cm⁻¹.

MS (EI) *m/z* (M⁺) calcd for C₁₃H₁₇N: 187.1, found 187.2.



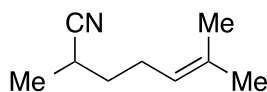
3,3-Dimethyl-2-phenethylbutanenitrile (Table 3.2, Entry 3). The title compound was prepared according to the General Procedure from (3-chloro-4,4-dimethylpentyl)benzene (95.0 μL , 0.440 mmol) as the electrophile. The product was purified by column chromatography on silica gel (hexanes \rightarrow 10% Et₂O/hexanes). Yellow oil. First run: 75.0 mg (85% yield). Second run: 74.1 mg (84% yield).

¹H NMR (500 MHz, CDCl₃) δ 7.34–7.29 (m, 2H), 7.25–7.20 (m, 3H), 3.01 (ddd, 1H, $J = 13.8, 8.9, 4.9$ Hz), 2.67 (dt, 1H, $J = 13.8, 8.5$ Hz), 2.25 (dd, 1H, $J = 11.6, 4.3$ Hz), 1.92–1.79 (m, 2H), 1.03 (s, 9H).

¹³C NMR (126 MHz, CDCl₃) δ 140.7, 129.0, 128.8, 126.7, 121.6, 43.8, 34.5, 33.3, 29.5, 27.8.

ATR-IR (neat) 3028, 2963, 2938, 2875, 2233, 1602, 1498, 1488, 1472, 1463, 1456, 1399, 1375, 1368, 1317, 1233, 1030, 770, 757, 701 cm^{-1} .

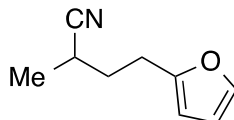
MS (EI) m/z (M^+) calcd for C₁₄H₁₉N: 201.2, found 201.2.



2,6-Dimethylhept-5-enitrile (Table 3.2, Entry 4) [54088-65-2].

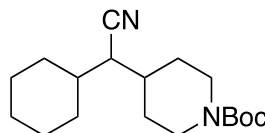
The title compound was prepared according to the General Procedure from 6-chloro-2-methylhept-2-ene (205 mg, 1.40 mmol) as the electrophile. The product was purified by column chromatography on silica gel (4% Et₂O/hexanes). Clear oil. First run: 161 mg (84% yield). Second run: 164 mg (85% yield).

^1H NMR (400 MHz, CDCl_3) δ 5.09–5.02 (m, 1H), 2.67–2.55 (m, 1H), 2.23–2.11 (m, 2H), 1.72–1.62 (m, 7H), 1.59–1.49 (m, 1H), 1.33–1.29 (m, 3H).



4-(Furan-2-yl)-2-methylbutanenitrile (Table 3.2, Entry 5) [71649-14-4]. The title compound was prepared according to the General Procedure from 2-(3-chlorobutyl)furan (221 mg, 1.40 mmol) as the electrophile. The product was purified by column chromatography on silica gel (10% Et_2O /hexanes). Yellow oil. First run: 160 mg (77% yield). Second run: 148 mg (71% yield).

^1H NMR (400 MHz, CDCl_3) δ 7.33–7.30 (m, 1H), 6.31–6.27 (m, 1H), 6.08–6.04 (m, 1H), 2.92–2.75 (m, 2H), 2.67–2.56 (m, 1H), 2.01–1.85 (m, 2H), 1.36–1.31 (m, 3H).



***t*-Butyl 4-(cyano(cyclohexyl)methyl)piperidine-1-carboxylate (Table 3.2, Entry 6).**

The title compound was prepared according to the General Procedure from tert-butyl 4-(chloro(cyclohexyl)methyl)piperidine-1-carboxylate (442 mg, 1.40 mmol) as the electrophile. The product was purified by column chromatography on silica gel (20→60% Et_2O /hexanes). Off-white solid. First run: 392 mg (91% yield). Second run: 406 mg (95% yield).

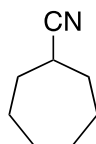
^1H NMR (500 MHz, CDCl_3) δ 4.28–4.06 (m, 2H), 2.74–2.61 (m, 2H), 2.22 (t, 1H, $J = 7.0$ Hz), 1.91–1.84 (m, 2H), 1.83–1.72 (m, 3H), 1.72–1.56 (m, 4H), 1.45 (s, 9H), 1.36–1.10 (m, 7H).

^{13}C NMR (126 MHz, CDCl_3) δ 155.0, 120.3, 80.0, 44.9, 36.0, 35.0, 32.0, 28.8, 26.4, 26.3, 26.1.

ATR-IR (neat) 2930, 2923, 2855, 2236, 1692, 1452, 1431, 1365, 1285, 1235, 1179, 1135 cm^{-1} .

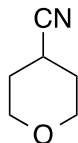
HRMS (ESI) m/z $[\text{M}-(\text{isobutylene})-(\text{CO}_2)+\text{H}]^+$ calcd for $\text{C}_{13}\text{H}_{23}\text{N}_2$: 207.2, found: 207.2.

Mp: 96.5–99.0 °C.



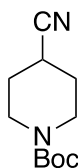
Cycloheptanecarbonitrile (Table 3.2, Entry 7) [32730-85-1]. The title compound was prepared according to the General Procedure from chlorocycloheptane (193 μL , 1.40 mmol) as the electrophile. The product was purified by column chromatography on silica gel (10→20% EtOAc/hexanes). Column fractions were analyzed by GC. Clear oil. First run: 138 mg (80% yield). Second run: 135 mg (78% yield).

^1H NMR (500 MHz, CDCl_3) δ 2.79 (tt, 1H, $J = 7.9, 4.6$ Hz), 1.96–1.82 (m, 4H), 1.80–1.70 (m, 2H), 1.67–1.53 (m, 6H).



Tetrahydro-2H-pyran-4-carbonitrile (Table 3.2, Entry 8) [4295-99-2]. The title compound was prepared according to the General Procedure from 4-chlorotetrahydro-2H-pyran (152 μL , 1.40 mmol) as the electrophile. The product was purified by column chromatography on silica gel (10 \rightarrow 50% EtOAc/hexanes). Column fractions were analyzed by GC. Tan oil. First run: 103 mg (66% yield). Second run: 111 mg (71% yield).

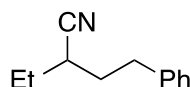
^1H NMR (500 MHz, CDCl_3) δ 3.91–3.85 (m, 2H), 3.62–3.56 (m, 2H), 2.86 (tt, 1H, $J = 8.2, 4.3$ Hz), 1.96–1.90 (m, 2H), 1.89–1.82 (m, 2H).



***t*-Butyl 4-cyanopiperidine-1-carboxylate** (Table 3.2, Entry 9) [91419-52-2]. The title compound was prepared according to the General Procedure from *tert*-butyl 4-chloropiperidine-1-carboxylate (277 μL , 1.40 mmol) as the electrophile. The product was purified by column chromatography on silica gel (40 \rightarrow 70% Et_2O /hexanes). Off-white solid. First run: 262 mg (89% yield). Second run: 248 mg (84% yield).

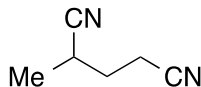
^1H NMR (500 MHz, CDCl_3) δ 3.69–3.60 (m, 2H), 3.37–3.29 (m, 2H), 2.83–2.76 (m, 1H), 1.91–1.83 (m, 2H), 1.82–1.74 (m, 2H), 1.47–1.43 (m, 9H).

Mp: 59.0–66.0 °C.



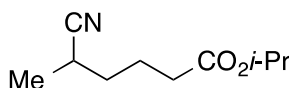
2-Ethyl-4-phenylbutanenitrile (Table 3.3, Entry 1) [1126479-77-3]. The title compound was prepared according to the General Procedure from (3-bromopentyl)benzene (259 μ L, 1.40 mmol) as the electrophile. The product was purified by column chromatography on silica gel (10 \rightarrow 20% Et₂O/hexanes). Tan oil. First run: 202 mg (83% yield). Second run: 205 mg (84% yield).

The ¹H NMR spectrum of the product was identical to that of Table 3.2, Entry 1.



2-Methylpentanedinitrile (Table 3.3, Entry 2) [4553-62-2]. The title compound was prepared according to the General Procedure from 4-bromopentanenitrile (162 μ L, 1.40 mmol) as the electrophile. The product was purified by column chromatography on silica gel (40 \rightarrow 80% Et₂O/hexanes). Yellow oil. First run: 124 mg (82% yield). Second run: 122 mg (81% yield).

¹H NMR (500 MHz, CDCl₃) δ 2.87–2.79 (m, 1H), 2.65–2.51 (m, 2H), 2.02–1.91 (m, 2H), 1.42–1.39 (m, 3H).



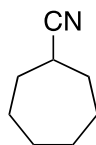
Isopropyl 5-cyanoheptanoate (Table 3.3, Entry 3). The title compound was prepared according to the General Procedure from isopropyl 5-bromohexanoate (237 μL , 1.40 mmol) as the electrophile. The product was purified by column chromatography on silica gel (20 \rightarrow 60% Et_2O /hexanes). Yellow oil. First run: 211 mg (82% yield). Second run: 208 mg (81% yield).

^1H NMR (500 MHz, CDCl_3) δ 5.05–4.96 (m, 1H), 2.66–2.58 (m, 1H), 2.32 (t, 2H, $J = 7.2$ Hz), 1.89–1.70 (m, 2H), 1.69–1.55 (m, 2H), 1.34–1.31 (m, 3H), 1.23 (d, 6H, $J = 6.3$ Hz).

^{13}C NMR (126 MHz, CDCl_3) δ 172.5, 122.8, 68.0, 34.0, 33.4, 25.5, 22.5, 22.0, 18.0.

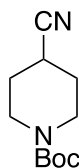
ATR-IR (neat) 2982, 2940, 2878, 2239, 1729, 1457, 1420, 1375, 1340, 1294, 1274, 1253, 1181, 1146, 1110 cm^{-1} .

MS (EI) m/z $[\text{M} - (\text{C}_3\text{H}_7\text{O})]^+$ calcd for $\text{C}_7\text{H}_{10}\text{NO}$: 124.1, found: 124.1.



Cycloheptanecarbonitrile (Table 3.3, Entry 4) [32730-85-1]. The title compound was prepared according to the General Procedure from bromocycloheptane (208 μL , 1.40 mmol) as the electrophile. The product was purified by column chromatography on silica gel (20 \rightarrow 40% Et_2O /hexanes). Column fractions were analyzed by GC. Yellow oil. First run: 157 mg (91% yield). Second run: 160 mg (93% yield).

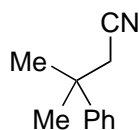
The ^1H NMR spectrum of the product was identical to that of Table 3.2, Entry 7.



***t*-Butyl 4-cyanopiperidine-1-carboxylate (Table 3.3, Entry 5) [91419-52-2].** The title compound was prepared according to the General Procedure from *tert*-butyl 4-bromopiperidine-1-carboxylate (276 μ L, 1.40 mmol) as the electrophile. The product was purified by column chromatography on silica gel (40 \rightarrow 80% Et₂O/hexanes). Off-white solid. First run: 242 mg (82% yield). Second run: 250 mg (85% yield).

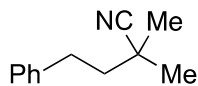
¹H NMR (500 MHz, CDCl₃) δ 3.69–3.60 (m, 2H), 3.37–3.29 (m, 2H), 2.83–2.76 (m, 1H), 1.91–1.83 (m, 2H), 1.82–1.74 (m, 2H), 1.47–1.43 (m, 9H).

Mp: 59.0–66.0 °C.



3-Methyl-3-phenylbutanenitrile (eq 2) [17684-33-2]. The title compound was prepared according to the General Procedure from (1-chloro-2-methylpropan-2-yl)benzene (226 μ L, 1.40 mmol) as the electrophile. The product was purified by column chromatography on silica gel (10 \rightarrow 20% EtOAc/hexanes). Tan oil. First run: 184 mg (83% yield). Second run: 174 mg (78% yield).

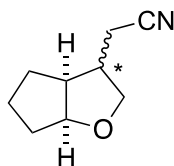
¹H NMR (500 MHz, CDCl₃) δ 7.40–7.34 (m, 4H), 7.28–7.24 (m, 1H), 2.62 (s, 2H), 1.52 (s, 6H).



2,2-Dimethyl-4-phenylbutanenitrile (eq 3) [75490-38-9]. The title compound was prepared according to the General Procedure from (3-chloro-3-methylbutyl)benzene (256 mg, 1.40 mmol) as the electrophile. The product was purified by column

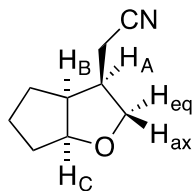
chromatography on silica gel (hexanes→10% Et₂O/hexanes). Clear oil. First run: 149 mg (61% yield). Second run: 153 mg (63% yield).

¹H NMR (500 MHz, CDCl₃) δ 7.35–7.27 (m, 2H), 7.25–7.18 (m, 3H), 2.85–2.76 (m, 2H), 1.88–1.78 (m, 2H), 1.42 (s, 6H).



2-((3a*S*,6a*S*)-Hexahydro-2*H*-cyclopenta[*b*]furan-3-yl)acetonitrile (eq 7). In an N₂-atmosphere glovebox, a 20-mL vial was charged with TBACN (266 mg, 0.991 mmol) and a stir bar. To this vial was added 8.3 mL of MeCN, and the solution was stirred vigorously for 5 minutes. Next, CuCl (9.33 mg) was weighed into an oven-dried 20-mL quartz test tube, and the TBACN solution was added to the tube. To this suspension was added trans-1-(allyloxy)-2-chlorocyclopentane (100 mg, 0.622 mmol), and the tube was capped with a rubber septum and sealed with electrical tape. The solution was stirred for another 3 minutes, and was then brought out of the glovebox and irradiated in the center of four, 15 watt UVC compact fluorescent light bulbs at room temperature` for 24 h. The ratio of diastereomers was determined by GC analysis of the unpurified reaction mixture. The product was isolated as a mixture of diastereomers by column chromatography (5% Et₂O/hexanes→Et₂O). Clear liquid. First run: 25 mg (27%, 2.3:1). Second run: 28 mg (30%, 2.1:1).

Major diastereomer. The major diastereomer could be purified by preparative HPLC (ZORBAX RX-SIL column, 9.4 x 250 mm, 20% EtOAc/hexanes).



¹H NMR (400 MHz, CDCl₃) δ 4.56 (td, 1H, *J* = 5.8, 2.5 Hz), 3.97—3.89 (m, 1H), 3.48 (t, 1H, *J* = 8.3 Hz), 2.75–2.62 (m, 2H), 2.46–2.33 (m, 2H), 1.87–1.58 (m, 5H), 1.53–1.41 (m, 1H).

2D NOESY (400 MHz, CDCl₃) δ [4.55 (H_C), 3.91 (H_{eq})], [4.55 (H_C), 2.68 (H_A/H_B)], [3.91 (H_{eq}), 4.55 (H_C)], [3.91 (H_{eq}), 2.68 (H_A/H_B)], [2.68 (H_A/H_B), 3.91 (H_{eq})], [2.68 (H_A/H_B), 4.55 (H_C)].

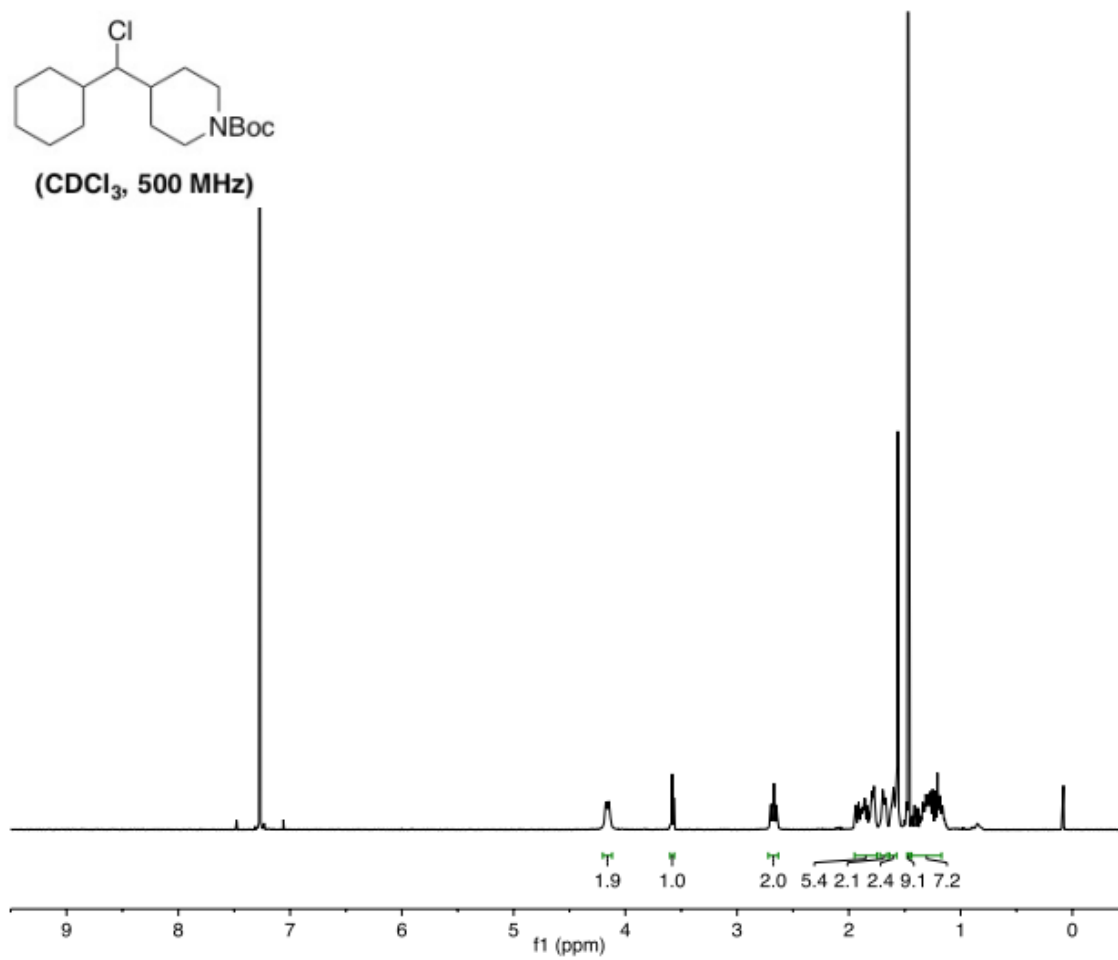
¹³C NMR (100 MHz, CDCl₃) δ 118.9, 86.5, 71.5, 46.1, 39.6, 34.2, 26.2, 25.7, 16.7.

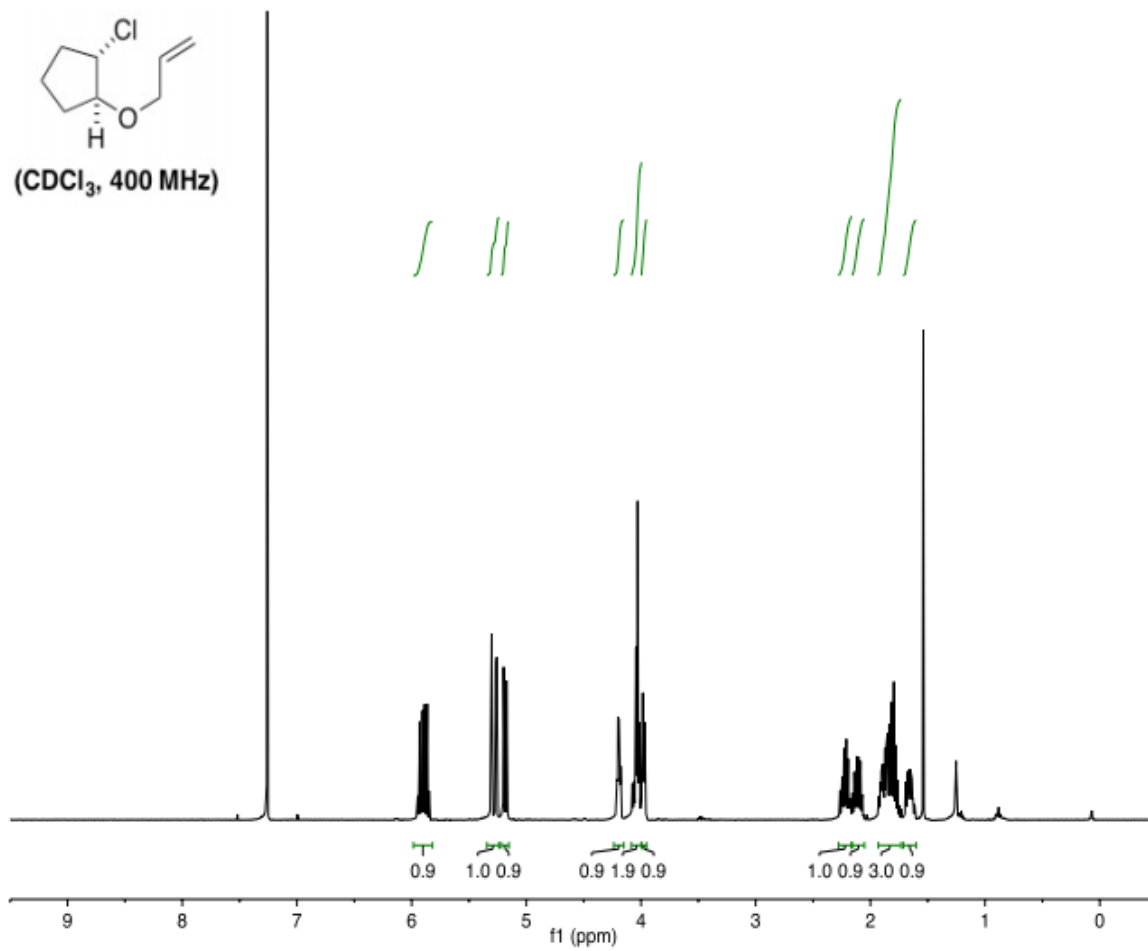
ATR-IR (neat) 2955, 2869, 2246, 1483, 1468, 1451, 1426, 1339, 1307, 1261, 1205, 1154, 1080, 1043, 960, 950, 922, 901, 806, 649 cm⁻¹.

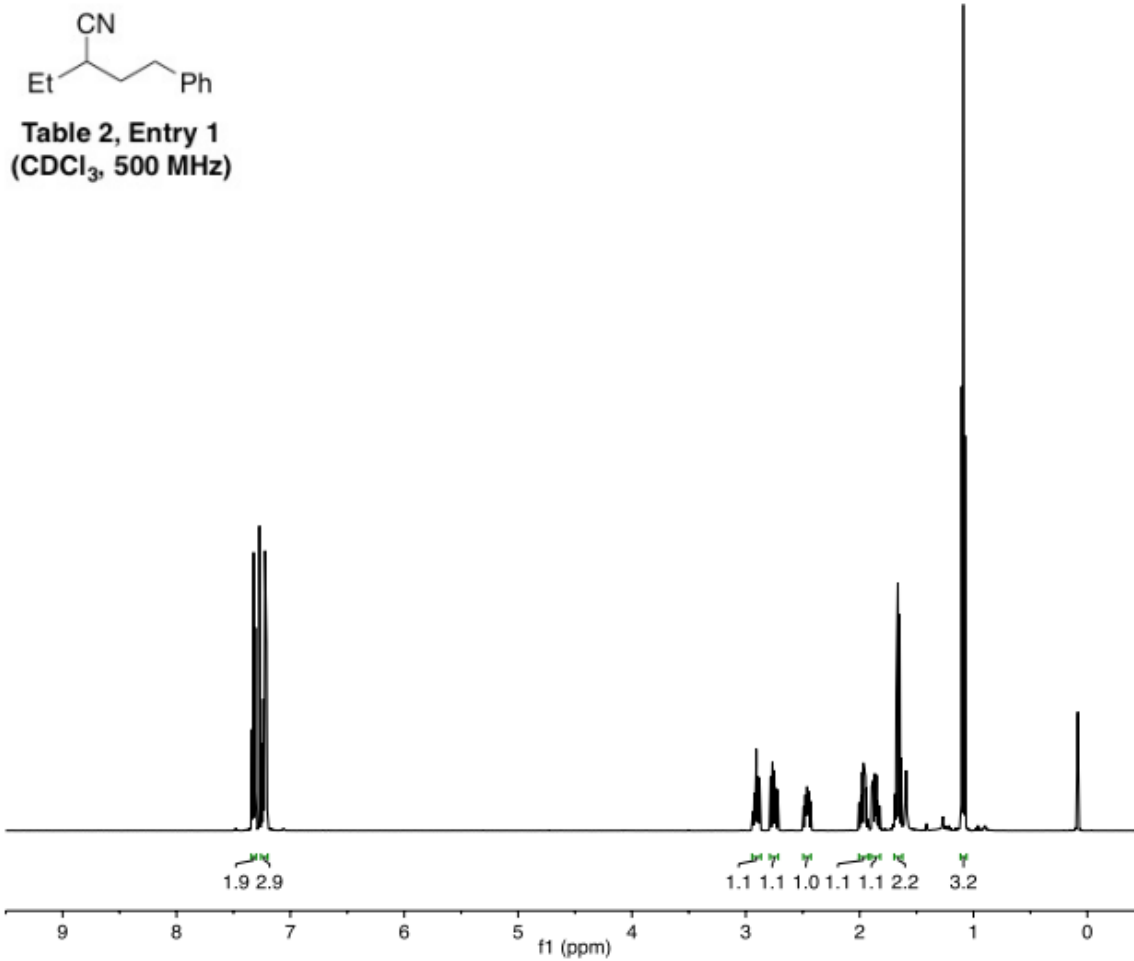
MS (EI) *m/z* (M⁺) calcd for C₉H₁₃NO: 151.1, found: 151.1.

B.4 Electrophile Competition Experiments (eq 4 and eq 5)

Inside a glovebox, tetrabutylammonium cyanide (26.8 mg, 0.10 mmol) was added to an oven-dried 10-mL quartz test tube. Then, CH₃CN (0.60 mL) and each alkyl halide (0.50 mmol) were added in turn, along with a stir bar. The reaction mixture was stirred for 2 min, and then a solution of CuI in CH₃CN (0.70 mL, 0.011 M) was added. The quartz test tube was capped with a rubber septum and wrapped with electrical tape, and the reaction was stirred for 1 min. The quartz tube was removed from the glovebox, and the resulting mixture was then stirred vigorously and irradiated in the center of four, 15 watt UVC compact fluorescent light bulbs at room temperature for 24 h. The ratio of products was determined by GC analysis after 24 h.

B.5 ^1H NMR Spectra





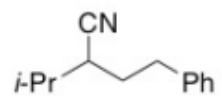
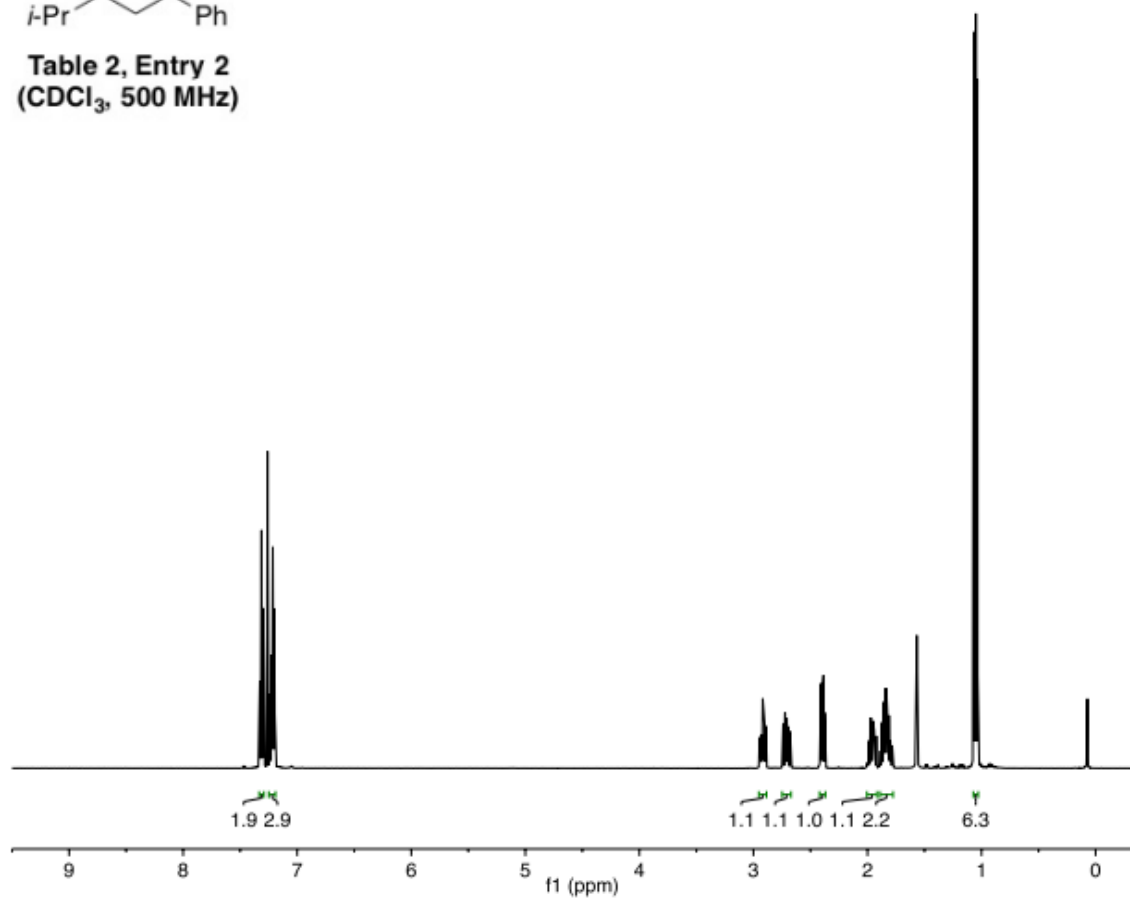


Table 2, Entry 2
(CDCl₃, 500 MHz)



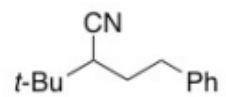
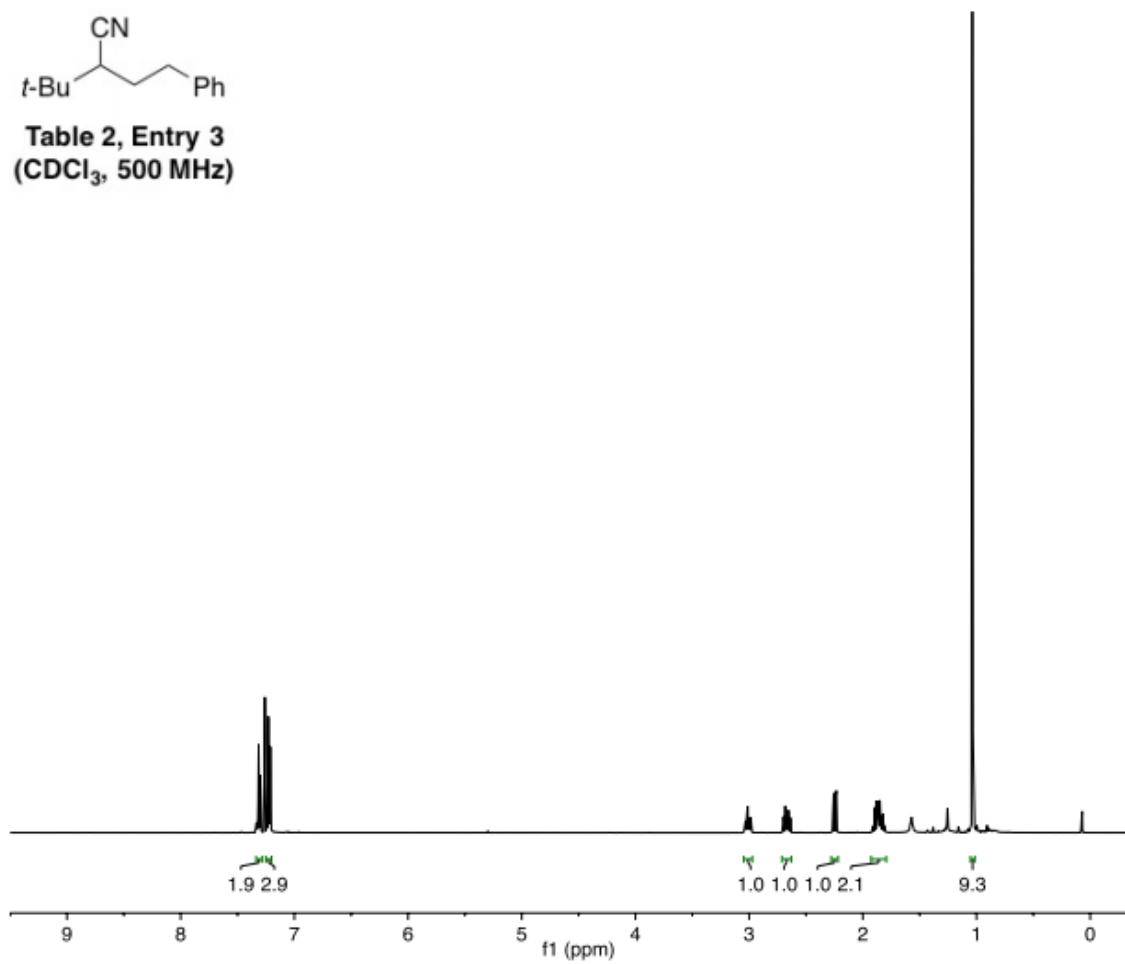


Table 2, Entry 3
(CDCl₃, 500 MHz)



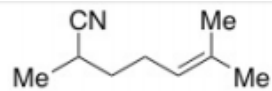
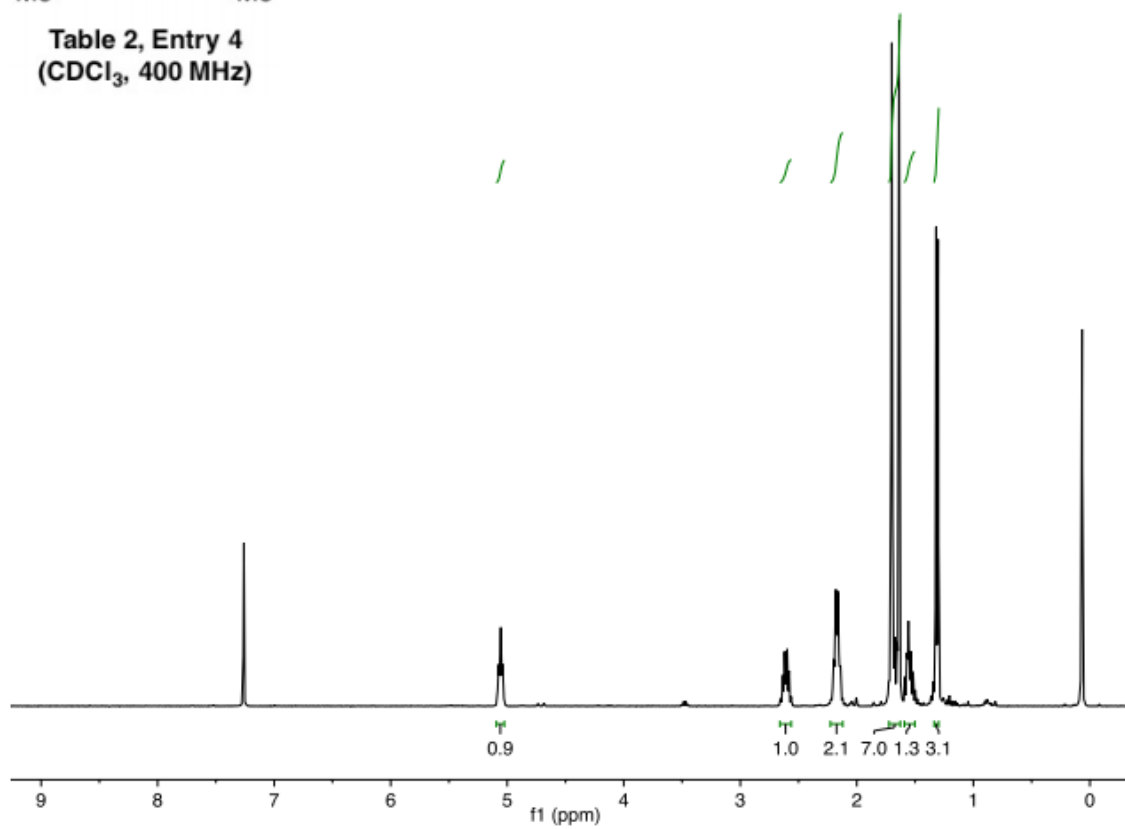


Table 2, Entry 4
(CDCl₃, 400 MHz)



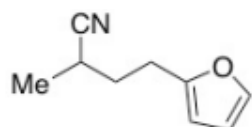
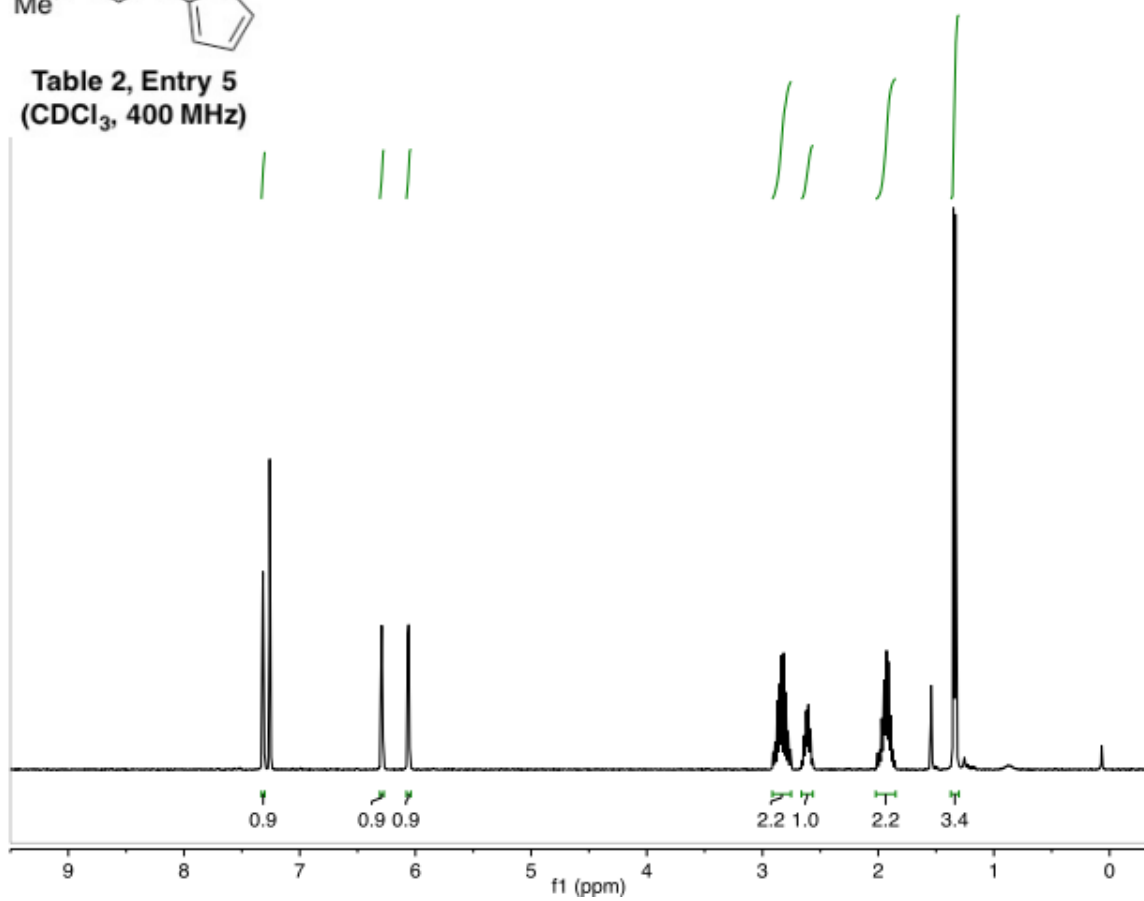


Table 2, Entry 5
(CDCl₃, 400 MHz)



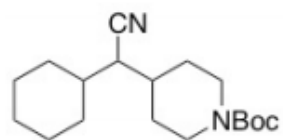
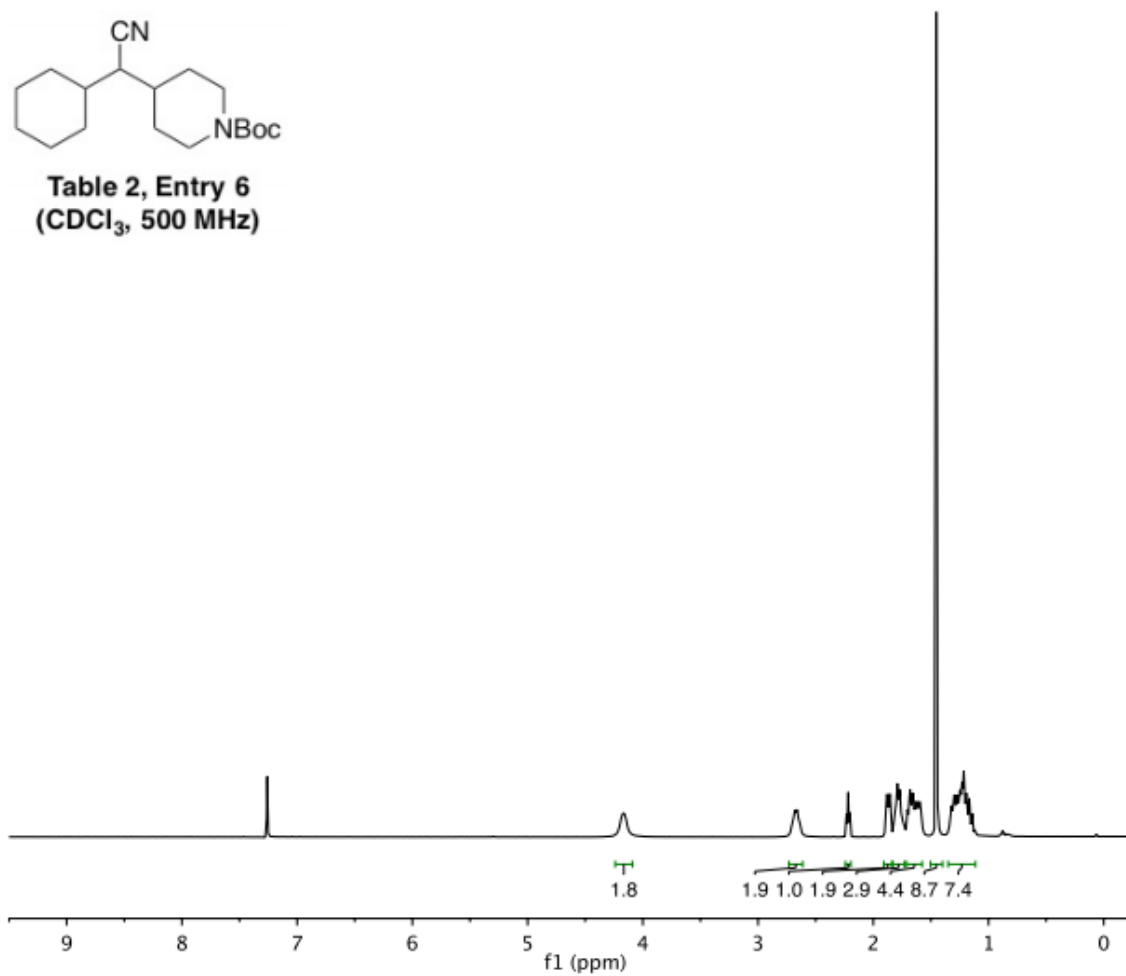


Table 2, Entry 6
(CDCl₃, 500 MHz)



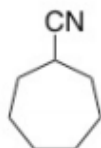


Table 2, Entry 7
(CDCl₃, 500 MHz)

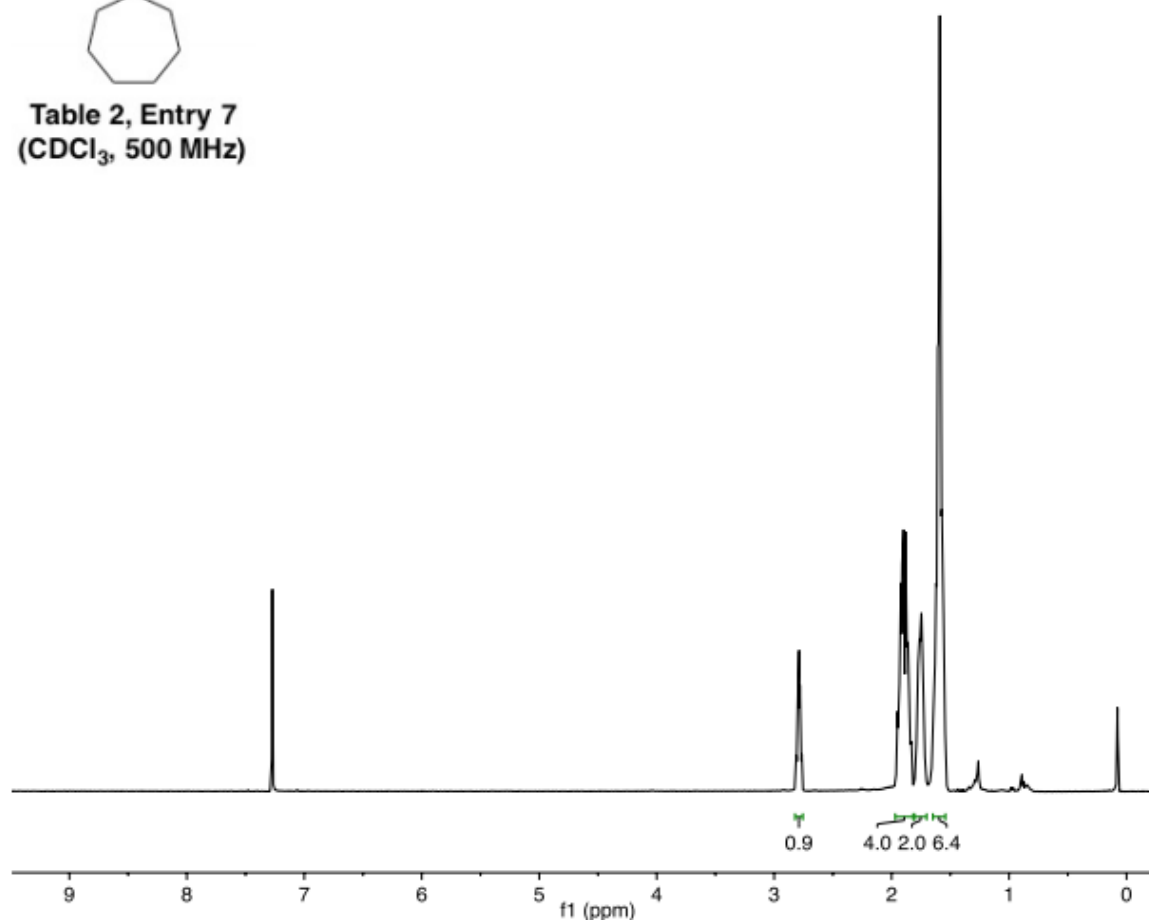
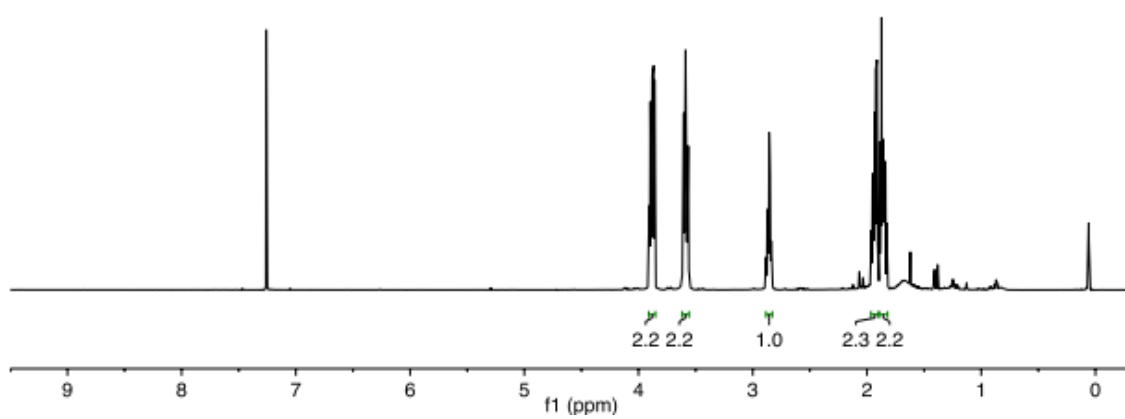




Table 2, Entry 8
(CDCl₃, 500 MHz)



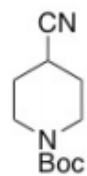
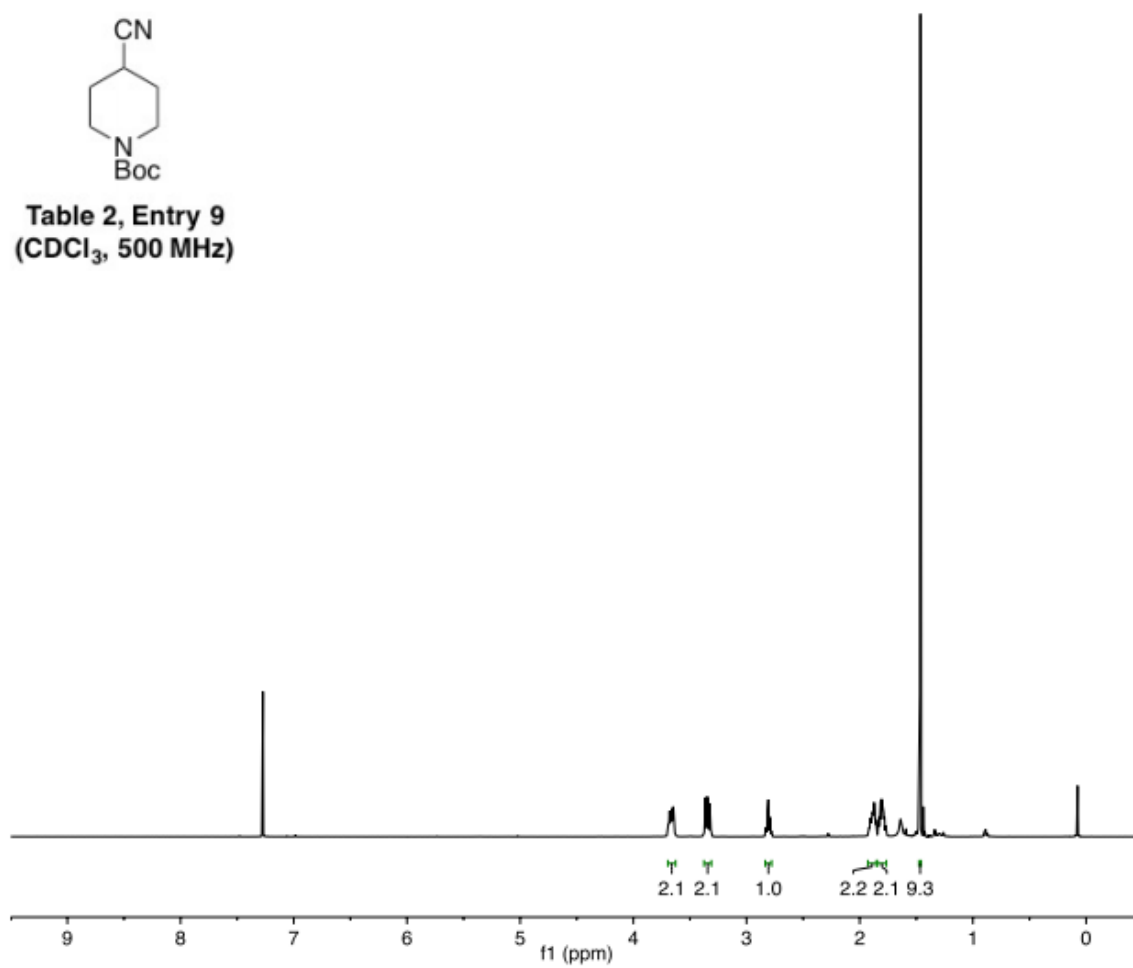


Table 2, Entry 9
(CDCl₃, 500 MHz)



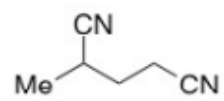
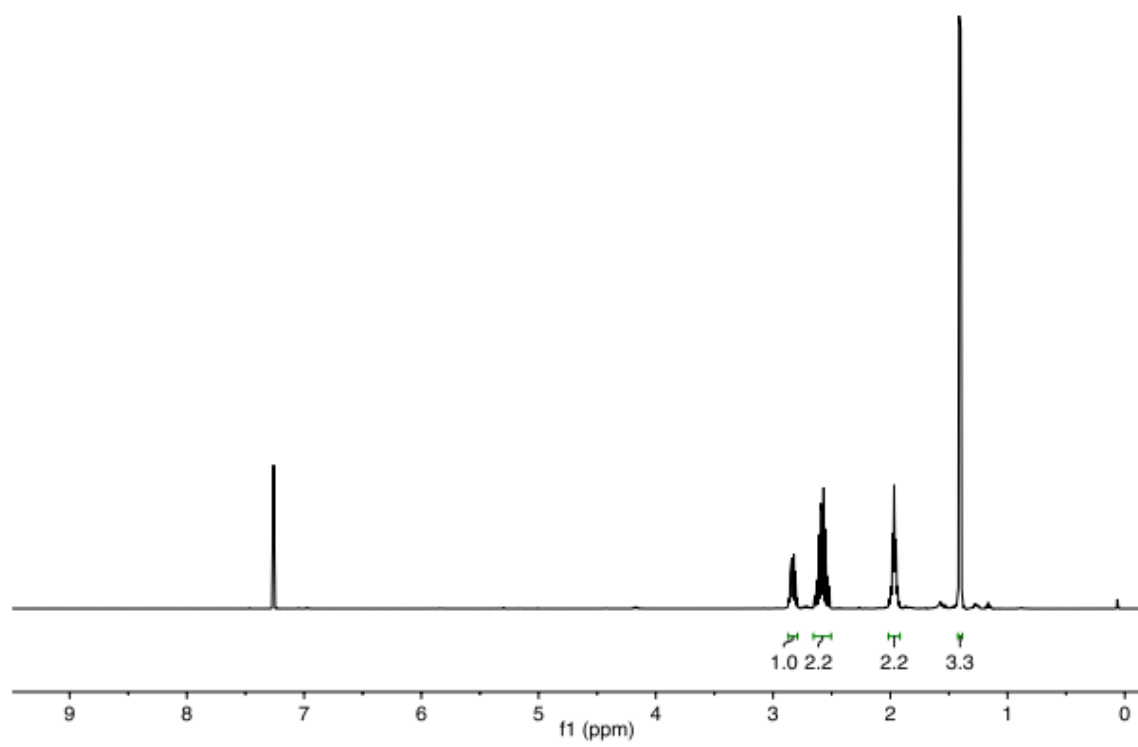


Table 3, Entry 2
(CDCl₃, 500 MHz)



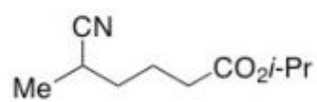
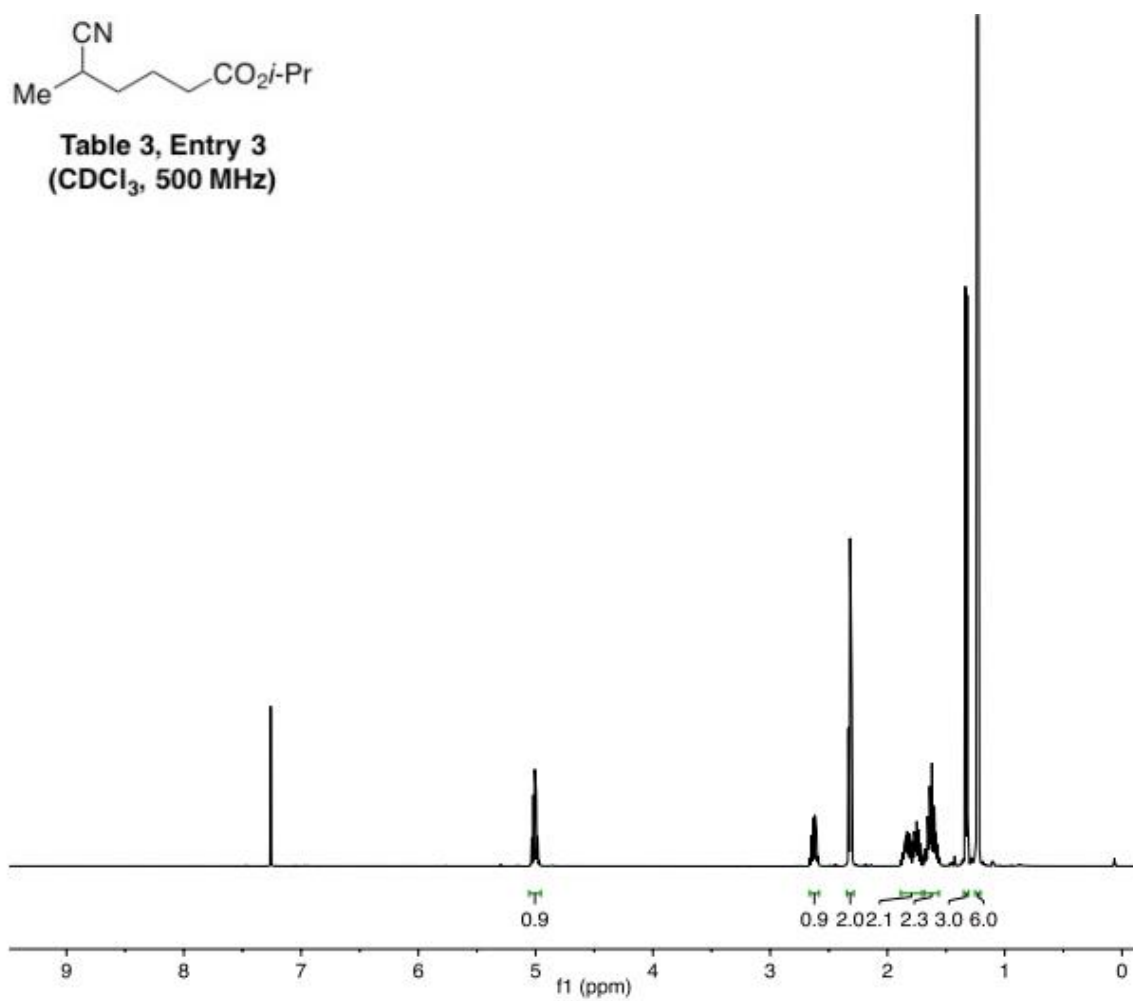
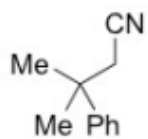
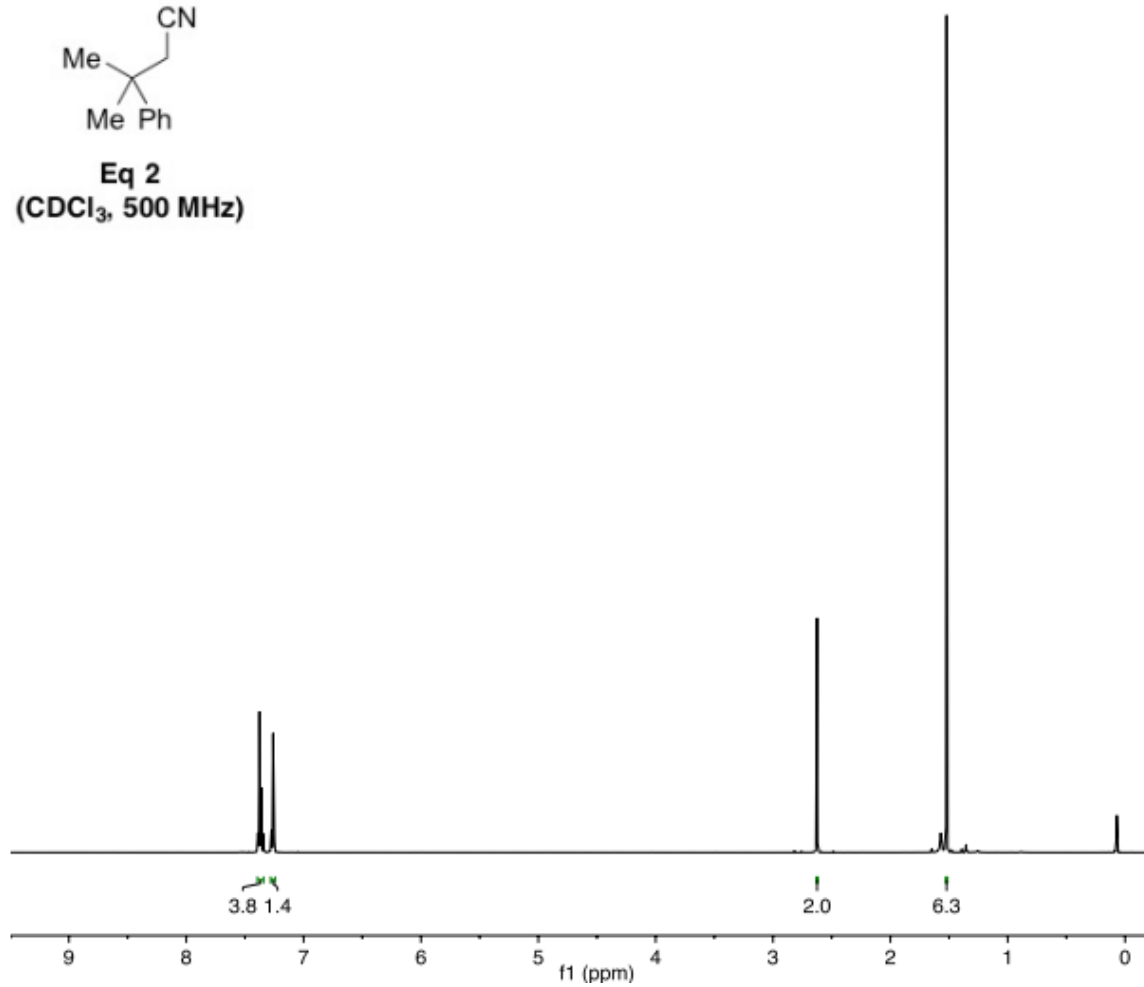


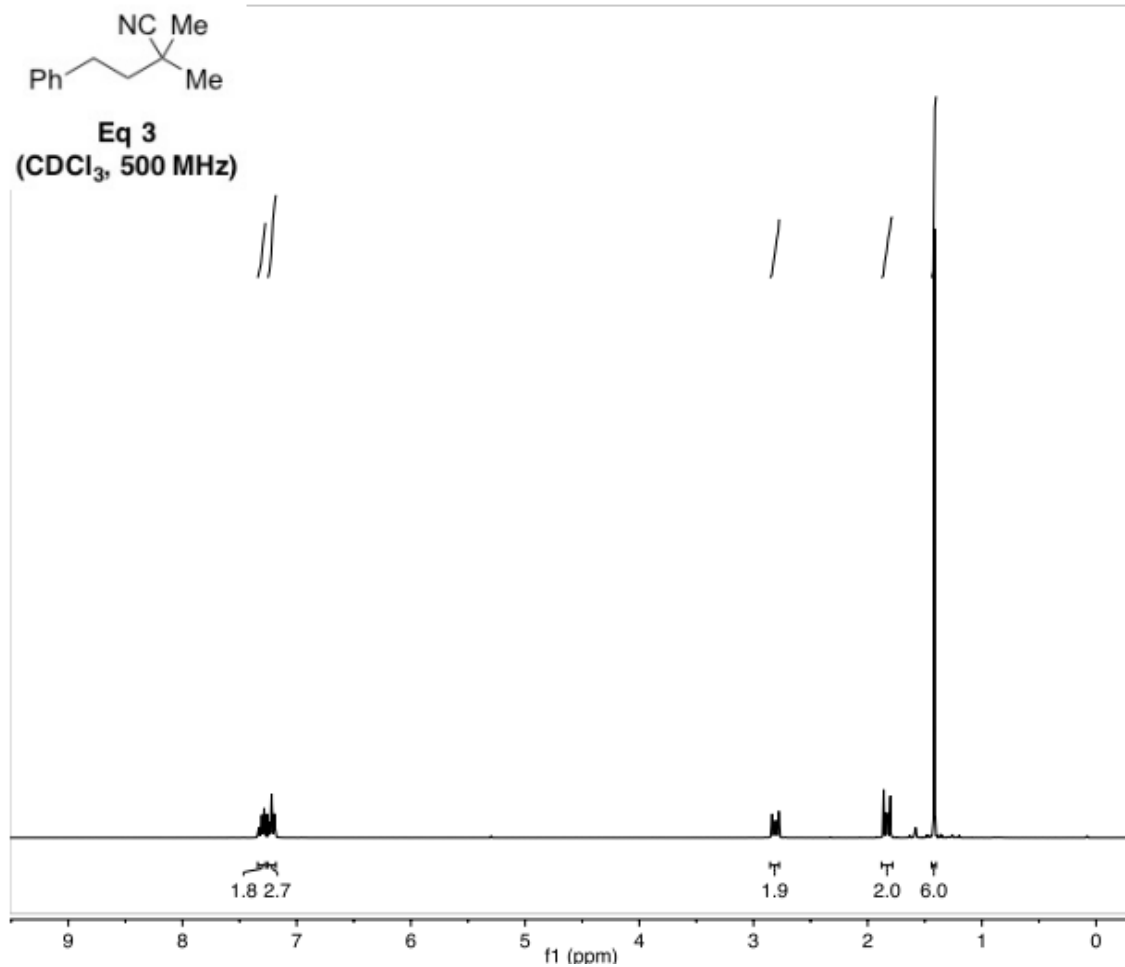
Table 3, Entry 3
(CDCl₃, 500 MHz)

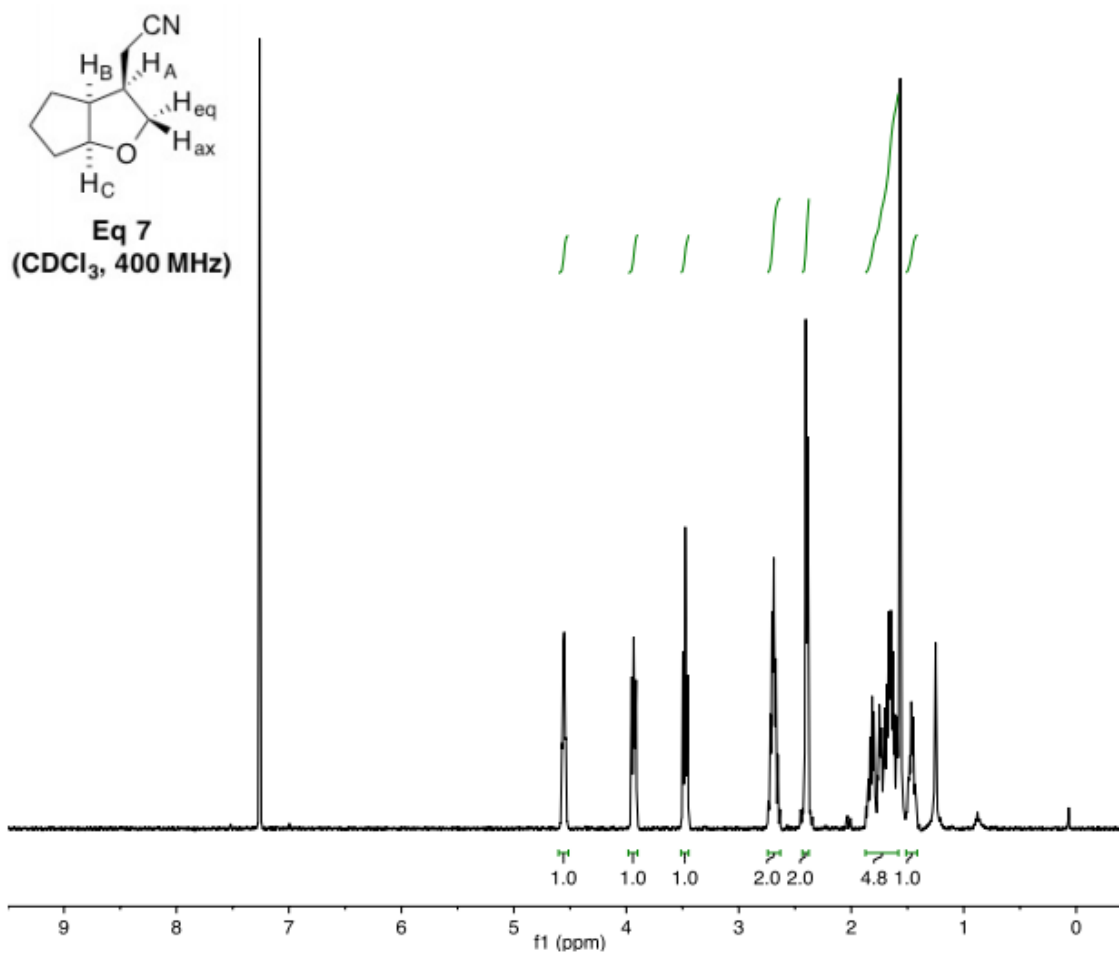




Eq 2
(CDCl₃, 500 MHz)







B.6 References

1. Powell, D. A.; Maki, T.; Fu, G. C. *J. Am. Chem. Soc.* **2005**, *127*, 510–511.

Appendix C : Supplementary Information for Chapter 4

C.1 General Information

Chemicals. Unless otherwise noted, all materials were purchased from commercial suppliers and used as received. All manipulations of air-sensitive materials were carried out in oven-dried glassware using standard Schlenk or glovebox techniques under an N₂ atmosphere. Solvents were deoxygenated and dried by thoroughly sparging with N₂ followed by passage through an activated column in a solvent purification system.

EPR, Infrared, and UV-vis Spectroscopy. X-band EPR measurements were made with a Bruker EMX spectrometer at 77 K. Simulation of EPR data was conducted using the software EasySpin.¹ IR measurements were recorded on a Bruker ALPHA Diamond ATR or a Bruker Vertex 80 spectrometer. Absorbance spectra were acquired on a Cary 50 UV-vis spectrophotometer with a Unisoku Scientific Instruments cryostat to maintain temperature.

NMR spectroscopy. ¹H, ²H, and ¹³C spectra were recorded on a Bruker Ascend 400, a Varian 400 MHz, or a Varian 500 MHz, or a Varian 600 MHz spectrometer. Referencing was done using either the proteo impurity in a deuterated solvent, or to the deuterium lock signal. Multiplicity and qualifier abbreviations are as follows: s = singlet, d = doublet, t = triplet, q = quartet, m = multiplet.

Gas chromatography-mass spectrometry (GC-MS). GC-MS data was collected at the Environmental Analysis Center at Caltech. Data was recorded on an Agilent MSD 5970 with an Agilent 5890 GC. The mass selective detector was set to 30 and 44 to detect for NO (m/z = 30) and N₂O (m/z = 44, 30). The detector was calibrated before each use with N₂O in the relevant volume of MeCN. Retention times were compared with pure samples of NO and N₂O at similar concentrations.

Catalytic Reactions (Table 4.1). Photocatalytic reactions were performed with a 500 W Hg arc lamp (Newport 6285; Oriel 66023 housing) with a 400 nm long pass filter in front of the lamp. A lens was used to focus the beam upon the reaction mixture, and was placed the same distance away for each catalytic run to ensure equal light intensities for each run. Heating of sample was prevented with the use of a fan between the lamp and the reaction mixture, and temperature readings after the reaction completed were found to be 25 °C. For Table 4.1. Reaction mixtures contained 0.55 mM [(Br)(μ -OAc)Co(^{Me}doen)Mg(Me₃TACN)][BPh₄] (**1**), 0.55 mM [(phen)Ir(ppy)₂][PF₆] (**2**), 82.5 mM NEt₃, 11 mM tetrabutylammonium nitrite, and 82.5 mM triethylammonium chloride dissolved in 5 mL of acetonitrile. Reactions were stirred vigorously during irradiation.

Photophysical Methods. Time-resolved luminescence and step-scan time-resolved Fourier-transform infrared (SS-TRIR) spectroscopy were performed in the Beckman Institute Laser Resource Center (BILRC; California Institute of Technology). Samples for room temperature luminescence measurements were prepared in dry (passage through alumina three times), degassed (three freeze-pump-thaw cycles) acetonitrile inside a nitrogen-filled glovebox, and transferred to a 1-cm path length fused quartz cuvette (Starna Cells) which was sealed with a high-vacuum Teflon valve (Kontes). Steady-state emission spectra were collected on a Jobin S4 Yvon Spec Fluorolog-3-11 with a Hamamatsu R928P photomultiplier tube detector with photon counting.

For luminescence and SS-TRIR spectroscopy at the nanosecond to microsecond time scale, a Q-switched Nd:YAG laser (Spectra-Physics Quanta-Ray PRO-Series; 355 nm; pulse duration 8 ns, operating at 10 Hz) was used as the source of the excitation pulse, with variable laser power. The third harmonic (355 nm) was pumped through a tunable

optical parametric oscillator (OPO, Spectra-Physics Quanta-Ray MOPO-700) to provide laser pulses at 460 nm. Transmitted light from the sample was detected with a photomultiplier tube (Hamamatsu R928). All instruments and electronics in these systems were controlled by software written in LabVIEW (National Instruments). Data manipulation was performed with MatlabR2014B.

TRIR was collected on a Bruker Vertex 80 spectrometer and the laser pulsing/data collection was triggered using OPUS software. Samples were prepared in a Harrick demountable liquid flow cell (DLC-S25) with CaF₂ windows and 500 μm path length (Teflon spacers). Time resolution was set to 50 ns, and spatial resolution was set to 8 or 16 cm^{-1} . The laser light was aligned so as to be collinear with the source IR beam. At each point of rest for the moveable mirror, the AC components of the phototriggered transient interferogram are processed by an external amplifier and Fourier transformed into a spectrum. CD₃CN was used as the solvent to allow for a spectral window between 1600 and 1700 cm^{-1} unobscured by solvent signals. Because of the IR bands from **2** and CD₃CN, the range from 1600 to 1700 cm^{-1} was the only window accessible for data analysis. Furthermore, TRIR runs were expedited (to improve sample longevity) with the use of an IR filter (Northumbria Optical Coatings Ltd, Serial No. SBP-5937-000296).

C.2 Procedure for Photocatalytic Nitrite Reduction

A solution of NEt_3 (0.41 mmol, 57.5 μL) and NEt_3HCl (0.41 mmol, 56.4 mg) dissolved in 2.5 mL MeCN was added to a solution of **1** (varying amounts, see below), **2** (varying amounts, see below), and tetrabutylammonium nitrite (0.055 mmol, 15.8 mg) in 2.5 mL MeCN and stirred vigorously in the dark (foil or an amber glass bottle was used). The solution was transferred to a 25 mL Schlenk tube which was wrapped in foil. The foil was then removed and the catalytic reaction mixture was irradiated with an arc lamp ($\lambda > 400$ nm) for 1 h.

We determined the concentration of ER at which the amount of N_2O was maximized by maintaining [**2**] at 4.0 mM and varying [**1**] (Figure C.1b). We chose a concentration of PS in the “plateau region” (Figure C.1a) to ensure that any changes in N_2O production would not be due to small differences in the concentration of the photosensitizer. As shown in Figure C.1b and Table C.1, the volume of N_2O is maximized at 0.55 mM **1**, but the TON is maximized when [Co] is low. The decrease in N_2O volume as the concentration of **1** is increased can be attributed to **1** competing with **2** for photons. One possible reason for the reduction in TON with increasing [**1**], a trend which has been observed in photocatalytic reactions with a Co electron relay, could be an intermolecular reaction between the reduced Co catalyst and other Co species which generates complexes which are inactive for catalysis.²

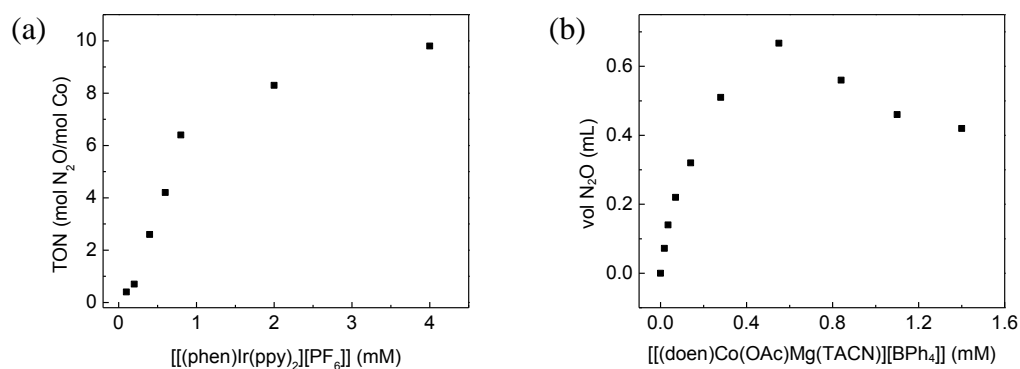


Figure C.1: (a) Variation in turnover number of N₂O as a function of photosensitizer concentration. [1] was kept at 0.55 mM in all cases. (b) Variation in volume of N₂O as a function of [1]. [2] was kept at 4.0 mM in all cases. All reactions were performed in identical reaction vessels the same distance away from an arclamp light source with a long pass filter ($\lambda > 400$ nm).

Table C.1: Effect of [1] on the Amount and Turnover Number of Nitrous Oxide Generated.

[1]	vol N ₂ O (mL) ^a	TON/Co
0.018	0.072	34
0.035	0.14	33
0.070	0.22	25
0.14	0.32	18
0.28	0.51	15
0.55	0.67	9.8
0.84	0.56	5.5
1.1	0.46	3.4
1.4	0.42	2.4

C.3 UV-Vis Absorbance and Fluorimetry Experiments

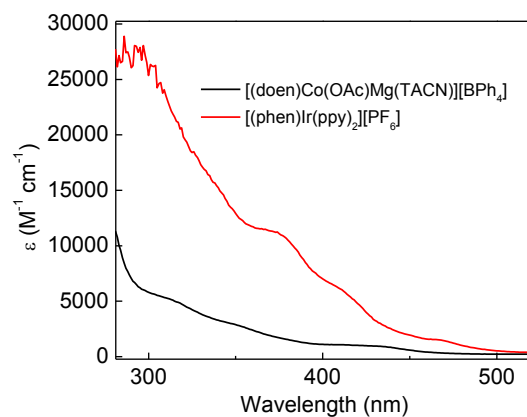


Figure C.2: UV-vis absorption spectrum of **1** and **2**.

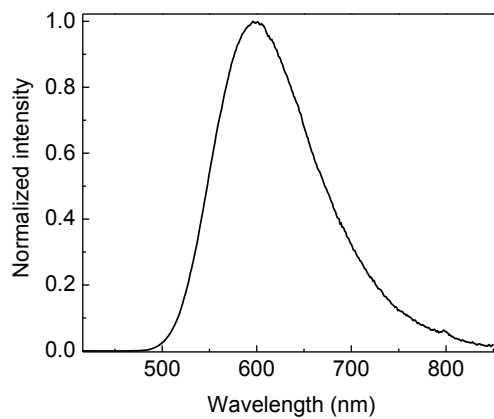


Figure C.3: Emission spectrum of **2**. Excitation wavelength = 400 nm, emission λ_{max} = 600 nm.

C.4 Stern-Volmer Quenching

2 was diluted in acetonitrile to make four 0.55 mM solutions (3 mL each). Triethylamine was added to three of these solutions with a microliter syringe to make 50, 100, and 150 mM solutions (21, 42, and 64 μL) to measure quenching rates with this reductive quencher. In a second, similar, set of experiments, the rate of quenching of **2*** with **1** was measured. In this case, a 1.5 mL solution of 1.1 mM **2** was added to solutions of **1** to make 1, 2, and 4 mM solutions of **1**. All solutions were pipetted into cuvettes with a path length of 1 cm. The lifetime of an emissive excited state of **2** as a function of NEt_3 or **1** was measured by luminescence spectroscopy ($\lambda_{\text{pump}} = 460 \text{ nm}$, $\lambda_{\text{probe}} = 600 \text{ nm}$). The lifetime of the emissive excited state of **2** was found to be 807 ns. The rate of electron transfer with NEt_3 was calculated to be $1.5 \times 10^8 \text{ M}^{-1} \text{ cm}^{-1}$; with **1**, it was found to be $1.6 \times 10^9 \text{ M}^{-1} \text{ cm}^{-1}$.

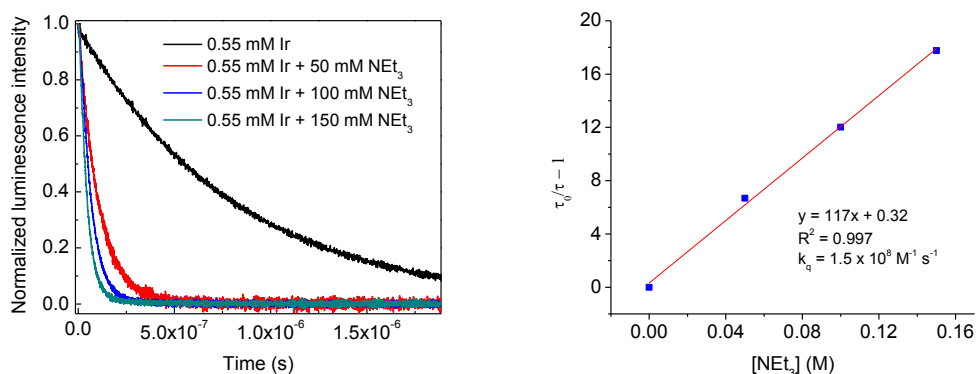


Figure C.4: Luminescence decays for **2** with varying NEt_3 concentrations.

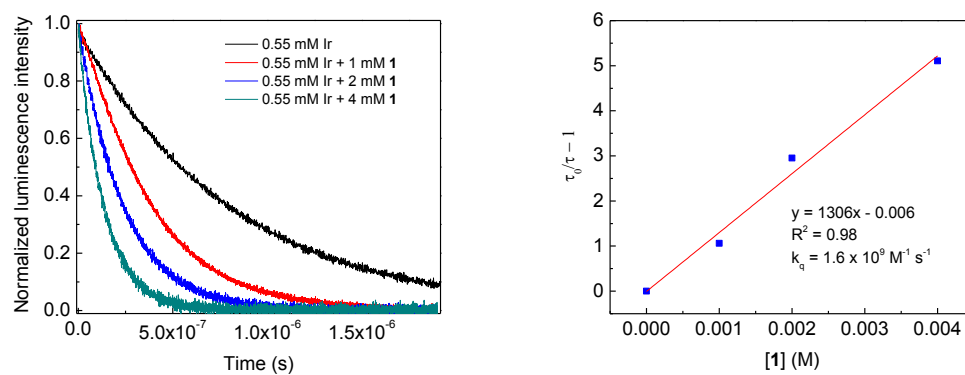


Figure C.5: Luminescence decays for **2** with varying **[1]**.

Table C.2: Excited state lifetime of **2** as a function of NEt_3 concentration (Figure C.4).

$[\text{NEt}_3]$ (mM)	Lifetime (ns)
0	807
50	105
100	62
150	43

Table C.3: Excited state lifetime of **2** as a function of Co (**1**) concentration (Figure C.5).

[1] (mM)	Lifetime (ns)
0	806
1	391
2	204
4	132

C.5 EPR Spectroscopy of {CoNO}⁹

[(Cl)(NO)Co(^{Me}doen)Mg(Me₃TACN)(H₂O)][BPh₄] (**4**) (2.4 mg, 0.0027 mmol) or **4**-¹⁵NO was dissolved in 200 μ L of butyronitrile and frozen at 77 K in an EPR tube. CoCp₂ (0.5 mg, 0.0027 mmol) dissolved in butyronitrile as a stock solution was added to this frozen glass, and allowed to freeze. Then, the solution was quickly thawed and shaken for 10 s, causing the reaction mixture to change from red to green, and refrozen at 77 K. An identical EPR spectrum for {CoNO}⁹ (Figure C.6, red trace) was obtained when **2** and NEt₃ were added to a solution of **4** and irradiated for 10 s.

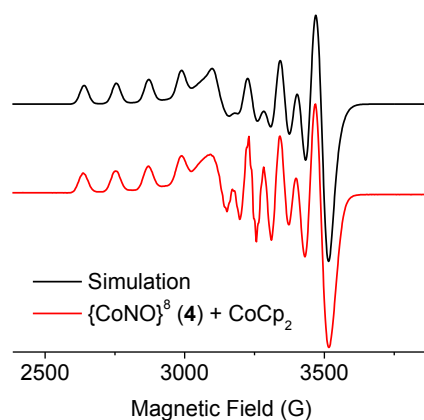


Figure C.6: EPR spectra (9.4 GHz, 77 K). Red trace: mixture of **4** and CoCp₂ in frozen butyronitrile glass; Black trace: simulation parameters: $g = [2.0430, 2.044, 2.209]$; isotropic linewidth (Gaussian lineshape, FWHM = 3.34 mT). Coupling to one Co nucleus was included with $A = [148\ 156\ 363.8]$.

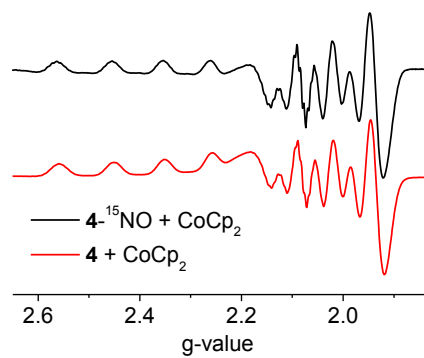


Figure C.7: EPR spectra (9.4 GHz, 77 K). Red trace: mixture of **4** and CoCp₂ in frozen butyronitrile glass; Black trace: mixture of 4-¹⁵NO and CoCp₂ in frozen butyronitrile glass.

C.6 Infrared Spectroscopy

For solution FTIR spectroscopy, all samples were made in 20 mL scintillation vials, and then the solution was pulled into a 5 or 10 mL Hamilton gastight syringe with a Luer lock to ensure air-free sample manipulation. This syringe was then screwed into the female Luer lock attached to the flow cell tubing, and solution was flowed between two syringes until there were no bubbles. The solution was irradiated with a blue LED through a fused silica window and a directing prism.

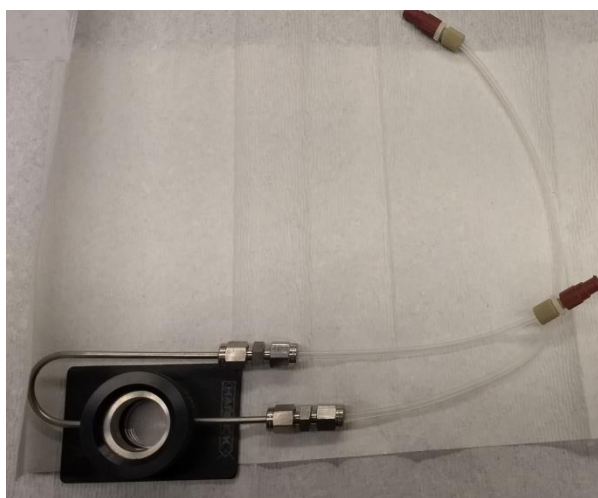


Figure C.8: Harrick demountable liquid flow cell (DLC-S25) with CaF_2 windows and 500 μm path length Teflon spacers.

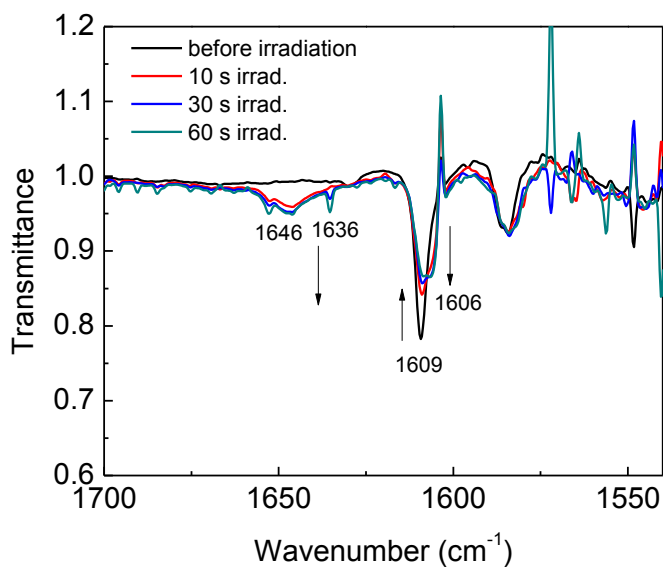


Figure C.9: Background/control solution IR (CD_3CN) of **2** and NEt_3 to assign Ir-based peaks.

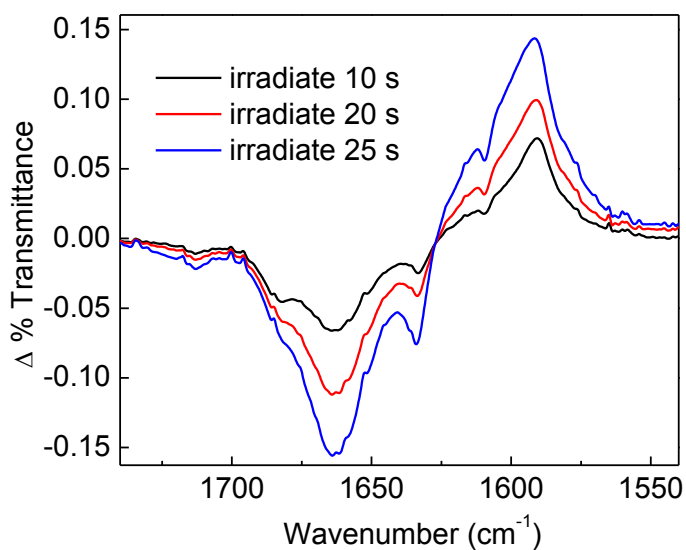


Figure C.10: Solution IR difference spectrum of $4\text{-}^{15}\text{NO}$ irradiated in the presence of **2** and NEt_3 . The peak at 1663 is due to the appearance of $\{\text{Co}^{15}\text{NO}\}^9$.

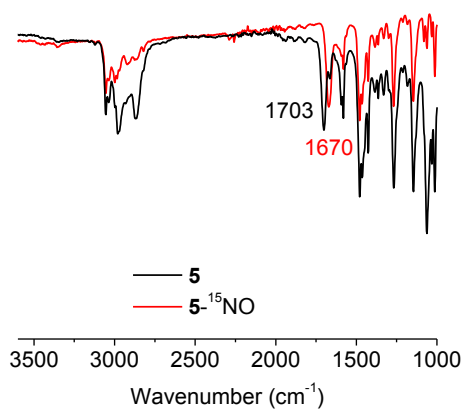


Figure C.11: ATR-IR (film) spectra of **5** and **5-¹⁵N**O. The stretch at 1701 cm⁻¹ arises from the ¹⁴N¹⁵O vibration; the corresponding ¹⁵N¹⁵O vibration appears at 1670 cm⁻¹.

C.7 GC-MS Data

In a glove box, a 0.5 mL solution of CoCp_2 (0.4 mg, 0.0022 mmol) was added by syringe to a septum-capped 2 mL solution of **4**, turning the reaction from brown-red to dark green. The reaction was stirred quickly at room temperature for 30 s. The solution was quickly removed from the box and the headspace was sampled after five minutes (Figure C.12). Free NO and N_2O were observed. Upon addition of acid, all free NO is gone.

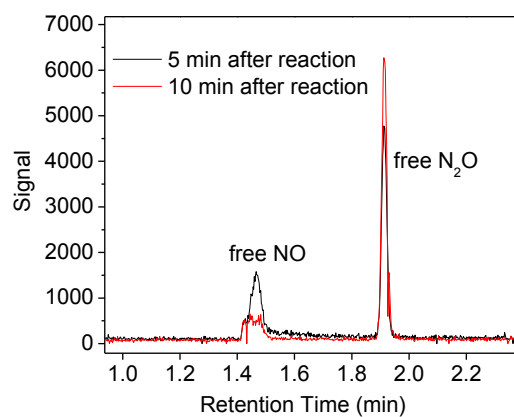


Figure C.12: Headspace analysis of a reaction of **4** and CoCp_2 over time.

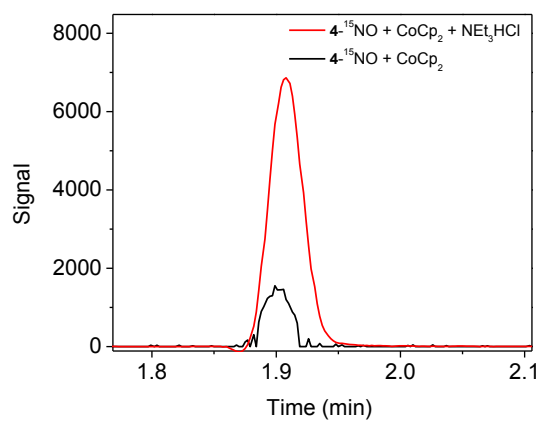


Figure C.13: Appearance of $^{15,15}\text{N}_2\text{O}$ at $m/z = 31$ (and $m/z = 46$) when 4- ^{15}NO is substituted for **4**.

C.8 Step-scan TRIR Data

Flow rates during laser irradiation and laser power (2 mJ/pulse) were optimized on this system to maximize signal.

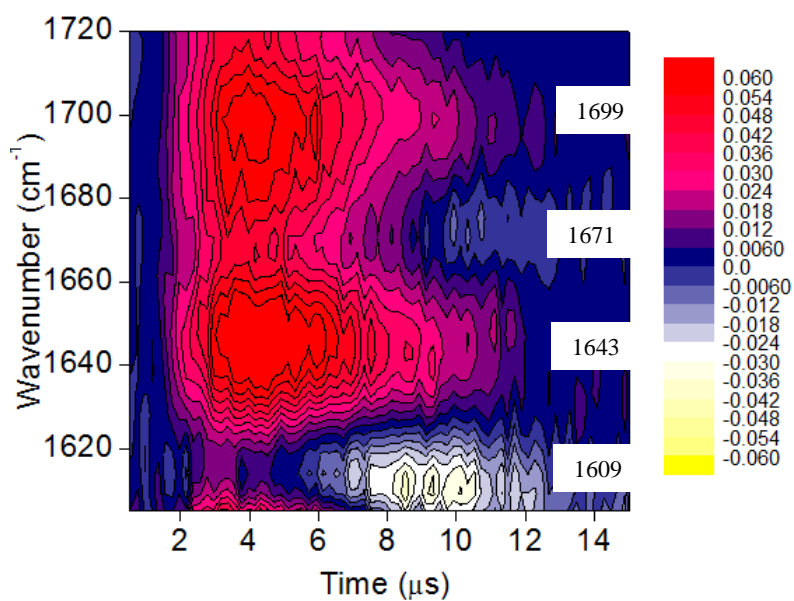


Figure C.14: TRIR data collected after phototriggering ($\lambda_{\text{exc}} = 460 \text{ nm}$) a reaction mixture containing 4 mM **4**-¹⁵NO, 6 mM **2**, and 150 mM NEt₃. Compare with Figure 4.5 in Chapter 4, which uses **4**-¹⁴NO.

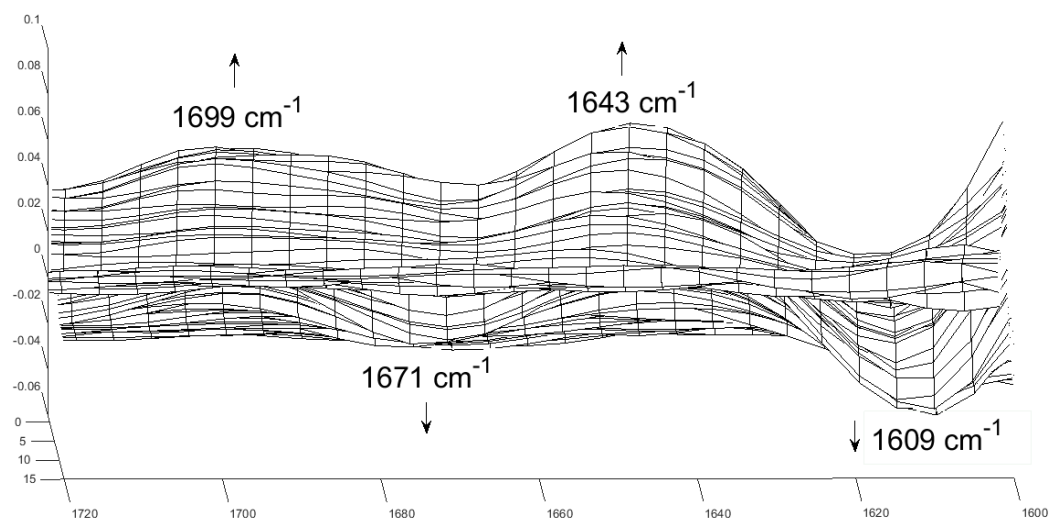


Figure C.15: A 3-dimensional rendering of TRIR results in Figure C.14.

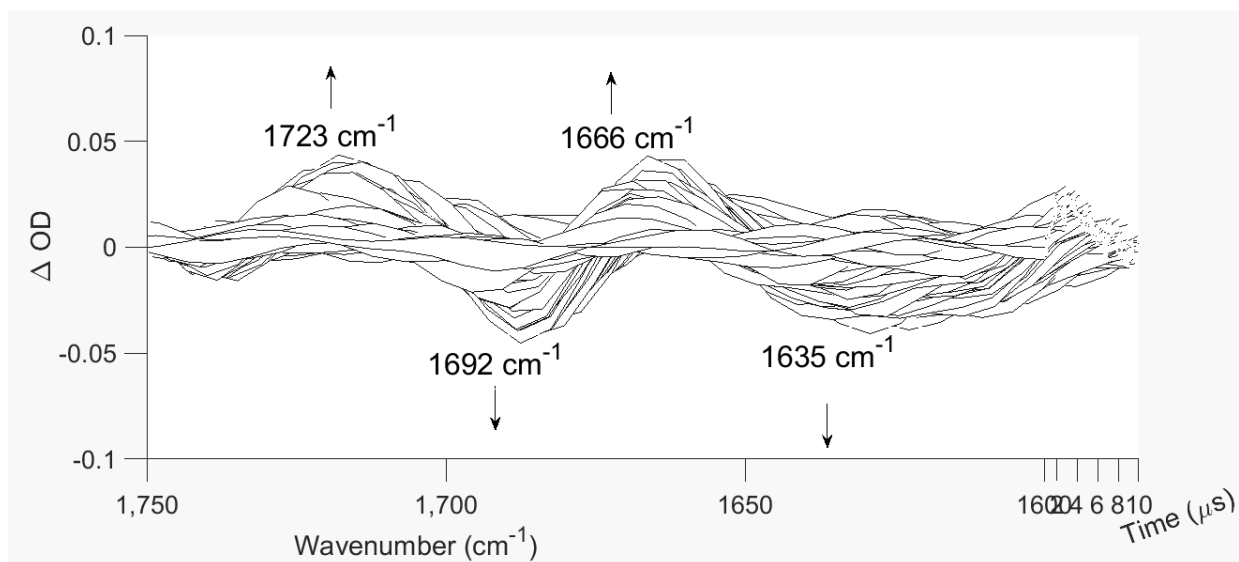


Figure C.16: A 3-dimensional rendering of TRIR results in Figure 4.5 in Chapter 4.

C.9 Synthesis of [(NO)Co(^{Me}doen)Mg(Me₃TACN)][(BPh₄)₂] (**5**)

A suspension of **4** (20 mg, 0.023 mmol) and AgBPh₄ (10.6 mg, 0.024 mmol) was stirred for 5 hours. The reaction changes color from dark red to dark orange-brown. The reaction was filtered through celite, and solvent was removed under vacuum. The solid was redissolved in dichloromethane, and filtered through celite again. Solvent was removed under vacuum, and the solution was redissolved in THF. Vapor diffusion of pentane vapor into the THF solution yielded dark brown needles (0.014 mmol, 65 % yield). The compound is not stable, and decomposes over the course of a few days. All studies with this compound were done immediately after purification. A new peak at 1663 cm⁻¹ in the IR spectrum arises from decomposition of this product.

¹H NMR (400 MHz, CD₃CN): δ 7.33-7.27 (m, 16H), 7.05–6.99 (m, 16H), 6.89-6.84 (m, 8H), 3.92–3.68 (m, 3H), 3.13–2.53 (m, 11H), 2.52–2.37 (m, 13 H), 2.37–2.26 (s, 6H), 2.24–2.02 (m, 4H).

ATR-IR (film): ν(¹⁴NO) = 1701, cm⁻¹; ν(¹⁵NO) = 1670 cm⁻¹ (Figure C.11).

We were unable to obtain satisfactory CHN analysis on this compound, likely due to lability of the coordinated NO ligand and the instability of the compound as evidenced by IR spectroscopy.

EA: Anal. Calc'd. for **5** (aquo ligand) (C₆₇H₇₉B₂CoMgN₈O₄): C, 69.06; H, 6.83; N, 9.62.
Found: C, 68.17; H, 7.46; N, 9.44.

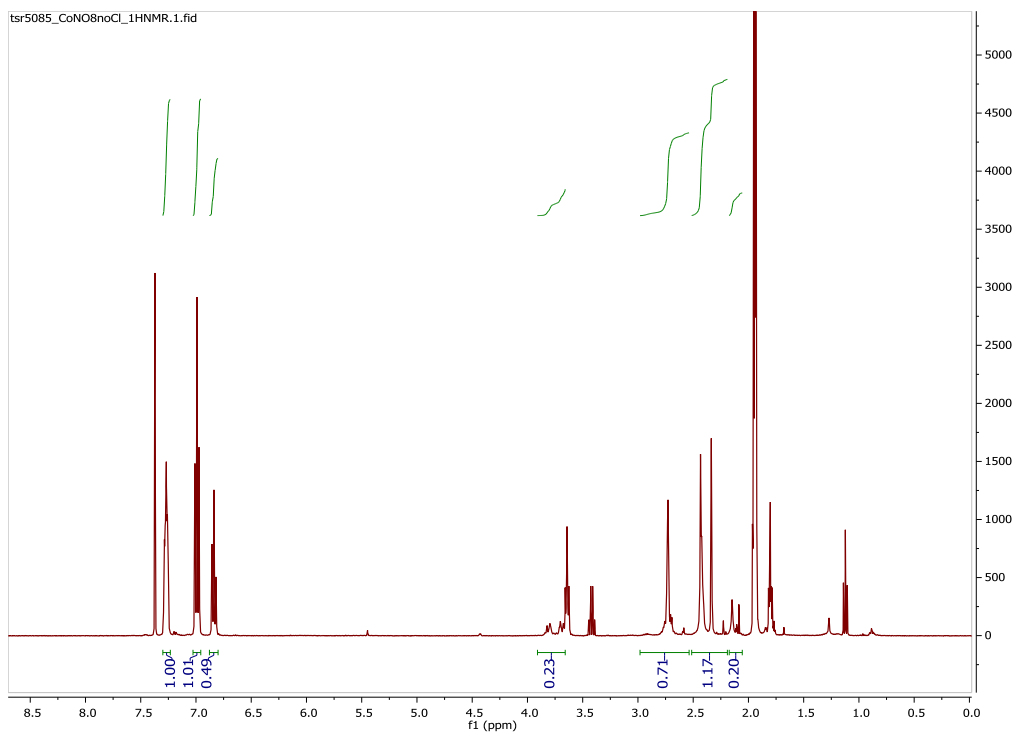


Figure C.17: ^1H NMR spectrum of **5**.

C.10 DFT Calculations

All stationary point geometries were calculated using dispersion corrected DFT-D₃³ with a TPSS functional,⁴ a def2-TZVP basis set on Co and a def2-SVP basis set on all other atoms.⁵ Calculations were performed on the full P₃^EFe scaffolds. Geometries were optimized using the Orca 3.0.3 package.⁶ All single point energy, frequency and solvation energy calculations were performed with the Orca 3.0.3 package. Frequency calculations were used to confirm true minima and to determine gas phase free energy values (G_{gas}). Single point solvation calculations were done using an SMD solvation model⁷ with diethyl ether solvent and were used to determine solvated internal energy (E_{soln}). Free energies of solvation were approximated using the difference in gas phase internal energy (E_{gas}) and solvated internal energy ($\Delta G_{\text{solv}} \approx E_{\text{soln}} - E_{\text{gas}}$) and the free energy of a species in solution was then calculated using the gas phase free energy (G_{gas}) and the free energy of solvation ($G_{\text{soln}} = G_{\text{gas}} + \Delta G_{\text{solv}}$).

Broken symmetry solutions for the putative {CoNO}⁹ species were found using the TPSSh functional with the def2-TZVP basis set on Co and the def2-SVP on all other atoms. An $S = 1/2$ solution in which an $S = 3/2$ Co center is antiferromagnetically coupled to an $S = 1$ NO unit was by optimizing the $S = 5/2$ species, after which the spin on the NO unit was flipped using the “flipspin” function in Orca 3.0.3 and an $S = 1/2$ state.

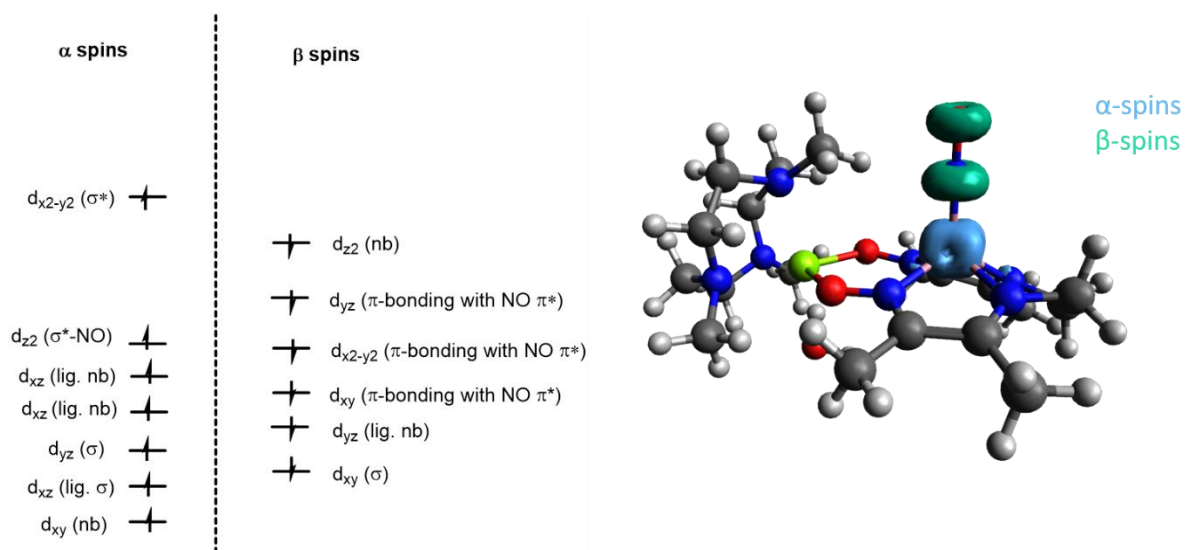


Figure C.18: Summary of broken symmetry solutions for the putative $\{\text{CoNO}\}^9$ species, with spin occupancies rendered from Kohn-Sham orbitals (left) and a spin density plot (right) showing unpaired α (blue) and β (green) spins.

C.11 X-Ray Structure of 5

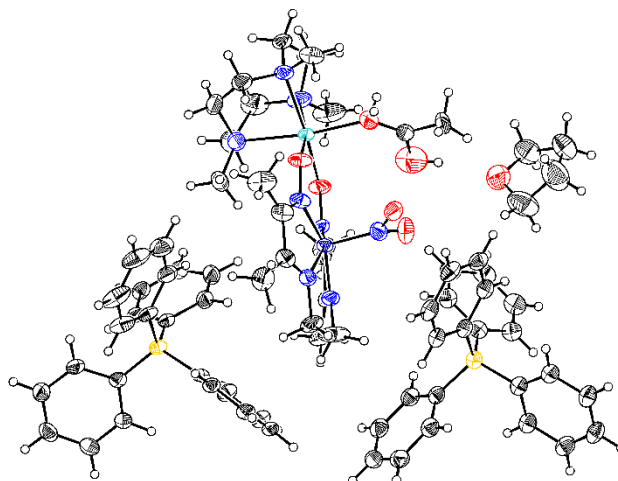


Table C.4: Crystal data and structure refinement for p16404 (Compound 5).

Identification code	p16404	
Empirical formula	C71.14 H86.02 B2 Co Mg N8 O5.35	
Formula weight	1243.60	
Temperature	100 K	
Wavelength	1.54178 Å	
Crystal system	Monoclinic	
Space group	P 1 21/n 1	
Unit cell dimensions	a = 18.856(3) Å	a = 90°
	b = 13.8620(19) Å	b = 100.655(10)°
	c = 26.097(3) Å	g = 90°
Volume	6703.5(16) Å ³	
Z	4	
Density (calculated)	1.232 Mg/m ³	
Absorption coefficient	2.539 mm ⁻¹	
F(000)	2643	
Crystal size	0.22 x 0.15 x 0.09 mm ³	
Theta range for data collection	3.190 to 79.335°.	
Index ranges	-23 ≤ h ≤ 23, -17 ≤ k ≤ 17, -33 ≤ l ≤ 33	
Reflections collected	154072	
Independent reflections	14432 [R(int) = 0.0757]	
Completeness to theta = 67.679°	100.0 %	

Absorption correction	Semi-empirical from equivalents
Max. and min. transmission	1.0000 and 0.8224
Refinement method	Full-matrix least-squares on F^2
Data / restraints / parameters	14432 / 0 / 840
Goodness-of-fit on F^2	1.031
Final R indices [$I > 2\sigma(I)$]	R1 = 0.0667, wR2 = 0.1705
R indices (all data)	R1 = 0.0848, wR2 = 0.1844
Extinction coefficient	n/a
Largest diff. peak and hole	1.366 and -0.524 e. \AA^{-3}

Table C.5: Atomic coordinates ($\times 10^5$) and equivalent isotropic displacement parameters ($\text{\AA}^2 \times 10^4$) for **5**. $U(\text{eq})$ is defined as one third of the trace of the orthogonalized U_{ij} tensor.

	x	y	z	$U(\text{eq})$
Co(1)	46465(2)	38021(3)	69165(2)	248(1)
Mg(1)	51484(5)	26695(7)	82337(3)	240(2)
O(1)	46916(13)	39633(15)	80315(7)	350(5)
O(2)	51696(12)	21154(17)	75184(7)	361(5)
O(3A)	60690(20)	38350(30)	69770(20)	437(16)
O(3B)	58220(30)	48320(40)	71560(20)	528(18)
O(4)	61779(14)	32150(20)	83148(11)	588(8)
O(5)	61830(40)	48310(40)	82950(20)	820(20)
O(4A)	61779(14)	32150(20)	83148(11)	588(8)
N(1)	44524(13)	43027(16)	75614(8)	252(5)
N(2)	41180(13)	48960(20)	66486(9)	319(6)
N(3)	43943(14)	33370(20)	62331(9)	319(6)
N(4)	48768(14)	24786(19)	70636(9)	299(5)
N(5)	55579(15)	42050(20)	69771(10)	357(6)
N(6)	55201(15)	12764(18)	86019(9)	333(6)
N(7)	50146(18)	29820(20)	90526(9)	421(7)
N(8)	40878(15)	19550(20)	82313(10)	391(6)
C(1)	40576(16)	50894(19)	75148(11)	279(6)
C(2)	38246(16)	53900(20)	69729(12)	303(6)
C(3)	40100(20)	50050(30)	60842(13)	583(12)
C(4)	40230(30)	40360(30)	58454(13)	548(11)
C(5)	44195(17)	24200(30)	61784(11)	355(7)
C(6)	47338(19)	19040(20)	66582(11)	360(7)
C(7)	38780(20)	56120(20)	79724(13)	428(8)
C(8)	32740(20)	61610(30)	68357(15)	464(9)
C(9)	41370(20)	18860(30)	56856(13)	526(10)
C(10)	48830(30)	8520(30)	66934(15)	547(10)
C(11)	55660(20)	13490(20)	91774(11)	376(7)
C(12)	55960(20)	23820(20)	93614(11)	426(8)
C(13)	49660(20)	5880(20)	83594(13)	450(9)

C(14)	42220(20)	9270(30)	83983(14)	479(9)
C(15)	42840(20)	26470(40)	91234(13)	569(11)
C(16)	37720(20)	25240(30)	86066(15)	544(10)
C(17)	62330(20)	9720(30)	84900(14)	464(9)
C(18)	51250(30)	39910(30)	92164(15)	684(14)
C(19)	36159(19)	19860(30)	77121(13)	462(9)
C(20)	65140(30)	39700(40)	82779(19)	407(14)
C(21)	72460(30)	40240(40)	81770(20)	427(15)
C(26)	56524(16)	77690(20)	67056(11)	289(6)
C(27)	59251(18)	86330(20)	69340(12)	339(7)
C(28)	60130(20)	88060(30)	74677(13)	405(8)
C(29)	58209(19)	81100(30)	77979(12)	416(8)
C(30)	55407(19)	72440(30)	75887(12)	393(7)
C(31)	54591(17)	70840(20)	70539(12)	346(7)
C(32)	59338(16)	64470(20)	60363(11)	273(6)
C(33)	65716(17)	61910(20)	63785(12)	316(6)
C(34)	69065(18)	53030(20)	63632(12)	351(7)
C(35)	66159(19)	46200(20)	59947(13)	366(7)
C(36)	59936(19)	48430(20)	56463(13)	351(7)
C(37)	56616(17)	57350(20)	56685(12)	311(6)
C(38)	47133(17)	75410(20)	57999(11)	289(6)
C(39)	41410(18)	76900(20)	60627(13)	337(7)
C(40)	34221(19)	77360(20)	58109(15)	393(7)
C(41)	32445(19)	76390(20)	52748(15)	417(8)
C(42)	38000(20)	74980(20)	49960(13)	396(8)
C(43)	45080(18)	74550(20)	52574(12)	343(7)
C(44)	59902(17)	83310(20)	57879(10)	285(6)
C(45)	56631(18)	92240(20)	56354(12)	331(7)
C(46)	60040(20)	99380(20)	53927(12)	379(7)
C(47)	66870(20)	97880(20)	52909(12)	388(7)
C(48)	70270(20)	89190(20)	54327(13)	383(7)
C(49)	66820(18)	82110(20)	56764(12)	326(6)
B(1)	55666(18)	75170(20)	60796(12)	273(6)
C(50)	15394(15)	33570(20)	66287(10)	247(5)
C(51)	21949(17)	37280(20)	69019(12)	331(7)
C(52)	22968(19)	39930(20)	74249(12)	378(7)

C(53)	17398(19)	38960(20)	76989(11)	360(7)
C(54)	10821(18)	35560(20)	74435(11)	314(6)
C(55)	9891(16)	32920(20)	69205(10)	257(6)
C(56)	18048(17)	19110(20)	60070(11)	292(6)
C(57)	24271(19)	16440(20)	63611(13)	387(7)
C(58)	27720(20)	7680(30)	63365(17)	529(10)
C(59)	25090(30)	1180(30)	59534(17)	573(11)
C(60)	19050(30)	3420(30)	55928(14)	553(11)
C(61)	15570(20)	12250(20)	56193(13)	433(8)
C(62)	5631(16)	29650(20)	57796(10)	262(6)
C(63)	1231(18)	21780(20)	58542(12)	364(7)
C(64)	-6240(20)	21940(30)	57041(13)	456(9)
C(65)	-9646(19)	30020(30)	54691(12)	399(7)
C(66)	-5560(17)	37930(20)	53817(11)	326(7)
C(67)	1930(16)	37640(20)	55354(10)	265(6)
C(68)	18419(15)	37270(20)	56710(10)	250(6)
C(69)	21384(16)	34340(20)	52418(10)	275(6)
C(70)	24269(16)	40890(20)	49284(10)	296(6)
C(71)	24361(16)	50630(20)	50368(11)	282(6)
C(72)	21626(17)	53770(20)	54630(12)	328(6)
C(73)	18808(18)	47190(20)	57718(12)	325(7)
B(2)	14379(18)	29820(20)	60181(11)	259(6)
O(6)	71270(30)	64150(30)	82791(17)	648(13)
C(22)	73940(40)	66850(70)	78070(30)	800(20)
C(23)	81730(50)	65430(80)	79460(30)	970(30)
C(24)	83370(30)	68050(50)	85090(20)	614(17)
C(25)	76240(30)	67750(50)	86950(20)	628(17)

Table C.6: Bond lengths [\AA] and angles [$^\circ$] for **5**.

Co(1)-N(1)	1.917(2)
Co(1)-N(2)	1.877(3)
Co(1)-N(3)	1.873(2)
Co(1)-N(4)	1.908(3)
Co(1)-N(5)	1.786(3)
Mg(1)-O(1)	2.017(2)
Mg(1)-O(2)	2.026(2)
Mg(1)-O(4)	2.057(3)
Mg(1)-O(4A)	2.057(3)
Mg(1)-N(6)	2.213(3)
Mg(1)-N(7)	2.240(3)
Mg(1)-N(8)	2.231(3)
O(1)-N(1)	1.314(3)
O(2)-N(4)	1.313(3)
O(3A)-N(5)	1.091(5)
O(3B)-N(5)	1.065(6)
O(4)-C(20)	1.237(6)
O(5)-H(5)	0.8554
O(5)-C(20)	1.350(8)
O(4A)-H(4AA)	0.9006
O(4A)-H(4AB)	0.8995
N(1)-C(1)	1.313(4)
N(2)-C(2)	1.290(4)
N(2)-C(3)	1.457(4)
N(3)-C(4)	1.480(4)
N(3)-C(5)	1.281(4)
N(4)-C(6)	1.312(4)
N(6)-C(11)	1.492(4)
N(6)-C(13)	1.468(4)
N(6)-C(17)	1.489(5)
N(7)-C(12)	1.489(4)
N(7)-C(15)	1.498(5)
N(7)-C(18)	1.465(5)
N(8)-C(14)	1.498(5)

N(8)-C(16)	1.467(5)
N(8)-C(19)	1.478(4)
C(1)-C(2)	1.462(4)
C(1)-C(7)	1.488(4)
C(2)-C(8)	1.487(4)
C(3)-H(3A)	0.9900
C(3)-H(3B)	0.9900
C(3)-C(4)	1.483(6)
C(4)-H(4A)	0.9900
C(4)-H(4B)	0.9900
C(5)-C(6)	1.469(4)
C(5)-C(9)	1.494(4)
C(6)-C(10)	1.485(5)
C(7)-H(7A)	0.9800
C(7)-H(7B)	0.9800
C(7)-H(7C)	0.9800
C(8)-H(8A)	0.9800
C(8)-H(8B)	0.9800
C(8)-H(8C)	0.9800
C(9)-H(9A)	0.9800
C(9)-H(9B)	0.9800
C(9)-H(9C)	0.9800
C(10)-H(10A)	0.9800
C(10)-H(10B)	0.9800
C(10)-H(10C)	0.9800
C(11)-H(11A)	0.9900
C(11)-H(11B)	0.9900
C(11)-C(12)	1.507(5)
C(12)-H(12A)	0.9900
C(12)-H(12B)	0.9900
C(13)-H(13A)	0.9900
C(13)-H(13B)	0.9900
C(13)-C(14)	1.501(6)
C(14)-H(14A)	0.9900
C(14)-H(14B)	0.9900
C(15)-H(15A)	0.9900

C(15)-H(15B)	0.9900
C(15)-C(16)	1.516(6)
C(16)-H(16A)	0.9900
C(16)-H(16B)	0.9900
C(17)-H(17A)	0.9800
C(17)-H(17B)	0.9800
C(17)-H(17C)	0.9800
C(18)-H(18A)	0.9800
C(18)-H(18B)	0.9800
C(18)-H(18C)	0.9800
C(19)-H(19A)	0.9800
C(19)-H(19B)	0.9800
C(19)-H(19C)	0.9800
C(20)-C(21)	1.455(8)
C(21)-H(21A)	0.9800
C(21)-H(21B)	0.9800
C(21)-H(21C)	0.9800
C(26)-C(27)	1.394(4)
C(26)-C(31)	1.408(4)
C(26)-B(1)	1.649(4)
C(27)-H(27)	0.9500
C(27)-C(28)	1.393(4)
C(28)-H(28)	0.9500
C(28)-C(29)	1.385(5)
C(29)-H(29)	0.9500
C(29)-C(30)	1.383(5)
C(30)-H(30)	0.9500
C(30)-C(31)	1.393(4)
C(31)-H(31)	0.9500
C(32)-C(33)	1.404(4)
C(32)-C(37)	1.405(4)
C(32)-B(1)	1.651(4)
C(33)-H(33)	0.9500
C(33)-C(34)	1.387(4)
C(34)-H(34)	0.9500
C(34)-C(35)	1.388(5)

C(35)-H(35)	0.9500
C(35)-C(36)	1.380(5)
C(36)-H(36)	0.9500
C(36)-C(37)	1.392(4)
C(37)-H(37)	0.9500
C(38)-C(39)	1.397(4)
C(38)-C(43)	1.402(4)
C(38)-B(1)	1.640(5)
C(39)-H(39)	0.9500
C(39)-C(40)	1.394(5)
C(40)-H(40)	0.9500
C(40)-C(41)	1.384(5)
C(41)-H(41)	0.9500
C(41)-C(42)	1.395(5)
C(42)-H(42)	0.9500
C(42)-C(43)	1.384(5)
C(43)-H(43)	0.9500
C(44)-C(45)	1.407(4)
C(44)-C(49)	1.398(4)
C(44)-B(1)	1.647(4)
C(45)-H(45)	0.9500
C(45)-C(46)	1.395(4)
C(46)-H(46)	0.9500
C(46)-C(47)	1.379(5)
C(47)-H(47)	0.9500
C(47)-C(48)	1.382(5)
C(48)-H(48)	0.9500
C(48)-C(49)	1.394(4)
C(49)-H(49)	0.9500
C(50)-C(51)	1.405(4)
C(50)-C(55)	1.399(4)
C(50)-B(2)	1.653(4)
C(51)-H(51)	0.9500
C(51)-C(52)	1.392(4)
C(52)-H(52)	0.9500
C(52)-C(53)	1.382(5)

C(53)-H(53)	0.9500
C(53)-C(54)	1.378(5)
C(54)-H(54)	0.9500
C(54)-C(55)	1.392(4)
C(55)-H(55)	0.9500
C(56)-C(57)	1.403(4)
C(56)-C(61)	1.404(5)
C(56)-B(2)	1.641(4)
C(57)-H(57)	0.9500
C(57)-C(58)	1.384(5)
C(58)-H(58)	0.9500
C(58)-C(59)	1.369(6)
C(59)-H(59)	0.9500
C(59)-C(60)	1.372(6)
C(60)-H(60)	0.9500
C(60)-C(61)	1.397(5)
C(61)-H(61)	0.9500
C(62)-C(63)	1.406(4)
C(62)-C(67)	1.399(4)
C(62)-B(2)	1.652(4)
C(63)-H(63)	0.9500
C(63)-C(64)	1.392(5)
C(64)-H(64)	0.9500
C(64)-C(65)	1.377(5)
C(65)-H(65)	0.9500
C(65)-C(66)	1.383(5)
C(66)-H(66)	0.9500
C(66)-C(67)	1.395(4)
C(67)-H(67)	0.9500
C(68)-C(69)	1.401(4)
C(68)-C(73)	1.400(4)
C(68)-B(2)	1.649(4)
C(69)-H(69)	0.9500
C(69)-C(70)	1.398(4)
C(70)-H(70)	0.9500
C(70)-C(71)	1.379(4)

C(71)-H(71)	0.9500
C(71)-C(72)	1.380(4)
C(72)-H(72)	0.9500
C(72)-C(73)	1.387(4)
C(73)-H(73)	0.9500
O(6)-C(22)	1.465(8)
O(6)-C(25)	1.389(7)
C(22)-H(22A)	0.9900
C(22)-H(22B)	0.9900
C(22)-C(23)	1.459(11)
C(23)-H(23A)	0.9900
C(23)-H(23B)	0.9900
C(23)-C(24)	1.489(10)
C(24)-H(24A)	0.9900
C(24)-H(24B)	0.9900
C(24)-C(25)	1.513(9)
C(25)-H(25A)	0.9900
C(25)-H(25B)	0.9900
N(2)-Co(1)-N(1)	81.96(10)
N(2)-Co(1)-N(4)	159.57(12)
N(3)-Co(1)-N(1)	154.73(11)
N(3)-Co(1)-N(2)	84.23(12)
N(3)-Co(1)-N(4)	82.47(11)
N(4)-Co(1)-N(1)	104.17(10)
N(5)-Co(1)-N(1)	98.38(12)
N(5)-Co(1)-N(2)	102.49(13)
N(5)-Co(1)-N(3)	105.23(12)
N(5)-Co(1)-N(4)	95.94(13)
O(1)-Mg(1)-O(2)	100.16(9)
O(1)-Mg(1)-O(4)	92.84(12)
O(1)-Mg(1)-O(4A)	92.84(12)
O(1)-Mg(1)-N(6)	167.25(11)
O(1)-Mg(1)-N(7)	87.68(10)
O(1)-Mg(1)-N(8)	93.15(11)
O(2)-Mg(1)-O(4)	93.15(12)
O(2)-Mg(1)-O(4A)	93.15(12)

O(2)-Mg(1)-N(6)	90.61(10)
O(2)-Mg(1)-N(7)	167.78(11)
O(2)-Mg(1)-N(8)	89.97(11)
O(4)-Mg(1)-N(6)	93.37(11)
O(4)-Mg(1)-N(7)	95.82(13)
O(4)-Mg(1)-N(8)	172.66(11)
O(4A)-Mg(1)-N(6)	93.37(11)
O(4A)-Mg(1)-N(7)	95.82(13)
O(4A)-Mg(1)-N(8)	172.66(11)
N(6)-Mg(1)-N(7)	80.62(10)
N(6)-Mg(1)-N(8)	79.95(11)
N(8)-Mg(1)-N(7)	80.19(11)
N(1)-O(1)-Mg(1)	128.25(17)
N(4)-O(2)-Mg(1)	127.65(18)
C(20)-O(4)-Mg(1)	142.2(3)
C(20)-O(5)-H(5)	108.1
Mg(1)-O(4A)-H(4AA)	111.2
Mg(1)-O(4A)-H(4AB)	111.4
H(4AA)-O(4A)-H(4AB)	102.6
O(1)-N(1)-Co(1)	127.01(19)
C(1)-N(1)-Co(1)	114.59(18)
C(1)-N(1)-O(1)	118.4(2)
C(2)-N(2)-Co(1)	116.6(2)
C(2)-N(2)-C(3)	127.7(3)
C(3)-N(2)-Co(1)	115.2(2)
C(4)-N(3)-Co(1)	115.5(2)
C(5)-N(3)-Co(1)	116.1(2)
C(5)-N(3)-C(4)	126.6(3)
O(2)-N(4)-Co(1)	126.33(19)
C(6)-N(4)-Co(1)	114.6(2)
C(6)-N(4)-O(2)	119.0(3)
O(3A)-N(5)-Co(1)	133.4(4)
O(3B)-N(5)-Co(1)	131.1(4)
C(11)-N(6)-Mg(1)	109.44(19)
C(13)-N(6)-Mg(1)	103.70(19)
C(13)-N(6)-C(11)	112.5(3)

C(13)-N(6)-C(17)	109.1(3)
C(17)-N(6)-Mg(1)	112.8(2)
C(17)-N(6)-C(11)	109.3(3)
C(12)-N(7)-Mg(1)	101.9(2)
C(12)-N(7)-C(15)	111.2(3)
C(15)-N(7)-Mg(1)	109.0(2)
C(18)-N(7)-Mg(1)	115.3(2)
C(18)-N(7)-C(12)	109.0(3)
C(18)-N(7)-C(15)	110.1(4)
C(14)-N(8)-Mg(1)	108.6(2)
C(16)-N(8)-Mg(1)	103.5(2)
C(16)-N(8)-C(14)	112.7(3)
C(16)-N(8)-C(19)	110.3(3)
C(19)-N(8)-Mg(1)	112.2(2)
C(19)-N(8)-C(14)	109.6(3)
N(1)-C(1)-C(2)	113.0(3)
N(1)-C(1)-C(7)	122.6(3)
C(2)-C(1)-C(7)	124.4(3)
N(2)-C(2)-C(1)	113.2(3)
N(2)-C(2)-C(8)	126.1(3)
C(1)-C(2)-C(8)	120.6(3)
N(2)-C(3)-H(3A)	110.0
N(2)-C(3)-H(3B)	110.0
N(2)-C(3)-C(4)	108.7(3)
H(3A)-C(3)-H(3B)	108.3
C(4)-C(3)-H(3A)	110.0
C(4)-C(3)-H(3B)	110.0
N(3)-C(4)-C(3)	110.4(3)
N(3)-C(4)-H(4A)	109.6
N(3)-C(4)-H(4B)	109.6
C(3)-C(4)-H(4A)	109.6
C(3)-C(4)-H(4B)	109.6
H(4A)-C(4)-H(4B)	108.1
N(3)-C(5)-C(6)	113.9(3)
N(3)-C(5)-C(9)	124.9(3)
C(6)-C(5)-C(9)	121.1(3)

N(4)-C(6)-C(5)	112.5(3)
N(4)-C(6)-C(10)	122.6(3)
C(5)-C(6)-C(10)	125.0(3)
C(1)-C(7)-H(7A)	109.5
C(1)-C(7)-H(7B)	109.5
C(1)-C(7)-H(7C)	109.5
H(7A)-C(7)-H(7B)	109.5
H(7A)-C(7)-H(7C)	109.5
H(7B)-C(7)-H(7C)	109.5
C(2)-C(8)-H(8A)	109.5
C(2)-C(8)-H(8B)	109.5
C(2)-C(8)-H(8C)	109.5
H(8A)-C(8)-H(8B)	109.5
H(8A)-C(8)-H(8C)	109.5
H(8B)-C(8)-H(8C)	109.5
C(5)-C(9)-H(9A)	109.5
C(5)-C(9)-H(9B)	109.5
C(5)-C(9)-H(9C)	109.5
H(9A)-C(9)-H(9B)	109.5
H(9A)-C(9)-H(9C)	109.5
H(9B)-C(9)-H(9C)	109.5
C(6)-C(10)-H(10A)	109.5
C(6)-C(10)-H(10B)	109.5
C(6)-C(10)-H(10C)	109.5
H(10A)-C(10)-H(10B)	109.5
H(10A)-C(10)-H(10C)	109.5
H(10B)-C(10)-H(10C)	109.5
N(6)-C(11)-H(11A)	109.2
N(6)-C(11)-H(11B)	109.2
N(6)-C(11)-C(12)	112.1(2)
H(11A)-C(11)-H(11B)	107.9
C(12)-C(11)-H(11A)	109.2
C(12)-C(11)-H(11B)	109.2
N(7)-C(12)-C(11)	112.2(3)
N(7)-C(12)-H(12A)	109.2
N(7)-C(12)-H(12B)	109.2

C(11)-C(12)-H(12A)	109.2
C(11)-C(12)-H(12B)	109.2
H(12A)-C(12)-H(12B)	107.9
N(6)-C(13)-H(13A)	109.3
N(6)-C(13)-H(13B)	109.3
N(6)-C(13)-C(14)	111.5(3)
H(13A)-C(13)-H(13B)	108.0
C(14)-C(13)-H(13A)	109.3
C(14)-C(13)-H(13B)	109.3
N(8)-C(14)-C(13)	112.8(3)
N(8)-C(14)-H(14A)	109.0
N(8)-C(14)-H(14B)	109.0
C(13)-C(14)-H(14A)	109.0
C(13)-C(14)-H(14B)	109.0
H(14A)-C(14)-H(14B)	107.8
N(7)-C(15)-H(15A)	109.2
N(7)-C(15)-H(15B)	109.2
N(7)-C(15)-C(16)	112.0(3)
H(15A)-C(15)-H(15B)	107.9
C(16)-C(15)-H(15A)	109.2
C(16)-C(15)-H(15B)	109.2
N(8)-C(16)-C(15)	112.6(3)
N(8)-C(16)-H(16A)	109.1
N(8)-C(16)-H(16B)	109.1
C(15)-C(16)-H(16A)	109.1
C(15)-C(16)-H(16B)	109.1
H(16A)-C(16)-H(16B)	107.8
N(6)-C(17)-H(17A)	109.5
N(6)-C(17)-H(17B)	109.5
N(6)-C(17)-H(17C)	109.5
H(17A)-C(17)-H(17B)	109.5
H(17A)-C(17)-H(17C)	109.5
H(17B)-C(17)-H(17C)	109.5
N(7)-C(18)-H(18A)	109.5
N(7)-C(18)-H(18B)	109.5
N(7)-C(18)-H(18C)	109.5

H(18A)-C(18)-H(18B)	109.5
H(18A)-C(18)-H(18C)	109.5
H(18B)-C(18)-H(18C)	109.5
N(8)-C(19)-H(19A)	109.5
N(8)-C(19)-H(19B)	109.5
N(8)-C(19)-H(19C)	109.5
H(19A)-C(19)-H(19B)	109.5
H(19A)-C(19)-H(19C)	109.5
H(19B)-C(19)-H(19C)	109.5
O(4)-C(20)-O(5)	120.0(6)
O(4)-C(20)-C(21)	125.0(6)
O(5)-C(20)-C(21)	114.8(5)
C(20)-C(21)-H(21A)	109.5
C(20)-C(21)-H(21B)	109.5
C(20)-C(21)-H(21C)	109.5
H(21A)-C(21)-H(21B)	109.5
H(21A)-C(21)-H(21C)	109.5
H(21B)-C(21)-H(21C)	109.5
C(27)-C(26)-C(31)	115.0(3)
C(27)-C(26)-B(1)	124.5(3)
C(31)-C(26)-B(1)	120.5(3)
C(26)-C(27)-H(27)	118.6
C(28)-C(27)-C(26)	122.8(3)
C(28)-C(27)-H(27)	118.6
C(27)-C(28)-H(28)	119.8
C(29)-C(28)-C(27)	120.4(3)
C(29)-C(28)-H(28)	119.8
C(28)-C(29)-H(29)	120.5
C(30)-C(29)-C(28)	118.9(3)
C(30)-C(29)-H(29)	120.5
C(29)-C(30)-H(30)	120.1
C(29)-C(30)-C(31)	119.8(3)
C(31)-C(30)-H(30)	120.1
C(26)-C(31)-H(31)	118.5
C(30)-C(31)-C(26)	123.1(3)
C(30)-C(31)-H(31)	118.5

C(33)-C(32)-C(37)	114.8(3)
C(33)-C(32)-B(1)	120.3(3)
C(37)-C(32)-B(1)	125.0(3)
C(32)-C(33)-H(33)	118.4
C(34)-C(33)-C(32)	123.1(3)
C(34)-C(33)-H(33)	118.4
C(33)-C(34)-H(34)	119.9
C(33)-C(34)-C(35)	120.1(3)
C(35)-C(34)-H(34)	119.9
C(34)-C(35)-H(35)	120.6
C(36)-C(35)-C(34)	118.8(3)
C(36)-C(35)-H(35)	120.6
C(35)-C(36)-H(36)	119.8
C(35)-C(36)-C(37)	120.4(3)
C(37)-C(36)-H(36)	119.8
C(32)-C(37)-H(37)	118.6
C(36)-C(37)-C(32)	122.8(3)
C(36)-C(37)-H(37)	118.6
C(39)-C(38)-C(43)	114.5(3)
C(39)-C(38)-B(1)	124.6(3)
C(43)-C(38)-B(1)	120.9(3)
C(38)-C(39)-H(39)	118.4
C(40)-C(39)-C(38)	123.2(3)
C(40)-C(39)-H(39)	118.4
C(39)-C(40)-H(40)	119.9
C(41)-C(40)-C(39)	120.3(3)
C(41)-C(40)-H(40)	119.9
C(40)-C(41)-H(41)	120.8
C(40)-C(41)-C(42)	118.4(3)
C(42)-C(41)-H(41)	120.8
C(41)-C(42)-H(42)	120.1
C(43)-C(42)-C(41)	119.9(3)
C(43)-C(42)-H(42)	120.1
C(38)-C(43)-H(43)	118.1
C(42)-C(43)-C(38)	123.7(3)
C(42)-C(43)-H(43)	118.1

C(45)-C(44)-B(1)	120.5(3)
C(49)-C(44)-C(45)	115.0(3)
C(49)-C(44)-B(1)	124.5(3)
C(44)-C(45)-H(45)	118.7
C(46)-C(45)-C(44)	122.6(3)
C(46)-C(45)-H(45)	118.7
C(45)-C(46)-H(46)	119.8
C(47)-C(46)-C(45)	120.3(3)
C(47)-C(46)-H(46)	119.8
C(46)-C(47)-H(47)	120.5
C(46)-C(47)-C(48)	119.0(3)
C(48)-C(47)-H(47)	120.5
C(47)-C(48)-H(48)	119.9
C(47)-C(48)-C(49)	120.2(3)
C(49)-C(48)-H(48)	119.9
C(44)-C(49)-H(49)	118.5
C(48)-C(49)-C(44)	122.9(3)
C(48)-C(49)-H(49)	118.5
C(26)-B(1)-C(32)	107.0(2)
C(38)-B(1)-C(26)	110.2(2)
C(38)-B(1)-C(32)	112.1(2)
C(38)-B(1)-C(44)	107.5(2)
C(44)-B(1)-C(26)	110.3(2)
C(44)-B(1)-C(32)	109.8(2)
C(51)-C(50)-B(2)	122.6(3)
C(55)-C(50)-C(51)	114.8(3)
C(55)-C(50)-B(2)	122.6(3)
C(50)-C(51)-H(51)	118.6
C(52)-C(51)-C(50)	122.9(3)
C(52)-C(51)-H(51)	118.6
C(51)-C(52)-H(52)	120.0
C(53)-C(52)-C(51)	120.1(3)
C(53)-C(52)-H(52)	120.0
C(52)-C(53)-H(53)	120.5
C(54)-C(53)-C(52)	119.0(3)
C(54)-C(53)-H(53)	120.5

C(53)-C(54)-H(54)	119.9
C(53)-C(54)-C(55)	120.2(3)
C(55)-C(54)-H(54)	119.9
C(50)-C(55)-H(55)	118.5
C(54)-C(55)-C(50)	123.0(3)
C(54)-C(55)-H(55)	118.5
C(57)-C(56)-C(61)	115.0(3)
C(57)-C(56)-B(2)	122.1(3)
C(61)-C(56)-B(2)	122.7(3)
C(56)-C(57)-H(57)	118.5
C(58)-C(57)-C(56)	123.0(4)
C(58)-C(57)-H(57)	118.5
C(57)-C(58)-H(58)	120.0
C(59)-C(58)-C(57)	120.1(4)
C(59)-C(58)-H(58)	120.0
C(58)-C(59)-H(59)	120.1
C(58)-C(59)-C(60)	119.7(3)
C(60)-C(59)-H(59)	120.1
C(59)-C(60)-H(60)	119.9
C(59)-C(60)-C(61)	120.1(4)
C(61)-C(60)-H(60)	119.9
C(56)-C(61)-H(61)	118.9
C(60)-C(61)-C(56)	122.2(4)
C(60)-C(61)-H(61)	118.9
C(63)-C(62)-B(2)	122.2(3)
C(67)-C(62)-C(63)	114.9(3)
C(67)-C(62)-B(2)	122.7(3)
C(62)-C(63)-H(63)	118.6
C(64)-C(63)-C(62)	122.8(3)
C(64)-C(63)-H(63)	118.6
C(63)-C(64)-H(64)	119.9
C(65)-C(64)-C(63)	120.1(3)
C(65)-C(64)-H(64)	119.9
C(64)-C(65)-H(65)	120.3
C(64)-C(65)-C(66)	119.4(3)
C(66)-C(65)-H(65)	120.3

C(65)-C(66)-H(66)	120.2
C(65)-C(66)-C(67)	119.7(3)
C(67)-C(66)-H(66)	120.2
C(62)-C(67)-H(67)	118.4
C(66)-C(67)-C(62)	123.1(3)
C(66)-C(67)-H(67)	118.4
C(69)-C(68)-B(2)	123.4(3)
C(73)-C(68)-C(69)	114.8(3)
C(73)-C(68)-B(2)	121.7(2)
C(68)-C(69)-H(69)	118.8
C(70)-C(69)-C(68)	122.4(3)
C(70)-C(69)-H(69)	118.8
C(69)-C(70)-H(70)	119.7
C(71)-C(70)-C(69)	120.5(3)
C(71)-C(70)-H(70)	119.7
C(70)-C(71)-H(71)	120.6
C(70)-C(71)-C(72)	118.8(3)
C(72)-C(71)-H(71)	120.6
C(71)-C(72)-H(72)	120.0
C(71)-C(72)-C(73)	120.1(3)
C(73)-C(72)-H(72)	120.0
C(68)-C(73)-H(73)	118.3
C(72)-C(73)-C(68)	123.4(3)
C(72)-C(73)-H(73)	118.3
C(56)-B(2)-C(50)	109.1(2)
C(56)-B(2)-C(62)	112.0(2)
C(56)-B(2)-C(68)	108.5(2)
C(62)-B(2)-C(50)	107.3(2)
C(68)-B(2)-C(50)	110.5(2)
C(68)-B(2)-C(62)	109.4(2)
C(25)-O(6)-C(22)	106.2(5)
O(6)-C(22)-H(22A)	110.9
O(6)-C(22)-H(22B)	110.9
H(22A)-C(22)-H(22B)	109.0
C(23)-C(22)-O(6)	104.1(6)
C(23)-C(22)-H(22A)	110.9

C(23)-C(22)-H(22B)	110.9
C(22)-C(23)-H(23A)	111.1
C(22)-C(23)-H(23B)	111.1
C(22)-C(23)-C(24)	103.3(7)
H(23A)-C(23)-H(23B)	109.1
C(24)-C(23)-H(23A)	111.1
C(24)-C(23)-H(23B)	111.1
C(23)-C(24)-H(24A)	110.6
C(23)-C(24)-H(24B)	110.6
C(23)-C(24)-C(25)	105.9(5)
H(24A)-C(24)-H(24B)	108.7
C(25)-C(24)-H(24A)	110.6
C(25)-C(24)-H(24B)	110.6
O(6)-C(25)-C(24)	105.7(5)
O(6)-C(25)-H(25A)	110.6
O(6)-C(25)-H(25B)	110.6
C(24)-C(25)-H(25A)	110.6
C(24)-C(25)-H(25B)	110.6
H(25A)-C(25)-H(25B)	108.7

Symmetry transformations used to generate equivalent atoms:

Table C.7: Anisotropic displacement parameters ($\text{\AA}^2 \times 10^4$) for **5**. The anisotropic displacement factor exponent takes the form: $-2p^2[h^2 a^*2U^{11} + \dots + 2hka^*b^*U^{12}]$

	U ¹¹	U ²²	U ³³	U ²³	U ¹³	U ¹²
Co(1)	243(2)	349(3)	150(2)	43(2)	31(2)	11(2)
Mg(1)	280(5)	294(5)	131(4)	32(3)	1(3)	-19(4)
O(1)	511(14)	360(11)	149(9)	10(8)	-16(9)	48(10)
O(2)	448(13)	453(12)	173(9)	43(8)	35(9)	159(10)
O(3A)	260(30)	460(30)	620(30)	190(20)	170(20)	70(20)
O(3B)	430(30)	570(40)	620(40)	-60(30)	170(30)	-190(30)
O(4)	394(14)	800(20)	515(15)	283(14)	-63(12)	-160(14)
O(5)	1120(50)	510(30)	740(40)	-190(30)	-70(30)	80(30)
O(4A)	394(14)	800(20)	515(15)	283(14)	-63(12)	-160(14)
N(1)	306(13)	246(11)	185(10)	33(9)	-2(9)	-49(10)
N(2)	262(13)	458(15)	246(12)	133(11)	74(10)	31(11)
N(3)	305(13)	455(15)	191(11)	52(10)	31(10)	-54(11)
N(4)	329(13)	428(14)	140(10)	-4(9)	43(9)	89(11)
N(5)	274(15)	492(17)	312(13)	54(12)	75(11)	-24(14)
N(6)	426(15)	321(13)	206(11)	28(9)	-65(10)	-24(11)
N(7)	670(20)	394(15)	171(11)	-4(10)	15(12)	40(14)
N(8)	342(15)	557(17)	270(12)	87(12)	52(11)	-81(13)
C(1)	339(16)	209(13)	279(14)	9(11)	31(11)	-50(11)
C(2)	286(15)	297(14)	334(15)	90(12)	78(12)	-26(12)
C(3)	700(30)	820(30)	270(16)	224(18)	208(17)	410(20)
C(4)	820(30)	530(20)	204(15)	131(14)	-142(16)	-220(20)
C(5)	343(17)	570(20)	164(12)	-8(13)	80(11)	-33(15)
C(6)	438(19)	420(17)	228(14)	-54(12)	76(13)	94(14)
C(7)	650(20)	261(15)	374(17)	-60(13)	91(16)	2(15)
C(8)	540(20)	402(19)	460(20)	169(15)	134(17)	119(16)
C(9)	710(30)	660(20)	220(15)	-75(15)	103(16)	-180(20)
C(10)	780(30)	490(20)	384(19)	-72(16)	139(19)	200(20)
C(11)	510(20)	364(16)	207(14)	66(12)	-55(13)	-77(14)
C(12)	650(20)	410(18)	172(13)	46(12)	-54(14)	-24(16)
C(13)	610(20)	340(17)	330(16)	43(13)	-88(15)	-114(16)
C(14)	530(20)	540(20)	347(17)	87(15)	3(15)	-252(18)

C(15)	660(30)	830(30)	269(16)	67(18)	209(17)	140(20)
C(16)	460(20)	800(30)	420(19)	92(19)	192(17)	40(20)
C(17)	510(20)	460(20)	375(18)	13(15)	-25(16)	134(17)
C(18)	1240(40)	430(20)	287(18)	-82(15)	-110(20)	120(20)
C(19)	314(17)	700(20)	353(17)	83(16)	10(14)	-124(17)
C(20)	420(30)	480(30)	270(20)	80(20)	-90(20)	-140(20)
C(21)	270(30)	550(30)	450(30)	20(30)	40(20)	-130(20)
C(26)	267(14)	329(15)	280(14)	-40(11)	71(11)	33(12)
C(27)	411(18)	337(16)	276(15)	-58(12)	77(13)	23(13)
C(28)	470(20)	427(18)	309(16)	-131(13)	49(14)	22(15)
C(29)	394(18)	620(20)	236(14)	-74(14)	72(13)	62(16)
C(30)	383(18)	530(20)	297(15)	34(14)	144(13)	62(15)
C(31)	344(17)	394(17)	321(15)	-36(13)	121(13)	-15(13)
C(32)	311(15)	264(13)	272(13)	-26(11)	125(11)	-31(12)
C(33)	368(17)	296(15)	306(15)	-22(11)	120(13)	-31(12)
C(34)	371(17)	374(16)	342(15)	76(13)	154(13)	34(13)
C(35)	490(20)	247(14)	417(17)	31(12)	242(15)	32(13)
C(36)	456(19)	253(14)	384(16)	-55(12)	182(14)	-46(13)
C(37)	356(16)	282(14)	316(14)	-28(12)	119(12)	-44(12)
C(38)	347(16)	199(13)	321(14)	-25(11)	65(12)	-23(11)
C(39)	376(17)	267(14)	375(16)	6(12)	94(13)	14(13)
C(40)	359(18)	263(15)	570(20)	72(14)	111(15)	31(13)
C(41)	368(18)	231(14)	600(20)	71(14)	-52(16)	-18(13)
C(42)	500(20)	244(14)	390(17)	-9(12)	-46(15)	-44(14)
C(43)	420(18)	273(14)	329(15)	-45(12)	53(13)	-53(13)
C(44)	389(16)	267(14)	205(12)	-85(10)	74(11)	-59(12)
C(45)	406(18)	271(14)	325(15)	-77(12)	90(13)	-43(13)
C(46)	530(20)	261(15)	349(16)	-28(12)	81(14)	-48(14)
C(47)	550(20)	308(16)	326(15)	-43(12)	139(15)	-129(15)
C(48)	436(19)	360(17)	386(17)	-30(13)	159(14)	-69(14)
C(49)	384(17)	297(15)	308(14)	-21(12)	90(13)	-22(13)
B(1)	309(17)	275(15)	242(14)	-55(12)	73(12)	-25(13)
C(50)	293(14)	251(13)	202(12)	49(10)	62(11)	23(11)
C(51)	328(16)	401(17)	271(14)	31(12)	74(12)	-57(13)
C(52)	392(18)	430(18)	285(15)	-18(13)	-10(13)	-136(14)
C(53)	530(20)	327(15)	210(13)	-39(11)	38(13)	-95(14)

C(54)	397(17)	330(15)	232(13)	11(11)	106(12)	-40(13)
C(55)	316(15)	250(13)	209(12)	11(10)	59(11)	-21(11)
C(56)	410(17)	283(14)	213(12)	83(11)	135(12)	53(12)
C(57)	401(18)	340(16)	436(18)	131(14)	114(15)	55(14)
C(58)	540(20)	410(20)	660(30)	168(18)	161(19)	157(17)
C(59)	820(30)	363(19)	620(20)	199(18)	330(20)	250(20)
C(60)	1060(40)	290(17)	372(18)	37(14)	300(20)	90(20)
C(61)	720(30)	316(16)	270(15)	55(12)	112(16)	103(16)
C(62)	337(15)	313(14)	140(11)	-3(10)	48(10)	-12(12)
C(63)	425(19)	359(16)	272(14)	105(12)	-26(13)	-56(14)
C(64)	430(20)	550(20)	353(17)	95(15)	-25(14)	-167(17)
C(65)	327(17)	560(20)	277(15)	-14(14)	-26(12)	-66(15)
C(66)	341(16)	382(16)	239(14)	-57(12)	11(12)	32(13)
C(67)	309(15)	292(14)	196(12)	-28(10)	47(11)	13(12)
C(68)	244(14)	305(14)	198(12)	51(10)	33(10)	64(11)
C(69)	332(15)	308(14)	176(12)	21(10)	26(11)	0(12)
C(70)	344(16)	400(16)	149(12)	24(11)	53(11)	5(13)
C(71)	271(15)	342(15)	233(13)	96(11)	44(11)	5(12)
C(72)	396(17)	262(14)	349(15)	61(12)	130(13)	36(13)
C(73)	410(17)	302(15)	304(14)	46(12)	174(13)	59(13)
B(2)	326(17)	287(15)	172(13)	35(11)	68(12)	35(13)
O(6)	720(30)	600(30)	600(30)	0(20)	40(20)	-130(20)
C(22)	680(50)	1220(70)	460(30)	-20(40)	30(30)	130(40)
C(23)	810(60)	1440(80)	620(40)	-40(50)	-20(40)	-280(50)
C(24)	450(30)	740(40)	640(40)	-110(30)	60(30)	40(30)
C(25)	660(40)	720(40)	490(30)	-80(30)	60(30)	10(30)

Table C.8: Hydrogen coordinates ($\text{\AA} \times 10^4$) and isotropic displacement parameters ($\text{\AA}^2 \times 10^3$) for p16404.

	x	y	z	U(eq)
H(5)	6502	5274	8308	123
H(4AA)	6467	2813	8176	88
H(4AB)	6395	3240	8652	88
H(3A)	4397	5412	5989	70
H(3B)	3541	5322	5954	70
H(4A)	3523	3816	5714	66
H(4B)	4277	4071	5546	66
H(7A)	3677	5158	8195	64
H(7B)	3523	6117	7852	64
H(7C)	4317	5905	8172	64
H(8A)	3467	6773	6989	70
H(8B)	2839	5991	6972	70
H(8C)	3151	6226	6456	70
H(9A)	3719	1497	5732	79
H(9B)	4515	1463	5600	79
H(9C)	3991	2348	5401	79
H(10A)	5357	740	6912	82
H(10B)	4880	593	6344	82
H(10C)	4511	528	6847	82
H(11A)	6003	1006	9356	45
H(11B)	5140	1029	9275	45
H(12A)	5549	2397	9733	51
H(12B)	6071	2660	9334	51
H(13A)	5057	-46	8533	54
H(13B)	4999	504	7988	54
H(14A)	3863	510	8178	58
H(14B)	4153	859	8764	58
H(15A)	4079	3121	9339	68
H(15B)	4333	2023	9312	68
H(16A)	3326	2203	8668	65

H(16B)	3637	3169	8456	65
H(17A)	6222	998	8113	70
H(17B)	6338	312	8615	70
H(17C)	6609	1408	8668	70
H(18A)	5605	4202	9169	103
H(18B)	5088	4049	9585	103
H(18C)	4756	4395	9005	103
H(19A)	3606	2643	7573	69
H(19B)	3126	1791	7743	69
H(19C)	3803	1543	7476	69
H(21A)	7273	3676	7854	64
H(21B)	7579	3730	8468	64
H(21C)	7378	4701	8141	64
H(27)	6057	9126	6716	41
H(28)	6205	9404	7606	49
H(29)	5881	8226	8162	50
H(30)	5404	6759	7809	47
H(31)	5264	6485	6918	41
H(33)	6784	6648	6633	38
H(34)	7336	5162	6605	42
H(35)	6841	4009	5983	44
H(36)	5791	4385	5390	42
H(37)	5233	5869	5425	37
H(39)	4247	7763	6431	40
H(40)	3053	7834	6008	47
H(41)	2756	7668	5101	50
H(42)	3692	7431	4627	48
H(43)	4876	7363	5058	41
H(45)	5192	9345	5700	40
H(46)	5764	10532	5297	45
H(47)	6920	10273	5126	47
H(48)	7497	8804	5364	46
H(49)	6928	7621	5771	39
H(51)	2586	3801	6722	40
H(52)	2750	4241	7594	45
H(53)	1809	4061	8058	43

H(54)	691	3502	7625	38
H(55)	531	3056	6754	31
H(57)	2621	2083	6630	46
H(58)	3192	617	6586	63
H(59)	2743	-485	5937	69
H(60)	1723	-105	5324	66
H(61)	1139	1367	5367	52
H(63)	346	1611	6014	44
H(64)	-901	1646	5764	55
H(65)	-1475	3016	5368	48
H(66)	-784	4353	5218	39
H(67)	464	4314	5471	32
H(69)	2144	2766	5161	33
H(70)	2618	3861	4639	36
H(71)	2627	5510	4822	34
H(72)	2167	6045	5545	39
H(73)	1705	4953	6067	39
H(22A)	7182	6267	7510	96
H(22B)	7277	7366	7712	96
H(23A)	8432	6968	7738	117
H(23B)	8304	5864	7892	117
H(24A)	8550	7459	8555	74
H(24B)	8682	6340	8706	74
H(25A)	7657	6348	9003	75
H(25B)	7483	7429	8791	75

Table C.9: Torsion angles [°] for **5**.

Co(1)-N(1)-C(1)-C(2)	2.5(3)
Co(1)-N(1)-C(1)-C(7)	-177.0(2)
Co(1)-N(2)-C(2)-C(1)	9.3(3)
Co(1)-N(2)-C(2)-C(8)	-167.5(3)
Co(1)-N(2)-C(3)-C(4)	27.5(4)
Co(1)-N(3)-C(4)-C(3)	6.6(4)
Co(1)-N(3)-C(5)-C(6)	-7.5(4)
Co(1)-N(3)-C(5)-C(9)	170.2(3)
Co(1)-N(4)-C(6)-C(5)	-0.4(4)
Co(1)-N(4)-C(6)-C(10)	179.3(3)
Mg(1)-O(1)-N(1)-Co(1)	-14.8(3)
Mg(1)-O(1)-N(1)-C(1)	167.9(2)
Mg(1)-O(2)-N(4)-Co(1)	23.8(4)
Mg(1)-O(2)-N(4)-C(6)	-157.7(2)
Mg(1)-O(4)-C(20)-O(5)	20.1(8)
Mg(1)-O(4)-C(20)-C(21)	-155.2(4)
Mg(1)-N(6)-C(11)-C(12)	-19.0(4)
Mg(1)-N(6)-C(13)-C(14)	-52.1(3)
Mg(1)-N(7)-C(12)-C(11)	-51.7(3)
Mg(1)-N(7)-C(15)-C(16)	-19.4(4)
Mg(1)-N(8)-C(14)-C(13)	-17.5(3)
Mg(1)-N(8)-C(16)-C(15)	-51.0(4)
O(1)-N(1)-C(1)-C(2)	-179.9(2)
O(1)-N(1)-C(1)-C(7)	0.6(4)
O(2)-N(4)-C(6)-C(5)	-179.1(3)
O(2)-N(4)-C(6)-C(10)	0.7(5)
N(1)-Co(1)-N(2)-C(2)	-6.5(2)
N(1)-Co(1)-N(2)-C(3)	-178.5(3)
N(1)-Co(1)-N(3)-C(4)	64.0(4)
N(1)-Co(1)-N(3)-C(5)	-101.5(3)
N(1)-Co(1)-N(5)-O(3A)	122.2(5)
N(1)-Co(1)-N(5)-O(3B)	-32.9(5)
N(1)-C(1)-C(2)-N(2)	-7.6(4)
N(1)-C(1)-C(2)-C(8)	169.4(3)

N(2)-Co(1)-N(3)-C(4)	6.9(3)
N(2)-Co(1)-N(3)-C(5)	-158.6(3)
N(2)-Co(1)-N(5)-O(3A)	-154.3(5)
N(2)-Co(1)-N(5)-O(3B)	50.7(5)
N(2)-C(3)-C(4)-N(3)	-20.7(5)
N(3)-Co(1)-N(2)-C(2)	152.3(2)
N(3)-Co(1)-N(2)-C(3)	-19.7(3)
N(3)-Co(1)-N(5)-O(3A)	-66.9(5)
N(3)-Co(1)-N(5)-O(3B)	138.1(5)
N(3)-C(5)-C(6)-N(4)	5.1(4)
N(3)-C(5)-C(6)-C(10)	-174.6(3)
N(4)-Co(1)-N(2)-C(2)	102.8(4)
N(4)-Co(1)-N(2)-C(3)	-69.3(4)
N(4)-Co(1)-N(3)-C(4)	171.3(3)
N(4)-Co(1)-N(3)-C(5)	5.8(2)
N(4)-Co(1)-N(5)-O(3A)	16.9(5)
N(4)-Co(1)-N(5)-O(3B)	-138.2(5)
N(5)-Co(1)-N(2)-C(2)	-103.3(2)
N(5)-Co(1)-N(2)-C(3)	84.6(3)
N(5)-Co(1)-N(3)-C(4)	-94.5(3)
N(5)-Co(1)-N(3)-C(5)	100.0(3)
N(6)-C(11)-C(12)-N(7)	50.2(4)
N(6)-C(13)-C(14)-N(8)	48.7(4)
N(7)-C(15)-C(16)-N(8)	49.6(5)
C(2)-N(2)-C(3)-C(4)	-143.6(4)
C(3)-N(2)-C(2)-C(1)	-179.7(3)
C(3)-N(2)-C(2)-C(8)	3.4(6)
C(4)-N(3)-C(5)-C(6)	-171.2(3)
C(4)-N(3)-C(5)-C(9)	6.6(5)
C(5)-N(3)-C(4)-C(3)	170.3(3)
C(7)-C(1)-C(2)-N(2)	171.9(3)
C(7)-C(1)-C(2)-C(8)	-11.0(5)
C(9)-C(5)-C(6)-N(4)	-172.7(3)
C(9)-C(5)-C(6)-C(10)	7.6(5)
C(11)-N(6)-C(13)-C(14)	66.1(3)
C(12)-N(7)-C(15)-C(16)	-131.0(3)

C(13)-N(6)-C(11)-C(12)	-133.7(3)
C(14)-N(8)-C(16)-C(15)	66.0(4)
C(15)-N(7)-C(12)-C(11)	64.4(4)
C(16)-N(8)-C(14)-C(13)	-131.5(3)
C(17)-N(6)-C(11)-C(12)	104.9(3)
C(17)-N(6)-C(13)-C(14)	-172.5(3)
C(18)-N(7)-C(12)-C(11)	-174.0(3)
C(18)-N(7)-C(15)-C(16)	108.1(4)
C(19)-N(8)-C(14)-C(13)	105.3(3)
C(19)-N(8)-C(16)-C(15)	-171.2(3)
C(26)-C(27)-C(28)-C(29)	-0.6(5)
C(27)-C(26)-C(31)-C(30)	-0.9(5)
C(27)-C(26)-B(1)-C(32)	130.4(3)
C(27)-C(26)-B(1)-C(38)	-107.5(3)
C(27)-C(26)-B(1)-C(44)	11.0(4)
C(27)-C(28)-C(29)-C(30)	-0.1(5)
C(28)-C(29)-C(30)-C(31)	0.2(5)
C(29)-C(30)-C(31)-C(26)	0.2(5)
C(31)-C(26)-C(27)-C(28)	1.1(5)
C(31)-C(26)-B(1)-C(32)	-48.3(4)
C(31)-C(26)-B(1)-C(38)	73.9(3)
C(31)-C(26)-B(1)-C(44)	-167.6(3)
C(32)-C(33)-C(34)-C(35)	0.5(5)
C(33)-C(32)-C(37)-C(36)	0.5(4)
C(33)-C(32)-B(1)-C(26)	-39.2(3)
C(33)-C(32)-B(1)-C(38)	-160.2(3)
C(33)-C(32)-B(1)-C(44)	80.4(3)
C(33)-C(34)-C(35)-C(36)	0.2(4)
C(34)-C(35)-C(36)-C(37)	-0.6(4)
C(35)-C(36)-C(37)-C(32)	0.2(5)
C(37)-C(32)-C(33)-C(34)	-0.8(4)
C(37)-C(32)-B(1)-C(26)	141.6(3)
C(37)-C(32)-B(1)-C(38)	20.6(4)
C(37)-C(32)-B(1)-C(44)	-98.8(3)
C(38)-C(39)-C(40)-C(41)	-0.5(5)
C(39)-C(38)-C(43)-C(42)	-0.9(4)

C(39)-C(38)-B(1)-C(26)	-3.9(4)
C(39)-C(38)-B(1)-C(32)	115.2(3)
C(39)-C(38)-B(1)-C(44)	-124.0(3)
C(39)-C(40)-C(41)-C(42)	-0.1(5)
C(40)-C(41)-C(42)-C(43)	0.2(5)
C(41)-C(42)-C(43)-C(38)	0.4(5)
C(43)-C(38)-C(39)-C(40)	1.0(4)
C(43)-C(38)-B(1)-C(26)	172.9(3)
C(43)-C(38)-B(1)-C(32)	-68.0(3)
C(43)-C(38)-B(1)-C(44)	52.7(3)
C(44)-C(45)-C(46)-C(47)	0.2(5)
C(45)-C(44)-C(49)-C(48)	0.0(4)
C(45)-C(44)-B(1)-C(26)	-81.2(3)
C(45)-C(44)-B(1)-C(32)	161.2(3)
C(45)-C(44)-B(1)-C(38)	39.0(3)
C(45)-C(46)-C(47)-C(48)	0.0(5)
C(46)-C(47)-C(48)-C(49)	-0.2(5)
C(47)-C(48)-C(49)-C(44)	0.2(5)
C(49)-C(44)-C(45)-C(46)	-0.2(4)
C(49)-C(44)-B(1)-C(26)	98.2(3)
C(49)-C(44)-B(1)-C(32)	-19.4(4)
C(49)-C(44)-B(1)-C(38)	-141.6(3)
B(1)-C(26)-C(27)-C(28)	-177.7(3)
B(1)-C(26)-C(31)-C(30)	177.9(3)
B(1)-C(32)-C(33)-C(34)	179.9(3)
B(1)-C(32)-C(37)-C(36)	179.7(3)
B(1)-C(38)-C(39)-C(40)	177.9(3)
B(1)-C(38)-C(43)-C(42)	-178.0(3)
B(1)-C(44)-C(45)-C(46)	179.3(3)
B(1)-C(44)-C(49)-C(48)	-179.4(3)
C(50)-C(51)-C(52)-C(53)	0.1(5)
C(51)-C(50)-C(55)-C(54)	-1.0(4)
C(51)-C(50)-B(2)-C(56)	77.6(3)
C(51)-C(50)-B(2)-C(62)	-160.8(3)
C(51)-C(50)-B(2)-C(68)	-41.6(4)
C(51)-C(52)-C(53)-C(54)	-1.5(5)

C(52)-C(53)-C(54)-C(55)	1.7(5)
C(53)-C(54)-C(55)-C(50)	-0.4(5)
C(55)-C(50)-C(51)-C(52)	1.2(4)
C(55)-C(50)-B(2)-C(56)	-99.6(3)
C(55)-C(50)-B(2)-C(62)	22.0(3)
C(55)-C(50)-B(2)-C(68)	141.2(3)
C(56)-C(57)-C(58)-C(59)	0.2(6)
C(57)-C(56)-C(61)-C(60)	0.4(5)
C(57)-C(56)-B(2)-C(50)	-34.5(4)
C(57)-C(56)-B(2)-C(62)	-153.1(3)
C(57)-C(56)-B(2)-C(68)	86.0(3)
C(57)-C(58)-C(59)-C(60)	0.4(6)
C(58)-C(59)-C(60)-C(61)	-0.6(6)
C(59)-C(60)-C(61)-C(56)	0.2(6)
C(61)-C(56)-C(57)-C(58)	-0.5(5)
C(61)-C(56)-B(2)-C(50)	150.9(3)
C(61)-C(56)-B(2)-C(62)	32.2(4)
C(61)-C(56)-B(2)-C(68)	-88.7(3)
C(62)-C(63)-C(64)-C(65)	0.3(5)
C(63)-C(62)-C(67)-C(66)	0.8(4)
C(63)-C(62)-B(2)-C(50)	-84.2(3)
C(63)-C(62)-B(2)-C(56)	35.6(3)
C(63)-C(62)-B(2)-C(68)	155.9(3)
C(63)-C(64)-C(65)-C(66)	0.3(5)
C(64)-C(65)-C(66)-C(67)	-0.4(5)
C(65)-C(66)-C(67)-C(62)	-0.2(4)
C(67)-C(62)-C(63)-C(64)	-0.9(4)
C(67)-C(62)-B(2)-C(50)	89.2(3)
C(67)-C(62)-B(2)-C(56)	-151.1(2)
C(67)-C(62)-B(2)-C(68)	-30.7(3)
C(68)-C(69)-C(70)-C(71)	0.7(5)
C(69)-C(68)-C(73)-C(72)	2.5(5)
C(69)-C(68)-B(2)-C(50)	149.9(3)
C(69)-C(68)-B(2)-C(56)	30.3(4)
C(69)-C(68)-B(2)-C(62)	-92.2(3)
C(69)-C(70)-C(71)-C(72)	0.7(4)

C(70)-C(71)-C(72)-C(73)	-0.4(5)
C(71)-C(72)-C(73)-C(68)	-1.3(5)
C(73)-C(68)-C(69)-C(70)	-2.2(4)
C(73)-C(68)-B(2)-C(50)	-33.3(4)
C(73)-C(68)-B(2)-C(56)	-152.9(3)
C(73)-C(68)-B(2)-C(62)	84.6(3)
B(2)-C(50)-C(51)-C(52)	-176.2(3)
B(2)-C(50)-C(55)-C(54)	176.4(3)
B(2)-C(56)-C(57)-C(58)	-175.6(3)
B(2)-C(56)-C(61)-C(60)	175.4(3)
B(2)-C(62)-C(63)-C(64)	173.0(3)
B(2)-C(62)-C(67)-C(66)	-173.0(3)
B(2)-C(68)-C(69)-C(70)	174.8(3)
B(2)-C(68)-C(73)-C(72)	-174.5(3)
O(6)-C(22)-C(23)-C(24)	-34.1(9)
C(22)-O(6)-C(25)-C(24)	-27.8(7)
C(22)-C(23)-C(24)-C(25)	17.6(9)
C(23)-C(24)-C(25)-O(6)	6.2(8)
C(25)-O(6)-C(22)-C(23)	39.7(8)

Symmetry transformations used to generate equivalent atoms:

Table C.10: Hydrogen bonds for **5** [\AA and $^\circ$].

D-H...A	d(D-H)	d(H...A)	d(D...A)	\angle (DHA)
O(5)-H(5)...O(6)	0.86	1.98	2.831(7)	171.8

Symmetry transformations used to generate equivalent atoms

C.12 References

1. Stoll, S.; Schweiger, A. *J. Magn. Reson.* **2006**, *178*, 42–55.
2. Goldsmith, J. I.; Hudson, W. R.; Lowry, M. S.; Anderson, T. H.; Bernhard, S. *J. Am. Chem. Soc.* **2005**, *127*, 7502–7510.
3. Grimme, S.; Antony, J.; Ehrlich, S.; Krieg, H. *J. Chem. Phys.* **2010**, *132*, 154104.
4. Tao, J. M.; Perdew, J. P.; Staroverov, V. N.; Scuseria, G. E. Climbing the density functional ladder: Nonempirical meta-generalized gradient approximation designed for molecules and solids. *Phys. Rev. Lett.* **2003**, *91*, 146401.
5. Weigend, F.; Ahlrichs, R. Balanced Basis Sets of Split Valence, Triple Zeta Valence and Quadruple Zeta Valence Quality for H to Rn: Design and Assessment of Accuracy. *Phys. Chem. Chem. Phys.* **2005**, *7*, 3297–3305.
6. (a) Valiev, M.; Bylaska, E. J.; Govind, N.; Kowalski, K.; Straatsma, T. P.; Van Dam, H. J. J.; Wang, D.; Nieplocha, J.; Apra, E.; Windus, T. L.; de Jong, W. A. NWChem: A Comprehensive and Scalable Open-Source Solution for Large Scale Molecular Simulations. *Comput. Phys. Commun.* **2010**, *181*, 1477–1489. (b) Neese, F. The ORCA program system. *Wiley interdisciplinary Reviews - Computational Molecular Science*, **2012**, *2:1*, 73-78.
7. (a) Klamt, A.; Schüürmann, G. COSMO: a new approach to dielectric screening in solvents with explicit expressions for the screening energy and its gradient. *J. Chem. Soc. Perkin Trans. 2.* **1993**, *2*, 799–805. (b) Marten, B.; Kim, K.; Cortis, C.; Friesner, R. A.; Murphy, R. B.; Ringnalda, M. N.; Sitkoff, D.; Honig, B. New Model for Calculation of Solvation Free Energies: Correction of Self-Consistent Reaction Field

Continuum Dielectric Theory for Short-Range Hydrogen-Bonding Effects. *J. Phys. Chem.* **1996**, *100*, 11775–11788.